UNIVERSITÀ DI PARMA

UNIVERSITA' DEGLI STUDI DI PARMA

DOTTORATO DI RICERCA IN
Scienza e Tecnologia dei Materiali

CICLO XXXVI

High efficiency and scalable pressure-less sintering of TiB_2 for enhanced strength and hardness applications

Coordinatore:
Chiar.mo Prof. Enrico Dalcanale

Tutore:
Chiar.ma Dott.ssa Diletta Sciti

Co-tutore:
Chiar.mo Dott. Simone Failla

Dottorando: Simone Taraborelli

Anni Accademici 2020/2021 – 2022/2023

Al mio, il tuo, il nostro obiettivo
che ad ogni passo, è sempre più vicino.

Abbreviations adopted

BF – Bright-Field

CIP – Cold Isostatic Pressing

CNB – Chevron Notched Beam

CTE – Coefficient of Thermal Expansion

EDM - Electrical Discharge Machining

EDS – Energy Dispersive X-Ray Spectroscopy

FS – Flexural Strength

HAADF – High-Angle Annular Dark Field

HEPBM – High-Energy-Planetary-Ball-Milling

HIP – Hot Isostatic Pressing

HP – Hot Pressing

HT – High Temperature

HV – Vickers Hardness

LPS – Liquid Phase Sintering

MWS – Microwave Sintering

PLS – Pressure-less Sintering

RP – Reactive Processing

RT – Room Temperature

SEM – Scanning Electron Microscopy

SH – Soft Homogenization

SPS – Spark Plasma Sintering

STEM – Scanning Transmission Electron Microscopy

TEM – Transmission Electron Microscopy

TMBs – Transition Metal Borides

XRD – X-Ray Diffraction

Abstract

Titanium diboride (TiB_2) is a promising material for commercial applications due to its excellent mechanical properties, melting point above 3000°C, wear resistance, and good electrical conductivity, similar to that of metals. However, its poor sinterability makes it difficult to fabricate fully dense components with good properties and mechanical performance. Sintering additives and different preparation methods can improve the sintering of TiB_2, but the effectiveness varies greatly.

In this thesis, various additives, preparation techniques, and sintering methods were systematically investigated to comprehensively analyze their impact. The main objective was to obtain a high-density material with good mechanical properties through pressure-less sintering, an easily scalable and very common technique at the industrial level.

This work can be divided into four parts:

In the first part, the impacts of different sintering aids (B_4C, Si_3N_4, and $MoSi_2$), preparation methods (ball-milling and high-energy-planetary-ball-milling), and their combination on the densification of TiB_2 were investigated through hot-pressing sintering. The shrinkage of the sample over time was recorded to study the densification rate and temperatures at which occurred. Residual porosity, microstructure, composition, and mechanical properties of the sintered material were measured to study how additives, preparation methods, and their possible synergy improved the densification of TiB_2. $MoSi_2$ added in amount of 5 vol% proved to be the best sintering aid, leading to complete densification due to the presence of a liquid phase. However, this left some silica pockets trapped between the grains. High-energy-planetary-ball-milling (HEPBM) alone was as effective in enhancing the sinterability thanks to grain refinements and WC doping, resulting in materials with a good relative density (93.4 %) and Vickers hardness (24.5 ± 0.6 GPa). The best result was obtained for the sample doped with $MoSi_2$ and prepared with high-energy-planetary-ball-milling. This sample achieved almost complete densification (> 98 %) by hot pressing at 1700°C and good Vickers hardness (24.4 ± 0.7 GPa) due to the synergistic effect of high-energy-milling and sintering aid.

The second part of this work was focused on pressure-less sintering treatments. Several sets of samples were sintered at various temperatures (from 1900 to 2100°C) and dwell times (from 60 to 120 minutes), to identify the best conditions. The amount of sintering aid was then optimized and scale-up tests were conducted at various temperatures for the best compositions. Residual porosity, microstructure, composition, and mechanical properties of the sintered materials were measured and compared to those obtained through hot pressing. Preliminary tests on sintering aids showed uncontrolled grain growth in all cases except for $MoSi_2$ additions. Higher densities and finer microstructures were achieved through high-energy-planetary-ball-milling, both without and with sintering aids. In the case of $MoSi_2$ addition, the additive and HEPBM worked together to create a

synergistic effect that results in better densification (98.1 %) and a finer microstructure (1.2 ± 0.6 μm). The effect increased as the amount of $MoSi_2$ was raised from 1 to 5 vol%. The Vickers hardness also followed the same trend, reaching the maximum value for the sample with 5 vol% of $MoSi_2$ (26.8 ± 2.7 GPa). The scale-up of the sample dimensions showed no significant variations in density, microstructure, and Vickers hardness.

The third part of the thesis explored the effect of high-energy-planetary-ball-milling with WC-Co media on the densification of TiB_2. Milling cycles of different durations were tested, and the resulting powders were characterized using XRD patterns, particle size analysis, SEM microscopy, and mass measurements. These powders were then pressure-less sintered, and the effects of milling time on densification, microstructure, and mechanical properties were evaluated. The reproducibility of the HEPBM process was investigated by repeating the same milling cycle one year later with more worn media. Finally, the role of WC was explored by preparing a mixture of TiB_2 and WC powders (without Co) and ball-milling the mixture. From HEPBM powders analysis it was observed that while the introduction of WC-Co increased linearly with time, the average particle size decreased significantly within the first 10 minutes after which the rate of size reduction slowed down progressively. Moreover, HEPBM mainly affected particles larger than 1.5 μm, while the added submicrometric WC-Co particles were smaller than 0.5 μm. All HEPBM samples pressure-less sintered at 2100°C for 60 minutes showed high relative densities (> 95%), while those added with simply ball-milled WC reached densities of around 75%, demonstrating the value of high-energy-planetary-ball-milling and the presence of Co during sintering.

The fourth part of this work was dedicated to mechanical thermal and electrical testing of pressure-less sintered TiB_2. Preliminary flexural strength tests were carried out in Faenza. Then, the mechanical, thermal, and electrical properties of specimens prepared at the Missouri University of Science and Technology were explored. Flexural strength and fracture toughness were measured at room and high temperature (1000-1600°C) to analyze the mechanical properties. Thermal conductivity tests were performed between 25 and 200°C, and between 200 and 2000°C, to obtain thermal properties. Electrical resistivity was measured for different currents at room temperature. The best flexural strength was obtained for TiB_2 sintered at 2100 °C in preliminary tests, but the specimens prepared at Missouri S&T had a narrower distribution of values. As the temperature increased, the flexural strength decreased, dropping above 1000°C and showing softening at 1600°C with non-elastic behavior and bending without breaking at low crosshead rates. Toughness remained relatively constant with temperature. Thermal properties (thermal conductivity, thermal diffusivity, and specific heat) were lower than those of monolithic TiB_2. The electrical resistivity of the material was similar to that of other transition metal borides and metals.

Overall, this thesis work presents an industrially scalable TiB_2 sintering strategy that utilizes high-energy-planetary-ball-milling, small amounts of sintering additives (< 5 vol%) and their synergy achieving good densities and microstructures. The thermomechanical properties (at room and high temperature) and the electrical properties of the resulting TiB_2 sintered through pressure-less-sintering have been analyzed and compared with the values present in the literature.

Keywords

- TiB_2
- Transition-metal borides
- High-energy-milling
- Hot-pressing sintering
- Pressure-less sintering
- Mechanical properties
- Thermal properties
- Electrical properties

List of publications

- Simone Taraborelli, Simone Failla, Elisa Sani, Diletta Sciti, Sintering, Mechanical and Optical Properties of TiB_2 Composites with and without High-Energy Milling, *Nanomaterials*. 13 (2023) 2683. https://doi.org/10.3390/nano13192683.

Table of contents

1. State of the art

1.1 Introduction

1.1.1 Transition metal borides

For several decades, transition metal borides (TMBs) such as TiB_2, ZrB_2, HfB_2, TaB_2, NbB_2 and CrB_2 have been explored because of their exceptional physical properties: indeed they display good thermal, mechanical, chemical and electrical properties, e.g., very high melting point, high hardness and also phonon and electron conduction; TMBs have been employed for a variety of applications such as wear resistant parts, electrodes [1–4], microelectronics [5], refractory linings [6–8], impact resistant armor, and cutting tools [9,10]. Furthermore, they have also attracted interest in the thermonuclear, aerospace and hypersonic fields.

However, in order to be used for economic applications these materials must be available in large quantities, at an affordable cost, have high reliability, long lifetime and finally a simple method of preparation is required. Unfortunately, many of the borides mentioned above do not satisfy all these prerequisites, and in particular the difficulty of sintering powder-derived parts limits their large-scale production and final cost.

The difficulty in sintering TMBs is bound to their unique properties, in fact they are a consequence of the strong covalent bonds present in the structure, which involve a low diffusion coefficient and a high melting temperature: therefore, sintering requires high temperatures, long dwell times and even high pressures.

1.1.2 Crystal Structure and Bonding

Boron can form various structural complexes containing one-, two-, and three-dimensional B networks depending on its electronic structure, therefore borides can display a wide range of compositions with metal:boron (M:B) ratios ranging from 4:1 (M_4B) to 1:12 (MB_{12}), where B:M ratio affects both properties and electronic structure [11].

In metal diborides, the largest and most important class of borides, there is a strong covalent bond between the boron atoms (B-B) and a weaker bond that combines a covalent and metallic character between titanium atoms (Ti-Ti) [12]; the strength of the M-B bond depends on the electron delocalization of the metal which acts as an electron donor, while boron acts as an electron acceptor [13–15]. Donor-acceptor interactions give M-B bonds ionic characteristics; however, these bonds also possess covalent characteristics emerging from the partial excitation of *d* electrons and the formation of *spd* hybrid configurations [16].

Titanium diboride (TiB_2) and others transition metal diborides of Group IV–VI (ZrB_2, HfB_2, TaB_2) possess primitive hexagonal crystal structures of the AlB_2 type.

AlB_2 structure is composed of alternating layers of boron and metal of hexagonal symmetry (Fig. 1.1 a), thus creating a two-dimensional, graphite-like, strong covalently bonded network for the boron atoms. The hexagonal unit cell belongs to the P6/mmm space group and contains one MB_2 formula unit. In the unit cell, M atoms are located at (0, 0, 0), while B atoms are at (1/3, 2/3, 1/2) and (2/3, 1/3, 1/2) (Fig 1.1 b).

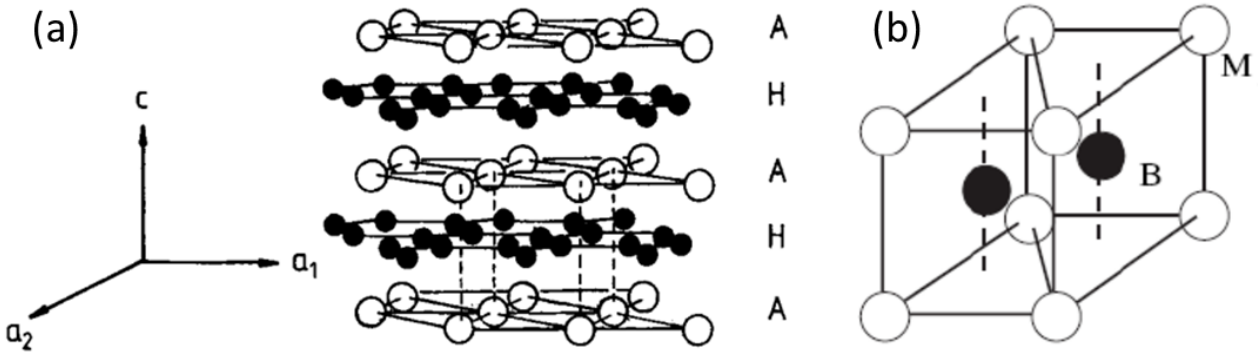

Fig. 1.1: (a) The alternating layers of the AlB_2 structure type [9] and (b) the hexagonal unit cell of single crystal TiB_2 [17].

Most of the properties of diborides like hardness, bulk modulus, melting temperature, coefficient of thermal expansion and thermal conductivity are determined by the strength and type of bonds. Specifically, hardness is influenced by the covalency of the M–B bonds (Fig. 1.2), the same forces that hold together the alternating boron and metal layers in these borides [18].

(a)

Boride	a (A°)	c (A°)	c/a	Bond ionicity (%)	Bond covalency (%)
MgB_2	3.083	3.521	1.14	96.8	3.2
TiB_2	3.028	3.228	1.07	22.8	77.2
VB_2	2.998	3.057	1.02	32.3	67.7
CrB_2	2.969	3.066	1.03	82.2	17.8
MnB_2	3.009	3.036	1.01	91.7	8.3
ZrB_2	3.170	3.533	1.11	81.9	18.1
HfB_2	3.142	3.476	1.11	79.8	20.2
NbB_2	3.086	3.306	1.07	52.1	47.9
TaB_2	3.088	3.241	1.05	50.7	49.3
AlB_2	3.009	3.262	1.08	91.8	8.2
YB_2	3.299	3.836	1.16	91.0	9.0

(b)

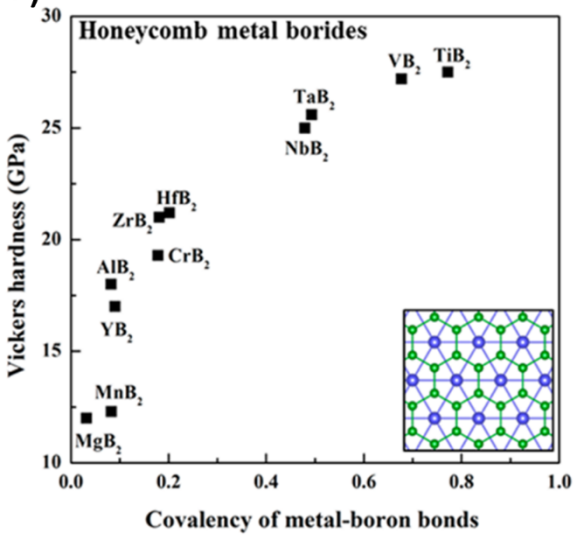

Fig. 1.2: (a) the M-B ionicity, covalency and lattice parameters of metal diborides with AlB_2 structure [19] and (b) Vickers hardness as a function of covalency of metal−boron bonds [18].

1.2 Titanium diboride

Among the transition metal borides, TiB_2 has the lowest density and the highest bond covalency (Fig. 1.2a). Titanium diboride exhibits exceptional hardness, high modulus, flexural strength (Table 1.1) and wear resistance making it a suitable material for impact armor, cutting tools and wear resistant coatings. Thanks to the good thermal and electrical conductivity, in addition to a chemical inertness, it is an excellent candidate for crucibles and electrical applications such as cathodes for aluminum electro-smelting and vacuum metal deposition equipment [20]. Moreover, electrical conductivity can be exploited in electro-discharge machining, a more cost-effective technique compared to conventional diamond tool machining for shaping the ceramic components.

Although TiB_2 has a high melting temperature (3225°C) it does not have good resistance to oxidation limiting its use for aerospace and high temperature applications in the presence of oxygen. It is also characterized by relatively low fracture toughness and exhibits sensitivity to slow subcritical crack growth [21] which limits its use to a wide range of engineering applications.

Property	**TiB_2 [22,23]**	**ZrB_2 [16,24]**	**HfB_2 [16,24]**	**TaB_2 [25]**	**VB_2 [18]**	**NbB_2 [26]**	**CrB_2 [27]**
Crystal Structure	Hexagonal P6/mmm AlB_2						
Density ($g\ cm^{-3}$)	4.52	6.12	12.21	12.60	5.07	6.97	5.22
Melting point (°C)	3225	3245	3380	3200	2745	2900	2200
Young's modulus (GPa)	565	489	445	551	577	539	-
Hardness (GPa)	25.0	23.0	19.8	25.6	27.2	20.3	22.1
Fracture toughness ($MPa\ m^{1/2}$)	6.2	3.6	3.3	4.5	-	4.0	3.7
Flexural strength (MPa)	400	450	510	555	-	-	-
CTE ($ppm\ K^{-1}$)	4.8	6.2	6.6	8.5	8.0	8.2	10.5
Thermal Conductivity [20] ($W\ m^{-1}\ K^{-1}$)	60-120	60	60-105	16-35	-	-	-
Electrical conductivity ($S\ m^{-1}$)	$4.9*10^6$	$1*10^7$	$9.1*10^6$	-	-	-	-
Oxidation resistance [20] (°C)	< 1200	< 1400	< 1400	< 1400	-	-	-

Table 1.1 Typical reference values for the material properties of some transition metal borides.

However, the main limiting factor in using TiB_2 for commercial applications is the difficulty of obtaining a completely dense material with good properties and mechanical performances due to its poor sinterability.

The densification of titanium diboride is hampered by the low self-diffusion coefficient of boron [28] and relatively high vapor pressure of its constituents [21], resulting from the presence of both ionic and covalent bonds [29] and consequently, long sintering times and high temperatures are required to obtain good densities (> 95% relative density).

To initiate grain boundary and volume diffusion in pure TiB_2 are necessary firing temperatures of 1800–2300°C. However, transition metal borides at high temperatures, as any material, show grain coarsening, including exaggerated grain growths, which lead to a variation of the mechanical properties. In particular, too large grain sizes in TMBs (>15 μm) are associated with a decrease in mechanical strength and formation of microcracks, partially due to thermal expansion anisotropy that cause residual thermal stresses [30].

Also, the presence of contaminants in the powders and the native oxide layer (composed of TiO_2 and B_2O_3) present on the surface of the grains regardless of the synthesis route can hinder sintering, cause uncontrolled grain growth or lead to the formation of trapped porosity [31,32]. Baik and Becher [33] studied the effects caused by the presence of oxides and divided them into two macro-areas based on sintering temperature:

- Low sintering temperatures (1400 to 1700°C), where the cause of the coarsening is the evaporation-condensation mechanism linked to B_2O_3 and other boron suboxides that enhance the grain growth without shrinkage;
- High sintering temperatures (1700°C or higher) in which the grains and particles growth is correlated to an increase in diffusivity due to titanium oxides.

To limit the negative effects due to the presence of oxygen, it is necessary to keep the total oxygen content below 0.5 wt% [33] or to use reducing agents to eliminate oxygen-bearing species.

To improve the densification of TMBs, sintering at lower temperatures and times, a series of techniques have been developed, listed below:

- use of various synthesis routes to obtain higher purity powders to minimize the effect due to contaminants or ultra-fine granulometry to increase the total particle surface for sintering mechanisms (section 1.3);
- various sintering techniques, adopting for example the use of an applied external pressure or electric current through the material (section 1.4.1);
- addition of sintering aids to promoting sintering and remove the oxide phases, also by liquid phase sintering, and improving the performance of the final material (section 1.4.2);

- reactive sintering (section 1.4.1.6) where the reaction between the constituents in the green body and its densification occur in the same thermal treatment [34,35];
- decrease particle grain size and introduction of defects through high energy milling (section 1.4.3) results in an increase of powder reactivity, internal energy, and surface area [20].

The final material properties (section 1.5), as well as purity, final porosity and grain size, vary significantly depending on the synthesis method, sintering technique and additives used, therefore it is necessary to tailor the production route according to the intended application.

1.3 Synthesis

There are many processing routes through which TiB_2 powders can be synthesized, these can be mainly divided into reactive, reduction and chemical processes which are distinguished by the reagents, the cost, and the final properties of the powder.

1.3.1 Reactive routes

Reactive processes are the simplest method and produce the highest quality TiB_2 starting from elemental precursor such as elemental boron (B) and titanium (Ti) or titanium hydride (TiH_2) in direct reactions (reaction 1.1 and 1.2). However, these processes are not applicable on a large scale due to the cost of the B and the low production rate in the reactors [9].

$$Ti + 2B \rightarrow TiB_2 \quad (1.1)$$

$$TiH_2 + 2B \rightarrow TiB_2 + H_2 \quad (1.2)$$

Both reaction 1 and 2 are highly exothermic ($\Delta H^o_{rxn} = -323.8$ kJ/mol and $\Delta H^o_{rxn} = -181.4$ kJ/mol, respectively, at 298 K [36,37]), especially the reaction 1.1 that is capable of self-sustaining once triggered: this type of reaction can be exploited in self-propagating high-temperature synthesis (SHS) or combustion synthesis, where a powdered mixture of the precursor elements is rapidly traversed by a combustion wave following ignition [38].

Although this technique allows to reach a high purity and a fine particle size (Figure 1.3.a), even ultrafine with additions of NaCl [39], at lower temperatures and processing times than other techniques, it is an uncontrolled reaction whose rapid cooling leads to large concentrations of lattice defects in the product [40].

1.3.2 Reduction routes

Reduction processes are the most common route, where titanium dioxide (TiO_2) (reactions 1.3-1.7) or titanium tetrachloride ($TiCl_4$) react with reducing agents such as C, B, B_4C, Al, Si and Mg. This process leads to the inevitable presence of impurities in the final powder, such as residual carbon, metals or oxides.

In materials where the presence of residual carbon is tolerated up to 3% by mass, carbothermal reduction (reaction 1.3a, Figure 1.3.b) is frequently used and it is the most used due to the high availability and low cost of the reagents [9,41]. This reaction is strongly endothermic with an enthalpy of formation at 298K of ΔH^{o}_{rxn}= 1322.7 kJ/mol, and becomes favorable at temperatures above 1600K for a p_{CO}/p = 1 or above 1300K for p_{CO}/p = 0.01 as shown by the Gibbs free energy equation (equation 3b) dependent on temperature (T) and relative pressure of CO (p_{CO}/p) [42].

Industrially, a mixture of the reagents is placed in a crucible, heated up to temperatures above 1500°C and kept at this temperature for around 15 hours, until the reaction is complete [43].

$$TiO_2 + B_2O_3 + 5\ C \rightarrow TiB_2 + 5\ CO^{\uparrow} \quad \textit{carbothermal reduction} \tag{1.3a}$$

$$\Delta G_T = 1338630 - 860.29T + 5RTln(p_{CO}/p),\ \text{J/mol} \tag{1.3b}$$

Boron and boron carbide can also be used as reducing agents in borothermal reduction (reaction 1.4, Figure 1.3.c) and boron carbide reduction (reaction 1.5), respectively. Borothermal reduction is particularly worthwhile when carbon contamination is to be avoided. The main advantage of these reactions is a higher purity and a finer particle size in the final product, however they are more expensive than carbothermal reduction [44,45]. The boron carbide process is carried out at 1600-2000°C (below the melting point of the boride) in tunnel furnaces under vacuum or in a hydrogen atmosphere.

$$TiO_2 + 4\ B \rightarrow TiB_2 + B_2O_2^{\uparrow} \quad \textit{borothermal reduction} \tag{1.4}$$

$$7\ TiO_2 + 5\ B_4C \rightarrow 7\ TiB_2 + 3\ B_2O_3^{\uparrow} + 5\ CO^{\uparrow} \quad \textit{boron carbide reduction} \tag{1.5}$$

The use of B_4C and C can be combined in boro/carbothermal reduction (reaction 1.6), this route allows the use of relatively cheap reagents and the achievement of a high purity TiB_2 with minimum losses of boron [46]. Furthermore, thanks to the combined action of B_4C and C, the densification of the final powders can be improved through the minimization of oxides in the synthesized material.

$$2\ TiO_2 + B_4C + 3\ C \rightarrow 2\ TiB_2 + 4\ CO^{\uparrow} \quad \textit{boro/carbothermal reduction} \tag{1.6}$$

One more possibility is the metallothermal reduction (reaction 1.7) which involves the reaction of TiO_2 and B_2O_3 with Al, Si or Mg in the metallic form. It cannot be used for materials for extreme environments applications, since the residual metallic impurities from this process could compromise the high temperatures properties [47,48]

$$TiO_2 + B_2O_3 + Al\ (Si, Mg) \rightarrow TiB_2 + Al_2O_3\ (SiO_2, MgO) \quad \textit{metallothermal reduction} \tag{1.7}$$

1.3.3 Chemical routes

Nanocrystalline TiB_2 can be obtained by chemical routes which include the solutions, reactions with boron-containing polymers, and pre-ceramic polymers which allow to reach particle sizes of up to 10-20 nm [49–51]. One of the principal methods for synthesizing TiB_2 involves the high-temperature hydrogen reduction of titanium tetrachloride ($TiCl_4$) and a boron halide (BX_3 with X = F, Cl, Br, etc). This process (reaction 1.8) is typically carried out at 1475°C [52].

$$TiCl_4 + 2\ BCl_3 + 5\ H_2 \rightarrow TiB_2 + 10\ HCl\uparrow \quad (1.8)$$

Bates et al. synthesized TiB_2 nanocrystallites (5-100 nm) through a solution phase process (reaction 1.9) involving $NaBH_4$ and $TiCl_4$, followed by heat treatment of the resulting amorphous precursor at temperatures ranging from 900 to 1100°C [53].

$$TiCl_4 + 2\ NaBH_4 \rightarrow TiB_2 + 2\ NaCl + 2\ HCl\uparrow + 3\ H_2\uparrow \quad (1.9)$$

Gu and coworkers employed a solvothermal method at 400°C in benzene to produce nanocrystalline TiB_2 [54]. This route involved a reaction between metallic sodium, amorphous boron powder, and $TiCl_4$ (reaction 1.10).

$$TiCl_4 + 2\ B + 4\ Na \rightarrow TiB_2 + 4\ NaCl \quad (1.10)$$

TiB_2 with nanometric particle size has been successfully synthesized also through the thermal decomposition of titanium borohydride (reaction 1.11) [52].

$$2\ Ti(BH_4)_3 \rightarrow 2\ TiB_2 + B_2H_6\uparrow + 9\ H_2\uparrow \quad (1.11)$$

Also sol–gel routes have been developed as energy-efficient and cost-effective methods for producing high-purity nanocrystalline TiB_2 powder (Figure 1.3.d) [55]. Nevertheless, extreme precaution had to be made during sub-micrometer powder handling due to their pyrophoric nature.

Regardless of the chosen synthesis route, it is essential to pay attention to controlling various powder characteristics, including initial particle size, particle size distribution, agglomeration, and purity. These factors play a crucial role in the subsequent densification process.

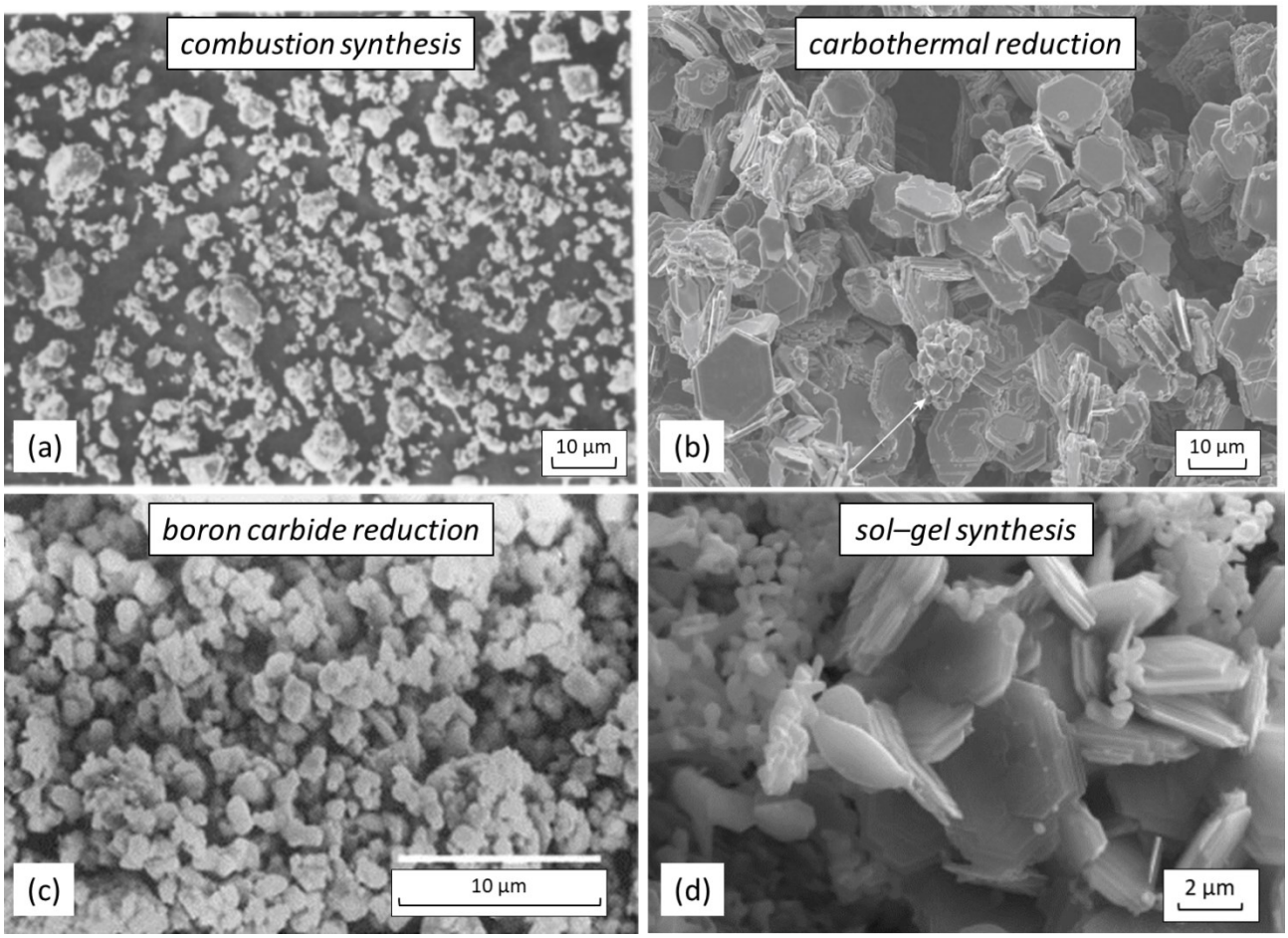

Fig. 1.3: Morphology and dimensions of TiB_2 powders synthesized through different routes: (a) sieved (< 10 pm) combustion-synthesized powders [40], (b) carbothermically reduced TiB_2 [42], (c) micrograins obtained by boron carbide reduction at 1800°C followed by milling with tungsten carbide media [56], (d) sol–gel-synthesized nanocrystalline TiB_2 powder [55].

1.4 Densification

Different sintering techniques, sintering additives and preparation methods can be used to improve the densification and properties of TiB_2, the main ones being described below.

1.4.1 Sintering methods

TMBs densification is usually achieved by solid-state sintering, in which the bonding and densification of particles are made by heating up the green body to a temperature corresponding to 70 – 90 % of their melting point. In solid-state sintering, the main transport mechanisms are lattice and grain-boundary diffusion. Occurring without the presence of a glassy phase, solid-state sintering is particularly useful for those materials with applications that require high electrical and thermal conductivities and good mechanical performance at elevated temperatures.

The use of pressure, pulsed current, or microwave radiation can reduce times and temperatures required for sintering leading to better final material properties.

1.4.1.1 Pressure-less sintering (PLS)

PLS is the cheapest and simplest method and allows to obtain the ceramic final material to near-net shape with complex geometries and/or large size using standard methods. It can also be made continuous, therefore is the most commonly used technique at an industrial level [57].

Pressure-less sintering is typically conducted in a resistance furnace with a graphite, tantalum or tungsten resistor or in an induction furnace with a graphite susceptor. The process is carried out under vacuum or atmospheres of Ar or H_2 [58].

As already mentioned, TiB_2 requires high temperatures to be able to sinter, obtaining high relative densities without any grain growth through conventional PLS is very difficult and may require one or more of the techniques to improve sintering listed above. To improve the densification in PLS, the methods adopted generally involve the use of sintering aids or powders with smaller initial particle sizes, obtained by an appropriate synthesis or by high-energy milling of the powders to the desired size. Baumgartner and Steiger [59] have demonstrated how it is possible to obtain TiB_2 up to a density higher than 99% using submicron powders obtained from a chemical route and sintered in PLS between 2100-2275°C for one hour (Fig. 1.4).

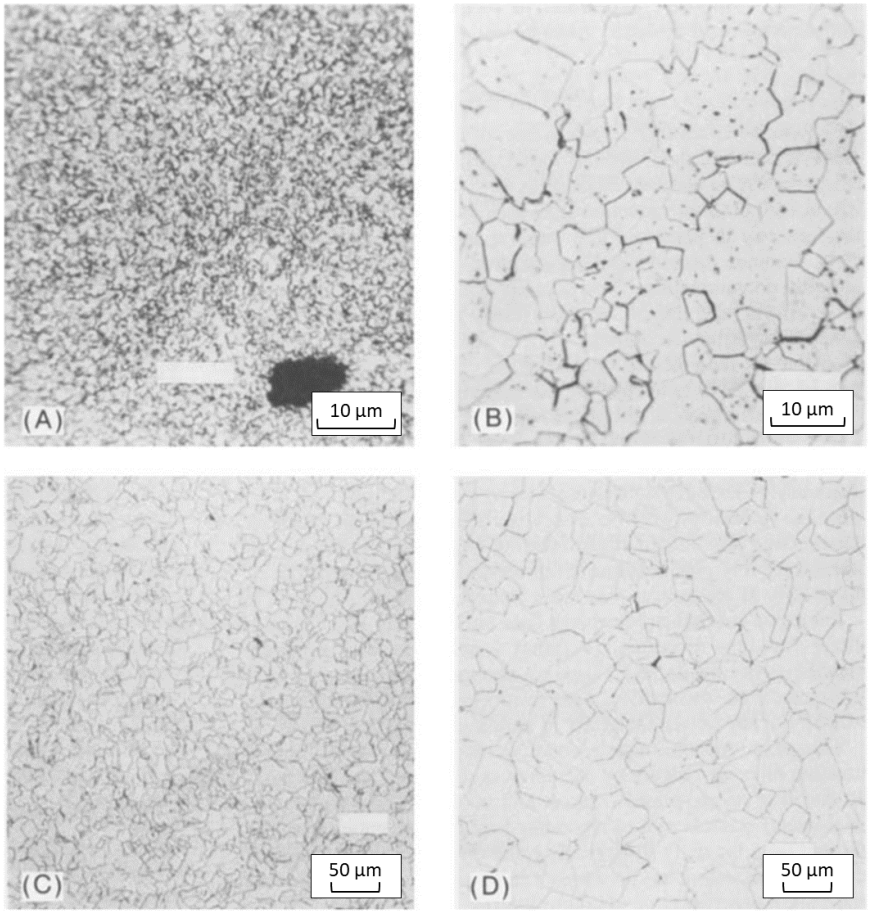

Fig. 1.4 Polished and etched TiB_2 microstructures produced at sintering temperatures of (A) 1800°C, (B) 2100°C, (C) 2200°C, and (D) 2275°C [59].

1.4.1.2 Hot pressing (HP)

By applying uniaxial pressure (usually between 20 and 50 MPa) during sintering, densification can be achieved at lower temperatures (1800-2000°C) and times. The simultaneous application of pressure and temperature is referred to as hot pressing sintering.

HP sintering like PLS is conducted under vacuum or in an inert atmosphere with heating via induction or graphite resistors. The dies normally used are of graphite (Fig. 1.5 a), which can be easily machined and normally does not react with the sample during hot pressing [58]. The possibility of measuring the displacement of the pistons during the sintering makes it possible to obtain a curve of the shrinkage of the sample as a function of time and temperature (Fig. 1.5 b), therefore, to study the evolution of densification and to better control the process and the final material.

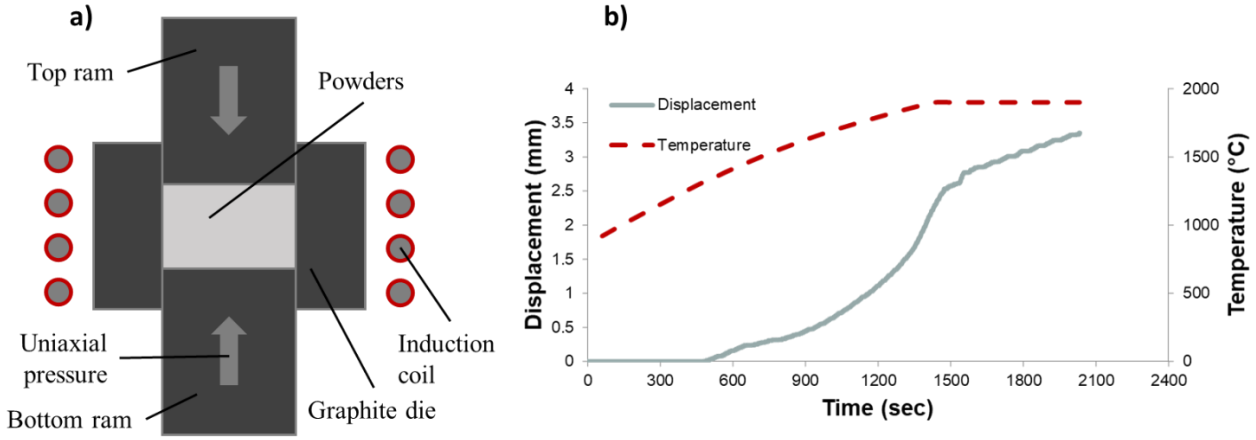

Fig. 1.5 (a) schematic representation of hot-pressing sintering and (b) sintering curve.

The hot-pressed composites have improved mechanical and thermal properties due to the fine-grained and denser microstructures than the PLS samples [57]. The main disadvantages of this technique concern the limitation to simple shapes and the difficulty of making the process continuous. Especially the former increases the final cost of products with complex geometries that would need further processing after sintering, since TiB_2 is difficult to machine, and its processing is expensive and complicated.

Raju et al. [60] reported that a relative density of 98% can be achieved for monolithic TiB_2 (without sintering aids) by HP sintering at 1800°C for 1 hour. The relative density can be further increased up to 99% at 1700°C using $MoSi_2$ as an additive.

1.4.1.3 Hot isostatic pressing (HIP)

It is possible to achieve high density for complex shapes ceramic materials in pressure assisted sintering by using an isostatic pressure that acts on the whole material in a uniform manner in hot isostatic sintering. Three routes (Fig. 1.6) can be adopted for this technique [61]:

- **Encapsulation method**: the green body is encapsulated by a membrane (typically a silica or Pyrex glass tube or a refractory metal container) which is deformable, impermeable to gases and allows the pressure to be applied isostatically. The main problems of this method are related to the encapsulation of large parts, the removal of the capsule without damaging the material, the prevention of reactions between the sample and the membrane and the cost;
- **Glass bath method**: this method bypasses the encapsulation step by immersing the green body in glass powder at a low softening temperature. It is necessary, however, to cover with a suitable coating material the sample to prevent the glass from penetrating the pores.
- **Sinter-plus HIP method**: to achieve the same benefits of applying isostatic pressure during densification without encapsulating, the green compacts is first pre-sintered under vacuum or in an inert atmosphere, and then in the same cycle, once the pores are closed, it is isostatically pressed at high temperature by introducing inert gas up to the desired pressure.

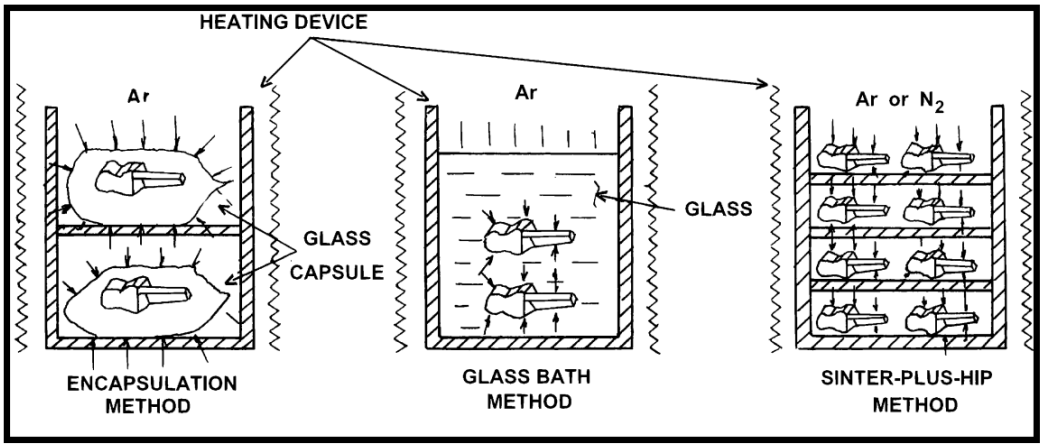

Fig. 1.6 Possible routes for the production of dense ceramics [62].

1.4.1.4 Spark plasma sintering (SPS)

Spark plasma sintering is a technique that through the simultaneous application of a uniaxial pressure and a pulsed direct current during sintering of the material reduces the time required for densification and grain growth [63–67].

Densification is improved both by direct heating of the die and the powder, if this is conductive as in the case of TiB_2 (but once sintering has started due to the presence of the oxide layer), and by high heating rates (up to hundreds of °C/min) reducing process times and grain growth. Mizuguchi et al. [68] compared ZrB_2 samples made for HP and for SPS, in the latter oxygen impurity was not detected even at the grain-boundaries because of the cleaning effect generated on the powder surfaces during spark plasma sintering. However, the sample also exhibited dislocations, the presence of which was associated with localized high stresses originating from rapid cooling.

High densities can be achieved with SPS even for monolithic TiB_2 in less than 10 minutes, Ahmadi et al. [69] achieved a relative density of 96% for TiB_2 and 100% for TiB_2 + 5 wt% AlN at 1900°C, for 7 min under 40 MPa pressure.

As for HP sintering, the disadvantages of this technique mainly concern the possibility of sintering only simple shapes and the difficulty of making a continuous process. However, the use of current can also promote unwanted reactions within the material giving rise to side products and a variation of the final properties. Mukhopadhyay et al. [70] observed the presence of TiB as a second phase at the matrix grain boundaries associated with a decrease in mechanical properties of TiB_2 compared to that obtained by hot pressing sintering.

1.4.1.5 Microwave sintering (MWS)

It is also possible to exploit the benefits of rapid and uniform heating in the bulk of the material as the SPS in microwave sintering in which the energy is directly coupled into the sample rather than being conducted into the specimen from an external heat source [71]. Even in this case the result is a faster densification and a lower grain growth.

There has been limited literature published on borides and carbides, renowned for their reflectivity. Because of the high loss of these species, the skin depth at 2.45 GHz is very shallow, of the order of millimeters, so microwave heating of these materials is a surface phenomenon comparable to inductive heating of a material like graphite [72].

Nonetheless, successful sintering of TiB_2 using this approach has been documented [73,74].

1.4.1.6 Reactive processing (RP)

In reactive processing, called reactive sintering (RS) if done without pressure or reactive hot pressing (RHP) if pressure-assisted, the final material is obtained directly from its precursors by making the synthesis and densification reactions take place simultaneously in a single in situ process. This technique can be divided into three categories: reaction of a porous solid preform in presence of a gas phase, solid preform reacting with liquid phase and reaction between solid powders [57].

Focusing on solid powders as precursors, they are heated up to the temperature at which the reaction gives the final product. As shown in the synthesis chapter (section 1.3), many reactions are exothermic and can increase the temperature locally, increasing the reaction rate or lead to overheating in some areas of the material. A transient liquid phase may form during the process and facilitate densification, if the melting temperature of one or more components is lower than the process temperatures or if a low temperature eutectic is formed [57].

The advantage of this process is that potentially a purer material with finer grain size and homogenized size distribution can be obtained. However, the lesser control over the process can lead

to the formation of side products from undesired reactions or intermediate products that remain within the material and cannot be removed between synthesis and sintering.

Starting from Ti and B_4C powders, Wen et al. [75] obtained an almost completely dense TiB_2-TiC_X sample at 1800°C for 60 min under a pressure of 35 MPa. No Ti_3B_4, TiB, Ti_2B_5 or free Ti phases were identified in the final material.

1.4.2 Sintering aids

The use of sintering additives is another strategy often used to improve the densification and final properties of ceramic materials. These sintering additives can be classified as:

1.4.2.1 Metallic additives and borides

Metallic additives such as Ti [76], Cr [77,78], Fe [79–82], Ni [82–85], Co [86,87] and Ta [85] or their combinations [86,88,89] were used successfully to achieve high relative density. These transition metals react with TiB_2 to form the corresponding metal borides, which have lower melting points and good wettability with TiB_2. To avoid the occurrence of reactions which consume titanium diboride, it is also possible to use the metallic borides directly as additives.

When the melting point of the metallic borides formed (Fe_3B, Ni_3B, Ni_2B, Co_3B etc) or other components is lower than the process temperature, the densification proceeds through a liquid phase sintering (LPS) mechanism. For instance, with addition of 1-3 vol.% of Ni or Ta high relative density (> 95%) was achieved via hot pressing at 2100°C for 60 minutes [85].

In the LPS, the liquid phase formed wets grain boundaries and forms a continuous boundary phase that promotes mass transfer and fills the pores, enhancing the densification of the compact. Through this mechanism it is possible to reduce the sintering temperature (1400 - 1700°C) and the process time however the higher mass transfer can cause also an accelerated grain growth [57,79]. Moreover, the evaporation of Fe-, Co-, or Ni- borides may cause entrapped gas pores.

The microstructures of liquid phase sintered TiB_2 (Fig. 1.7) are similar to those of other hard metals like WC-Co etc. The TiB_2 particles form a rigid skeleton of crystals, less faceted than in solid stat sintering, surrounded by the metal borides that act as a binder [29]. These binders must exhibit the ability to adequately wet, and partially dissolve and reprecipitate titanium diboride during the sintering process. At the same time, it is crucial to inhibit the formation of brittle and comparatively soft binary or ternary borides, as they tend to consume a significant portion of the ductile binder [90]. Therefore, hot pressing technique is necessary to achieve a uniform distribution of the liquid phase, particle rearrangement, and complete elimination of residual porosity.

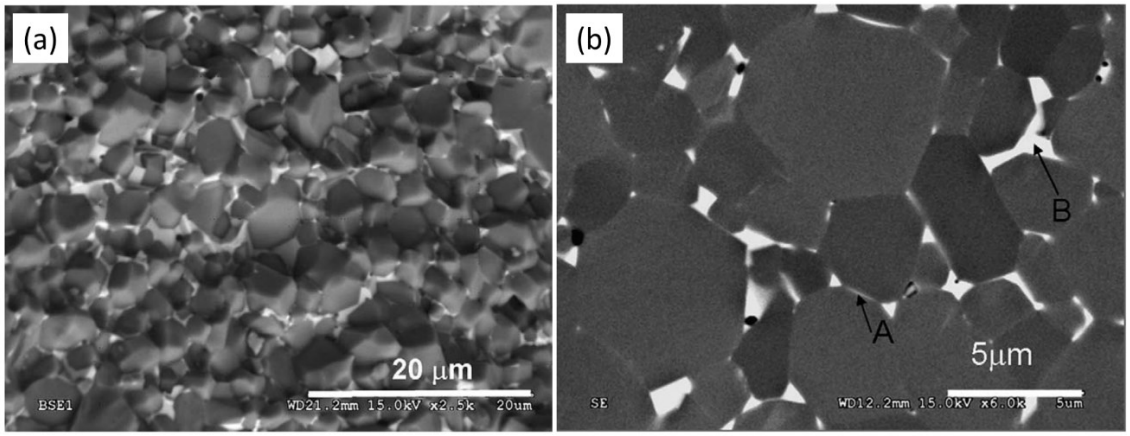

Fig. 1.7 SEM micrograph of the (a) fracture and (b) polished surface of TiB_2/Ni composites [84].

Tennery et al. [10] observed that the hot-pressed TiB_2 microstructure remained similar regardless of the initial Ni content, within the range of 10 to 20 wt % Ni, measuring just Ni_3B and TiB_2 phases. During the densification process, a significant amount of nickel is exuded from the compacts, resulting in similar final Ni contents across the compositions. According to their findings, the production of superior ceramics, characterized by high strength and other desirable properties, is achievable when most of the liquid phase is exuded from the compact under the applied pressure at high temperature in the die. This exudation process is strongly influenced by the particle size distribution and the oxygen content of the TiB_2 powders.

However, inclusion of a metallic binder is highly undesirable for high-temperature structural applications due to the low melting point of either the sintering liquid or metallic additives, resulting in incipient fusion and the degradation in the high-temperature properties [29]. Non-metallic additives are preferable for this type of application.

1.4.2.2 Carbon and carbides

Carbon [33,91] and other carbides such as SiC [31,92–95], B_4C [96–100], WC [101,102], TiC [75,103,104], TaC [105,106], NbC [107] can react with the thin oxygen-rich layer improving sinterability and reducing final grain size as described previously.

Torizuka et al. [92] sintered TiB_2 with SiC as sintering aid via a two-step sintering process: a first PLS sintering at 1500, 1700 or 1900°C in vacuum for 4 hours, followed by a HIP sintering at 1600°C under 200 MPa pressure for 2 hours. They showed that SiC sintering aids did not react with TiB_2, while the reaction with TiO_2 took place and produced SiO_2 and TiC (reaction 1.12). The increase in sinterability is associated with SiO_2 being liquid at process temperatures resulting in liquid phase sintering. The highest density value was obtained for SiC content equal to 2.5 wt%, at 1700 and 1900°C PLS beyond which the porosity started to rise again. Anyway, HIPing was necessary for the final densification and allowed 99% relative density to be achieved.

$TiO_2 + SiC \rightarrow SiO_2 + TiC$ (1.12)

Chen et al. [99] observed that the higher relative density and mechanical properties (flexural strength, hardness and fracture toughness) were obtained when B_4C was added at 10 wt% upon densification at 1850 for 10 minutes by SPS under a pressure of 48 MPa in vacuum. TiB_2-TaC spark-plasma sintered at 2050-2100°C for 5 minutes under 40MPa and TiB_2-NbC spark-plasma sintered at 2000°C for 5-30 minutes under 40MPa also showed the best results when the carbide was added at 10 wt% or less [106,107].

While SiC and B_4C does not react with TiB_2, Demirskyi et al. [105] reported the presence of a core-shell-like structure after spark-plasma sintering at 2000°C for 10 minutes under 40 MPa due to the reaction of TiB_2 and TaC resulting in a solid solution phase of tantalum titanium carboboride (Ti,Ta)(C,B) that surround the TiB_2 core (Figure 1.8). NbC also reacted with TiB_2 during the spark-plasma sintering at 2000°C leading to the formation of (Nb,Ti)C and (Ti,Nb)B phases [107].

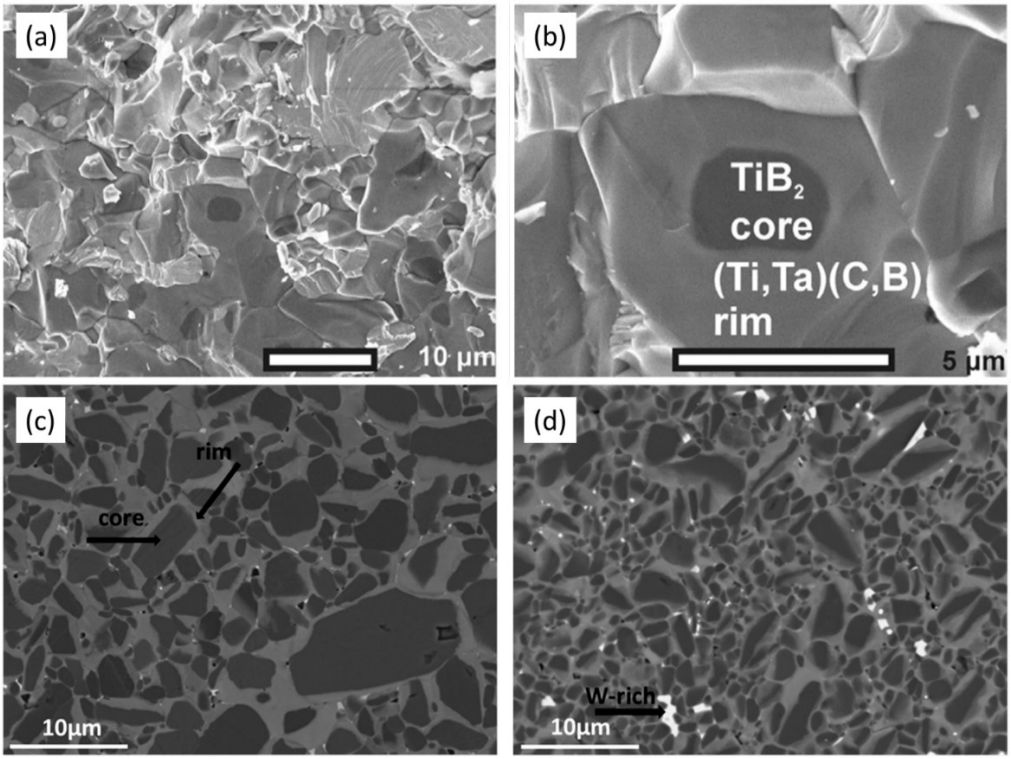

Fig. 1.8 Core-shell structure present in (a and b) TiB_2–TaC spark-plasma sintered ceramic [105] and (c) hot-pressed TiB_2 milled with WC media for 8 hours and (d) 24 hours [101].

Chao et al. [101] introduced inclusions of WC and some Co into the matrix by ball milling with WC-Co media obtaining high values of density, hardness, and elastic modulus after hot-pressing at 1900-1950°C for 30 min under 25 MPa of pressure. The WC added can react with surface TiO_2 and possibly with TiB_2 via reactions 1.13 and 1.14, equivalent to those observed in HfB_2 [108]. The final microstructure is of the core-shell type where the TiB_2 cores are surrounded by a shell of mixed boride $(Ti,W)B_2$ (Figure 1.6 c and d).

$$TiO_2 + 3\ WC \rightarrow TiC + 3\ W + 2\ CO^{\uparrow} \quad (1.13)$$

$$TiB_2 + 2\ WC \rightarrow TiC + 2\ WB + C \quad (1.14)$$

1.4.2.3 Nitrides

Also the addition of ceramic nitrides like Si_3N_4 [109,110], AlN [111] or TiN [112] has proven to be an effective method to improve the densification of TiB_2 by eliminating the surface oxide phase present on the particles and forming secondary phases such as TiN and BN.

Li et al. [111] evaluated the effects of AlN addition with amounts between 2.5 and 20 wt%. While AlN improved sinterability and mechanical properties (flexural strength, fracture toughness, Vickers hardness, and elastic modulus) in small amounts (≤ 5 wt%) by removing particle surface TiO_2 via reaction 1.15, when it was added in larger amounts (≥ 10 wt%) the trend was reversed. A relative density of 98% was achieved for TiB_2 + 5 wt% AlN hot-pressed at 1800°C for 60 minutes under an applied pressure of 30 MPa.

$$3\ TiO_2 + 4\ AlN \rightarrow 3\ TiN + 2\ Al_2O_3 + \frac{1}{2}\ N_2^{\uparrow} \quad (1.15)$$

Traces of BN were also found in the sample due to the subsequent reaction between product N_2 and TiB_2 according to reaction 1.16.

$$TiB_2 + \frac{3}{2}\ N_2 \rightarrow TiN + 2BN \quad (1.16)$$

Similarly, Si_3N_4 in small amount (≤ 2.5 wt%) can enhance densification, mechanical properties and suppress grain growth through the elimination of the oxide phase with reactions 1.17 and 1.18.

$$3\ TiO_2 + Si_3N_4 \rightarrow 3\ TiN + 3\ SiO_2 + \frac{1}{2}\ N_2^{\uparrow} \quad (1.17)$$

$$2\ B_2O_3 + Si_3N_4 \rightarrow 4\ BN + 3\ SiO_2 \quad (1.18)$$

For amounts > 5 wt% of Si_3N_4 mechanical properties and densification are not improved, due to extensive formation of secondary phases at the grain boundaries [109].

Shayesteh et al [112] observed that the presence of TiN (5 wt%) in TiB_2 spark-plasma sintered at 1900°C for 7 minutes under 40 MPa leads to an almost complete densification (99.9%) and to the formation of in-situ nano-sized hBN secondary phase. Evidence that TiN itself also plays a role in promoting sintering of TiB_2 with nitrides aids.

1.4.2.4 Oxides

Although the presence of oxygen has negative effects on sinterability as shown above, some oxides such as ZrO_2 [113–116], Al_2O_3 [117], Nb_2O_5 and Y_2O_3 [118] have been successfully used in sintering obtaining good density values and mechanical properties.

Muraoka et al. [114] have obtained higher density values than monolithic TiB_2 with ZrO_2 amounts between 10 and 30 mol% (also Y_2O_3 was present at 2 mol%) by hot isostatic pressing for 120 minutes at 1500°C under 196 MPa, no reaction between TiB_2 and ZrO_2 was observed, contrary to the results of Watanahe and Shoubu [113] who conducted hot pressing at higher temperature (1800-1900°C) and observed the formation of considerable amount (≈ 45 vol%) of t-ZrO_2 and (Ti,Zr)B_2.

ZrO_2 has a remarkable toughening effect via microcracking and stress-induced transformation mechanisms by increasing the fracture toughness to a maximum of 11.2 MPa $m^{1/2}$ with 30 mol% of additive, almost 3 times higher than monolithic TiB_2. The bending strength was increased from 645 MPa for the sample without additive to a maximum of 910 with 20 mol% ZrO_2 (Figure 1.9).

González et al. [118] obtained high densities and hardness values higher than monolithic TiB_2 for the samples sintered for SPS at 1950°C with Nb_2O_5, ZrO_2 and Y_2O_3 as additives, respectively. From the interaction of TiB_2 with ZrO_2 and Nb_2O_5, phases of (Zr,Ti)B_2 and (Nb,Ti)B_2 respectively were formed. In the case of Y_2O_3, the presence of a secondary phase consisting of Ti, B, O and Y was associated with the formation of Y_3BO_6 at the interface between the two phases [119].

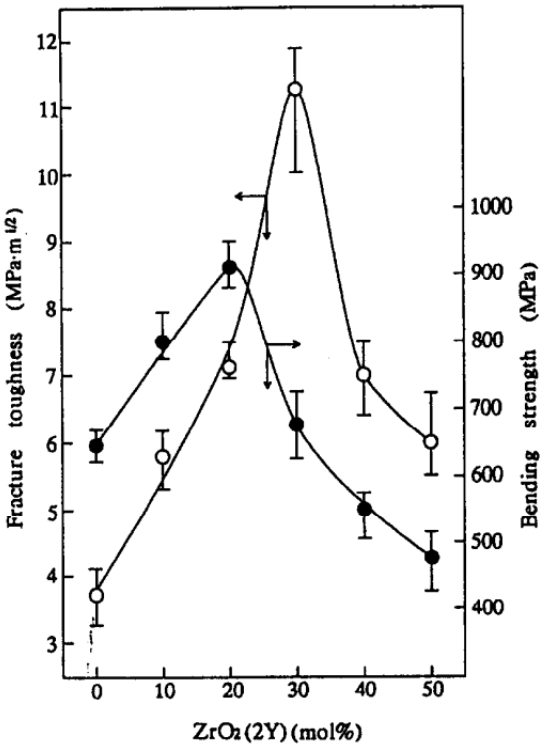

Fig. 1.9 Fracture toughness and bending strength of TB_2-ZrO_2 (2 mol% Y_2O_3) composites densified by hot isostatic pressing for 120 minutes at 1500°C under 196 MPa [114].

1.4.2.5 Disilicides

Metal disilicides ($MeSi_2$ with Me = Ti [120–124], Mo [60,125–128], Cr [129] and W [130]) have been added improving densification and oxidation resistance of TiB_2.

Raju et al. [120] hot-pressed TiB_2 with various amounts of $TiSi_2$ at 1650°C showing an improvement with increasing amount of additive. Samples up to 5 wt% of $TiSi_2$ after sintering were mainly composed of TiB_2 and Ti_5Si_3 while in the sample with 10 wt% of disilicide also $TiSi_2$ phases were identified. Ti_5Si_3 has been indicated to come from the reaction between $TiSi_2$ and TiO_2 which produces it together with SiO_2, the latter however has not been clearly identified in the matrix.

Since the $TiSi_2$ (T_m = 1540°C) is melted at the process temperature the densification proceeds mainly by liquid phase sintering. The sample with 5 wt% $TiSi_2$ achieved the maximum value of hardness, elastic modulus, flexural strength, and fracture toughness at room temperature.

At 900°C TiB_2–2.5 wt.% $TiSi_2$ has the highest hardness value, while TiB_2–5 wt.% $TiSi_2$ maintains the higher strength up to 500°C, at 1000°C the flexural strength of all additived materials drops compared to monolithic TiB_2 due to grain pullouts and microcracking [121].

The addition of $MoSi_2$ resulted in the reaction with TiO_2 and the formation of Mo_5Si_3 and Ti_5Si_3 in the work conducted by Raju et al. [60]. After sintering TiB_2 with WSi_2 additions, Murthy et al. [130] observed the disappearance of WSi_2 and the appearance of W_5Si_3 and SiO_2 peaks in the XRD spectra.

1.4.3 High Energy Planetary Ball Milling (HEPBM)

High energy planetary ball milling with WC-Co media is another method currently used to improve the sintering of TiB_2-based materials: the powders are milled in a planetary mill (Fig. 1.10) with grinding media and inner walls of the jar made of WC-Co.

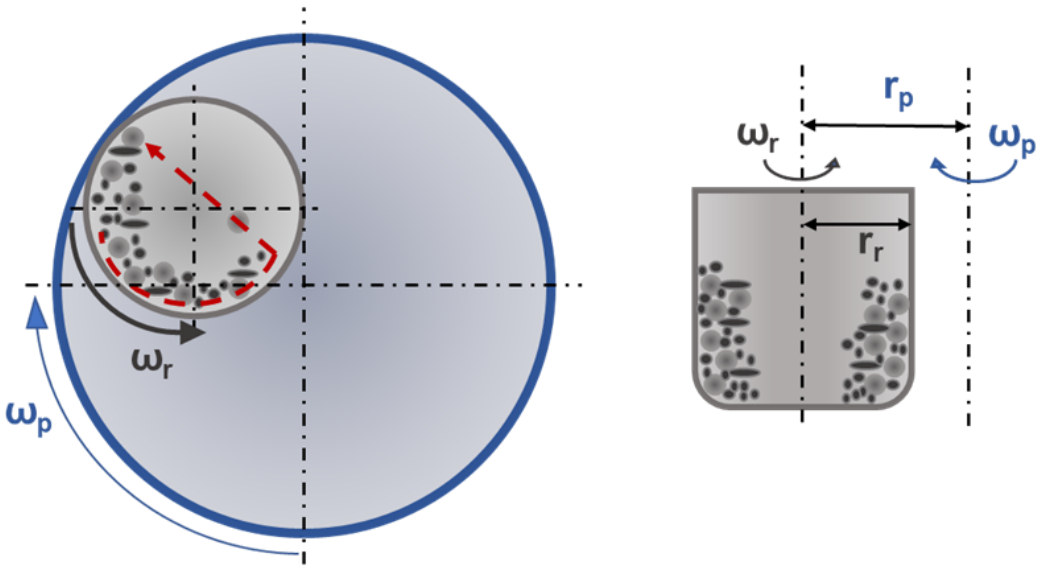

Fig. 1.10 A schematic diagram of the planetary ball mill and the jar [131].

HEPBM improves densification by reducing grain size from a few microns down to hundreds of nanometers [132,133], increasing the surface area and surface energy of the particles, introducing defects, and in addition, the debris from the grinding media remaining in the powder acts as a sintering additive [87,134–136].

The main drawbacks of this method concern the control of milling and contamination, since the WC-Co media decrease in mass and size as they are consumed by the HEPBM cycles and the difficulty of scaling planetary milling to an industrial level.

Sintering of TiB_2 high energy milled with WC-Co results in a core-shell structure where pure TiB_2 grains are surrounded by a shell of $(Ti,W)B_2$ solid solution with variable W content. The final microstructure suggests a densification mechanism involving a transient liquid phase and diffusion at high temperatures [137]. As the amount of W in the solid solution increases, the hardness and stiffness at room temperature decrease due to enhanced activation of dislocation plasticity, potentially resulting in greater energy absorption prior to failure.

1.5 Material properties

To evaluate the real effect of synthesis, sintering methods and additives on the final material density measurements and microstructural analyzes are only the first step, in fact, these parameters have repercussions on the material properties and applications even for samples with the same porosity or size of the grains. The main properties that are usually measured are described below.

1.5.1 Elastic properties

Elastic properties can be evaluated through two independent moduli, the elastic modulus E and the shear modulus G. Both moduli are intrinsic properties of the material which mainly depends on its porosity and composition, increasing as the density and purity of TiB_2 increases (Fig. 1.11). They are usually measured by strain measurement, resonance and ultrasonic methods [138].

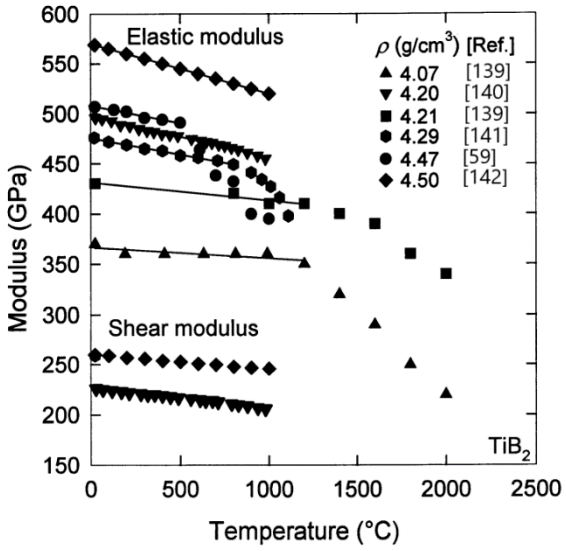

Fig. 1.11 The temperature dependence of the elastic and shear moduli of TiB_2 for various densities [22].

Spoor et al. [143] calculated a maximum E of 569 GPa and a maximum G of 259 GPa for TiB_2 at full density using equation 1.19, where E and P are the measured modulus and porosity fraction, respectively, and E_0 is the modulus of the fully dense material:

$$E = E_0(1 - 2P + P^2) \quad (1.19)$$

Among the different TMBs, TiB_2 exhibits the highest room-temperature elastic modulus [20].

Although the elastic and shear modulus can vary widely due to porosity, the value of both moduli decreases with a constant slope for temperatures below 1000°C which is dE/dT = –(0.032 ± 0.015) GPa/K for E and dG/dT = –(0.015 ± 0.002) GPa/K for G (Fig. 1.8) [22]. For temperatures above 1000°C the elastic modulus decreases rapidly as the temperature increases.

1.5.2 Strength

Strength for polycrystalline ceramic materials generally refers to the flexural strength, which can be measured with 3-point or 4-point bending. In addition, specimen sizes can also vary, thus results are not always directly comparable.

However, flexural strength shows a direct dependence on the particle size (Fig. 1.12 a) and density (Fig. 1.10) of the final material. In particular, Fahrenholtz et al. [16] highlighted how TMBs strengths, in general, show an inverse square root relation with grain size ($GS^{-1/2}$) as would be expected for ceramics free from other, larger flaws (Fig 1.12 b).

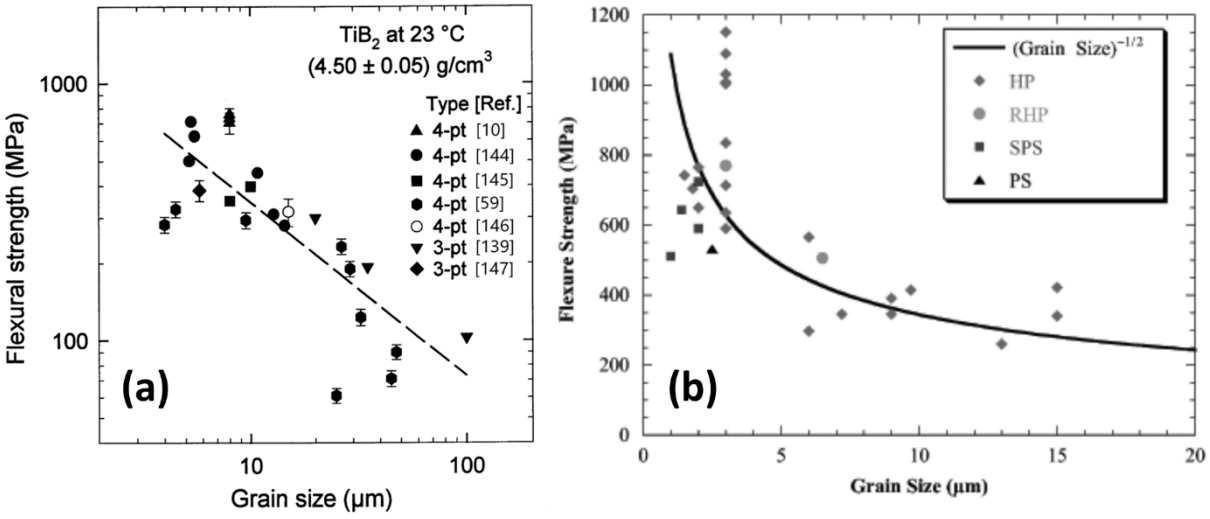

Fig. 1.12 Room temperature flexural strength as a function of grain size for (a) TiB_2 at a fixed density [22] and (b) literature diborides [16].

The high temperature strength properties are also very sensitive to microstructural phase assemblage, grain boundary phases, the content and the type of additives [20,121]. For example, metallic additives (chapter 1.4.2.1) that promote densification through liquid phase sintering, in addition to causing grain growth, have been shown to be detrimental to strength at high temperatures [21].

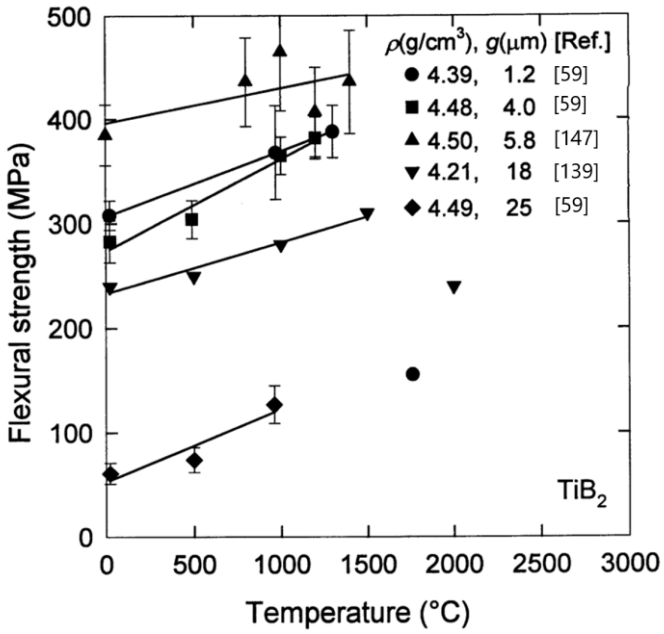

Fig. 1.13 The temperature dependence of the flexural strength of TiB_2 in three-point bending for various densities and grain sizes [22].

At elevated temperatures up to 1500°C, the flexural strength increases with a constant and very similar slope between samples of various densities and particle sizes (Fig. 1.13). The mean value calculated by Munro [22] is $(\partial\sigma_f/\partial T) = (0.06 \pm 0.02)$ MPa/K. The increase of TiB_2 strength with temperature can be attributed to the relaxation of residual internal stresses that arise from anisotropic thermal expansion stress [59].

1.5.3 Fracture Toughness

One of the main limitations of TiB_2 is its low fracture toughness making it sensitive to small surface and internal flaws [148]. This property is mainly influenced by density, grain size, which finds its optimum between 5 and 12 μm [22], and by the type and content of additives and chemical impurities.

As can be seen from Fig. 1.14 the toughness value for TiB_2 can vary greatly depending on the sintering cycle and sintering aid.

Raju and Basu [120] observed an increase in fracture toughness with the amount of $TiSi_2$ sintering aid and a maximum of 5.8 MPa for TiB_2 - 5wt%$TiSi_2$. The increase in toughness was associated with crack deflection by ceramic particulates. Crack deflection enhances the fracture toughness by reducing the stress intensity at the crack tip during propagation, consequently decreasing the driving force acting on the crack. It is widely recognized that either residual strain within the composite or weak matrix/second-phase interfaces can lead to crack deflection.

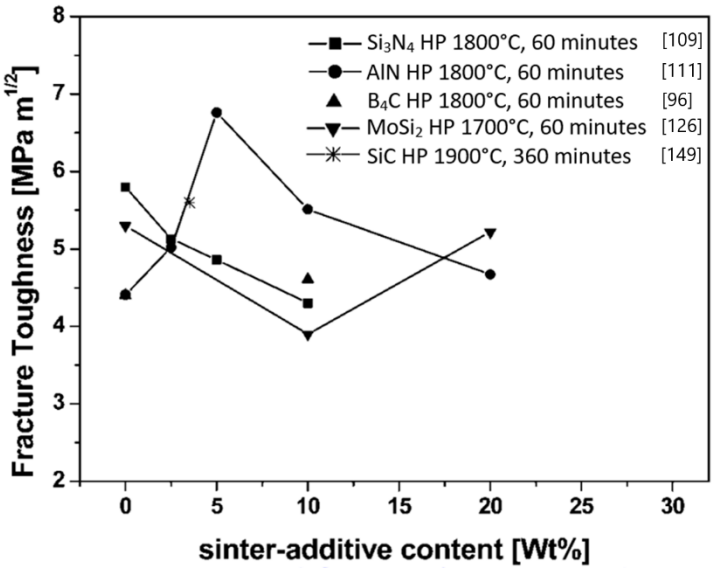

Fig. 1.14 Fracture toughness as a function of the type and content of additives. [21].

1.5.4 Hardness

Hardness, usually carried out by indentation, is one of the most used mechanical measures to test the quality of ceramic materials such as borides and carbides. It is strongly influenced by density and grain size but also residual stresses, toughening phases, microstructural textures and composition of grain boundaries. Furthermore, the value may vary depending on the method used and the load applied [150].

The room temperature hardness for fully dense TiB2 is approximately 25 GPa [74,126,151], the use of additives improves hardness mainly by reducing the grain size and increasing the relative density of the material. The sintering technique also has a remarkable effect, Mukhopadhyay et al. [70] have observed how the use of SPS can significantly reduce the hardness, probably due to the formation of TiB which has a lower hardness value (16 GPa).

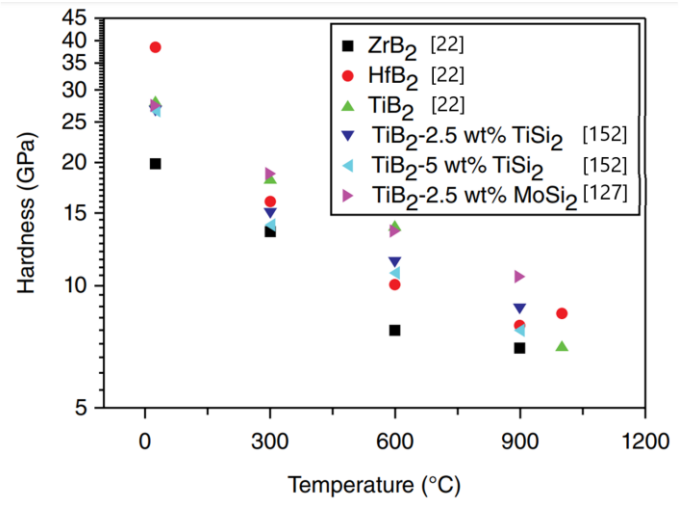

Fig. 1.15 The temperature dependence of the hardness of TiB_2 and other borides [20].

Temperature dependence of hardness is a standard analytical tool to evaluate high-temperature mechanical behavior [20,29]. For metal borides, as for other ceramic materials, the hardness decreases with increasing temperature (Fig. 1.15), due to the increased deformation during indentation caused by the high temperature softening of the material.

1.5.5 Thermal properties

The specific heat (C_P), the amount of energy absorbed per unit mass to increase the temperature 1 K, does not depend on grain size or the type of impurity [22]. It increases as the temperature increases, with greater rate below 500°C and with a smaller but constant slope above that temperature (Fig. 1.16).

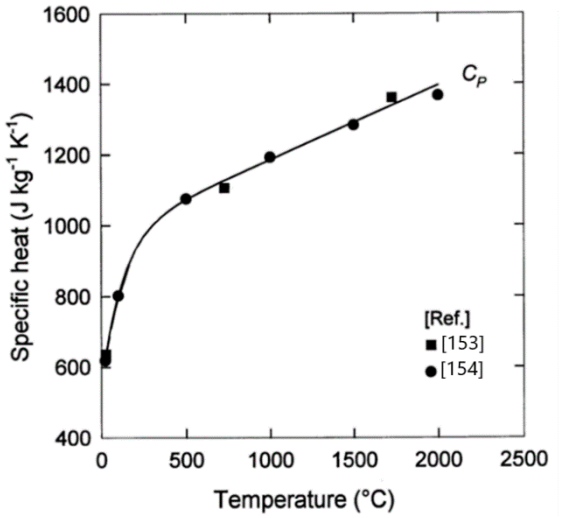

Fig. 1.16 Specific Heat C_P of TiB_2 as a function of temperature [22].

Thermal conductivity measures the ability of TiB_2 to transmit heat, it depends on temperature and other physical factors that can influence the movement of phonons, such as porosity, and is therefore related to the steady-state heat flow. It can be calculated as:

$$\kappa = \rho C_P D \tag{20}$$

Where ρ is the density, C_P the specific heat and D the thermal diffusivity. Unlike conductivity, thermal diffusivity measures the aptitude of a substance to transmit, not heat, but a temperature variation and pertains to transient heat flow.

From the few data available in the literature (Fig. 1.17), it appears that diffusivity decrease while thermal conductivity remains constant for TiB_2 as the temperature increases.

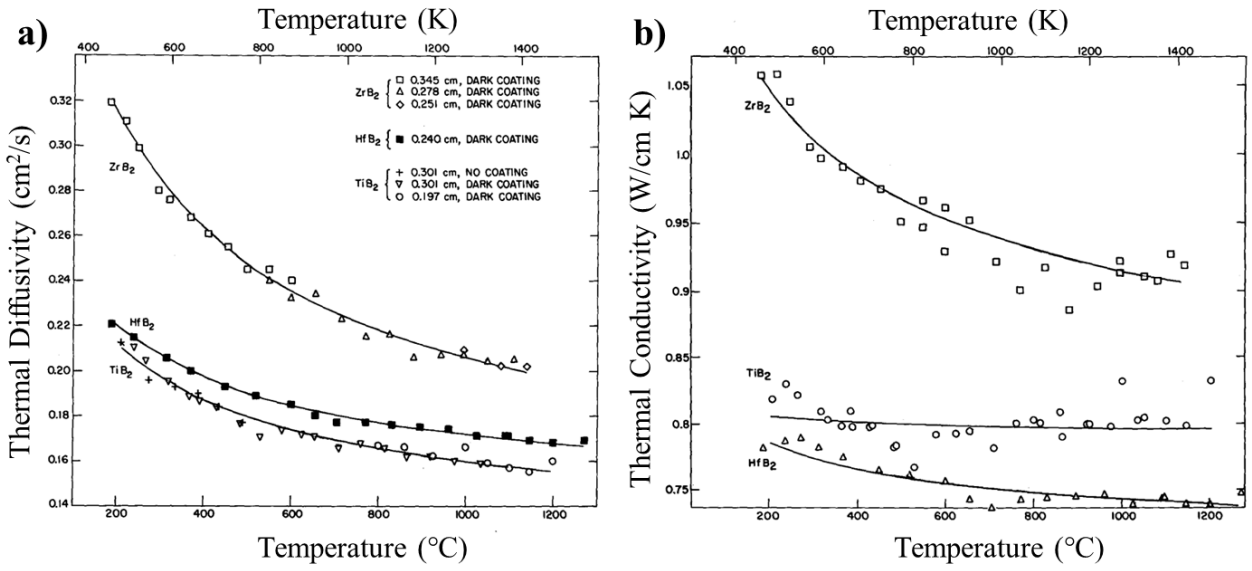

Fig. 1.17 (a) Thermal Diffusivity D and (b) Thermal Conductivity κ of TiB_2 , ZrB_2 and HfB_2 as a function of temperature [155].

1.5.6 Electrical properties

The electrical resistivity, which indicates how much TiB_2 resists the passage of an electric current and therefore also how conductive it is, depends on the density and on the quantity and type of impurities. McLeod et al. [156] observed an increase in resistivity with porosity and comparable values between monocrystalline and high relative density (99%) polycrystalline samples.

The electrical resistivities of TiB_2 and ZrB_2 as a function of temperature are shown in Fig. 1.17, both materials exhibit metal-like electrical conduction behavior, where resistivity increases with temperature due to increased scattering of conducting electrons by lattice phonons [23].

It is interesting to note that the resistivity of pure titanium metal (42 Ω·cm at room temperature) is much larger than that of TiB_2 [157].

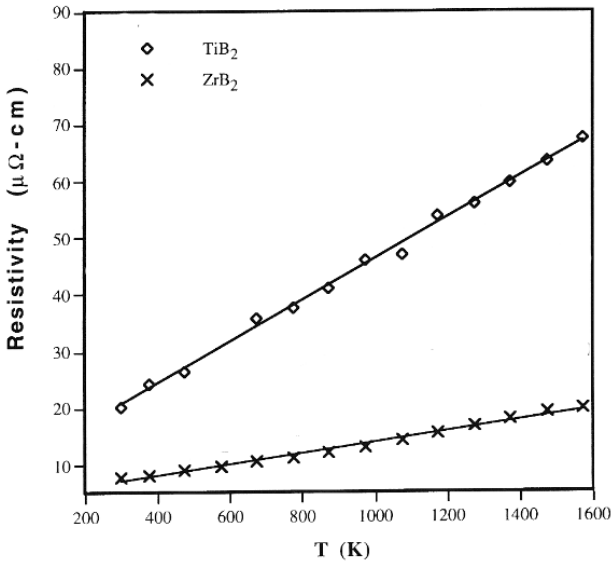

Fig. 1.17 Electrical resistivity of TiB_2 and ZrB_2 as a function of temperature [23].

1.6 Ceramic materials for ballistic applications

The main function of ballistic protection is to prevent the penetration of a projectile; therefore, it is possible to evaluate its effectiveness through the ability to stop various types of projectiles and one or more numbers of shots. Furthermore, since it has to be worn on person, it should be as light as possible. Finally, a last parameter to consider from a commercial point of view is the final cost of the product.

The evaluation criteria for a ballistic material are therefore the relative density, energy absorption capacity, damage resistance, and multiple impact resistance [158]. Ceramic materials such as alumina (Al_2O_3, density 3,95 g/cm³), silicon carbide (SiC, density 3,21 g/cm³) and boron carbide (B_4C, density 2,52 g/cm³) are excellent materials for ballistic protection due to their high hardness, good mechanical properties and low density, which provide a great mechanical strength/density ratio compared to other materials [159,160].

Alumina is the most cost-effective and most widely used technical ceramic of these [161,162] B_4C on the other hand has the highest cost, lowest density and best mechanical properties of the three [163], finally, SiC has intermediate cost and properties [164].

The thickness of the ceramic specimen has a significant effect on the ballistic performance [165,166]. For alumina and silicon carbide in particular, performance increases linearly as thickness increases. The advantage of lighter materials is the possibility of increasing the thickness for the same weight of the final product [167].

1.6.1 Mechanical properties and ballistic performance

Despite the large number of studies done to delineate the relationship between mechanical properties and ballistic performance in the past (Table 1.2), the contribution and effect of each property is still not fully understood [168,169]. Typically, the properties sought in ballistic materials are hardness, flexural strength, fracture toughness, and Young's modulus [160,169,170].

Ceramic property	Effect on ballistic performance
Density	Bulletproof armor weight
Hardness	Projectile damage
Young Modulus	Propagation of shock waves
Mechanical Resistance	Resistance to multiple impacts
Fracture Toughness	Multiple impacts resistance; field durability
Fracture mode (inter- or trans-granular)	Energy absorption

Table 1.2 Relationship of properties of ceramic materials with emphasis on ballistic performance [158].

Generally, hardness and fracture toughness show an inverse relationship in ceramic materials, however both play a crucial role in stopping the projectile. The hardness should be at least higher than that of the projectile [171], thus higher tungsten carbide–cobalt core/tungsten carbide AP tip commonly used in projectiles, as it helps to shatter and erode the projectile on impact (Fig. 1.18). On the other hand, fracture toughness reduces shattering and improves the ability to withstand multiple shots of the material, making it more effective [172].

Fracture toughness can be increased through toughening methods such as in the case of ZrO_2 addition (section 1.4.2.4) where residual stresses generate microcracks which can deflect and branch the main crack. However, it is not easy to optimize the amount of stress and microcracks in the material which can result in a significant decrease in the mechanical properties.

Since failure in ceramic bodies subjected to ballistic impacts is governed by bending stresses [161,173,174], higher flexural strength also results in a better ability to withstand multiple shots, in fact it improves the amount of load it can withstand before breaking [160].

The elastic modulus influences the impedance and the propagation of the shock wave, reducing its speed and increasing the absorbed energy [175]. Furthermore, higher modulus values lead to a longer dwell time and therefore a greater interaction between ceramic and projectile which results in greater damage to the projectile and better ballistic performance [176].

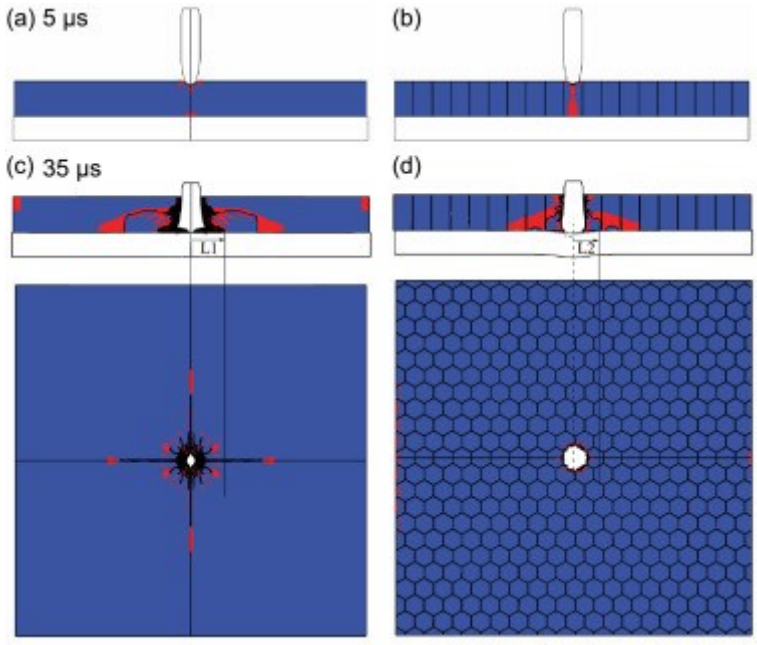

Fig. 1.18 Damage pattern of the two armor designs at 5 µs and 35 µs [177].

1.6.2 Microstructure

The microstructure of ballistic ceramic materials is essential in order to achieve the desired mechanical properties, and therefore the ballistic performance, in the final product [178,179]. The most important parameters are the relative density, which dramatically influences the elastic modulus, and the grain size which has an impact on hardness and flexural strength [160].

For this reason, the choice and optimization of the synthesis and sintering process is essential to control not only the final cost of the material but also the microstructure and its properties.

The mode of fracture is also important, as it determines the amount of energy absorbed by the fragmentation of the material. In particular, an intergranular fracture, since it takes a more tortuous path through grain boundaries and involves a greater surface area, results in higher energy absorption than a transgranular fracture [180,181].

1.6.3 Titanium diboride

Despite the advantages listed above, the alumina-based ceramics, although cheaper, have lower performances and are progressively less used, while boron carbide has a phase change collapse of the crystal structure under the action of extremely high speed and pressure, an amorphization phenomenon of weakening the elastic resistance occurs, and it is very expensive to produce [182]. For these reasons, TiB_2 appears to be an attractive alternative option, given the very high hardness and strength that are particularly sought after in ballistic materials. Due to the higher density, however, TiB_2 is not suitable for personal protection as much as vehicle protection, in fact it was successfully adopted by the M2IFV modified infantry combat vehicles by the American Cerayne and Cercom [182].

1.7 References

[1] R.C. Dorward, J.R. Payne, Energy savings through the use of an improved aluminum reduction-cell cathode. Technical progress report, April 1, 1981-June 30, 1981, Kaiser Aluminum and Chemical Corp., Pleasanton, CA (USA). Center for Technology, 1981. https://www.osti.gov/biblio/5268401 (accessed July 8, 2023).

[2] B. Stucker, W. Bradley, P.T. Eubank, S. Norasetthekul, B. Bozkurt, Zirconium diboride/copper EDM electrodes from selective laser sintering, in: 1997 Int. Solid Free. Fabr. Symp., 1997.

[3] B. Stucker, M. Malhotra, X. Qu, Recent developments in selective laser sintering of ZyrkonTM EDM electrodes, in: Int. Congr. Appl. Lasers Electro-Opt., Laser Institute of America, San Diego, California, USA, 1999: pp. F158–F161. https://doi.org/10.2351/1.5059268.

[4] Z.J. Jin, M. Zhang, D.M. Guo, R.K. Kang, Electroforming of Copper/ZrB_2 Composites Coatings and Its Performance as Electro-Discharge Machining Electrodes, Key Eng. Mater. 291–292 (2005) 537–542. https://doi.org/10.4028/www.scientific.net/KEM.291-292.537.

[5] J. Sung, D.M. Goedde, G.S. Girolami, J.R. Abelson, Remote-plasma chemical vapor deposition of conformal ZrB2 films at low temperature: A promising diffusion barrier for ultralarge scale integrated electronics, J. Appl. Phys. 91 (2002) 3904–3911. https://doi.org/10.1063/1.1436296.

[6] K. Kiyoharu, S. Satoshi, K. Otojirou, I. Toshihiro, K. Tetsuhiko, N. Hiroshi, I. Takaya, H. Yuichi, Corrosion Resistance and Electric Resistance of ZrB_2 Monolithic Refractory, Taikabutsu Overseas. 24 (2004) 206.

[7] Kida O., 木田音次郎, Monolithic refractory material and waste melting furnace using the same, JP2000335969A, 2000. https://patents.google.com/patent/JP2000335969A/en?oq=+JP2000335969 (accessed June 12, 2023).

[8] N. Kaji, H. Shikano, I. Tanaka, Development of ZrB2-Graphite Protective Sleeve for Submerged Nozzle., Taikabutsu Overseas. 14 (1994) 39–43.

[9] R. Telle, L.S. Sigl, K. Takagi, Boride-Based Hard Materials, in: R. Riedel (Ed.), Handb. Ceram. Hard Mater., Wiley-VCH Verlag GmbH, Weinheim, Germany, 2000: pp. 802–945. https://doi.org/10.1002/9783527618217.ch22.

[10] V.J. Tennery, C.B. Finch, C.S. Yust, G.W. Clark, Structure-Property Correlations for TiB2-Based Ceramics Densified using Active Liquid Metals, in: R.K. Viswanadham, D.J. Rowcliffe, J. Gurland (Eds.), Sci. Hard Mater., Springer US, Boston, MA, 1983: pp. 891–909. https://doi.org/10.1007/978-1-4684-4319-6_49.

[11] G. Akopov, M.T. Yeung, R.B. Kaner, Rediscovering the Crystal Chemistry of Borides, Adv. Mater. 29 (2017) 1604506. https://doi.org/10.1002/adma.201604506.

[12] Y. Han, Y. Dai, D. Shu, J. Wang, B. Sun, Electronic and bonding properties of TiB2, J. Alloys Compd. 438 (2007) 327–331. https://doi.org/10.1016/j.jallcom.2006.08.056.

[13] W.N. Lipscomb, D. Britton, Valence Structure of the Higher Borides, J. Chem. Phys. 33 (1960) 275–280. https://doi.org/10.1063/1.1731097.

[14] S.A. Nemnonov, A.Z. Menshikov, K.M. Kolobova, E.Z. Kurmayev, V.A. Trapeznikov, Study of the Electronic Structure and Interatomic Bonds in Some Compounds and Binary Alloys by the Method of X-Ray Spectroscopy, Trans. Metall. Soc. Aime. 245 (1969). https://www.elibrary.ru/item.asp?id=23096835 (accessed June 14, 2023).

[15] A.H. Silver, P.J. Bray, NMR Study of Bonding in Some Solid Boron Compounds, J. Chem. Phys. 32 (1960) 288–292. https://doi.org/10.1063/1.1700918.

[16] W.G. Fahrenholtz, G.E. Hilmas, I.G. Talmy, J.A. Zaykoski, Refractory Diborides of Zirconium and Hafnium, J. Am. Ceram. Soc. 90 (2007) 1347–1364. https://doi.org/10.1111/j.1551-2916.2007.01583.x.

[17] I.R. Shein, A.L. Ivanovskii, Elastic properties of mono- and polycrystalline hexagonal AlB_2-like diborides of s, p and d metals from first-principles calculations, J. Phys. Condens. Matter. 20 (2008) 415218. https://doi.org/10.1088/0953-8984/20/41/415218.

[18] P. Wang, R. Kumar, E.M. Sankaran, X. Qi, X. Zhang, D. Popov, A.L. Cornelius, B. Li, Y. Zhao, L. Wang, Vanadium Diboride (VB_2) Synthesized at High Pressure: Elastic, Mechanical, Electronic, and Magnetic Properties and Thermal Stability, Inorg. Chem. 57 (2018) 1096–1105. https://doi.org/10.1021/acs.inorgchem.7b02550.

[19] X.L. Chen, Q.Y. Tu, M. He, L. Dai, L. Wu, The bond ionicity of MB_2 (M = Mg, Ti, V, Cr, Mn, Zr, Hf, Ta, Al and Y), J. Phys. Condens. Matter. 13 (2001) L723–L727. https://doi.org/10.1088/0953-8984/13/29/105.

[20] B.R. Golla, T. Bhandari, A. Mukhopadhyay, B. Basu, Titanium Diboride, in: W.G. Fahrenholtz, E.J. Wuchina, W.E. Lee, Y. Zhou (Eds.), Ultra-High Temp. Ceram., John Wiley & Sons, Inc, Hoboken, NJ, 2014: pp. 316–360. https://doi.org/10.1002/9781118700853.ch13.

[21] B. Basu, G.B. Raju, A.K. Suri, Processing and properties of monolithic TiB2 based materials, Int. Mater. Rev. 51 (2006) 352–374. https://doi.org/10.1179/174328006X102529.

[22] R.G. Munro, Material properties of titanium diboride, J. Res. Natl. Inst. Stand. Technol. 105 (2000) 709. https://doi.org/10.6028/jres.105.057.

[23] M. Rahman, C.C. Wang, W. Chen, S.A. Akbar, C. Mroz, Electrical Resistivity of Titanium Diboride and Zirconium Diboride, J. Am. Ceram. Soc. 78 (1995) 1380–1382. https://doi.org/10.1111/j.1151-2916.1995.tb08498.x.

[24] E. Zapata-Solvas, D.D. Jayaseelan, H.T. Lin, P. Brown, W.E. Lee, Mechanical properties of ZrB2- and HfB2-based ultra-high temperature ceramics fabricated by spark plasma sintering, J. Eur. Ceram. Soc. 33 (2013) 1373–1386. https://doi.org/10.1016/j.jeurceramsoc.2012.12.009.

[25] X. Zhang, G.E. Hilmas, W.G. Fahrenholtz, Synthesis, densification, and mechanical properties of TaB2, Mater. Lett. 62 (2008) 4251–4253. https://doi.org/10.1016/j.matlet.2008.06.052.

[26] K. Sairam, J.K. Sonber, T.S.R.Ch. Murthy, C. Subramanian, R.K. Fotedar, R.C. Hubli, Reaction spark plasma sintering of niobium diboride, Int. J. Refract. Met. Hard Mater. 43 (2014) 259–262. https://doi.org/10.1016/j.ijrmhm.2013.12.011.

[27] J.K. Sonber, T.S.R.Ch. Murthy, C. Subramanian, S. Kumar, R.K. Fotedar, A.K. Suri, Investigation on synthesis, pressureless sintering and hot pressing of chromium diboride, Int. J. Refract. Met. Hard Mater. 27 (2009) 912–918. https://doi.org/10.1016/j.ijrmhm.2009.05.008.

[28] H. Schmidt, G. Borchardt, C. Schmalzried, R. Telle, S. Weber, H. Scherrer, Self-diffusion of boron in TiB2, J. Appl. Phys. 93 (2002) 907–911. https://doi.org/10.1063/1.1530715.

[29] G.B. Raju, B. Basu, Development of High Temperature TiB_2-Based Ceramics, Key Eng. Mater. 395 (2008) 89–124. https://doi.org/10.4028/www.scientific.net/KEM.395.89.

[30] N.L. Okamoto, M. Kusakari, K. Tanaka, H. Inui, M. Yamaguchi, S. Otani, Temperature dependence of thermal expansion and elastic constants of single crystals of ZrB2 and the suitability of ZrB2 as a substrate for GaN film, J. Appl. Phys. 93 (2002) 88–93. https://doi.org/10.1063/1.1525404.

[31] A. Sabahi Namini, S.N. Seyed Gogani, M. Shahedi Asl, K. Farhadi, M. Ghassemi Kakroudi, A. Mohammadzadeh, Microstructural development and mechanical properties of hot pressed SiC reinforced TiB2 based composite, Int. J. Refract. Met. Hard Mater. 51 (2015) 169–179. https://doi.org/10.1016/j.ijrmhm.2015.03.014.

[32] A. Masi, C. Alvani, A.A. Armenio, M. Bellusci, G. Celentano, C.F. Zignani, F. Fabbri, A.L. Barbera, F. Padella, M. Pentimalli, E. Silva, A. Vannozzi, F. Varsano, Effect of oxygen contamination on densification of Fe(Se,Te), J. Phys. Conf. Ser. 1559 (2020) 012051. https://doi.org/10.1088/1742-6596/1559/1/012051.

[33] S. Baik, P.F. Becher, Effect of Oxygen Contamination on Densification of TiB2, J. Am. Ceram. Soc. 70 (1987) 527–530. https://doi.org/10.1111/j.1151-2916.1987.tb05699.x.

[34] A.L. Chamberlain, W.G. Fahrenholtz, G.E. Hilmas, Reactive hot pressing of zirconium diboride, J. Eur. Ceram. Soc. 29 (2009) 3401–3408. https://doi.org/10.1016/j.jeurceramsoc.2009.07.006.

[35] O. Popov, V. Vishnyakov, L. Poperenko, I. Yurgelevych, T. Avramenko, A. Ovcharenko, Reactively sintered TiB2-based heteromodulus UHT ceramics with in-situ formed graphene for machinable concentrated solar light absorbers, Ceram. Int. 48 (2022) 17828–17836. https://doi.org/10.1016/j.ceramint.2022.03.053.

[36] Thermochemical Data of Pure Substances, 3rd Edition | Wiley, Wiley.Com. (n.d.). https://www.wiley.com/en-ae/Thermochemical+Data+of+Pure+Substances%2C+3rd+Edition-p-9783527619825 (accessed July 6, 2023).

[37] J. Zhao, H. Ding, X. Tian, W. Zhao, H. Hou, Thermodynamic Calculation on the Formation of Titanium Hydride, Chin. J. Chem. Phys. 21 (2008) 569–574. https://doi.org/10.1088/1674-0068/21/06/569-574.

[38] S.K. Mishra, L.C. Pathak, Self-Propagating High-Temperature Synthesis (SHS) of Advanced High-Temperature Ceramics, Key Eng. Mater. 395 (2009) 15–38. https://doi.org/10.4028/www.scientific.net/KEM.395.15.

[39] A.K. Khanra, L.C. Pathak, S.K. Mishra, M.M. Godkhindi, Effect of NaCl on the synthesis of TiB2 powder by a self-propagating high-temperature synthesis technique, Mater. Lett. 58 (2004) 733–738. https://doi.org/10.1016/j.matlet.2003.06.003.

[40] M. Ouabdesselam, Z.A. Munir, The sintering of combustion-synthesized titanium diboride, J. Mater. Sci. 22 (1987) 1799–1807. https://doi.org/10.1007/BF01132409.

[41] R.V. Krishnarao, J. Subrahmanyam, Studies on the formation of TiB2 through carbothermal reduction of TiO2 and B2O3, Mater. Sci. Eng. A. 362 (2003) 145–151. https://doi.org/10.1016/S0921-5093(03)00523-9.

[42] I.A. Blokhina, V.V. Ivanov, S.D. Kirik, N.S. Nikolaeva, Carbothermal synthesis of TiB2 powders of micron size, Inorg. Mater. 52 (2016) 550–557. https://doi.org/10.1134/S0020168516060017.

[43] N.J. Welham, Mechanical enhancement of the carbothermic formation of TiB2, Metall. Mater. Trans. A. 31 (2000) 283–289. https://doi.org/10.1007/s11661-000-0072-8.

[44] W.G. Fahrenholtz, J. Binner, J. Zou, Synthesis of ultra-refractory transition metal diboride compounds, J. Mater. Res. 31 (2016) 2757–2772. https://doi.org/10.1557/jmr.2016.210.

[45] W.-M. Guo, Z.-G. Yang, G.-J. Zhang, Synthesis of submicrometer HfB2 powder and its densification, Mater. Lett. 83 (2012) 52–55. https://doi.org/10.1016/j.matlet.2012.06.012.

[46] J.K. Sonber, T.S.R.Ch. Murthy, C. Subramanian, S. Kumar, R.K. Fotedar, A.K. Suri, Investigations on synthesis of ZrB2 and development of new composites with HfB2 and TiSi2, Int. J. Refract. Met. Hard Mater. 29 (2011) 21–30. https://doi.org/10.1016/j.ijrmhm.2010.06.007.

[47] K. Nishiyama, T. Ono, A. Nakayama, H. Sakai, M. Koishi, M. Abe, Nano-atomization of titanium diboride using ordered mixture and metallothermic reaction methods, Surf. Coat. Int. Part B Coat. Trans. 86 (2003) 169–174. https://doi.org/10.1007/BF02699649.

[48] T. Ohkubo, T. Ono, K. Nishiyama, S. Niwa, H. Sakai, M. Koishi, M. Abe, Preparation of ZrB_2 and HfB_2 by Metallothermic Reduction of ZrO_2, $ZrSiO_4$, and HfO_2, J. Jpn. Soc. Powder Powder Metall. 52 (2005) 664–669. https://doi.org/10.2497/jjspm.52.664.

[49] Y.M. Burov, Y.M. Grigoŕsev, S.G. Kuz'minskaya, Thermodynamic study of synthesis of titanium boride by the method of condensation combustion of gases, Combust. Explos. Shock Waves. 33 (1997) 548–552. https://doi.org/10.1007/BF02672740.

[50] L. Chen, Y. Gu, Z. Yang, L. Shi, J. Ma, Y. Qian, Preparation and some properties of nanocrystalline ZrB2 powders, Scr. Mater. 50 (2004) 959–961. https://doi.org/10.1016/j.scriptamat.2004.01.018.

[51] L. Chen, Y. Gu, L. Shi, Z. Yang, J. Ma, Y. Qian, Synthesis and oxidation of nanocrystalline HfB2, J. Alloys Compd. 368 (2004) 353–356. https://doi.org/10.1016/j.jallcom.2003.08.086.

[52] D.L. Segal, Chemical Routes for the Preparation of Powders, in: R. Freer (Ed.), Springer Netherlands, Dordrecht, 1990: pp. 3–11. https://doi.org/10.1007/978-94-009-2101-6_1.

[53] S.E. Bates, W.E. Buhro, C.A. Frey, S.M.L. Sastry, K.F. Kelton, Synthesis of titanium boride (TiB)2 nanocrystallites by solution-phase processing, J. Mater. Res. 10 (1995) 2599–2612. https://doi.org/10.1557/JMR.1995.2599.

[54] Y. Gu, Y. Qian, L. Chen, F. Zhou, A mild solvothermal route to nanocrystalline titanium diboride, J. Alloys Compd. 352 (2003) 325–327. https://doi.org/10.1016/S0925-8388(02)01173-8.

[55] Ľ. Bača, N. Stelzer, Adapting of sol–gel process for preparation of TiB2 powder from low-cost precursors, J. Eur. Ceram. Soc. 28 (2008) 907–911. https://doi.org/10.1016/j.jeurceramsoc.2007.09.028.

[56] C. Subramanian, T.S.R.Ch. Murthy, A.K. Suri, Synthesis and consolidation of titanium diboride, Int. J. Refract. Met. Hard Mater. 25 (2007) 345–350. https://doi.org/10.1016/j.ijrmhm.2006.09.003.

[57] L. Rangaraj, C. Divakar, V. Jayaram, Processing of Refractory Metal Borides, Carbides and Nitrides, Key Eng. Mater. 395 (2009) 69–88. https://doi.org/10.4028/www.scientific.net/KEM.395.69.

[58] H. Pastor, Metallic Borides: Preparation of Solid Bodies — Sintering Methods and Properties of Solid Bodies, in: V.I. Matkovich (Ed.), Boron Refract. Borides, Springer, Berlin, Heidelberg, 1977: pp. 457–493. https://doi.org/10.1007/978-3-642-66620-9_25.

[59] H.R. Baumgartner, R.A. Steiger, Sintering and properties of titanium diboride made from powder synthesized in a plasma-arc heater, J. Am. Ceram. Soc. 67 (1984) 207–212.

[60] G.B. Raju, A. Mukhopadhyay, K. Biswas, B. Basu, Densification and high-temperature mechanical properties of hot pressed TiB2–(0–10 wt.%) MoSi2 composites, Scr. Mater. 61 (2009) 674–677. https://doi.org/10.1016/j.scriptamat.2009.05.031.

[61] M.H. Bocanegra-Bernal, Hot Isostatic Pressing (HIP) technology and its applications to metals and ceramics, J. Mater. Sci. 39 (2004) 6399–6420. https://doi.org/10.1023/B:JMSC.0000044878.11441.90.

[62] T. Fujikawa, M. Moritoki, T. Kanda, K. Homma, H. Okada, Hot Isostatic Pressing: its application in high performance ceramics, in: Proc Int Conf Ceram Comp Engine, 1983.

[63] A. Mukhopadhyay, B. Basu, Consolidation–microstructure–property relationships in bulk nanoceramics and ceramic nanocomposites: a review, Int. Mater. Rev. (2013). https://doi.org/10.1179/174328007X160281.

[64] T. Nishimura, X. Xu, K. Kimoto, N. Hirosaki, H. Tanaka, Fabrication of silicon nitride nanoceramics—Powder preparation and sintering: A review, Sci. Technol. Adv. Mater. 8 (2007) 635–643. https://doi.org/10.1016/j.stam.2007.08.006.

[65] R. Orrù, R. Licheri, A.M. Locci, A. Cincotti, G. Cao, Consolidation/synthesis of materials by electric current activated/assisted sintering, Mater. Sci. Eng. R Rep. 63 (2009) 127–287. https://doi.org/10.1016/j.mser.2008.09.003.

[66] Z.A. Munir, D.V. Quach, M. Ohyanagi, Electric Current Activation of Sintering: A Review of the Pulsed Electric Current Sintering Process: Electric Current Activation of Sintering, J. Am. Ceram. Soc. 94 (2011) 1–19. https://doi.org/10.1111/j.1551-2916.2010.04210.x.

[67] R. Raj, M. Cologna, J.S.C. Francis, Influence of Externally Imposed and Internally Generated Electrical Fields on Grain Growth, Diffusional Creep, Sintering and Related Phenomena in Ceramics, J. Am. Ceram. Soc. 94 (2011) 1941–1965. https://doi.org/10.1111/j.1551-2916.2011.04652.x.

[68] T. Mizuguchi, S. Guo, Y. Kagawa, Transmission electron microscopy characterization of spark plasma sintered ZrB2 ceramic, Ceram. Int. 36 (2010) 943–946. https://doi.org/10.1016/j.ceramint.2009.10.025.

[69] Z. Ahmadi, Z. Hamidzadeh Mahaseni, M. Dashti Germi, M. Shahedi Asl, Microstructure of spark plasma sintered TiB2 and TiB2–AlN ceramics, Adv. Ceram. Prog. 5 (2019) 36–40. https://doi.org/10.30501/acp.2019.93129.

[70] A. Mukhopadhyay, T. Venkateswaran, B. Basu, Spark plasma sintering may lead to phase instability and inferior mechanical properties: A case study with TiB2, Scr. Mater. 69 (2013) 159–164. https://doi.org/10.1016/j.scriptamat.2013.02.027.

[71] S. Zhu, W.G. Fahrenholtz, G.E. Hilmas, S.C. Zhang, E.J. Yadlowsky, M.D. Keitz, Microwave sintering of a ZrB2–B4C particulate ceramic composite, Compos. Part Appl. Sci. Manuf. 39 (2008) 449–453. https://doi.org/10.1016/j.compositesa.2008.01.003.

[72] J.D. Katz, Microwave Sintering of Ceramics, Annu. Rev. Mater. Sci. 22 (1992) 153–170. https://doi.org/10.1146/annurev.ms.22.080192.001101.

[73] C.E. Holcombe, N.L. Dykes, Microwave sintering of titanium diboride, J. Mater. Sci. 26 (1991) 3730–3738. https://doi.org/10.1007/BF01184963.

[74] D. Demirskyi, J. Cheng, D. Agrawal, A. Ragulya, Densification and grain growth during microwave sintering of titanium diboride, Scr. Mater. 69 (2013) 610–613. https://doi.org/10.1016/j.scriptamat.2013.07.012.

[75] G. Wen, S.B. Li, B.S. Zhang, Z.X. Guo, Reaction synthesis of TiB2–TiC composites with enhanced toughness, Acta Mater. 49 (2001) 1463–1470. https://doi.org/10.1016/S1359-6454(01)00034-9.

[76] M. Vajdi, F. Sadegh Moghanlou, Z. Ahmadi, A. Motallebzadeh, M. Shahedi Asl, Thermal diffusivity and microstructure of spark plasma sintered TiB2SiCTi composite, Ceram. Int. 45 (2019) 8333–8344. https://doi.org/10.1016/j.ceramint.2019.01.141.

[77] Y.S. Kang, S.H. Kang, D.J. Kim, Effect of addition of Cr on the sintering of TiB2 ceramics, J. Mater. Sci. 40 (2005) 4153–4155. https://doi.org/10.1007/s10853-005-4153-3.

[78] J. Matsushita, A. Sano, Sinterability of TiB_2 Ceramics Containing Cr and C as the Sintering Aids, J. Ceram. Soc. Jpn. 100 (1992) 593–595. https://doi.org/10.2109/jcersj.100.593.

[79] E.S. Kang, C.W. Jang, C.H. Lee, C.H. Kim, D.K. Kim, Effect of Iron and Boron Carbide on the Densification and Mechanical Properties of Titanium Diboride Ceramics, J. Am. Ceram. Soc. 72 (1989) 1868–1872. https://doi.org/10.1111/j.1151-2916.1989.tb05993.x.

[80] T. Jüngling, R. Oberacker, F. Thümmler, L.S. Sigl, K.A. Schmetz, Pressureless sintering of TiB2-Fe-materials, PMI Powder Metall. Int. 23 (1991) 296–300.

[81] J.M. Missiaen, J.M. Chaix, The homogeneity of phase repartition in TiB2–Fe composites using variance and covariance analysis, J. Microsc. 175 (1994) 195–204. https://doi.org/10.1111/j.1365-2818.1994.tb03485.x.

[82] M.-A. Einarsrud, E. Hagen, G. Pettersen, T. Grande, Pressureless Sintering of Titanium Diboride with Nickel, Nickel Boride, and Iron Additives, J. Am. Ceram. Soc. 80 (1997) 3013–3020. https://doi.org/10.1111/j.1151-2916.1997.tb03227.x.

[83] M.K. Ferber, P.F. Becher, C.B. Finch, Effect of Microstructure on the Properties of TiB2 Ceramics, J. Am. Ceram. Soc. 66 (1983) C-2-C–3. https://doi.org/10.1111/j.1151-2916.1983.tb09974.x.

[84] J. Jaroszewicz, A. Michalski, Preparation of a TiB2 composite with a nickel matrix by pulse plasma sintering with combustion synthesis, J. Eur. Ceram. Soc. 26 (2006) 2427–2430. https://doi.org/10.1016/j.jeurceramsoc.2005.05.001.

[85] Ľ. Bača, Z. Lenčéš, C. Jogl, E. Neubauer, M. Vitkovič, A. Merstallinger, P. Šajgalík, Microstructure evolution and tribological properties of TiB2/Ni–Ta cermets, J. Eur. Ceram. Soc. 32 (2012) 1941–1948. https://doi.org/10.1016/j.jeurceramsoc.2011.10.039.

[86] R. González, M.G. Barandika, D. Oña, J.M. Sánchez, A. Villellas, A. Valea, F. Castro, New binder phases for the consolidation of TiB2 hardmetals, Mater. Sci. Eng. A. 216 (1996) 185–192. https://doi.org/10.1016/0921-5093(96)10408-1.

[87] D. Ağaoğulları, H. Gökçe, İ. Duman, M.L. Öveçoğlu, Influences of metallic Co and mechanical alloying on the microstructural and mechanical properties of TiB2 ceramics prepared via pressureless sintering, J. Eur. Ceram. Soc. 32 (2012) 1949–1956. https://doi.org/10.1016/j.jeurceramsoc.2011.10.033.

[88] S.H. Kang, D.J. Kim, E.S. Kang, S.S. Baek, Pressureless Sintering and Properties of Titanium Diboride Ceramics Containing Chromium and Iron, J. Am. Ceram. Soc. 84 (2001) 893–895. https://doi.org/10.1111/j.1151-2916.2001.tb00763.x.

[89] J.M. Sánchez, M.G. Barandika, J. Gil-Sevillano, F. Castro, Consolidation, microstructure and mechanical properties of newly developed TiB2-Based materials, Scr. Metall. Mater. 26 (1992) 957–962. https://doi.org/10.1016/0956-716X(92)90690-G.

[90] T. Jüngling, L.S. Sigl, R. Oberacker, F. Thümmler, K.A. Schwetz, New Hardmetals based on TiB2, Int. J. Refract. Met. Hard Mater. 12 (1993) 71–88. https://doi.org/10.1016/0263-4368(93)90018-B.

[91] J. Fei, W. Wang, A. Ren, Y. Ji, J. Zhou, M. Zhu, Mechanical properties and densification of short carbon fiber-reinforced TiB2/C composites produced by hot pressing, J. Alloys Compd. 584 (2014) 87–92. https://doi.org/10.1016/j.jallcom.2013.09.004.

[92] S. Torizuka, K. Sato, H. Nishio, T. Kishi, Effect of SiC on Interfacial Reaction and Sintering Mechanism of TiB2, J. Am. Ceram. Soc. 78 (1995) 1606–1610. https://doi.org/10.1111/j.1151-2916.1995.tb08858.x.

[93] D.S. King, W.G. Fahrenholtz, G.E. Hilmas, Silicon carbide–titanium diboride ceramic composites, J. Eur. Ceram. Soc. 33 (2013) 2943–2951. https://doi.org/10.1016/j.jeurceramsoc.2013.03.031.

[94] M. Shahedi Asl, A. Sabahi Namini, M. Ghassemi Kakroudi, Influence of silicon carbide addition on the microstructural development of hot pressed zirconium and titanium diborides, Ceram. Int. 42 (2016) 5375–5381. https://doi.org/10.1016/j.ceramint.2015.12.072.

[95] Z. Ahmadi, B. Nayebi, M. Shahedi Asl, I. Farahbakhsh, Z. Balak, Densification improvement of spark plasma sintered TiB2-based composites with micron-, submicron- and nano-sized SiC particulates, Ceram. Int. 44 (2018) 11431–11437. https://doi.org/10.1016/j.ceramint.2018.03.202.

[96] S. Tuffé, J. Dubois, G. Fantozzi, G. Barbier, Densification, microstructure and mechanical properties of TiB2-B4C based composites, Int. J. Refract. Met. Hard Mater. 14 (1996) 305–310. https://doi.org/10.1016/S0263-4368(96)00012-1.

[97] H. Itoh, Y. Tsunekawa, S. Tago, H. Iwahara, Synthesis and sinterability of composite powder of the TiB2-B4C system, J. Alloys Compd. 191 (1993) 191–195. https://doi.org/10.1016/0925-8388(93)90063-S.

[98] S.G. Huang, K. Vanmeensel, O.J.A. Malek, O. Van der Biest, J. Vleugels, Microstructure and mechanical properties of pulsed electric current sintered B4C–TiB2 composites, Mater. Sci. Eng. A. 528 (2011) 1302–1309. https://doi.org/10.1016/j.msea.2010.10.022.

[99] D. Chen, K. Zhang, J. Zeng, H. Guo, B. Li, High-strength TiB2-B4C composite ceramics sintered by spark plasma sintering, Int. J. Appl. Ceram. Technol. 19 (2022) 1949–1955. https://doi.org/10.1111/ijac.14051.

[100] T.S. Srivatsan, G. Guruprasad, D. Black, M. Petraroli, R. Radhakrishnan, T.S. Sudarshan, Microstructural development and hardness of TiB2–B4C composite samples: Influence of consolidation temperature, J. Alloys Compd. 413 (2006) 63–72. https://doi.org/10.1016/j.jallcom.2005.04.209.

[101] S. Chao, J. Goldsmith, D. Banerjee, Titanium diboride composite with improved sintering characteristics, Int. J. Refract. Met. Hard Mater. 49 (2015) 314–319. https://doi.org/10.1016/j.ijrmhm.2014.06.008.

[102] J. Song, C. Huang, B. Zou, H. Liu, L. Liu, J. Wang, Effects of sintering additives on microstructure and mechanical properties of TiB2–WC ceramic–metal composite tool

materials, Int. J. Refract. Met. Hard Mater. 30 (2012) 91–95. https://doi.org/10.1016/j.ijrmhm.2011.07.008.

[103] S.K. Bhaumik, C. Divakar, A.K. Singh, G.S. Upadhyaya, Synthesis and sintering of TiB2 and TiB2–TiC composite under high pressure, Mater. Sci. Eng. A. 279 (2000) 275–281. https://doi.org/10.1016/S0921-5093(99)00217-8.

[104] H. Zhao, Y.-B. Cheng, Formation of TiB2–TiC composites by reactive sintering, Ceram. Int. 25 (1999) 353–358. https://doi.org/10.1016/S0272-8842(98)00048-0.

[105] D. Demirskyi, T. Nishimura, Y. Sakka, O. Vasylkiv, High-strength TiB 2 –TaC ceramic composites prepared using reactive spark plasma consolidation, Ceram. Int. 42 (2016) 1298–1306. https://doi.org/10.1016/j.ceramint.2015.09.065.

[106] D. Demirskyi, Y. Sakka, High-temperature reaction consolidation of TaC–TiB2 ceramic composites by spark-plasma sintering, J. Eur. Ceram. Soc. 35 (2015) 405–410. https://doi.org/10.1016/j.jeurceramsoc.2014.08.007.

[107] D. Demirskyi, Y. Sakka, O. Vasylkiv, High-temperature reactive spark plasma consolidation of TiB2–NbC ceramic composites, Ceram. Int. 41 (2015) 10828–10834. https://doi.org/10.1016/j.ceramint.2015.05.022.

[108] D.-L. Hu, Q. Zheng, H. Gu, D.-W. Ni, G.-J. Zhang, Role of WC additive on reaction, solid-solution and densification in HfB2–SiC ceramics, J. Eur. Ceram. Soc. 34 (2014) 611–619. https://doi.org/10.1016/j.jeurceramsoc.2013.10.007.

[109] J.-H. Park, Y.-H. Koh, H.-E. Kim, C.S. Hwang, E.S. Kang, Densification and Mechanical Properties of Titanium Diboride with Silicon Nitride as a Sintering Aid, J. Am. Ceram. Soc. 82 (2004) 3037–3042. https://doi.org/10.1111/j.1151-2916.1999.tb02199.x.

[110] Z. Hamidzadeh Mahaseni, M. Dashti Germi, Z. Ahmadi, M. Shahedi Asl, Microstructural investigation of spark plasma sintered TiB2 ceramics with Si3N4 addition, Ceram. Int. 44 (2018) 13367–13372. https://doi.org/10.1016/j.ceramint.2018.04.171.

[111] L.-H. Li, H.-E. Kim, E. Son Kang, Sintering and mechanical properties of titanium diboride with aluminum nitride as a sintering aid, J. Eur. Ceram. Soc. 22 (2002) 973–977. https://doi.org/10.1016/S0955-2219(01)00403-4.

[112] F. Shayesteh, S.A. Delbari, Z. Ahmadi, M. Shokouhimehr, M. Shahedi Asl, Influence of TiN dopant on microstructure of TiB2 ceramic sintered by spark plasma, Ceram. Int. 45 (2019) 5306–5311. https://doi.org/10.1016/j.ceramint.2018.11.228.

[113] T. Watanahe, K. Shoubu, Mechanical Properties of Hot-Pressed TiB2-ZrO2 Composites, J. Am. Ceram. Soc. 68 (1985) C-34-C–36. https://doi.org/10.1111/j.1151-2916.1985.tb15273.x.

[114] Y. Muraoka, M. Yoshinaka, K. Hirota, O. Yamaguchi, Hot isostatic pressing of TiB2-ZrO2(2 mol% Y2O3) composite powders, Mater. Res. Bull. 31 (1996) 787–792. https://doi.org/10.1016/0025-5408(96)00069-4.

[115] R. Telle, S. Meyer, G. Petzow, E.D. Franz, Sintering behaviour and phase reactions of TiB2 with ZrO2 additives, Mater. Sci. Eng. A. 105–106 (1988) 125–129. https://doi.org/10.1016/0025-5416(88)90488-0.

[116] M. Lv, W. Chen, C. Liu, Fabrication and mechanical properties of TiB2/ZrO2 functionally graded ceramics, Int. J. Refract. Met. Hard Mater. 46 (2014) 1–5. https://doi.org/10.1016/j.ijrmhm.2014.04.019.

[117] M. Gu, C. Huang, S. Xiao, H. Liu, Improvements in mechanical properties of TiB2 ceramics tool materials by the dispersion of Al2O3 particles, Mater. Sci. Eng. A. 486 (2008) 167–170. https://doi.org/10.1016/j.msea.2007.09.040.

[118] J. González, M. Rodríguez, I. Figueroa, M.-E. Villafuerte-Castrejón, G. Díaz, Development of AlN and TiB2 Composites with Nb2O5, Y2O3 and ZrO2 as Sintering Aids, Materials. 10 (2017) 324. https://doi.org/10.6092/unibo/amsdottorato/2045.

[119] M. Ito, N. Hasegawa, T. Nakano, Reduction in densification temperature by TiB2 addition during sintering of oxides, J. Phys. Conf. Ser. 232 (2010) 012006. https://doi.org/10.1088/1742-6596/232/1/012006.

[120] G.B. Raju, B. Basu, Densification, Sintering Reactions, and Properties of Titanium Diboride With Titanium Disilicide as a Sintering Aid, J. Am. Ceram. Soc. 90 (2007) 3415–3423. https://doi.org/10.1111/j.1551-2916.2007.01911.x.

[121] G.B. Raju, B. Basu, N.H. Tak, S.J. Cho, Temperature dependent hardness and strength properties of TiB2 with TiSi2 sinter-aid, J. Eur. Ceram. Soc. 29 (2009) 2119–2128. https://doi.org/10.1016/j.jeurceramsoc.2008.11.018.

[122] G.B. Raju, K. Biswas, B. Basu, Microstructural characterization and isothermal oxidation behavior of hot-pressed TiB2–10wt.% TiSi2 composite, Scr. Mater. 61 (2009) 104–107. https://doi.org/10.1016/j.scriptamat.2009.03.027.

[123] D. Jain, K.M. Reddy, A. Mukhopadhyay, B. Basu, Achieving uniform microstructure and superior mechanical properties in ultrafine grained TiB2–TiSi2 composites using innovative multi stage spark plasma sintering, Mater. Sci. Eng. A. 528 (2010) 200–207. https://doi.org/10.1016/j.msea.2010.09.022.

[124] B.R. Golla, B. Basu, Hot-pressed TiB2–10wt.% TiSi2 ceramic with extremely good thermal transport properties at elevated temperatures (up to 1273K), Scr. Mater. 68 (2013) 79–82. https://doi.org/10.1016/j.scriptamat.2012.09.013.

[125] T.S.R.Ch. Murthy, R. Balasubramaniam, B. Basu, A.K. Suri, M.N. Mungole, Oxidation of monolithic TiB2 and TiB2–20wt.% MoSi2 composite at 850°C, J. Eur. Ceram. Soc. 26 (2006) 187–192. https://doi.org/10.1016/j.jeurceramsoc.2004.10.025.

[126] T.S.R.Ch. Murthy, B. Basu, R. Balasubramaniam, A.K. Suri, C. Subramanian, R.K. Fotedar, Processing and Properties of TiB2 with MoSi2 Sinter-additive: A First Report, J. Am. Ceram. Soc. 89 (2006) 131–138. https://doi.org/10.1111/j.1551-2916.2005.00652.x.

[127] G.B. Raju, B. Basu, A.K. Suri, Oxidation Kinetics and Mechanisms of Hot-Pressed TiB2–MoSi2 Composites, J. Am. Ceram. Soc. 91 (2008) 3320–3327. https://doi.org/10.1111/j.1551-2916.2008.02656.x.

[128] G.B. Raju, B. Basu, A.K. Suri, Thermal and electrical properties of TiB2–MoSi2, Int. J. Refract. Met. Hard Mater. 28 (2010) 174–179. https://doi.org/10.1016/j.ijrmhm.2009.08.002.

[129] T.S.R.Ch. Murthy, J.K. Sonber, C. Subramanian, R.K. Fotedar, S. Kumar, M.R. Gonal, A.K. Suri, A new TiB2+CrSi2 composite – Densification, characterization and oxidation studies, Int. J. Refract. Met. Hard Mater. 28 (2010) 529–540. https://doi.org/10.1016/j.ijrmhm.2010.02.012.

[130] T.S.R.Ch. Murthy, J.K. Sonber, C. Subramanian, R.C. Hubli, A.K. Suri, Densification, characterization and oxidation studies of TiB2–WSi2 composite, Int. J. Refract. Met. Hard Mater. 33 (2012) 10–21. https://doi.org/10.1016/j.ijrmhm.2012.02.002.

[131] H. Ghayour, M. Abdellahi, M. Bahmanpour, Optimization of the high energy ball-milling: Modeling and parametric study, Powder Technol. 291 (2016) 7–13. https://doi.org/10.1016/j.powtec.2015.12.004.

[132] U. Ravi Kiran, M. Prem Kumar, M. Sankaranarayana, A.K. Singh, T.K. Nandy, High energy milling on tungsten powders, Int. J. Refract. Met. Hard Mater. 48 (2015) 74–81. https://doi.org/10.1016/j.ijrmhm.2014.06.025.

[133] X. Zhang, Z. Zhang, B. Nie, H. Chen, G. Wang, J. Mu, X. Zhang, H. Che, W. Wang, Ultrafine-grained boron carbide ceramics fabricated via ultrafast sintering assisted by high-energy ball milling, Ceram. Int. 44 (2018) 7291–7295. https://doi.org/10.1016/j.ceramint.2018.01.011.

[134] M. Yao, Y. Wang, L. Chen, J. Ouyang, H. Li, H. Gu, Y. Zhou, Mechanical properties and microstructural evolution of pressureless sintered ceramics obtained from high-energy ball-milled TiB2–TiC powders, Mater. Sci. Eng. A. 819 (2021) 141510. https://doi.org/10.1016/j.msea.2021.141510.

[135] D. Sciti, S. Failla, S. Turan, U. Savaci, P. Galizia, Properties and ballistic tests of strong B4C-TiB2 composites densified by gas pressure sintering, J. Eur. Ceram. Soc. 43 (2023) 1334–1342. https://doi.org/10.1016/j.jeurceramsoc.2022.11.066.

[136] S. Failla, C. Melandri, L. Zoli, G. Zucca, D. Sciti, Hard and easy sinterable B4C-TiB2-based composites doped with WC, J. Eur. Ceram. Soc. 38 (2018) 3089–3095. https://doi.org/10.1016/j.jeurceramsoc.2018.02.041.

[137] L. Silvestroni, S. Failla, N. Gilli, C. Melandri, U. Savacı, S. Turan, D. Sciti, Disclosing small scale length properties in core-shell structured B4C-TiB2 composites, Mater. Des. 197 (2021) 109204. https://doi.org/10.1016/j.matdes.2020.109204.

[138] M.M. Opeka, I.G. Talmy, E.J. Wuchina, J.A. Zaykoski, S.J. Causey, Mechanical, Thermal, and Oxidation Properties of Refractory Hafnium and zirconium Compounds, J. Eur. Ceram. Soc. 19 (1999) 2405–2414. https://doi.org/10.1016/S0955-2219(99)00129-6.

[139] V. Mandorf, J. Hartwig, E.J. Seldin, High temperature properties of titanium diboride, High Temp. Mater. II GM Ault WF Barclay HP Munger Eds Gordon Breach N. Y. (1963) 455–467.

[140] D.E. Wiley, W.R. Manning, O. Hunter, Elastic properties of polycrystalline TiB2, ZrB2 and HfB2 from room temperature to 1300 °K, J. Common Met. 18 (1969) 149–157. https://doi.org/10.1016/0022-5088(69)90134-9.

[141] R.A. Andrievski, B.U. Asanov, Temperature dependence of the Young's modulus of the composite TiB2-Fe, J. Mater. Sci. Lett. 10 (1991) 147–148. https://doi.org/10.1007/BF02352831.

[142] M.-J. Pan, P.A. Hoffman, D.J. Green, J.R. Hellmann, Elastic properties and microcracking behavior of particulate titanium diboride–silicon carbide composites, J. Am. Ceram. Soc. 80 (1997) 692–698.

[143] P.S. Spoor, J.D. Maynard, M.J. Pan, D.J. Green, J.R. Hellmann, T. Tanaka, Elastic constants and crystal anisotropy of titanium diboride, Appl. Phys. Lett. 70 (1997) 1959–1961. https://doi.org/10.1063/1.118791.

[144] P.F. Becher, C.B. Finch, M.K. Ferber, Effect of residual nickel content on the grain size dependent mechanical properties of TiB 2, J. Mater. Sci. Lett. 5 (1986) 195–197.

[145] C. Tracy, M. Slavin, D. Viechnicki, Ceramic fracture during ballistic impact, Fractography Glas. Ceram. Westerville Ohio 1988. 22 (1988) 295–306.

[146] K. Cho, R.N. Katz, I. Bar-On, A.R.L.A.P.G. MD, Mechanical Properties of Hot Pressed Titanium Diboride, Army Res. Lab. Rep. ARL-TR-1185 Natl. Tech. Inf. Serv. Wash. DC. (1986).

[147] J. Matsushita, T. Suzuki, A. Sano, High temperature strength of TiB2 ceramics, J. Ceram. Soc. Jpn. 101 (1993) 1074–1077.

[148] A.N. Ranade, L. Rama Krishna, Z. Li, J. Wang, C.S. Korach, Y.-W. Chung, Relationship between hardness and fracture toughness in Ti–TiB2 nanocomposite coatings, Surf. Coat. Technol. 213 (2012) 26–32. https://doi.org/10.1016/j.surfcoat.2012.10.007.

[149] B. Basu, J. Vleugels, O. Van Der Biest, Fretting wear behavior of TiB2-based materials against bearing steel under water and oil lubrication, Wear. 250 (2001) 631–641. https://doi.org/10.1016/S0043-1648(01)00670-6.

[150] A. Zerr, R. Riedel, Introduction: Novel ultrahard materials, Handb. Ceram. Hard Mater. 1 (2000) 45–73.

[151] A. Mukhopadhyay, G.B. Raju, B. Basu, A.K. Suri, Correlation between phase evolution, mechanical properties and instrumented indentation response of TiB2-based ceramics, J. Eur. Ceram. Soc. 29 (2009) 505–516. https://doi.org/10.1016/j.jeurceramsoc.2008.06.030.

[152] E.W. Neuman, G.E. Hilmas, W.G. Fahrenholtz, Strength of Zirconium Diboride to 2300°C, J. Am. Ceram. Soc. 96 (2013) 47–50. https://doi.org/10.1111/jace.12114.

[153] R.A. Cutler, Engineering Properties of Borides, Eng. Mater. Handb. 4 (1991) 787–803.

[154] M.E. Schlesinger, Melting points, crystallographic transformation, and thermodynamic values, ASM Int. Eng. Mater. Handb. 4 (1991) 883–891.

[155] T.M. Branscomb, O. Hunter Jr., Improved Thermal Diffusivity Method Applied to TiB2, ZrB2, and HfB2 from 200°–1300°C, J. Appl. Phys. 42 (2003) 2309–2315. https://doi.org/10.1063/1.1660541.

[156] A.D. McLeod, J.S. Haggerty, D.R. Sadoway, Electrical Resistivities of Monocrystalline and Polycrystalline TiB2, J. Am. Ceram. Soc. 67 (1984) 705–708. https://doi.org/10.1111/j.1151-2916.1984.tb19505.x.

[157] F.W. Vahldiek, Electrical resistivity, elastic modulus, and debye temperature of titanium diboride, J. Common Met. 12 (1967) 202–209. https://doi.org/10.1016/0022-5088(67)90115-4.

[158] P. Poubel Mendonça da Silveira, T. Teixeira da Silva, M. Pereira Ribeiro, P. Jesus, A. Gomes, A Brief Review of Alumina, Silicon Carbide and Boron Carbide Ceramic Materials for Ballistic Applications, (2021) 1–11. https://doi.org/10.20935/AL3742.

[159] T. Benitez, S. Y. Gómez, A.P.N. de Oliveira, N. Travitzky, D. Hotza, Transparent ceramic and glass-ceramic materials for armor applications, Ceram. Int. 43 (2017) 13031–13046. https://doi.org/10.1016/j.ceramint.2017.07.205.

[160] A.B. Dresch, J. Venturini, S. Arcaro, O.R.K. Montedo, C.P. Bergmann, Ballistic ceramics and analysis of their mechanical properties for armour applications: A review, Ceram. Int. 47 (2021) 8743–8761. https://doi.org/10.1016/j.ceramint.2020.12.095.

[161] J. Jiusti, E.H. Kammer, L. Neckel, N.J. Lóh, W. Trindade, A.O. Silva, O.R.K. Montedo, A. De Noni, Ballistic performance of Al2O3 mosaic armors with gap-filling materials, Ceram. Int. 43 (2017) 2697–2704. https://doi.org/10.1016/j.ceramint.2016.11.087.

[162] G.J. Appleby-Thomas, K. Jaansalu, A. Hameed, J. Painter, J. Shackel, J. Rowley, A comparison of the ballistic behaviour of conventionally sintered and additively manufactured alumina, Def. Technol. 16 (2020) 275–282. https://doi.org/10.1016/j.dt.2019.06.020.

[163] C. Kaufmann, D. Cronin, M. Worswick, G. Pageau, A. Beth, Influence of Material Properties on the Ballistic Performance of Ceramics for Personal Body Armour, Shock Vib. 10 (2003) 51–58. https://doi.org/10.1155/2003/357637.

[164] A. Morka, T. Niezgoda, P. Kędzierski, A. Boczkowska, P. Chabera, A. Oziębło, A. Witek, Comparison of numerical and experimental study of armour system based on alumina and silicon carbide ceramics, Bull. Pol. Acad. Sci. Tech. Sci. 2015 63 No 2 363-367. (2015). https://journals.pan.pl/dlibra/publication/97596/edition/84184 (accessed August 1, 2023).

[165] Y.V. Popov, V.A. Markov, V.I. Pusev, V.V. Selivanov, The relative thickness of the barriers and its fundamental importance in armored ballistics, J. Phys. Conf. Ser. 1459 (2020) 012007. https://doi.org/10.1088/1742-6596/1459/1/012007.

[166] J. Cao, J. Lai, J. Zhou, N. Kang, L. Du, Y. Miao, Experiments and simulations of the ballistic response of ceramic composite armors, J. Mech. Sci. Technol. 34 (2020) 2783–2793. https://doi.org/10.1007/s12206-020-0611-8.

[167] Z. Rosenberg, E. Dekel, Terminal Ballistics, Springer, Berlin, Heidelberg, 2012. https://doi.org/10.1007/978-3-642-25305-8.

[168] M.V. Silva, D. Stainer, H.A. Al-Qureshi, O.R.K. Montedo, D. Hotza, Alumina-Based Ceramics for Armor Application: Mechanical Characterization and Ballistic Testing, J. Ceram. 2014 (2014) e618154. https://doi.org/10.1155/2014/618154.

[169] D. Hu, Y. Zhang, Z. Shen, Q. Cai, Investigation on the ballistic behavior of mosaic SiC/UHMWPE composite armor systems, Ceram. Int. 43 (2017) 10368–10376. https://doi.org/10.1016/j.ceramint.2017.05.071.

[170] I.G. Crouch, M. Kesharaju, R. Nagarajah, Characterisation, significance and detection of manufacturing defects in Reaction Sintered Silicon Carbide armour materials, Ceram. Int. 41 (2015) 11581–11591. https://doi.org/10.1016/j.ceramint.2015.06.083.

[171] M. Flinders, D. Ray, A. Anderson, R.A. Cutler, High-Toughness Silicon Carbide as Armor, J. Am. Ceram. Soc. 88 (2005) 2217–2226. https://doi.org/10.1111/j.1551-2916.2005.00415.x.

[172] P.G. Karandikar, G. Evans, S. Wong, M.K. Aghajanian, M. Sennett, A review of ceramics for armor applications, Adv. Ceram. Armor IV. 29 (2009) 163–175.

[173] R. Goel, M.D. Kulkarni, K.S. Pandya, N.K. Naik, Stress wave micro–macro attenuation in ceramic plates made of tiles during ballistic impact, Int. J. Mech. Sci. 83 (2014) 30–37. https://doi.org/10.1016/j.ijmecsci.2014.03.020.

[174] M. Mirkhalaf, A. Sunesara, B. Ashrafi, F. Barthelat, Toughness by segmentation: Fabrication, testing and micromechanics of architectured ceramic panels for impact applications, Int. J. Solids Struct. 158 (2019) 52–65. https://doi.org/10.1016/j.ijsolstr.2018.08.025.

[175] E.J. Haney, G. Subhash, Damage Mechanisms Perspective on Superior Ballistic Performance of Spinel over Sapphire, Exp. Mech. 53 (2013) 31–46. https://doi.org/10.1007/s11340-012-9634-0.

[176] A. Krell, E. Strassburger, Order of influences on the ballistic resistance of armor ceramics and single crystals, Mater. Sci. Eng. A. 597 (2014) 422–430. https://doi.org/10.1016/j.msea.2013.12.101.

[177] G. Guo, S. Alam, L.D. Peel, Numerical analysis of ballistic impact performance of two ceramic-based armor structures, Compos. Part C Open Access. 3 (2020) 100061. https://doi.org/10.1016/j.jcomc.2020.100061.

[178] J.D. Hogan, L. Farbaniec, M. Shaeffer, K.T. Ramesh, The Effects of Microstructure and Confinement on the Compressive Fragmentation of an Advanced Ceramic, J. Am. Ceram. Soc. 98 (2015) 902–912. https://doi.org/10.1111/jace.13353.

[179] R.W. Rice, C.Cm. Wu, F. Boichelt, Hardness–Grain-Size Relations in Ceramics, J. Am. Ceram. Soc. 77 (1994) 2539–2553. https://doi.org/10.1111/j.1151-2916.1994.tb04641.x.

[180] M. Flinders, D. Ray, R.A. Cutler, Toughness-Hardness Trade-Off in Advanced SiC Armor, in: Ceram. Armor Armor Syst., John Wiley & Sons, Ltd, 2006: pp. 37–48. https://doi.org/10.1002/9781118406793.ch3.

[181] D. Ray, M. Flinders, A. Anderson, R.A. Cutler, Hardness/Toughness Relationship for Sic Armor, in: 27th Annu. Cocoa Beach Conf. Adv. Ceram. Compos. Ceram. Eng. Sci. Proc., John Wiley & Sons, Ltd, 2003: pp. 401–410. https://doi.org/10.1002/9780470294802.ch58.

[182] **李其松**, 张振昊, 孙海滨, 张玉军, Titanium diboride/silicon carbide composite bulletproof material and preparation method and application thereof, CN111348920B, 2022. https://patents.google.com/patent/CN111348920B/en?oq=CN111348920B (accessed September 5, 2023).

2. Aim of the work

Titanium diboride (TiB_2) is a prominent technical ceramic due to its exceptional properties. As the lightest transition-metal diboride (TMBs), it exhibits remarkable mechanical characteristics: high hardness, flexural strength, and elastic modulus [1–5]. Additionally, TiB_2 exhibits superior wear resistance and a very high melting temperature (over 3000°C) [6–8]. Notably, it distinguishes itself from other technical ceramics such as Al_2O_3, SiC, and B_4C by its good electrical conductivity, similar to the one of the metals [9–11], this feature could be effectively exploited with electro-discharge machining, which is a more cost-effective technique compared to conventional diamond tool machining for shaping the ceramic components.

Despite these excellent properties, TiB_2 does not have good resistance to oxidation limiting its use for aerospace and high temperature applications in the presence of oxygen. It is also characterized by relatively low fracture toughness and exhibits sensitivity to slow subcritical crack growth [12] which limits its use to a wide range of engineering applications.

The main limiting factor in using TiB_2 for commercial applications is the difficulty of obtaining a completely dense material with good properties and mechanical performances due to its poor sinterability. This is primarily due to the low self-diffusion coefficient and relatively high vapor pressure of its constituents, [12] resulting from the presence of both ionic and covalent bonds [13]. Furthermore, the presence of an oxide layer (TiO_2 and B_2O_3) on the surface of TiB_2 powder promotes excessive grain growth through vapor or surface transport mechanisms during the sintering process, leading to the formation of porosity that becomes trapped within the grains [14,15].

To improve the densification of TMBs, a series of strategies can be used, including the use of various synthesis routes to obtain finer and less contaminated powders [16], pressure- or current-assisted sintering techniques [17,18], the addition of sintering aids [19–22], high-energy-milling of the powders to reduce the dimensions, introduce defects and possible mechanical alloying [23–26].

The main objective of this thesis was to obtain a high-density material with good mechanical properties through pressure-less sintering, a widely used and scalable industrial technique.

The main objective of this thesis was to obtain a high-density material with good mechanical, thermal and electrical properties through pressure-less sintering, an easily scalable and very common technique at an industrial level. To achieve this goal, different sintering aids were chosen, in particular: a carbide, B_4C [27–31]; a nitride, Si_3N_4 [32,33]; and a silicide, $MoSi_2$ [34–38]. The effect of sintering aids, of high-energy-milling with WC-Co media and their possible synergy have been systematically investigated with hot-pressing (1700-1900°C) and pressure-less sintering (1900-2200°C) techniques to comprehensively analyze their impact on TiB_2 densification, reactions and secondary phases formed during the sintering.

This thesis work was divided into four parts:

1. Impacts of sintering aid, high-energy milling, and their synergy on TiB_2 sintering were evaluated using hot-pressing sintering in the first part of this thesis. The shrinkage of the sample over time was recorded to study the densification rate and temperatures at which it occurs. Microstructural analysis was performed to hypothesize reactions and densification mechanisms based on observations of the microstructure and secondary phases. Vickers hardness and indentation fracture toughness measurements were used to explore the mechanical properties of the various compositions.

2. In the second part, the effect of sintering aids and powder preparation methods was investigated in pressure-less sintering. Best sintering conditions were identified with sets of tests at a range of temperatures (from 1900 to 2100°C) and dwell times (from 60 to 120 minutes). For the best compositions identified, scale-up tests were carried out and the amount of additive used was optimized. Residual porosity, microstructure, composition, and mechanical properties of the sintered materials were measured and compared to those obtained from hot-pressing.

3. The third part of the thesis studied the effect and optimization of high-energy milling with WC-Co media on TiB_2 green powders microstructure and densification. The variation in grain size and the increase in the quantity of WC-Co introduced in powders as the milling time increased were analyzed as a function of milling time. Pressure-less-sintering was used to investigate the effect of HEPBM on sintering. Reproducibility tests were performed. To better understand the effect of HEPBM on TiB_2 green powders microstructure and densification, mixtures with simply mixed WC (without Co) were also tested.

4. The fourth part of this thesis work investigated the mechanical, thermal, and electrical properties of pressure-less sintered TiB_2. Flexural strength and fracture toughness were measured at room and high temperature (1000–1600°C) with different test rate to assess the mechanical properties. Laser flash tests were performed between 25 and 200 °C, and between 200 and 2000 °C, to measure the thermal properties (thermal conductivity, thermal diffusivity, and specific heat). Electrical resistivity was measured at different currents at room temperature and compared with other ceramic and metallic materials.

This work was carried out at the Institute of Science, Technology and Sustainability for Ceramics (CNR-ISSMC former ISTEC) in Faenza (Ravenna, Italy), with a period abroad at the Missouri University of Science and Technology in Rolla, Missouri.

2.1 References

[1] D.E. Wiley, W.R. Manning, O. Hunter, Elastic properties of polycrystalline TiB2, ZrB2 and HfB2 from room temperature to 1300 °K, Journal of the Less Common Metals. 18 (1969) 149–157. https://doi.org/10.1016/0022-5088(69)90134-9.

[2] T. Jüngling, L.S. Sigl, R. Oberacker, F. Thümmler, K.A. Schwetz, New Hardmetals based on TiB2, International Journal of Refractory Metals and Hard Materials. 12 (1993) 71–88. https://doi.org/10.1016/0263-4368(93)90018-B.

[3] R.G. Munro, Material Properties of Titanium Diboride, J Res Natl Inst Stand Technol. 105 (2000) 709–720. https://doi.org/10.6028/jres.105.057.

[4] T.S.R.Ch. Murthy, J.K. Sonber, C. Subramanian, R.K. Fotedar, S. Kumar, M.R. Gonal, A.K. Suri, A new TiB2+CrSi2 composite – Densification, characterization and oxidation studies, International Journal of Refractory Metals and Hard Materials. 28 (2010) 529–540. https://doi.org/10.1016/j.ijrmhm.2010.02.012.

[5] Z. Ahmadi, Z. Hamidzadeh Mahaseni, M. Dashti Germi, M. Shahedi Asl, Microstructure of spark plasma sintered TiB2 and TiB2–AlN ceramics, Advanced Ceramics Progress. 5 (2019) 36–40. https://doi.org/10.30501/acp.2019.93129.

[6] V. Mandorf, J. Hartwig, E.J. Seldin, High temperature properties of titanium diboride, High Temperature Materials II, GM Ault, WF Barclay, and HP Munger, Eds., Gordon and Breach, New York. (1963) 455–467.

[7] J. Matsushita, T. Suzuki, A. Sano, High temperature strength of TiB2 ceramics, Journal of the Ceramic Society of Japan. 101 (1993) 1074–1077.

[8] C. Subramanian, T.S.R.Ch. Murthy, A.K. Suri, Synthesis and consolidation of titanium diboride, International Journal of Refractory Metals and Hard Materials. 25 (2007) 345–350. https://doi.org/10.1016/j.ijrmhm.2006.09.003.

[9] F.W. Vahldiek, Electrical resistivity, elastic modulus, and debye temperature of titanium diboride, Journal of the Less Common Metals. 12 (1967) 202–209. https://doi.org/10.1016/0022-5088(67)90115-4.

[10] M. Rahman, C.C. Wang, W. Chen, S.A. Akbar, C. Mroz, Electrical Resistivity of Titanium Diboride and Zirconium Diboride, Journal of the American Ceramic Society. 78 (1995) 1380–1382. https://doi.org/10.1111/j.1151-2916.1995.tb08498.x.

[11] A Table of Electrical Conductivity and Resistivity of Common Materials, ThoughtCo. (n.d.). https://www.thoughtco.com/table-of-electrical-resistivity-conductivity-608499 (accessed October 16, 2023).

[12] B. Basu, G.B. Raju, A.K. Suri, Processing and properties of monolithic TiB2 based materials, International Materials Reviews. 51 (2006) 352–374. https://doi.org/10.1179/174328006X102529.

[13] G.B. Raju, B. Basu, Development of High Temperature TiB2-Based Ceramics, Key Engineering Materials. 395 (2009) 89–124. https://doi.org/10.4028/www.scientific.net/KEM.395.89.

[14] A. Sabahi Namini, S.N. Seyed Gogani, M. Shahedi Asl, K. Farhadi, M. Ghassemi Kakroudi, A. Mohammadzadeh, Microstructural development and mechanical properties of hot pressed SiC reinforced TiB2 based composite, International Journal of Refractory Metals and Hard Materials. 51 (2015) 169–179. https://doi.org/10.1016/j.ijrmhm.2015.03.014.

[15] S. Baik, P.F. Becher, Effect of Oxygen Contamination on Densification of TiB2, J American Ceramic Society. 70 (1987) 527–530. https://doi.org/10.1111/j.1151-2916.1987.tb05699.x.

[16] R. Telle, L.S. Sigl, K. Takagi, Boride-Based Hard Materials, in: R. Riedel (Ed.), Handbook of Ceramic Hard Materials, Wiley-VCH Verlag GmbH, Weinheim, Germany, 2000: pp. 802–945. https://doi.org/10.1002/9783527618217.ch22.

[17] H. Pastor, Metallic Borides: Preparation of Solid Bodies — Sintering Methods and Properties of Solid Bodies, in: V.I. Matkovich (Ed.), Boron and Refractory Borides, Springer, Berlin, Heidelberg, 1977: pp. 457–493. https://doi.org/10.1007/978-3-642-66620-9_25.

[18] L. Rangaraj, C. Divakar, V. Jayaram, Processing of Refractory Metal Borides, Carbides and Nitrides, Key Engineering Materials. 395 (2009) 69–88. https://doi.org/10.4028/www.scientific.net/KEM.395.69.

[19] Y.S. Kang, S.H. Kang, D.J. Kim, Effect of addition of Cr on the sintering of TiB2 ceramics, J Mater Sci. 40 (2005) 4153–4155. https://doi.org/10.1007/s10853-005-4153-3.

[20] M. Shahedi Asl, A. Sabahi Namini, M. Ghassemi Kakroudi, Influence of silicon carbide addition on the microstructural development of hot pressed zirconium and titanium diborides, Ceramics International. 42 (2016) 5375–5381. https://doi.org/10.1016/j.ceramint.2015.12.072.

[21] L.-H. Li, H.-E. Kim, E. Son Kang, Sintering and mechanical properties of titanium diboride with aluminum nitride as a sintering aid, Journal of the European Ceramic Society. 22 (2002) 973–977. https://doi.org/10.1016/S0955-2219(01)00403-4.

[22] B.R. Golla, B. Basu, Hot-pressed TiB2–10wt.% TiSi2 ceramic with extremely good thermal transport properties at elevated temperatures (up to 1273K), Scripta Materialia. 68 (2013) 79–82. https://doi.org/10.1016/j.scriptamat.2012.09.013.

[23] D. Ağaoğulları, H. Gökçe, İ. Duman, M.L. Öveçoğlu, Influences of metallic Co and mechanical alloying on the microstructural and mechanical properties of TiB2 ceramics prepared via pressureless sintering, Journal of the European Ceramic Society. 32 (2012) 1949–1956. https://doi.org/10.1016/j.jeurceramsoc.2011.10.033.

[24] M. Yao, Y. Wang, L. Chen, J. Ouyang, H. Li, H. Gu, Y. Zhou, Mechanical properties and microstructural evolution of pressureless sintered ceramics obtained from high-energy ball-milled TiB2–TiC powders, Materials Science and Engineering: A. 819 (2021) 141510. https://doi.org/10.1016/j.msea.2021.141510.

[25] D. Sciti, S. Failla, S. Turan, U. Savaci, P. Galizia, Properties and ballistic tests of strong B4C-TiB2 composites densified by gas pressure sintering, Journal of the European Ceramic Society. 43 (2023) 1334–1342. https://doi.org/10.1016/j.jeurceramsoc.2022.11.066.

[26] S. Failla, C. Melandri, L. Zoli, G. Zucca, D. Sciti, Hard and easy sinterable B4C-TiB2-based composites doped with WC, Journal of the European Ceramic Society. 38 (2018) 3089–3095. https://doi.org/10.1016/j.jeurceramsoc.2018.02.041.

[27] S. Tuffé, J. Dubois, G. Fantozzi, G. Barbier, Densification, microstructure and mechanical properties of TiB2-B4C based composites, International Journal of Refractory Metals and Hard Materials. 14 (1996) 305–310. https://doi.org/10.1016/S0263-4368(96)00012-1.

[28] H. Itoh, Y. Tsunekawa, S. Tago, H. Iwahara, Synthesis and sinterability of composite powder of the TiB2-B4C system, Journal of Alloys and Compounds. 191 (1993) 191–195. https://doi.org/10.1016/0925-8388(93)90063-S.

[29] S.G. Huang, K. Vanmeensel, O.J.A. Malek, O. Van der Biest, J. Vleugels, Microstructure and mechanical properties of pulsed electric current sintered B4C–TiB2 composites, Materials Science and Engineering: A. 528 (2011) 1302–1309. https://doi.org/10.1016/j.msea.2010.10.022.

[30] D. Chen, K. Zhang, J. Zeng, H. Guo, B. Li, High-strength TiB2-B4C composite ceramics sintered by spark plasma sintering, International Journal of Applied Ceramic Technology. 19 (2022) 1949–1955. https://doi.org/10.1111/ijac.14051.

[31] T.S. Srivatsan, G. Guruprasad, D. Black, M. Petraroli, R. Radhakrishnan, T.S. Sudarshan, Microstructural development and hardness of TiB2–B4C composite samples: Influence of consolidation temperature, Journal of Alloys and Compounds. 413 (2006) 63–72. https://doi.org/10.1016/j.jallcom.2005.04.209.

[32] J.-H. Park, Y.-H. Koh, H.-E. Kim, C.S. Hwang, E.S. Kang, Densification and Mechanical Properties of Titanium Diboride with Silicon Nitride as a Sintering Aid, Journal of the American Ceramic Society. 82 (1999) 3037–3042. https://doi.org/10.1111/j.1151-2916.1999.tb02199.x.

[33] Z. Hamidzadeh Mahaseni, M. Dashti Germi, Z. Ahmadi, M. Shahedi Asl, Microstructural investigation of spark plasma sintered TiB2 ceramics with Si3N4 addition, Ceramics International. 44 (2018) 13367–13372. https://doi.org/10.1016/j.ceramint.2018.04.171.

[34] G.B. Raju, A. Mukhopadhyay, K. Biswas, B. Basu, Densification and high-temperature mechanical properties of hot pressed TiB2–(0–10 wt.%) MoSi2 composites, Scripta Materialia. 61 (2009) 674–677. https://doi.org/10.1016/j.scriptamat.2009.05.031.

[35] T.S.R.Ch. Murthy, R. Balasubramaniam, B. Basu, A.K. Suri, M.N. Mungole, Oxidation of monolithic TiB2 and TiB2–20wt.% MoSi2 composite at 850°C, Journal of the European Ceramic Society. 26 (2006) 187–192. https://doi.org/10.1016/j.jeurceramsoc.2004.10.025.

[36] T.S.R.Ch. Murthy, B. Basu, R. Balasubramaniam, A.K. Suri, C. Subramanian, R.K. Fotedar, Processing and Properties of TiB2 with MoSi2 Sinter-additive: A First Report, Journal of the American Ceramic Society. 89 (2006) 131–138. https://doi.org/10.1111/j.1551-2916.2005.00652.x.

[37] G.B. Raju, B. Basu, A.K. Suri, Oxidation Kinetics and Mechanisms of Hot-Pressed TiB2–MoSi2 Composites, Journal of the American Ceramic Society. 91 (2008) 3320–3327. https://doi.org/10.1111/j.1551-2916.2008.02656.x.

[38] G.B. Raju, B. Basu, A.K. Suri, Thermal and electrical properties of TiB2–MoSi2, International Journal of Refractory Metals and Hard Materials. 28 (2010) 174–179. https://doi.org/10.1016/j.ijrmhm.2009.08.002.

3. Experimental

This chapter describes the materials, techniques, and instruments used to produce and analyze the samples.

3.1 Material processing

This thesis focused on developing a TiB_2-based material that can be easily sintered via pressure-less sintering and scaled to industrial production. To achieve this objective, several steps are necessary:

- choice of sintering aids;
- powder treatment;
- shaping;
- sintering process;
- finishing;

Each step in this process is critical to the final result, which is the sum of all the steps, influenced by the previous one. Moreover, the properties of the final material depend not only on its density but also on how the sample was prepared and sintered. Therefore, an accurate and precise methodology is required.

3.1.1 Raw materials and preparation of mixtures

The powders to obtain the samples were prepared by mixing TiB_2 powders with each sintering aid in turn. Commercial titanium diboride was used as the main ingredient with a view to an industrial development that can start from TiB_2 powders present in large quantities on the market and at an accessible price. The sintering additives selected for the compositions tested in this thesis were boron carbide (B_4C), silicon nitride (Si_3N_4), molybdenum disilicide ($MoSi_2$), and tungsten carbide (WC). The following commercial powders were used to prepare the mixtures:

- TiB_2 (H.C. Starck, Grade F, D_{90} 4.0 -7.0 µm, D_{50} 2.5-3.5 µm, < 4.5 µm, impurities (wt. %): 0.4 C, 2.5 O, 0.5 N, 0.1 Fe);
- B_4C (H.C. Starck Grade HS-A, D_{90} 2.0-4.0 µm, D_{50} 0.6-1.2 µm, B:C ratio 3.7, impurities (wt. %): 0.7 N, 1.7 O, 0.05 Fe, 0.15 Si, 0.05 Al);
- Si_3N_4 (α-Si_3N_4, H.C. Starck Grade M 11, α > 90%, D90 1.3 µm, D_{50} 0.6 µm, D_{10} 0.3 µm, impurities (wt. %): 0.5 O, 0.5 C, 0.08 Al, 0.01 Ca, 0.008 Fe);
- $MoSi_2$ (Sigma Aldrich, purity > 99% average particle size < 2 µm, metallic impurities (< 2000 PPM): 400 ppm Al, 12 ppm Ba, 16ppm Cr, 400 Fe, 12 ppm K, 39 ppm W);
- WC (H.C. Starck, Grade D60, fisher number 0.60-0.70 µm, impurities: < 0.4 % O, < 0.08 % C_{free}, < 150 ppm Fe, < 100 ppm Co, < 100 ppm Mo, < 70 ppm Ni, < 50 ppm Cr);

To prepare the soft homogenized (SH) mixtures of powders we used the wet ball milling technique. The powders were weighed and placed inside a polyethylene bottle with ethanol and WC-Co spheres (diameter 10mm) and the mixing was carried out for 24 hours on a jar turner (≈ 60 rpm). The ratio of the masses of powder, solvent and beads used was 1:1:1.

The use of a solvent serves to facilitate mixing and to better disperse the heat generated. A non-aqueous solvent, ethanol, was used to prevent oxidation of the powders which hinders their densification [1]. Low rotational speeds and spheres of a very hard material (WC-Co) were used to be able to break up the aggregates in the powders and improve mixing without significantly reducing the grain size or contaminating the mixture.

After mixing, the powders were dried using a rotary evaporator (80 °C and -40 mmHg) to prevent the preferential sedimentation of heavier powders and then passed through a 250-mesh sieve with a brush to break up any agglomerates.

3.1.2 High-energy-planetary-ball-milling

High-Energy-Planetary-Ball-Milling (HEPBM) was used to reduce the grain size of the powders, increasing the surface area, and to introduce submicron WC debris. This technique was used to mill commercial TiB_2 powder or mixtures already homogenized by wet ball milling.

The powders were placed in a WC jar (Fig. 3.1) with WC-Co spheres (6 wt. % Co, 0.5 mm diameter) and ethanol. The same mass was used for powders and solvent (120 g) while the mass of the added spheres (about 500 g) varied during the experiments due to their erosion (about 10 g per cycle), as explained in detail in chapter 6.

The jar was then placed in a planetary mill (Pulverisette 6 Classi Line, Fritsch Planetary Mill) and rotated at 400 rpm with cycles of 5 minutes of milling and 15 minutes of pause to avoid overheating. At the end of the procedure the solvent was removed by evaporation in an oven at 80°C overnight, while the powders were passed through a 125-mesh sieve with a brush to break up the agglomerates formed during the evaporation and recover the spheres.

Fig. 3.1 WC jar and planetary mill (Pulverisette 6 Classi Line, Fritsch Planetary Mill).

The estimation of the WC-Co contamination in the powders was made considering the mean value between the mass obtained by the HEPBM powders and the mass lost from the WC jar and WC-Co spheres. The grain size and quality of the powders before and after HEPBM were measured by sedimentation analysis (Sedigraph 5100, Micrometrics, Atlanta, USA), XRD spectrographs and SEM micrographs.

3.1.3 Powder molding

The preparation of the green compacts into a disc shape from the powders was done through two techniques: uniaxial pressing and cold isostatic pressing. For both techniques, the geometric density of the samples was measured after pressing using the following equation:

$$\rho_{\text{geometric}} = \frac{4m}{\pi d^2 h} \tag{3.1}$$

where m is the mass of the sample, d is the diameter and h the height of the powder disc measured with a caliper.

In uniaxial pressing, the powders are weighed, placed inside a stiff steel die (Fig. 3.2), and compacted with uniaxial pressure of 25-50 MPa. The final relative density is approximately 50%.

Cold isostatic pressing is done to obtain higher relative densities and a more uniform pressing after linear pressing. The uniaxially pressed discs are vacuum sealed inside plastic bags and then immersed in hydraulic oil in a pressure chamber. A pressure of 250-300 MPa is applied to the fluid which transfers it uniformly onto the samples. In this case the final relative density is about 60%.

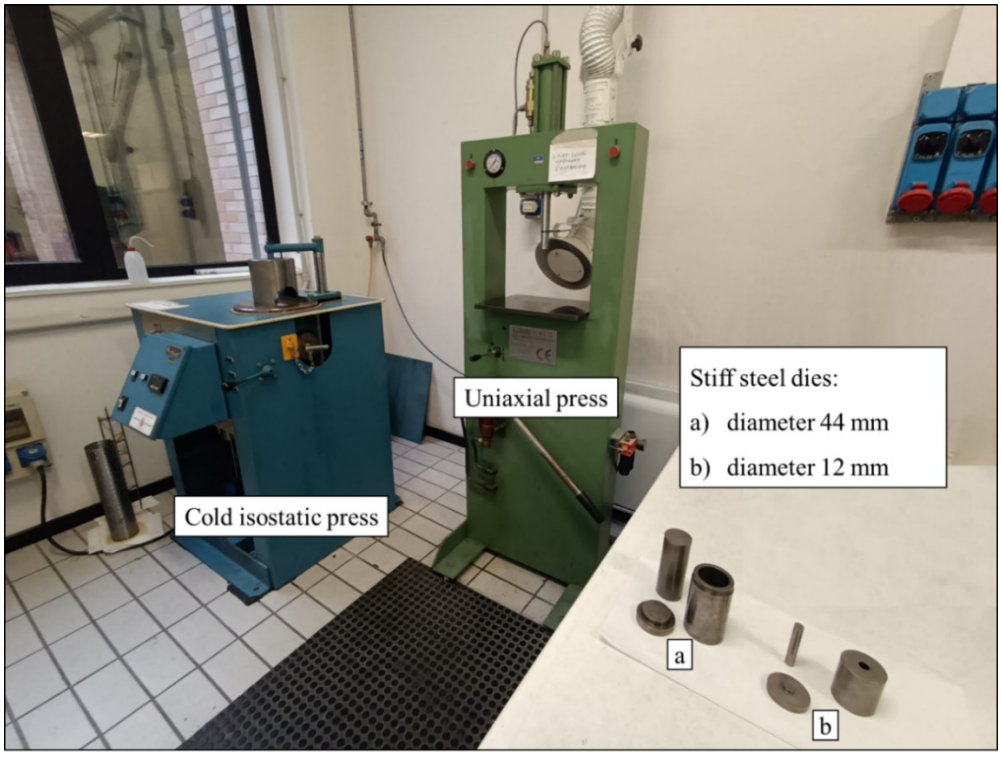

Fig. 3.2 Powder forming laboratory equipment: presses and dies utilized.

The samples for hot-pressing sintering were just linearly pressed into a mold with an internal diameter of 44 mm and the powder was weighed to reach a final height of approximately 7 mm. The pressure used was 25 MPa.

The pressure-less sintered samples were prepared in two formats: a first format of small dimensions (green diameter 12 mm) to make a preliminary screening of the most effective compositions, and one of larger dimensions (green diameter 44 mm) to evaluate the effect of the scale up on the densification and morphology of the sample. The smaller format was linearly pressed at 50 MPa, while the larger format at a pressure of 25 MPa. Both were then cold isostatically pressed at a pressure of 300 MPa to achieve a higher green density and compensate for the lack of pressure during sintering.

3.1.4 Powder sintering

During sintering, ceramic powder particles aggregate to form a dense material with improved mechanical properties, without the massive melting of the material. To achieve this result, it is generally necessary to keep the material at high temperatures for long periods of time. However, under these conditions, grain growth can occur, and depending on the material it could result in a deterioration of the mechanical properties and the formation of internal stresses.

To sinter faster at a lower temperature and avoid these phenomena, pressure-assisted techniques can be used. Applying pressure during densification accelerates sintering at a lower temperature, but this limits the material to simple geometries that can withstand uniform pressure.

In this thesis, two sintering methods were used to densify the samples: hot-pressing sintering to study the sintering of the mixtures (Chapter 4) and pressure-less sintering to evaluate a more easily scalable industrial approach (Chapter 5).

The final density of the material is measured both as apparent density, by Archimedes' principle (Equation 3.2) and relative density, calculated using the formula (1-P), where P is the percent porosity measured by image analysis (Image -ProAnalyzer 7.0 software) on micrographs of the polished sample cross section. To better distinguish the secondary phases from the porosity, EDS analyzes (section 3.2.3) were carried out on the same surfaces examined in the calculation of the residual porosity. Relative density cannot be directly obtained from Archimedes' principle because the theoretical density of each mixture is difficult to determine due to the reactions that occur during sintering. Archimedes' apparent density is obtained from the following equation:

$$\rho_{\text{archimede}} = \frac{m_{dry}}{m_{dry} - m_{sub}} * \rho_{liquid} \tag{3.2}$$

where m_{dry} is the mass of the dry sample, m_{sub} is the mass of the sample totally immersed in a liquid and ρ_{liquid} is the density of the liquid.

3.1.4.1 Hot-Pressing Sintering (HP)

In the hot-pressing technique (Ing. Allaria MP20 / II Alto Vuoto, IT), a constant uniaxial pressure (30-40 MPa) is applied to the sample placed in a graphite die by means of two vertical pistons, while it is heated. The applied pressure and temperature promote sintering. The evolution of the sintering process can be studied by analyzing the displacement of the pistons as a function of temperature and time.

This is done by plotting a sintering curve, which shows the change in piston displacement as a function of temperature or time. The sintering curve can be divided into three stages:

- Heating stage: The powders are compressed, but the temperature is insufficient for any shrinkage. Only minor displacements can be observed.
- Sintering stage: When the sample reaches the minimum temperature necessary to sinter under the given sintering conditions, shrinkage begins to be observed and becomes more significant and rapid as the temperature increases.
- Final densification stage: In this stage, the material is fully densified and the piston displacement no longer changes.

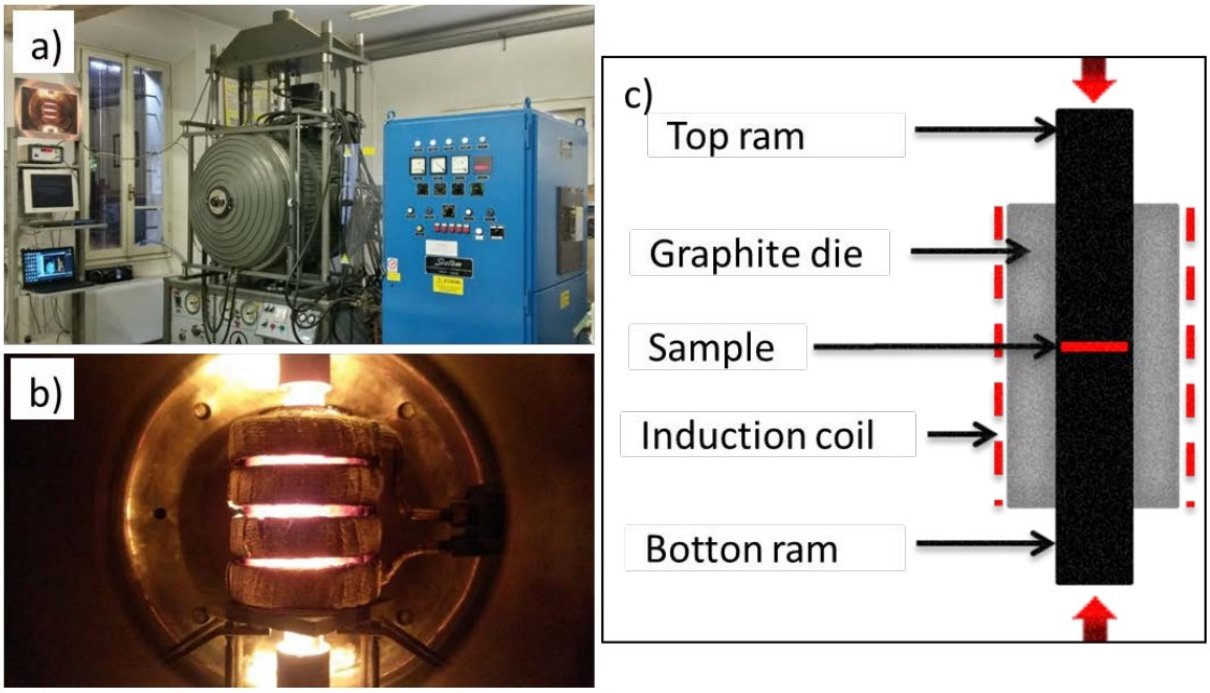

Fig. 3.3 a) Vacuum hot-pressing (HP) with induction heating system (Ing. Allaria MP20 / II Alto Vuoto, IT); b) induction coil (internal chamber of the oven, working condition 1900 °C); c) simplifying scheme of the hot-pressing process.

From the sintering curve it is possible to determine at which temperature the shrinkage of the material begins, the shrinkage rate and to recognize one or more phases during the process. It is also possible to replace the displacement of the pistons with the relative density of the sample to be able to compare the different mixtures.

The relative density of the sample at time t (ρ_t) during sintering can be calculated according to the following equation:

$$\rho_t = \rho_f \left(\frac{h_f}{h_0 - d_t}\right) \tag{3.3}$$

where ρ_f is the final relative density, h_f the final height of the sample, h_0 the initial height of the sample and d_t the displacement of the pistons at time t. For simplicity, the equation assumes that the theoretical density does not change significantly with temperature.

Hot-pressing was conducted in medium vacuum (10 Pa) in a graphite kiln where the graphite susceptor was heated by induction heating, with a heating rate about 80°C/min and free cooling. The hot-pressing schedule was determined during the heating process based on the recorded shrinkage measured by the displacement of the rams.

3.1.4.2 Pressure-less sintering (PLS)

Pressure-less sintering is a simple technique in which the sample is just heated to the sintering temperature and kept at that temperature. Without pressure, sintering is not promoted as well, so higher temperatures and times are required to achieve good densification. However, the simplicity of pressure-less sintering makes it easily scalable and therefore the most common industrial technique.

In this thesis work, this technique was used to test preparation methods and sintering conditions easily applicable to an industrial setting. Since a sintering curve was not possible, as in the case of hot-pressing, sets of tests were conducted at various temperatures (1900-2100°C, heating rate 10 °C/min) and holding times (60-120 minutes) to identify the best conditions.

To further evaluate the sintering process, two sample sizes were tested: a smaller one to optimize sintering conditions and evaluate compositions using this technique compared to HP, and a larger one to assess the effects of scaling up the process.

Small size (12 mm diameter) samples were sintered in an argon atmosphere (1.2 bar) between 1900 and 2200°C with holding times between 60 and 120 minutes. Since the furnace chamber is large enough to accommodate up to 4 samples of the small sizes, different sample set were sintered together under the same condition to increase the number of results.

The best results were repeated for the larger sample sizes (diameter 44 mm) of the more promising compositions with additional sintering cycles to optimize density and microstructure.

Fig. 3.4 LHTG 200-300/24-1G Carbolite Gero high performance oven.

3.1.5 Sample machining

After sintering, higher density samples have high hardness and resistance to abrasion, this results in the difficulty of cutting them with the classic method of the rotating diamond blade. Since TiB_2 has good electrical conductivity, it was possible to cut it by electrical discharge machining using wire EDM. This technique was used to obtain the cross sections of the samples and to prepare the bars for the mechanical tests.

After cutting, polishing down to 0.25 µm was carried out with a semi-automatic polishing machine (Tegramin-25, Struers, Italy) directly on the cross sections for SEM, EDS, and XRD analysis and measurements of hardness and intentional fracture toughness.

Regarding the bars for the mechanical tests prepared during my stay at the Missouri University of Science and Technology, surface grinding with a fully automated surface grinder (FSG-3A818, Chevalier, Santa Fe Springs, CA) using a 600-grit diamond grinding wheel, was first used to remove the oxidized surface and reach the final dimensions of the bar, ensuring that the sides were parallel. Then it was proceeded to the final steps of chamfering the edges and polishing the tensile surface for the specimens for flexural strength, and preparing the Chevron notch for the fracture toughness bars.

3.2 Microstructural characterization

The microstructure of a material is determined by its composition, the distribution of the phases present, the morphological and crystallographic characteristics, and determines its mechanical, chemical, thermal and electrical properties.

Microstructural characterization was useful in this thesis work to determine the reactions that occurred during sintering and the products of these reactions. It was also necessary to better understand the effects of sintering aids, preparation methods such as high-energy-planetary-ball-milling, and sintering techniques on the microstructure of TiB_2.

The main techniques for microstructural characterization used in this work were X-Ray Diffraction (XRD), Scanning Electron Microscopy (SEM) and Energy Dispersive X-Ray Spectroscopy (EDS).

3.2.1 X-Ray diffraction analysis

X-ray diffraction (XRD) is a non-destructive technique that allows to determine the chemical composition, the crystallographic structure and the physical properties of the materials. While XRD is usually used for qualitative and quantitative analyses of crystalline phases in materials, it can also be employed for characterization of solid solutions, crystallite size and shape, crystal orientation, internal elastic strains/stresses or the effect of temperature [2].

XRD analysis is based on the elastic scattering of X-ray by the electron clouds acting as scatterers. X-rays are high-frequency electromagnetic waves with a wavelength that generally varies between 10 nm and 1 pm, however the wavelength in X-ray analyzes is around 1Å (10 pm) thus the same order magnitude as the spacing between the crystallographic planes of the atomic structure.

A regular array of scatterers (Fig. 3.5), such as in the case of a crystal lattice, where the atoms repeat periodically in nearly perfect order, produces a regular array of spherical waves. While in most directions the waves cancel each other out through destructive interference, they combine constructively in a few specific directions, determined by Bragg's law [3]:

$$n\lambda = 2d \sin\theta \qquad (3.4)$$

where n is an integer (1,2,3…n) that represents the “harmonic order” of the diffraction, λ is the wavelength of the beam, d is the spacing between diffracting planes and θ is the incident angle at which a diffraction peak is measured.

The result of the diffraction of a given λ of X-rays by a crystalline lattice is a series of peaks where each of theirs represents the spacing between a family of planes which can be calculated from the θ angle at which it can be measured.

Each crystalline cell presents a unique set of peaks at different θ angles and intensities, the qualitative analysis of a spectrogram is therefore usually achieved by comparison with standard reference patterns (JCPDS standard) [4].

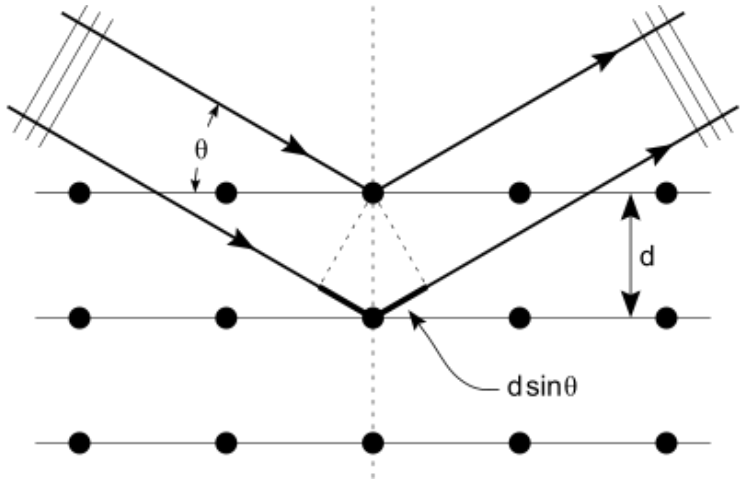

Fig. 3.5 Representation of the Bragg's law.

Most of powder diffractometers use Bragg-Brentano parafocusing geometry [5], Fig. 3.6, where the main parts of the instrumentation are X-ray source, sample holder and detector. In this geometry, the incident and diffracted beams move on a circle which is centered on the sample and the incident angle (θ) between X-ray source and the sample is the half of the detector angle (2θ).

Two different goniometer configurations are possible:

- θ-2θ scan, where the X-ray tube is fixed while the sample rotates at θ/min and the detector at 2θ/min;
- θ-θ scan, where the sample is fixed while source and detector move at the same speed of θ/min.

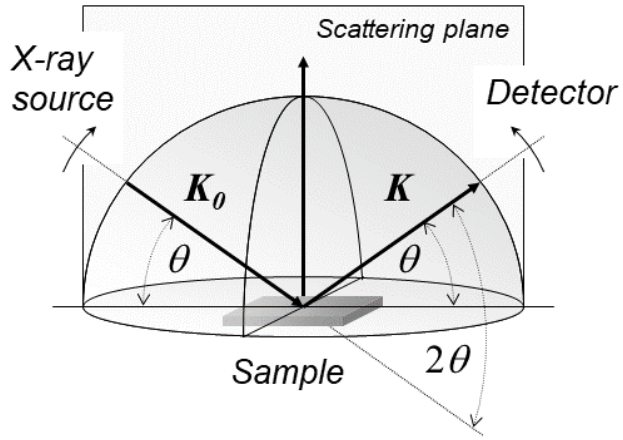

Fig. 3.6 Hemisphere of diffraction for an X-ray diffractometer with a Bragg-Brentano geometry [6].

The X-ray source consists of a cathode of tungsten filament that emit electron when heated, and a metal anode (typically copper, molybdenum, or cobalt) that emits X-rays when hit by the emitted electrons, accelerated by a high voltage. This geometry offers high-resolution and high beam-intensity analysis at the cost of very precise alignment requirements and carefully prepared samples.

In this work, the instrument used for X-ray diffraction analysis on powders and polished surfaces of solid sintered sample presents Bragg-Brentano θ-θ geometry (D8 Advance, Bruker, Germany), LYNXEYE detector and a Cu Kα radiation as X-ray source (λ=1.54178 Å). The analysis conditions of the spectrograms were steps of 0.02° for 0.5 sec from 20° to 80°.

3.2.2 Scanning electron microscopy

Scanning electron microscopy (SEM) was used to analyze the microstructure of the sintered materials, i.e. the size and morphology of the grains, pores and secondary phases.

SEM is an imaging technique that allows to obtain high-resolution images at high magnifications of the sample surface (>100k) through a scanning electron microscope where an electron beam is focused through electromagnetic lenses on the sample surface and allows to obtain images in various modes. In order to be analyzed using this technique, samples must be conductive and stable in vacuum (10^{-5}-10^{-6} Pa).

A scanning electron microscope (Fig. 3.7) consists of an electron source or "gun", electromagnetic lenses, a sample stage and detectors for the various signals of interest. The electron beam is typically produced by thermionic emission (TE gun) but it is also possible to exploit the field-emission (FE gun) or Schottky-emission (SE gun) effects.

In TE guns a cathode composed of a thin filament (0.1 mm) usually of tungsten is heated to high temperatures (2800 K) to emit electrons by thermionic effect. In this type of guns, the electron beam is generally 15-20 μm.

To generate a field-emission it is necessary that a high voltage is applied to a very clean metal surface and in an ultra-high vacuum (about 10^{-8} Pa). In FE guns the emitter is usually sharp single crystal tungsten with a tip radius of about 100 nm. The electron beam of these emitters is smaller than that of the TE guns guaranteeing a higher final resolution, furthermore, in this case there is no chromatic aberration, which TE has instead. [7].

SE guns are thermally assisted, combining the benefits of thermionic and field emission sources. Schottky emitters are made by coating a tungsten tip with a layer of zirconium oxide (ZrO_2) which facilitates the thermal emission of electrons when the source is heated, decreasing the work function of the tip. Although the electron beam in the SE guns is wider compared to the FE guns, it has greater stability which is its primary advantage [7].

In all the previously described guns the electron source acts as a cathode and to create a beam the electrons produced must all flow in the same direction, for this an anode is used which attracts them, accelerates them, and passes them on toward the column.

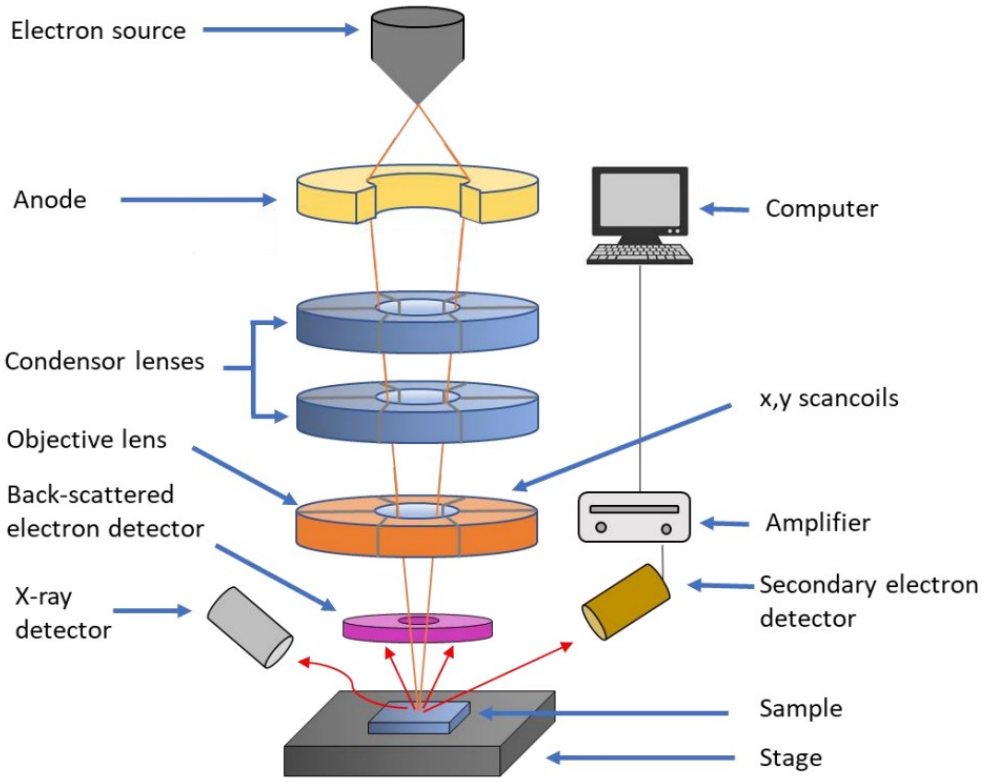

Fig. 3.7 Schematic representation of a scanning electron microscope (SEM).

The electron beam, generally with energy ranging from 0.2 keV to 40 keV, gets focused through one or two condenser lenses into a focal point that measures approximately 0.4 nm to 5 nm in width. This beam traverses sets of scanning coils or deflector plates arranged in pairs within the electron column, often within the ultimate lens. These components alter the beam's trajectory along the x and y axes, causing it to sweep systematically in a grid-like pattern across a rectangular section of the sample's surface.

The sample is mounted on a specimen stage, inside a vacuum analysis chamber. This stage can move horizontally (along the X and Y axes), vertically (Z axis) and can also rotate and tilt. From the interaction between the electron beam and the sample, several types of signals emerge, including backscattered electrons (BSE), secondary electrons (SE), and characteristic X-rays. These signals are collected by special detectors and processed to generate images of the sample.

As the primary electron beam reaches the surface of the sample it gradually loses energy due to scattering and absorption within a teardrop-shaped volume known as the interaction volume. The size of this volume (Fig. 3.8 a) can range from 0.1 to 5 µm in the sample surface and depends on the energy of the electron beam, the density, and the atomic number of the specimen.

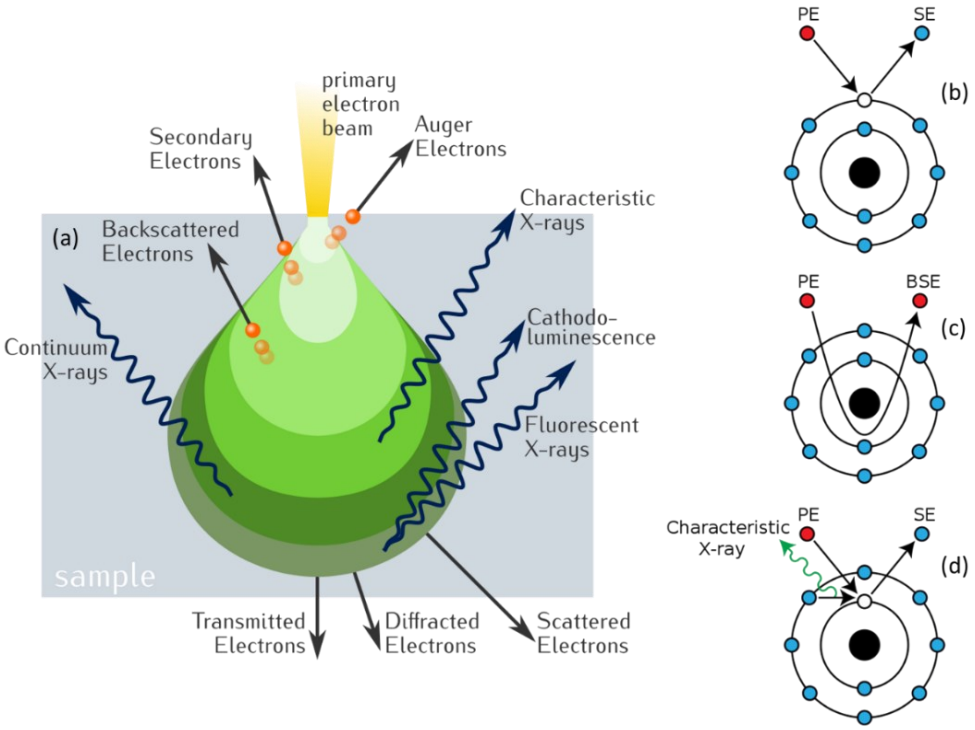

Fig. 3.8 (a) Electron volume interaction with matter and mechanisms of emission of (b) secondary electrons, (c) backscattered electrons, and (d) characteristic X-rays from atoms of the sample.

The most common imaging method is obtained from low-energy (< 50eV) secondary electrons (Fig. 3.8 b) emitted from the valence band of the sample atoms following inelastic interaction with beam's electrons. Since their energy is low, only those generated in a few nanometers below the surface are detected, while those in depth are rapidly reabsorbed, therefore it is used for surface analysis.

The backscattered electrons (Fig. 3.8 c) originate from high-energy electrons (>50 eV) that interact with the atomic nuclei of the sample via elastic scattering. Being high-energy, they provide information on regions at relative depth compared to other signals, and since the nuclei of heavy elements backscatter electrons better, they are very sensitive to the composition of the sample. Dedicated backscattered electron detectors are placed above the sample and have a circular shape.

The interaction between the electron beam and the sample can produce characteristic X-rays (Fig. 3.8 d) which can be measured using an energy-dispersive spectrophotometer and that are mainly analyzed for elemental microanalysis.

In this work a FE-SEM (field emission gun scanning electron microscope) was used to record micrographs of polished cross sections or fractures of the specimen. Specifically, the electronic source was a Schottky-emission electron gun (Zeiss Sigma, Carl Zeiss Microscopy Gmbh, Germany) equipped with detectors for secondary electrons (SE2), low energy electrons (SE1) and backscattered electrons (BSE).

3.2.3 Energy- dispersive X-ray spectroscopy

Energy-dispersive X-ray spectroscopy (EDS) was used coupled to SEM to make qualitative and semi-quantitative analyzes on the microstructure of the samples.

EDS is an analytical technique which allows to perform elemental analysis or chemical characterization by measuring the characteristic X-ray fluorescence emitted by the sample as a result of irradiation with a beam of electrons or X-ray.

The incident beam can interact with the atoms of the sample causing the excitation of electrons from inner shells and their expulsion, these electronic vacancies can be filled by higher energy electrons from the outer layers, releasing energy during the electron transitions due to relaxation. The energy is usually released via X-ray fluorescence and is equal to the difference between the energy levels of the electron transition. Since these transitions are unique and characteristic for each element, it is possible to carry out elemental microanalysis of the sample by measuring the X-rays emitted with an energy-dispersive spectrophotometer.

A representation of the x-ray fluorescence phenomenon is shown in Figure 3.9, the energy levels are labeled with a capital letter (K, L, M, etc.) which refers to the orbital (where K is the innermost orbital with the lowest energy) while the transitions are labeled by the letter of the arrival orbital and by Greek letters (α, β, etc.) which refer to the dimension of the transition (α for one level of difference, β instead for two levels). Thus, a relaxation from L to K or from M to K will be described as Kα or Kβ, while a relaxation from M to L will be termed Lα. This method is known as Siegbahn notation [8].

The instrumentation typically consists of an excitation source (electron beam or X-ray beam), an X-ray detector, and an analyzer. It is usually integrated with other instruments that use electron beams (e.g., electron microscopes, scanning electron microscopes (SEM), and scanning transmission electron microscopes (STEM)) or X-ray beams (e.g., XRF spectrometers).

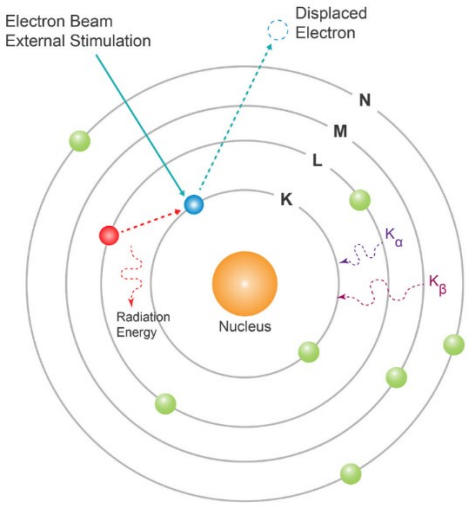

Fig. 3.9 representation of the X-ray fluorescence phenomenon.

The result of the analysis is a spectrum (Fig. 3.10) with the energy of the X-rays in KeV on the x-axis and the intensity of these on the y-axis from which it is possible to obtain the energy of the transitions that have taken place and their number.

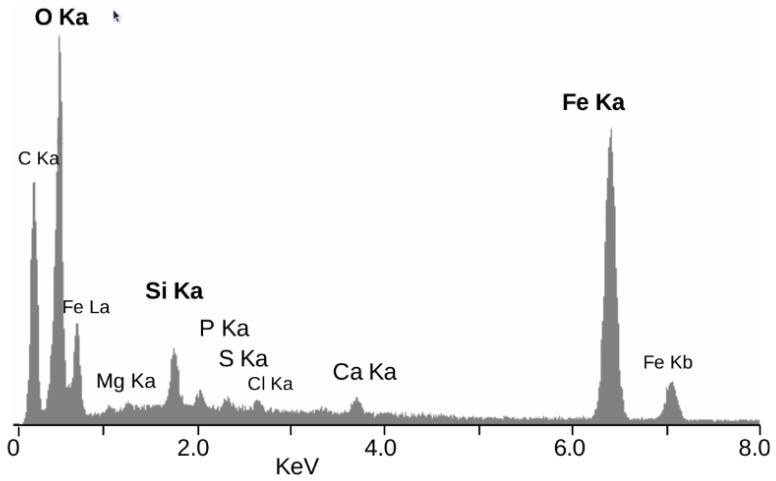

Fig. 3.10 example of an EDS spectrum.

The EDS analysis allows to identify the elements present in a certain portion of the sample, however it can be difficult to identify elements present in traces or with a low atomic weight: for example, H and He which have only one orbital do not give rise to X-ray fluorescence.

Since it is not a particularly sensitive method, it is mainly used for qualitative analyses, however it is possible to carry out quantitative analyzes after a calibration with a metal standard. Accuracy and sensitivity of the analysis depend on the composition of the sample and on the energy of the incident beam: light elements are harder to detect because as their atomic number decreases, it becomes increasingly difficult to ionize an atom, and the ionized atom produced is less likely to generate X-rays, thus giving a lower signal. Also, longer wavelength X-rays produced by these elements are absorbed more rapidly within the sample so most X-rays from light elements that reach the detector come from near the surface of the sample. Furthermore, if in order to improve the accuracy for heavy elements, that require high energies to emit X-rays, it is necessary to use more energetic electron beams. this can reduce the accuracy with respect to light atoms due to the greater penetration of a beam electronic with more energy [9].

During this thesis work EDS analyzes (Oxford Energy X-act, Oxford Instruments, UK, interfaced by INCA software) were performed to determine the composition of the samples after sintering. In particular, the instrumentation is coupled with the previously described scanning electron microscope.

3.3 Mechanical testing

3.3.1 Vickers hardness

Hardness is defined as the resistance of a material to the penetration of a hard penetrator of specific geometry and charged in a defined way (CEN ENV 843, 1992). Different factors can influence hardness:

- interatomic bound;
- type and number of dislocations required for plastic deformation;
- microstructural parameters such as mean grain size, porosity and composition [10].

A penetrator is placed under static load on the surface with an applied specific force for a certain time. After the load is removed, the dimensions of the produced impression are measured with an optical microscope: the hardness is calculated from the measured dimensions and the value of the applied load. In addition to plastic deformation, a sample subjected to penetration can give rise to incipient cracks or brittle fractures according to various mechanisms. For this work, the hardness was measured using a static method [11].

In this thesis work, Vickers micro-hardness, HV 1.0 (GPa), was measured using a standard micro-hardness tester. This method is often easier to use than other hardness tests because the required calculations are independent of the indenter size. It is also the most common hardness test used in ceramic research.

A hard indenter, typically made of diamond, is pressed into the sample. The load on the indenter is increased until it reaches a predetermined value (9.81 N for HV 1.0). The load may then be held constant (10-15 seconds) or removed. The area of the resulting indentation is measured and the hardness, HV, is calculated as follows:

$$HV = \frac{2Fsin\frac{136^\circ}{2}}{d^2} = 18544\frac{F}{d^2} \tag{3.5}$$

where F si the maximum load (kgf) and d^2 is the residual indentation area (mm) (Fig. 3.11).

In this thesis work, the hardness was measured using the Vickers indentation method (Innovatest Falcon 505, Rupac, Netherlands), with a 1 kg (9.81 N) load held for 10 seconds. The indentation area was measured using optical microscopy.

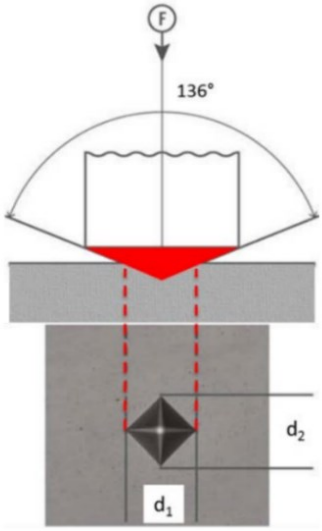

Figure 3.11 Vickers hardness indentation.

3.3.2 Flexural strength

Flexural strength represents the maximum stress that a material can tolerate before fracture in a bending test [12]. For a bulk ceramic, the flexural strength depends on different factors such as size, shape grain size, density, pores and flaws distribution. In fact, residual porosity, large grains can decrease the mechanical properties. More in detail, the pores decrease the area where the load is applied and can act as defects where the stress is concentrated and leads to a catastrophic failure [13].

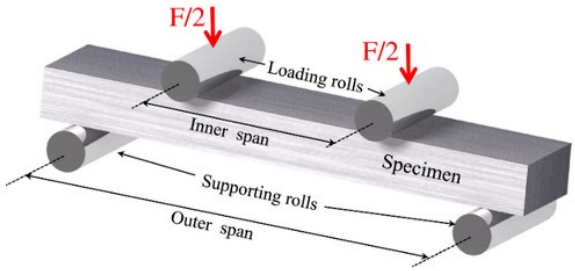

Figure 3.12 Four-point flexural strength test geometry.

All flexural strength tests were performed with four-point geometry (Fig. 3.12) using a semi-articulated test fixture with an outer span of 20 mm and an inner span of 10 mm (Fig. 3.13). Then the bending resistance value was calculated using the following equation:

The flexural strength value was then calculated using the following equation:

$$\sigma = \frac{3F(L-L_0)}{2bd^2} \tag{3.6}$$

Where F is the force, L and L_0 are the outer and inner support span respectively and b and d are the width and thickness respectively.

Figure 3.13 Illustration of Z050, Zwick-Roell (left) and a semi-articulated test fixture for the four-point bending strength test (right).

Tensile testing of ceramics is time-consuming and expensive to conduct, especially when fabricating the specimens. Therefore, this thesis work used two types of specimen preparation: a faster and cheaper method involving simple cutting via EDM with chamfering of the edges but without grinding, and a more accurate but expensive method including surface grinding and tensile surface lapping. The former preparation and test were carried out at the CNR in Faenza, and the latter preparation and tests were conducted during the period abroad at the Missouri University of Science and Technology.

Four-point bending strength tests performed in Faenza were carried out only at room temperature on specimen with dimensions of 25 mm x 2.5 mm x 2 mm using a semi-articulated test fixture with a outer span of 20 mm and inner span of 10 mm, using a screw-driver testing machine (Z050, Zwick-Roell, Germany) and a displacement rate of 1.0 mm/min, Fig. 3.13.

For test specimens obtained via electrical discharge machining at Missouri S&T using wire EDM (HSS150, Aegi), the oxidized surface was removed and the final dimensions were achieved by surface grinding (see section 3.1.5). Flexural strength A bars (25 mm x 2.0 mm x 1.5 mm) were prepared according to ASTM C1161–02c, the edges were chamfered by hand using 15 µm diamond abrasives and the surface subjected to traction was polished down to 0.25 µm with a semi-automatic polishing machine. The four-point flexural strength was measured at room temperature with a displacement rate of 0.5 mm/min, using a screw-driven instrumented load frame (Model 5881, Instron, Norwood, MA), employing a fully articulating fixture with load and support spans of 10 and 20 mm [14].

High-temperature flexural strength testing was conducted at Missouri S&T using a mechanical testing setup that comprised a screw-driven instrumented load frame (model 33R4204, Instron), and an inductively heated graphite hot zone (model SI-30KWLF, Superior Induction Technology) situated inside an environmental chamber. Temperature control was achieved through a two-color optical pyrometer (model SR-35C15, Ircon Inc.) and a programmable PID controller (model 2404, Eurotherm).

The test specimens were affixed to a fully articulating graphite 4-point bend fixture using cyanoacrylate adhesive. The specimens were then subjected to a heating rate of approximately 50°C/min until reaching the target temperature, where they were held for 5 minutes to ensure temperature equilibration prior to testing. To maintain a linear elastic response until failure, the crosshead displacement rate was adjusted (Table 7.3) in accordance with ASTM C1211 [15].

3.3.3 Fracture toughness

Fracture toughness is a critical property of materials that it is defined as the ability of a material to resist the propagation of a crack [16]. Fracture toughness is measured in terms of the stress intensity factor, K, which is a measure of the stress concentration at the tip of a crack. The critical stress intensity factor, K_{Ic}, is the value of K in mode I loading measured under plane strain conditions that leads to brittle fracture [17,18].

K_{Ic} depends on the nature of the material, the value is generally higher for ductile materials and lower for brittle materials, such as ceramics. One way to determine KIc is through indentation testing. This method is popular for bulk ceramics because it is relatively simple to perform [19–21]. In an indentation test, a hard indenter is pressed into the surface of the specimen. This creates cracks that radiate outward from the corners of the indent. The length of these cracks can be correlated to the material's fracture toughness.

Other fracture toughness evaluation methods for ceramic materials involve introducing a notch where the stresses concentrate [22]. In Fig. 3.14 are illustrated the different notch geometries.

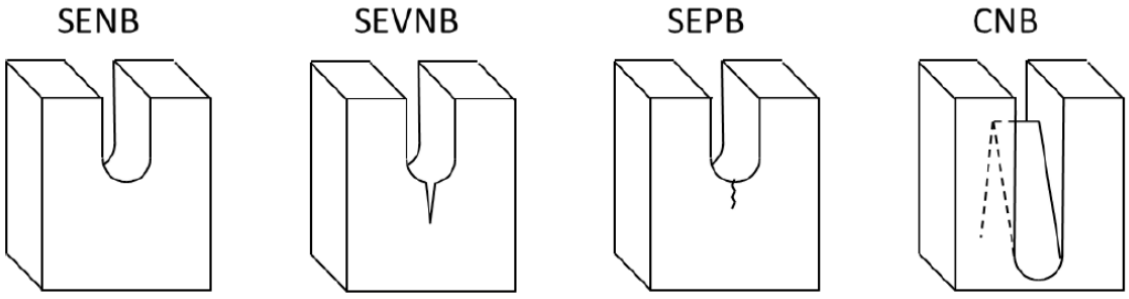

Figure 3.14 Schematic representation of the different notch geometries.

The chevron notched beam (CNB) method is a fracture toughness testing method that uses a specimen with a triangle-shaped notch. The application of a load initiates a crack at the top of the triangle, which then propagates through the specimen. The CNB method has several advantages over other fracture toughness testing methods, including that it can be used on small sample sizes and is relatively easy to perform and analyse, moreover, this method avoids the issue of crack tip curvature.

The CNB fracture toughness is calculated from the maximum load (P_{max}) measured in a four-point bending test using the "slice model equations" of Munz [22]. The CNB model and these equations are reported in Figure 3.15, where y* is the dimensionless stress intensity factor coefficient, B and W are the thickness and width of the specimen, S_1 and S_2 are the spacing between the rollers, a_0 e a_1 are the crack lengths (measured from load line), and α_0 e α_1 are the dimensionless ratios between the crack lengths and the width of the specimen.

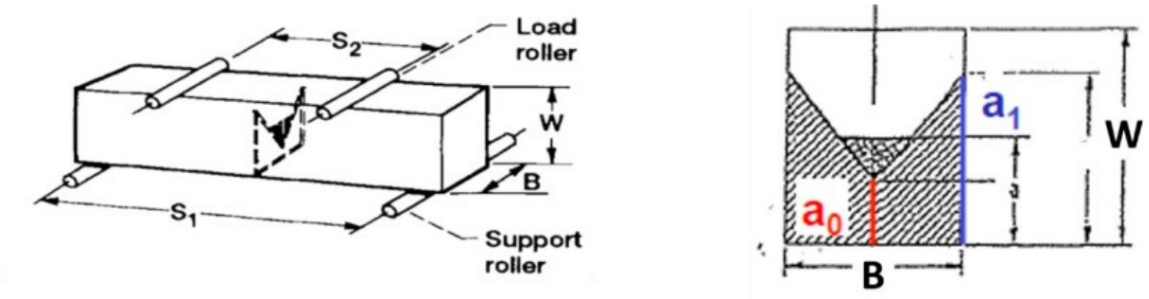

$$\left.\begin{aligned}\alpha_0 &= \frac{a_0}{W}\\ \alpha_1 &= \frac{a_1}{W}\end{aligned}\right\} \quad y^* = (3.08 + 5\alpha_0 + 8.33\alpha_0^2)\frac{(S_1 - S_2)}{W}\left(1 + 0.007\sqrt{\frac{S_1 S_2}{W^2}}\right)\left(\frac{\alpha_1 - \alpha_0}{1 - \alpha_0}\right)$$

$$K_{Ic} = \frac{P_{max}}{B\sqrt{W}}y^*$$

Figure 3.15 Chevron notched beam (CNB) model and equations for the determination of K_{Ic}.

In this thesis, fracture toughness (K_{Ic}) was measured using four-point bending test with chevron notch configuration "A," in accordance with ASTM C1421 standards but with a shorter length due to the initial sample's size.

Six fracture toughness specimens were prepared, featuring final dimensions of 25 mm × 3 mm × 4 mm. A chevron notch was machined using a dicing saw (Accu-cut 5200; Aremco Products) equipped with a 150-µm thick diamond wafering blade. For both room temperature and elevated temperature testing, the same procedural approach and equipment employed for flexural strength testing was applied. Notably, the crosshead rate was adjusted (Table 7.4) in correspondence with temperature conditions.

3.4 Thermal testing

In this thesis work the thermal properties measured were thermal diffusivity, thermal conductivity and specific heat. Thermal conductivity (k) is a measure of how easily heat can be transferred through a material and is measured in W/m K. Specific heat capacity (c_p) is a measure of how much heat is required to raise the temperature of a unit mass of a material by one degree Celsius and has J/kg K as its unit of measurement. Finally, thermal diffusivity (D) is the thermal conductivity normalized on density and specific heat capacity of the material studied and is measured in m^2/s and is calculated from equation [23,24]:

$$D = \frac{k}{\rho c_p} \tag{3.7}$$

where k is the thermal conductivity, ρ the density and cp the specific heat capacity. Thermal diffusivity is usually measured trough the laser flash method.

3.4.1 Laser flash analysis

Laser flash analysis is a non-destructive technique for measuring the thermal diffusivity of materials. It is the most common technique for this purpose and is based on the following principle: a short pulse of energy (from a laser or flash lamp) is applied to one face of a sample, and the resulting temperature rise on the opposite face is measured (Fig. 3.16). The thermal diffusivity of the sample can then be calculated using the following equation [24,25]:

$$D = 1.38 \frac{x^2}{\pi^2 t_{1/2}} \tag{3.8}$$

where D is the thermal diffusivity (m^2/s), x is the sample thickness (m) and $t_{1/2}$ is the half temperature rise time (s).

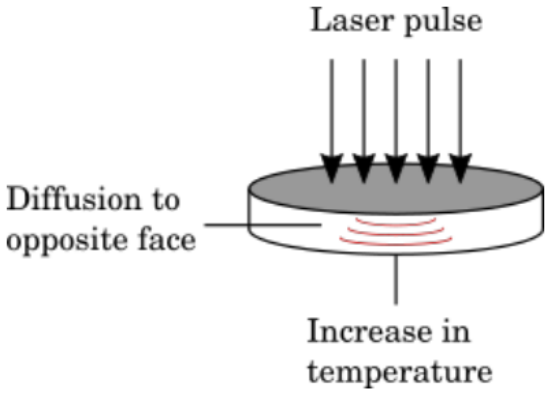

Figure 3.16 Representation of the laser flash analysis setup: a radiation source, typically a laser, heats the surface of the target at a fixed rate, and the temperature is monitored on the back side of the specimen as function of time [24].

In this thesis work, a circular specimen with a diameter of 12.7 mm and a height of 2.0 mm was cut, grinded and prepared for thermal testing. The thermal diffusivity was then measured using a thermal property analyzer (Flashline L-S2, Anter Corporation) by employing the laser flash method. To reduce reflection of the laser and ensure uniform energy absorption during testing, a thin layer of graphite spray was applied to the prepared disc. Thermal diffusivity values were obtained through an average of three measurements at each measured temperature, which ranged from 25 to 200°C, with data points recorded at intervals of around 25°C, and from 200 to 2000°C, with data points recorded at intervals of around 200°C. Subsequently, the measured thermal diffusivity values, along with the bulk densities obtained through Archimedes' measurements and estimated heat capacities, were used in the equation 3.8 to calculate the thermal conductivity.

3.5 Electrical testing

In this thesis, to evaluate the electrical properties of the material, a measurement of the electrical resistivity was carried out using the Von der Pauw method. Electrical resistivity (ρ) is a property of a material that measures its resistance to the flow of electric current. It is defined as the resistance of a conductor of unit length and unit cross-sectional area and is measured in Ω m.

The Van der Pauw method is a technique used to measure the resistivity of a conducting material. The method is based on Ohm's law, which states that the electrical resistance of a conductor is directly proportional to the length of the conductor and inversely proportional to its cross-sectional area. In the Van der Pauw method, the sample is placed in a four-point configuration, as shown in the Figure 3.17. Four contacts are placed on the edge of the sample.

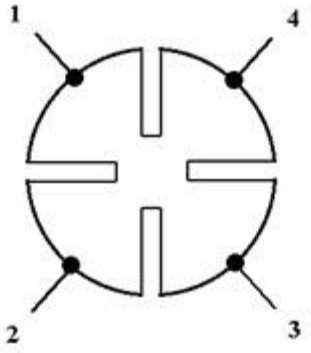

Figure 3.17 Representation of the Van der Pauw method setup.

A current is applied between two contacts, and the voltage is measured between the other two contacts. The resistance between the two measurement points is then calculated as follows:

$$\Omega = \frac{V_{\Delta}}{I} \tag{3.9}$$

The resistivity was calculated using the following equation:

$$\rho = \frac{A}{\Delta}\Omega = \frac{A}{\Delta} \cdot \frac{V_{\Delta}}{I} \ (\mu\Omega \ cm) \tag{3.10}$$

where ρ is the resistivity, A is the cross-sectional area of the disc (cm^2), Δ is the distance between the inner probes (cm), Ω is the calculated resistance (μΩ), V_{Δ} is the measured voltage drop between the inner probes (μV), and I is the applied amperage (A).

The same cylindrical sample, with a diameter of 12.7 mm and a height of 2.0 mm, was also employed to measure its electrical properties. Electrical resistivity was determined using the Van der Pauw method, utilizing an in-house fixture powered by a KEITHLEY 2230G-30-1 power source, at room temperature. The specimen disc was positioned within an alumina fixture, featuring four wire contacts constructed from inconel wire. The electrical resistivity was determined as the average of three measurements, corresponding to three different current values: 0.2 A, 0.3 A, and 0.4 A.

3.6 References

[1] S. Baik, P.F. Becher, Effect of Oxygen Contamination on Densification of TiB2, J American Ceramic Society. 70 (1987) 527–530. https://doi.org/10.1111/j.1151-2916.1987.tb05699.x.

[2] M. Gonon, Case Studies in the X-ray Diffraction of Ceramics, in: M. Pomeroy (Ed.), Encyclopedia of Materials: Technical Ceramics and Glasses, Elsevier, Oxford, 2021: pp. 560–577. https://doi.org/10.1016/B978-0-12-818542-1.00005-9.

[3] B.D. Cullity, Elements of x-ray diffraction, 2d ed, Addison-Wesley Pub. Co, Reading, Mass, 1978.

[4] T.N. Blanton, T.C. Huang, H. Toraya, C.R. Hubbard, S.B. Robie, D. Louër, H.E. Göbel, G. Will, R. Gilles, T. Raftery, JCPDS—International Centre for Diffraction Data round robin study of silver behenate. A possible low-angle X-ray diffraction calibration standard, Powder Diffraction. 10 (1995) 91–95. https://doi.org/10.1017/S0885715600014421.

[5] E.J. Mittemeijer, U. Welzel, Modern Diffraction Methods, n.d. https://www.wiley.com/en-us/Modern+Diffraction+Methods-p-9783527322794 (accessed September 5, 2023).

[6] M. Birkholz, Thin Film Analysis by X-Ray Scattering, 2006. https://www.wiley.com/en-mx/Thin+Film+Analysis+by+X+Ray+Scattering-p-9783527607594 (accessed September 5, 2023).

[7] J. Orloff, Handbook of Charged Particle Optics, 2008. https://www.routledge.com/Handbook-of-Charged-Particle-Optics/Orloff/p/book/9781420045543 (accessed September 5, 2023).

[8] J.I. Goldstein, D.E. Newbury, J.R. Michael, N.W.M. Ritchie, J.H.J. Scott, D.C. Joy, Scanning Electron Microscopy and X-Ray Microanalysis, Springer New York, New York, NY, 2018. https://doi.org/10.1007/978-1-4939-6676-9.

[9] J. Konopka, T.F. Scientific, Options for Quantitative Analysis of Light Elements by SEM/EDS, (n.d.).

[10] L. Silvestroni, Development and characterization of non-oxide ceramic composites for mechanical and tribological applications, Alma Mater Studiorum Università di Bologna, 2009.

[11] S. Failla, Sintering and characterization of high hardness/high toughness/high entropy structural ceramics for severe environments, Doctoral thesis, Universita' degli studi di Parma. Dipartimento di Scienze chimiche, della vita e della sostenibilità ambientale, 2020. https://www.repository.unipr.it/handle/1889/4033 (accessed October 23, 2023).

[12] W.D.C. Jr, D.G. Rethwisch, Callister's Materials Science and Engineering, John Wiley & Sons, 2020.

[13] M. Mor, Fabrication and characterization of UHTCMCs for tribological applications, Doctoral thesis, Università degli studi di Parma. Dipartimento di Scienze chimiche, della vita e della

sostenibilità ambientale, 2023. https://www.repository.unipr.it/handle/1889/5398 (accessed October 23, 2023).

[14] ASTM International. ASTMC1161 Standard Test Method for Flexural Strength of Advanced Ceramics at Ambient. ASTM International; 2018., (n.d.).

[15] A.C. Murchie, J.L. Watts, W.G. Fahrenholtz, G.E. Hilmas, Mechanical properties of borothermally synthesized zirconium diboride at elevated temperatures, Int J Applied Ceramic Tech. 18 (2021) 1235–1243. https://doi.org/10.1111/ijac.13755.

[16] D.R. Askeland, P.P. Fulay, W.J. Wright, The Science and Engineering of Materials, SI Edition, Cengage Learning, 2011.

[17] S. Suresh, Fatigue of Materials, 2nd ed., Cambridge University Press, Cambridge, 1998. https://doi.org/10.1017/CBO9780511806575.

[18] G.A. Gogotsi, Fracture toughness of ceramics and ceramic composites, Ceramics International. 29 (2003) 777–784. https://doi.org/10.1016/S0272-8842(02)00230-4.

[19] A.G. Evans, E.A. Charles, Fracture Toughness Determinations by Indentation, Journal of the American Ceramic Society. 59 (1976) 371–372. https://doi.org/10.1111/j.1151-2916.1976.tb10991.x.

[20] G.D. Quinn, R.C. Bradt, On the Vickers Indentation Fracture Toughness Test, Journal of the American Ceramic Society. 90 (2007) 673–680. https://doi.org/10.1111/j.1551-2916.2006.01482.x.

[21] E. Rocha-Rangel, Fracture Toughness Determinations by Means of Indentation Fracture, in: Nanocomposites with Unique Properties and Applications in Medicine and Industry, IntechOpen, 2011. https://doi.org/10.5772/18127.

[22] D.G. Munz, J.L. Shannon, R.T. Bubsey, Fracture toughness calculation from maximum load in four point bend tests of chevron notch specimens, Int J Fract. 16 (1980) R137–R141. https://doi.org/10.1007/BF00013393.

[23] L. Vozár, W. Hohenauer, Flash method of measuring the thermal diffusivity. A review, High Temperatures-High Pressures. 36 (2004) 253–264.

[24] A. Vinci, Fabrication and characterization of fibre reinforced UHTC composites, Doctoral thesis, Universita' degli studi di Parma. Dipartimento di Scienze chimiche, della vita e della sostenibilità ambientale, 2019. https://www.repository.unipr.it/handle/1889/3735 (accessed October 24, 2023).

[25] W.J. Parker, R.J. Jenkins, C.P. Butler, G.L. Abbott, Flash Method of Determining Thermal Diffusivity, Heat Capacity, and Thermal Conductivity, Journal of Applied Physics. 32 (2004) 1679–1684. https://doi.org/10.1063/1.1728417.

4. Hot-pressing sintering studies on TiB_2

This chapter investigates the use of various sintering aids (B_4C, Si_3N_4, and $MoSi_2$), different preparation methods (ball-milling and high-energy-planetary-ball-milling), and their combination to improve the densification of TiB_2 through hot-pressing sintering. The shrinkage of the sample over time was recorded to study the trend of densification and the temperatures at which it occurs. Residual porosity, microstructure, composition, and mechanical properties of the sintered material were measured to study the mechanism by which additives, preparation methods and their possible synergy improve the densification of TiB_2. Finally, the best compositions were highlighted and compared with literature values.

4.1 Introduction

To improve the sintering of TiB_2, sintering additives and/or specific preparation methods are required. Metallic additives can improve sintering, but the resulting material is less suitable for high temperature applications, therefore non-metallic additives of different categories, specifically a carbide (B_4C), a nitride (Si_3N_4) and a silicide ($MoSi_2$) have been investigated in this chapter.

TiB_2 and additives were either just soft homogenized by wet-ball-milling (SH) for 24 hour or further high-energy-milled for 30 minutes (after wet-ball-milling) with WC-Co media (HEPBM).

The aim of ball-milling was to mix powders without changing their grain size, while HEPBM has been used to improve densification through the reduction of particle size, increasing the surface area and the introduction of debris from the grinding media that act as sintering aids [1–4].

The details of the sintering cycles and quantitative data on microstructural features are summarized in Table 4.1. The hot-pressing schedule was determined during the heating process based on the recorded shrinkage measured by the displacement of the rams. The displacement component due to piston expansion was subtracted from the total displacement according to the equation:

$$D_c = D_T - L_p \alpha \Delta T \tag{4.1}$$

where D_c is the correct displacement, D_T is the displacement at T, L_p is the initial length and α is the coefficient of thermal expansion of the piston material and ΔT is the change in temperature.

Due to the reactions between the matrix, sintering aids and oxide phase, it was not possible to calculate a theoretical density for the different compositions, except for T sample, which consisted of solely as-received TiB_2. The relative density of samples was calculated as (1-P) where P represents the percent porosity determined through image analysis on backscattered electron micrographs of the polished cross sections. Secondary phases and porosity were recognized through EDS analysis.

Part of the content of this chapter has been published in Nanomaterials 13 (2023) as "*S. Taraborelli, S. Failla, E. Sani, D. Sciti, Sintering, Mechanical and Optical Properties of TiB2 Composites with and without High-Energy-Milling.*"

Each percent porosity and mean grain size measurement was repeated on five different images, and the standard deviation between measurements was reported as the measurement error. To measure the grain size in the samples where a core-shell structure was observed, the contact edges between the shells, more easily visible in backscattered electron micrographs, were considered.

Label	Sintering aid, Process (vol%)	Max temp./time (°C, min)	Apparent density (g/cm^3)	Relative density (%)	Crystalline phases after sintering	Mean grain size (TiB_2, μm)
T	-	1950, 20	3.45	≈ 76	TiB_2	3.2 ± 1.4
TC	5 B_4C, SH	1900, 15	3.71	≈ 78	TiB_2	2.4 ± 1.4
TS	5 Si_3N_4, SH	1900, 15	4.28	85.6 ± 0.7*	TiB_2, TiN	3.1 ± 1.6
TM	5 $MoSi_2$, SH	1900, 10	4.43	95.1 ± 0.6*	TiB_2, $MoSi_2$	1.8 ± 0.8
T-h	HEPBM	1900, 10	4.60	93.4 ± 0.1	TiB_2, WB, W_2CoB_2	1.0 ± 0.5
TC-h	5 B_4C, HEPBM	1900, 10	4.22	87.9 ± 0.9	TiB_2, WB	1.3 ± 0.1
TS-h	5 Si_3N_4, HEPBM	1830, 10	4.54	92.4 ± 0.7*	TiB_2, TiN, WB	0.9 ± 0.4
TM-h	5 $MoSi_2$, HEPBM	1700, 10	4.67	94.7 ± 0.7*	TiB_2, TiC, TiSi, MoB, WB,	0.8 ± 0.5

Table 4.1 Sintering parameters and microstructural features of hot-pressed TiB_2 composites at 35 MPa. Notes: SH—24h wet-ball-milling, HEPBM— 24h wet-ball-milling and 30 min high-energy-planetary-ball-milling, *— porosities mainly filled by silica pockets (empty porosities < 2%).

4.2 Sintering behavior and microstructural features

The densification behavior was clearly affected by both the addition of sintering agents and the high-energy-planetary-ball-milling of the powders, as shown in Fig. 4.1 a and b which present the relative density plotted against time. From this type of graph, it can be observed at which temperature the shrinkage starts, and the maximum temperature needed for complete densification.

It can be noted that for the as-received TiB_2 powder, densification was very slow and only began after 10 minutes at 1950°C. In contrast, for the powder mixtures containing the sintering additives, densification started at lower temperatures: 1630°C for TC (addition of B_4C), 1770°C for TS (addition of Si_3N_4) and 1710°C for TM-h (addition of $MoSi_2$), see curve in Fig 4.1 a. The addition of boron carbide increased densification rate, but the final relative density remained below 80%. Si_3N_4 and $MoSi_2$ notably improved sintering, as indicated by a steep increase in the densification curve and the presence of SiO_2 pockets after sintering for both samples.

The steep change in the slope of the curve could be indication of liquid phase formation and increase of the densification rate due to particle rearrangement.

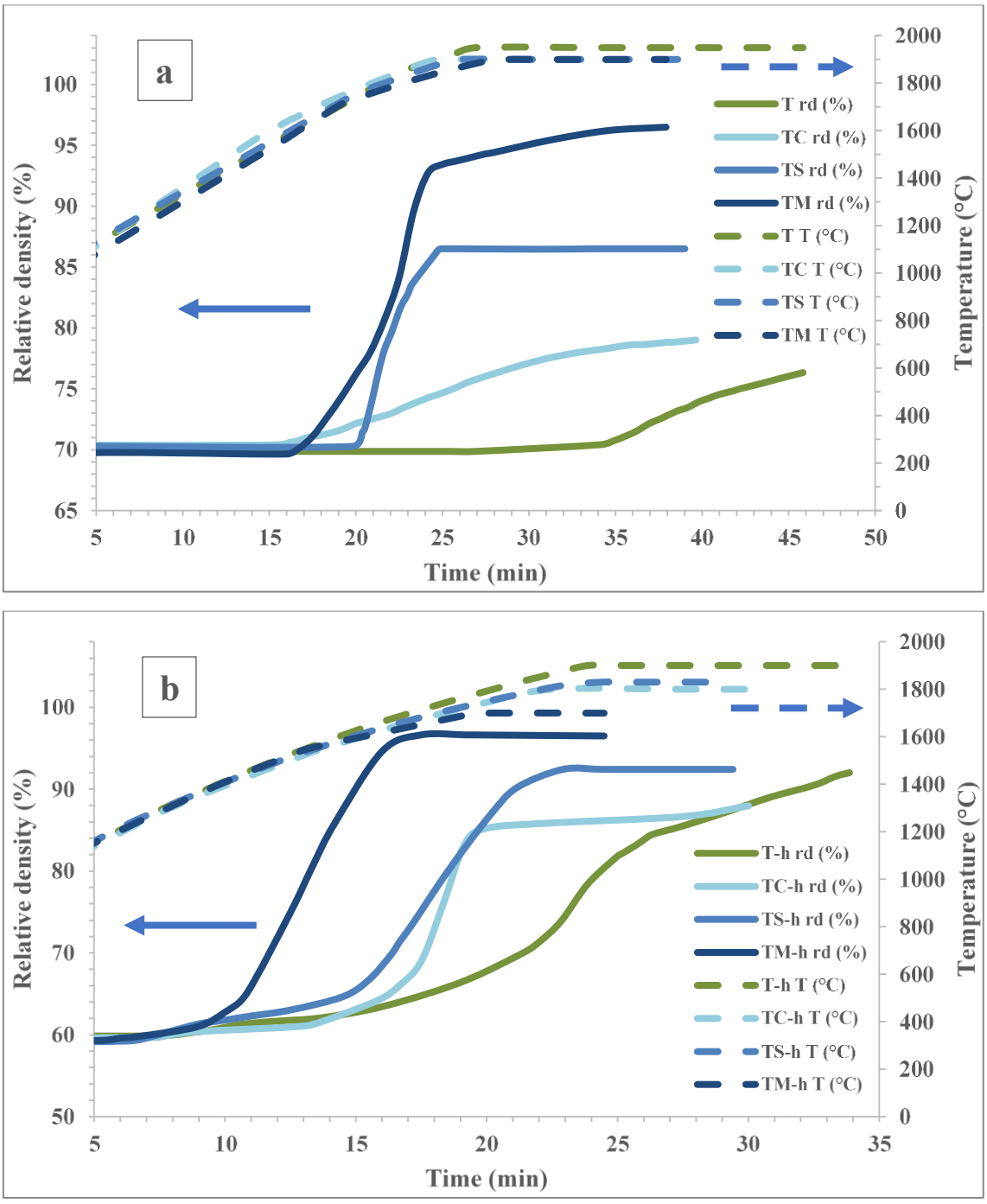

Fig. 4.1 Comparison of densification curves for HP sintered samples just soft homogenized by wet-ball-milling (a) and high-energy-planetary-ball-milled (b).

In the case of high-energy-planetary-ball-milled powders, densification initiated at 1570°C for T-h (reference, no sintering aids), 1530°C for TC-h (addition of B_4C), 1560 °C for TS-h (addition of Si_3N_4) and 1250°C for TM-h (addition of $MoSi_2$).

For the just high-energy-planetary-ball-milled TiB_2 ceramic, the increase in the shrinkage rate was more gradual. In contrast, a steep increase like what was observed for the TS and TM samples was also noticed for the three systems with either B_4C, Si_3N_4 and $MoSi_2$.

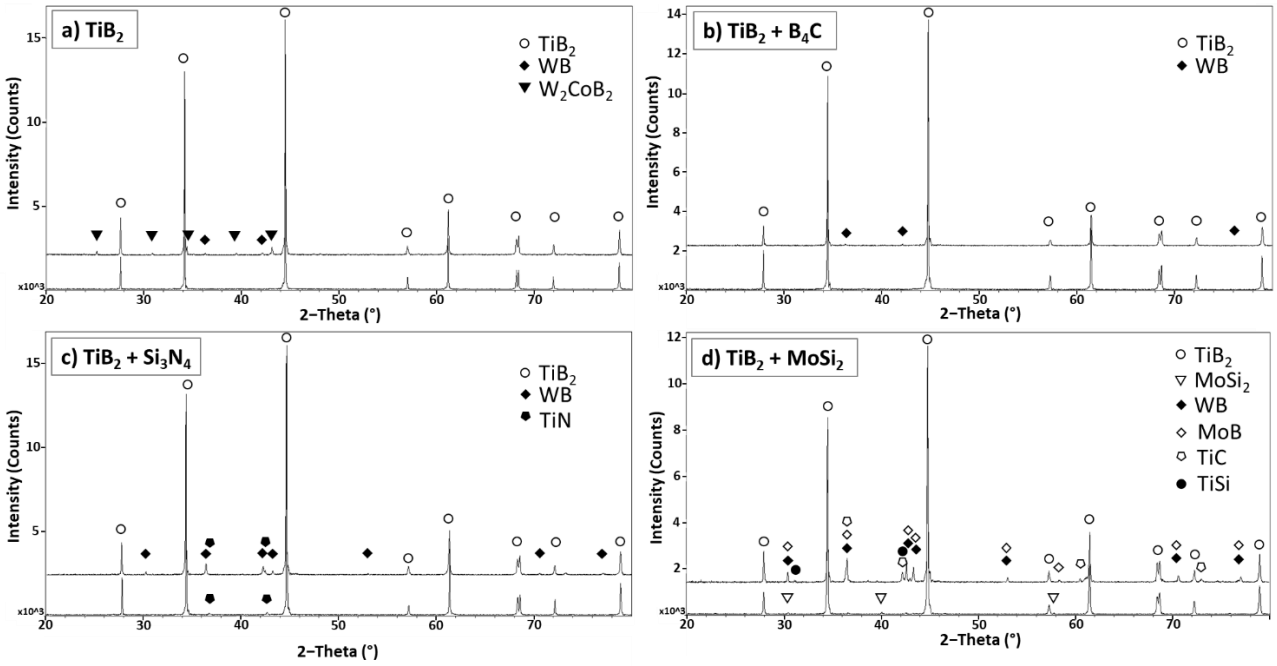

Fig. 4.2 X-ray diffraction patterns for the soft homogenized (line below) and high energy milled (line above) sintered sample of TiB_2 without additives (a), with 5 vol% of B_4C (b), 5 vol% of Si_3N_4 (c) and 5 vol% of $MoSi_2$ (d).

X-ray diffraction patterns (Fig. 4.2) recorded TiB_2 (TiB_2: JCPDF card 35-0741) in all the samples and WB for the high-energy-milled ones, along with minor secondary phases depending on the sintering aid and the preparation method employed. After sintering, no B_4C or Si_3N_4 peaks were detected, while $MoSi_2$ was still present in the softly homogenized sample. Moreover, TiN was observed in the Si_3N_4 samples (TS and TS-h) originating from the reaction between Si_3N_4 and TiO_2.

W_2CoB_2 was only found in the high-energy-planetary-ball-milled sample of TiB_2 without additives (T-h), TM-h ($MoSi_2$) exhibited phases of MoB, TiC and TiSi.

An overview of the microstructural features of both just ball-milled and high-energy-planetary-ball-milled samples is provided in Table 4.1. It can be observed that all samples treated with high-energy-planetary-ball-milling displayed a higher degree of densification, the highest densification grades were obtained for TiB_2 samples densified with $MoSi_2$ as sintering aid (TM and TM-h) which reached final relative densities equal to 95.1% for the soft homogenized sample and 94.7% for the HEPBM sample.

A detailed description of the microstructure is given below.

4.2.1 TiB_2 without additives

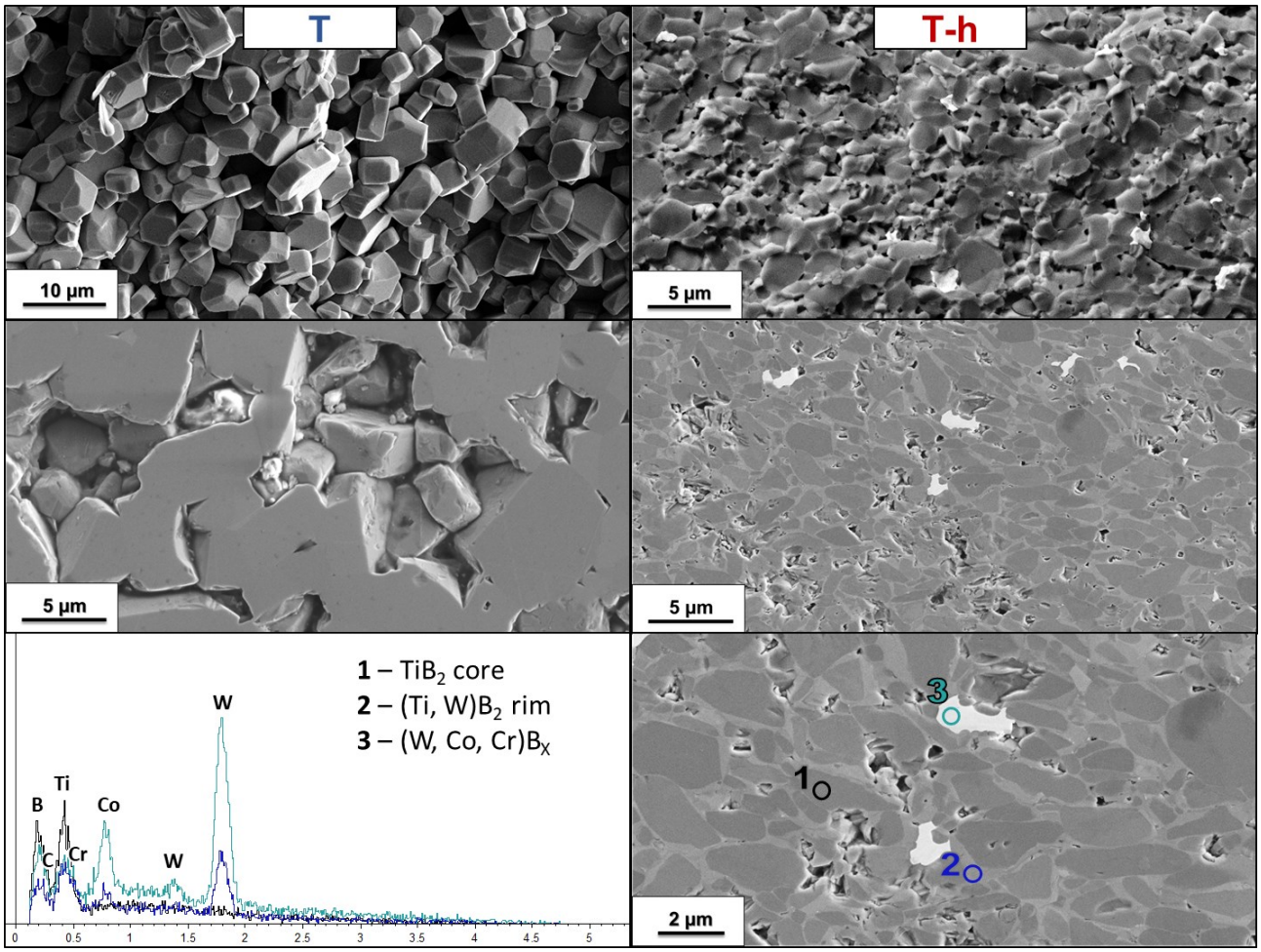

Fig. 4.3 SEM micrograph of T (left column) and T-h (right column) samples fractured and polished sections and EDS spectrum of T-h sample polished section (third row).

The EDS spectrum of the three different phases confirmed the absence of the other metals in the TiB_2 cores, and the presence of W and Co in TiB_2 solid solution rims. Moreover, the presence of Cr and C can be observed in the mixed boride coming from WC-Co grinding media: chromium is indeed present in lower quantities than Co and carbon is attributable to residual unreacted carbide.

4.2.2 Boron carbide as additive

TiB_2 without sintering aids (T) has very minimal densification, in fact as can be seen in Figure 4.3 only few necks have formed between the grains. Adding 5 vol% B_4C soft homogenized (Fig. 4.4, left column) improved sintering and densification rate but after 15 minutes at 1900°C although the necks had already formed, the pores were still interconnected, therefore the material is in an intermediate stage where pores are closing, and the relative density is less than 80%. With the additional aid of high-energy-planetary-ball-milling, a microstructure with closed porosities and a relative density of around 89% is reached.

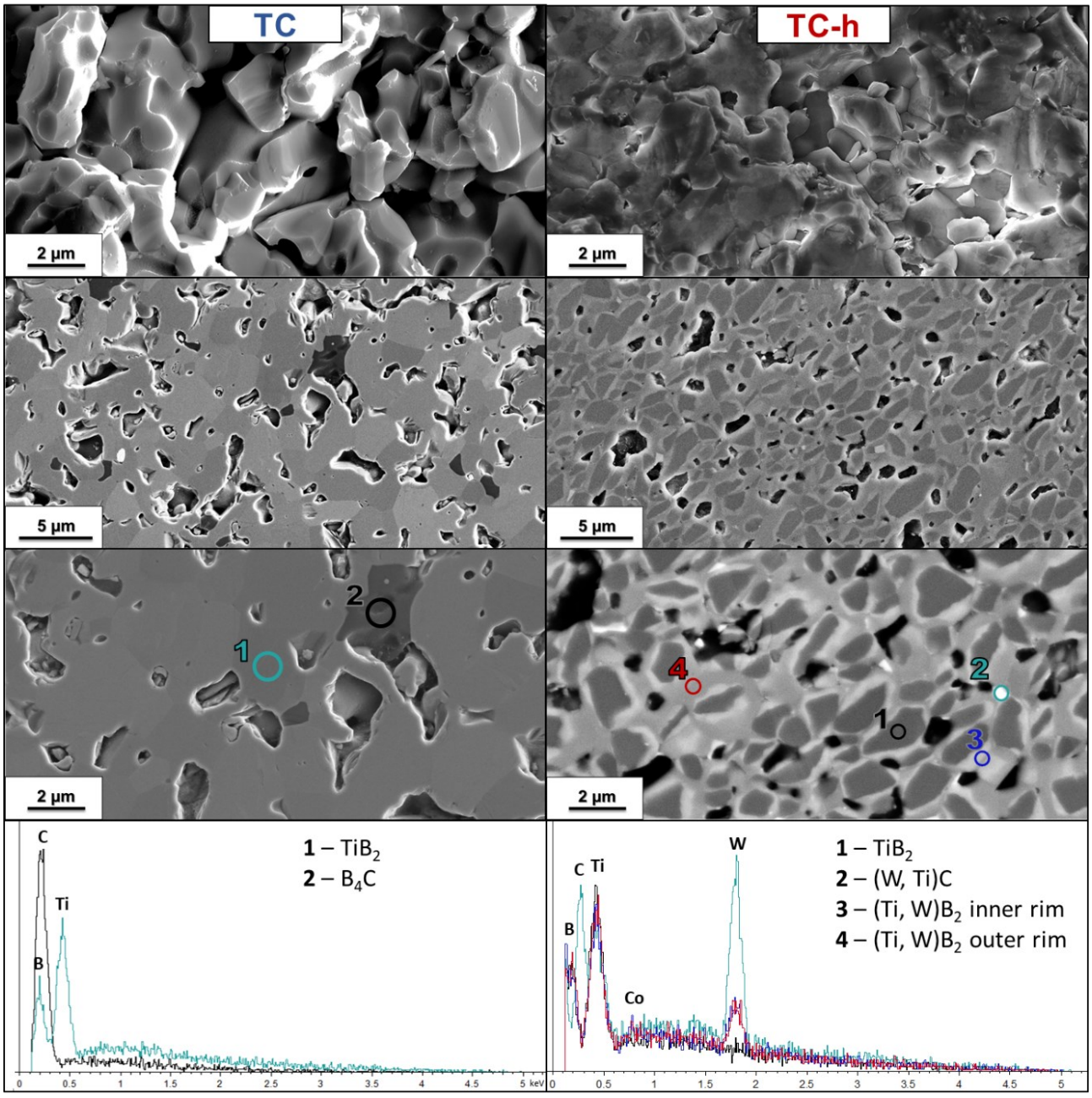

Fig. 4.4 SEM micrograph of TiB_2 with 5 vol% B_4C soft homogenized (TC, left column) and high-energy-planetary-ball-milled (TC-h, right column) samples fractured and polished sections and EDS spectrum of polished sections.

Although XRD spectra did not record the presence of residual crystalline B_4C, from the polished surface SEM images of TC sample dark B_xC_y phases were detected by EDS (Fig. 4.4, left column). In the HEPBM sample (TC-h) B_4C instead is not present and wider rims than other HEPBM samples can be noted. Moreover, EDS revealed that the white contrasting phases in TC-h micrographs is WC with a lower Co content and not WB.

The core-rim microstructure had two types of rims: an inner one of a lighter color, therefore heavier atomically, and an outer one of a darker grey color. The EDS spectra of these rims showed no significant differences in the composition.

4.2.3 Silicon nitride as additive

The SEM micrograph of TS (5 vol% Si_3N_4) polished surface shows a bulk with 14% of residual porosity, however SEM image of the fracture appears to be totally dense and without any porosity (Fig. 4.5). This is due to the large presence of amorphous compounds like BN and SiO_2 products from the reaction between Si_3N_4 and oxide phases (B_2O_3 and TiO_2).

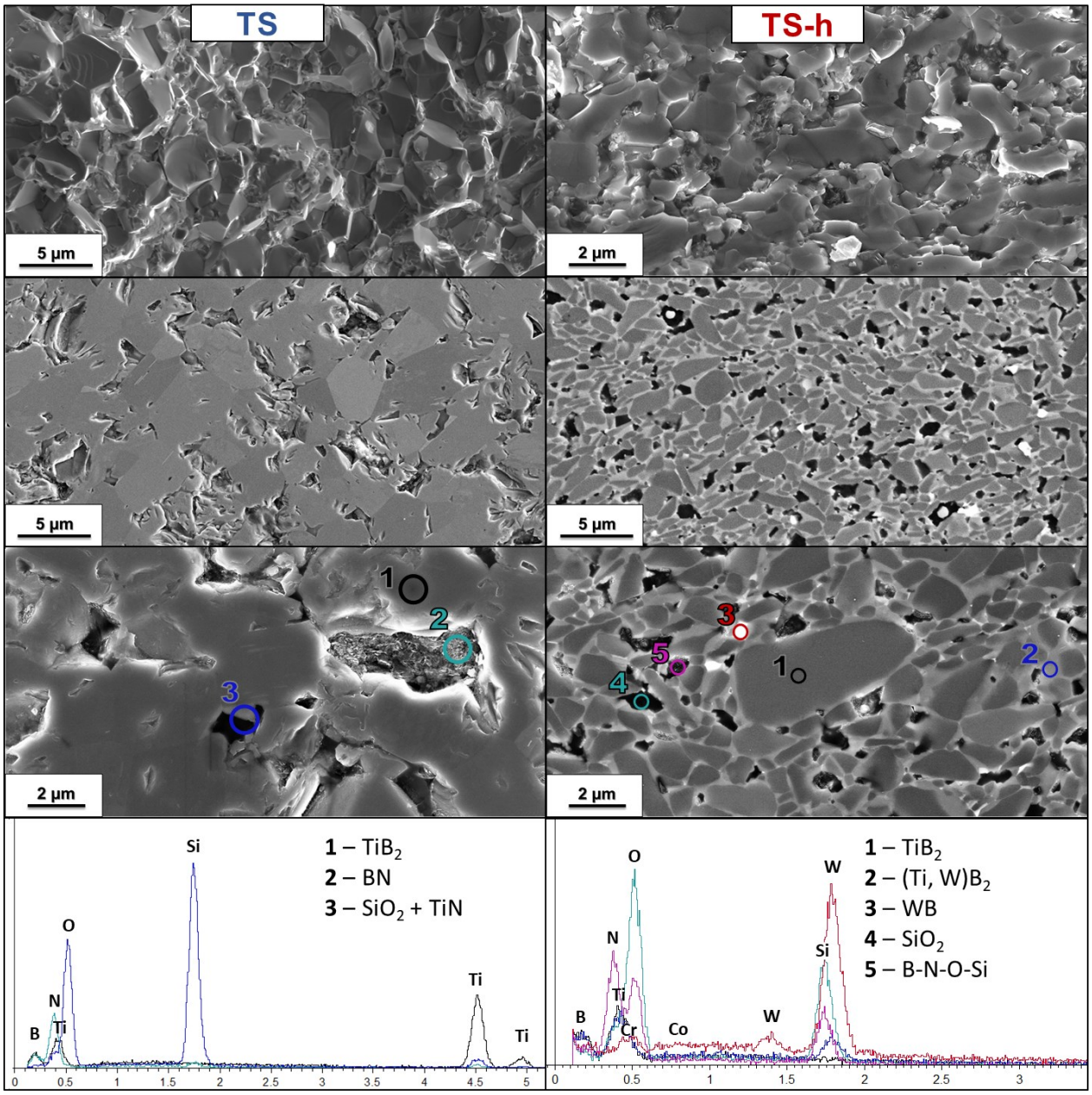

Fig. 4.5 SEM micrograph of TiB_2 with 5 vol.% Si_3N_4 soft homogenized (TS, left column) and high-energy-planetary-ball-milled (TS-h, right column) samples fractured and polished sections and EDS spectrum of polished sections.

Porosities in TS sample polished section revealed the presence of secondary phases when observed with InLens mode. In detail, phases of h-BN were recognized, with the characteristic lamellar structure, SiO_2, a darker phase, and TiN, which having a higher molecular weight than TiB_2 appears as a light gray phase in the SE2 mode. EDS spectra confirmed these phases (Fig. 4.5).

SEM micrograph of HEPBM sample with 5 vol% Si_3N_4 (TS-h) shows the typical core-shell structure of TiB_2 with WB inclusions in addition to the phases already seen in the soft homogenized sample. Despite the presence of WC contamination in the powders which reacted with the oxide phases to form WB, the formation of SiO_2 and BN phases can still be noted. In addition, an amorphous phase containing B, O, N and Si was identified among the grains.

4.2.4 Molybdenum disilicide as additive

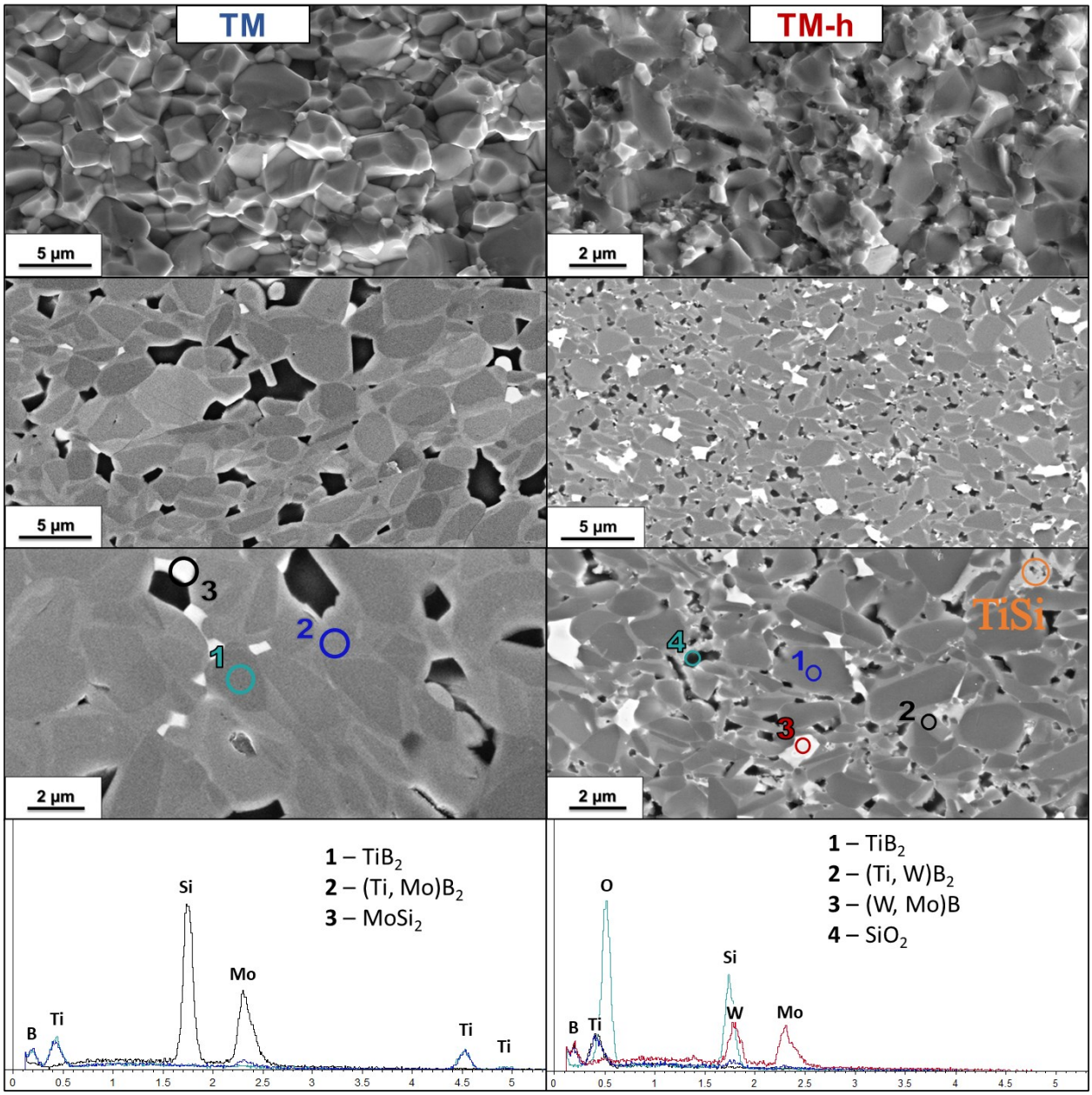

Fig. 4.6 SEM micrograph of TiB_2 with 5 vol.% $MoSi_2$ soft homogenized (TC, left column) and high-energy-planetary-ball-milled (TC-h, right column) samples fractured and polished sections and EDS spectrum of polished sections.

As already observed for TS, also TM sample (with 5 vol% $MoSi_2$ soft homogenized) does not have empty pores but silica pockets produced by the reaction between $MoSi_2$ and B_2O_3. A solid solution containing Mo instead of W with TiB_2 was formed leading to a similar core shell structure to that of the HEPBM sample. No MoB was spotted but XRD and EDS confirmed the presence of unreacted $MoSi_2$, which appears as a white phase.

In the HEPBM sample (TM-h) WC and $MoSi_2$ phases combined resulting in a core shell structure where the cores of TiB_2 were surrounded by a rim composed of solid solution of mixed boride of Ti, W, Mo (and Co in minor part) with inclusions of mixed borides of W, Mo (and Co). Again, complete densification of the matrix was interrupted by the formation of silica pockets (Fig. 4.6). The rims in this sample are very narrow and light grey colored TiSi phases can be spotted.

4.3 Densification mechanisms

The densification behavior was highly affected by the sintering aid and the high-energy-planetary-ball-milling procedure. Starting from the as received powder, the effect of HEPBM with WC-Co media was twofold: on one hand high-energy-planetary-ball-milling reduced the mean particle size, activating the particle surface; on the other, contamination from WC led to elimination of surface oxides through surface reactions on the TiB_2 particles (TiO_2 and B_2O_3) [5,4,6].

The most probable reactions are [6–9]:

$$TiO_{2\,(s)} + 3\ WC_{(s)} \rightarrow TiC_{(s)} + 3\ W_{(s)} + 2\ CO_{(g)} \quad (4.1)$$

$$3\ TiB_{2\,(s)} + TiO_{2\,(s)} + 6\ WC_{(s)} \rightarrow 4\ TiC_{(s)} + 6\ WB_{(s)} + 6\ CO_{(g)} \quad (4.2)$$

$$3\ WC_{(s)} + B_2O_{3\,(s)} \rightarrow 2\ WB_{(s)} + W + 3\ CO_{(g)} \quad (4.3)$$

$$Co_{(l)} + 2\ WC_{(s)} + 2\ B_{(s)} \rightarrow W_2CoB_{2\,(s)} + 2\ C_{(s)} \quad (4.4)$$

WC inclusions favored the elimination of surface oxides, while release of W resulted in the formation of core shell structures in TiB_2. Although the formation of TiC seems favored, it was not detected with EDS and XRD methods. The large presence of WB inclusions and the absence of TiC therefore suggest a greater relevance of reaction 4.3 between WC and B_2O_3.

The addition of sintering aids made the picture even more complex with other reactions taking place. In addition to reactions 4.1-4.4, B_4C reduced the oxygen-carrying chemical species present on the surfaces of the TiB_2 powder particles through the following reaction:

$$7\ TiO_{2\,(s)} + 5\ B_4C_{(s)} \rightarrow 7\ TiB_{2\,(s)} + 5\ CO_{(g)} + 3\ B_2O_{3\,(l)} \quad (4.5)$$

WC inclusions can also react with B_4C via the reaction:

$$2WC_{(s)} + B_4C_{(s)} \rightarrow 2\ WB_{2\,(s)} + 3\ C_{(s)} \quad (4.6)$$

The main effect of Si_3N_4 was to remove surface oxides from TiB_2 powder particles and forming liquid phases according to [10]:

$$Si_3N_{4\,(s)} + 2\ B_2O_{3\,(l)} \rightarrow 4\ BN_{(s)} + 3\ SiO_{2\,(l)} \quad (4.7)$$

$$2\ Si_3N_{4\,(s)} + 6\ TiO_{2\,(s)} \rightarrow 6\ TiN_{(s)} + 6\ SiO_{2\,(l)} + N_{2\,(g)} \quad (4.8)$$

$$2\ TiB_{2\,(s)} + 3\ N_{2\,(g)} \rightarrow 2\ TiN_{(s)} + 4\ BN_{(s)} \quad (4.9)$$

Subsequently, the liquid formed at about 1600°C was very likely to be due to the reaction of Si_3N_4 remaining from reactions (4.7) and (4.8) with SiO_2 and TiB_2. During cooling, BN, TiN and SiO_2 pockets precipitated from the liquid phase (Fig. 4.5), but part of it was retained along the grain boundaries in form of amorphous Si-O-B-N-Ti films.

Similar to other borides, for $MoSi_2$ addition densification is presumed to be assisted by a transient liquid phase, due to the reaction between $MoSi_2$ and surface oxide impurities on the diboride particles [11,12]. Several reaction paths were indicated, as suggested by the variety of crystalline and amorphous phases identified in the dense microstructures. The presence of crystalline MoB (only for HEPBM sample) and pockets of amorphous SiO_2 suggests the following reaction occurs:

$$2\ MoSi_{2\,(s)} + B_2O_{3\,(l)} \rightarrow 2\ MoB_{(s)} + 2.5\ Si_{(l)} + 1.5\ SiO_{2\,(l)} \quad (4.10)$$

Reaction 10 implies removal of B_2O_3 from boride particle surface and formation of Si- or Si-O-based liquids. According to the Mo-Si-B phase diagram (Fig. 4.7), liquids could form at temperatures as low as 1350°C.

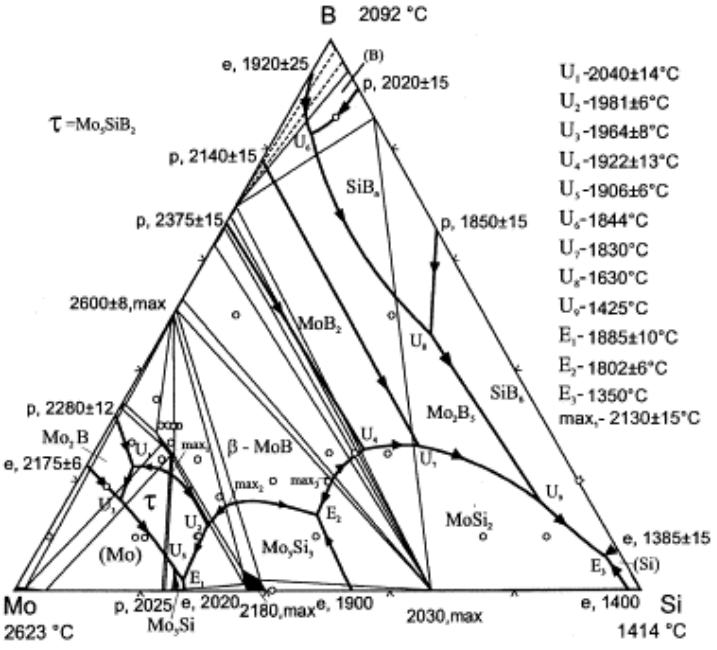

Fig. 4.7 Melting diagram of Mo–Si–B system [13].

Formation of liquid promotes mass transfer mechanisms, by partial dissolution of the boride matrix. The observed formation of epitaxial core-shell structures suggests a solution re-precipitation mechanism even if diffusion of Mo into the diboride lattice could also occur. During cooling the transient liquid-phase solidifies, resulting in the formation of discrete crystalline phases.

The mixing of TiB_2, WB and MoB resulted in a core-shell microstructure (Fig. 4.6) with TiB_2 core, a mixed boride rim with the three metals (Ti, W, Mo)B_X and (W, Mo)B_X particles.

4.4 Mechanical properties

Hardness and fracture toughness measurements were conducted for all the samples except T and TC, as their relative density was below 80% (Table 4.2). The hardness of the samples was negatively influenced by porosity and the presence of softer phases, while it increased with a decrease in the mean grain size. In this batch of materials, the highest hardness value, 24.5 GPa, was observed for T-h, indicating that high-energy-planetary-ball-milling (HEPBM) has a comparable effect on hardness as the addition of additives. Moreover, both samples with the addition of $MoSi_2$ (TM and TM-h) exhibited similar hardness values due to their higher relative density and relatively small mean grain size. The lowest hardness value, 20 GPa, was recorded for TC-h, which had the highest porosity among the high-energy-milled samples.

Label	Sintering aid, Process (vol%)	Max temp./time (°C, min)	Apparent density (g/cm^3)	Relative density (%)	Mean grain size (TiB_2, μm)	HV1 (GPa)	K_{Ic} (MPa $m^{1/2}$)
T	-	1950, 20	3.45	≈ 76	3.2 ± 1.4	-	-
TC	5 B_4C, SH	1900, 15	3.71	≈ 78	2.4 ± 1.4	-	-
TS	5 Si_3N_4, SH	1900, 15	4.28	85.6*	3.1 ± 1.6	22.2 ± 1.6	5.4 ± 0.8
TM	5 $MoSi_2$, SH	1900, 10	4.43	95.1*	1.8 ± 0.8	24.4 ± 1.3	5.4 ± 0.2
T-h	HEPBM	1900, 10	4.60	93.4	1.0 ± 0.5	24.5 ± 0.6	5.0 ± 1.0
TC-h	5 B_4C, HEPBM	1900, 10	4.22	87.9	1.3 ± 0.1	19.6 ± 0.8	4.1 ± 0.1
TS-h	5 Si_3N_4, HEPBM	1830, 10	4.54	92.4*	0.9 ± 0.4	23.2 ± 0.6	3.6 ± 0.2
TM-h	5 $MoSi_2$, HEPBM	1700, 10	4.67	94.7*	0.8 ± 0.5	24.4 ± 0.7	3.5 ± 0.1

Table 4.2 Sintering parameters, microstructural features and mechanical properties of hot-pressed TiB_2 composites.

Notes: SH—24h wet-ball-milling, HEPBM— 24h wet-ball-milling and 30 min high-energy-planetary-ball-milling, *— porosities mainly filled by silica pockets (empty porosities < 2%).

Sample composition	Sintering method, temp., dwell time (°C, min)	Relative density (%)	MGS (TiB_2, μm)	HV1 (GPa)	K_{Ic} (MPa $m^{1/2}$)	References
TiB_2	HP, 1800, 60	90	-	24	5.8	Park et al. [10]
TiB_2	MWS, 1700, 10	95.5	2.0	24	5.6	Demirskyi et al. [15]
TiB_2	SPS, 2000, 5	96	6-10	23.5	5.5	Demirskyi and Sakka [16]
TiB_2	HEPBM, HP, 1900, 10	93.4	1.0	24.5	5.0	Present work
TiB_2 + 2.5 wt.% Si_3N_4	HP, 1800, 60	99	-	27	5.1	Park et al. [10]
TiB_2 + 10 wt.% Si_3N_4	HP, 1800, 60	96	-	20	5.4	Park et al. [10]
TiB_2 + 3.6 wt.% Si_3N_4	HP, 1900, 15	85.6*	3.1	22.2	5.4	Present work
TiB_2 + 3.6 wt.% Si_3N_4	HEPBM, HP, 1830, 15	92.4*	0.9	23.2	3.6	Present work
TiB_2 + 6.8 wt.% $MoSi_2$	HP, 1900, 10	95.1*	1.8	24.4	5.4	Present work
TiB_2 + 6.8 wt.% $MoSi_2$	HEPBM, HP, 1900, 10	94.7*	0.8	24.4	3.5	Present work
TiB_2 + 10 wt.% $MoSi_2$	HP, 1700, 60	99.3	1-2	27	4.0	Ch. Murthy et al. [17]
TiB_2 + 20 wt.% $MoSi_2$	HP, 1700, 60	98.7	1-2	25	5.0	Ch. Murthy et al. [17]
TiB_2 + 10 wt.% TaC	SPS, 2000, 5	>98	2-4	28.8	5.9	Demirskyi and Sakka [16]

Table 4.3 Sintering parameters, microstructural characteristics and mechanical properties of TiB_2 samples sintered with different sintering methods and different amounts of additives.

Notes: HP—hot-pressing, MWS—microwave sintering, SPS—spark-plasma sintering, SH—24h wet-ball-milling, HEPBM— 24h wet-ball-milling and 30 min high-energy-planetary-ball-milling, *— porosities mainly filled by silica pockets (empty porosities < 2%).

Generally, the toughness of TiB_2 is greater for grain sizes between 5 and 12 μm [14]. A mild porosity can also increase toughness because the pores can act as a "sink" for cracking (both empty porosities and silica pockets). In accordance with theory, the fracture toughness measurements shown sensitive to the presence of defects, secondary phases, and their dispersion in the material.

The highest fracture toughness value, 5.4 MPa $m^{1/2}$ was measured for TS and TM samples, which were soft homogenized with Si_3N_4 and $MoSi_2$, respectively. These samples exhibited large pockets of silica embedded within the material. T-h also showed similar level of toughness, while the HEPBM samples with aids displayed lower values, approximately 4 MPa $m^{1/2}$ or below, despite their high relative density.

The highest hardness and fracture toughness values obtained in this study are comparable to the limits reported in the literature for TiB_2 samples with very high relative density, see Table 4.3, achieved through various sintering techniques such as hot-pressing, spark-plasma and microwave sintering.

4.5 Conclusions

TiB_2 ceramics were prepared through hot-pressing-sintering after just wet-ball-milling (soft homogenization) or also high-energy-planetary-ball-milling (after ball-milling) using WC-Co media for four different compositions: TiB_2 as received and with 5 vol% of B_4C, Si_3N_4 or $MoSi_2$ as sintering aid. The addition of sintering aids, except for B_4C which only had a slight improvement in sintering, accelerated the densification process but also resulted in the formation of secondary phases. Specifically, a liquid phase was formed at around 1600°C when using Si_3N_4 or $MoSi_2$ as aids, which improved the densification rate but left silica pockets within the bulk material after sintering.

High-energy-planetary-ball-milling proved to be highly effective in reducing the size of the starting powders, leading to improved densification. The presence of carbon from WC doping exerted a cleaning action, contributing to elimination of surficial oxide phases. W remnants were incorporated in the TiB_2 lattice, resulting in the formation of core-shell structures, the development of which was influenced by temperature and holding time.

Even without the addition of sintering aids, high-energy-planetary-ball-milling of TiB_2 alone resulted in a relative density of 93.4% and the highest recorded Vickers hardness of 24.5. The best material was the one added with 5 vol% $MoSi_2$ and high-energy-milled, which achieved almost complete densification (although limited by the presence of silica pockets) at 1700°C. This material also exhibited a Vickers hardness of 24.4 GPa, indicating its superior hardness properties.

4.6 References

[1] D. Ağaoğulları, H. Gökçe, İ. Duman, M.L. Öveçoğlu, Influences of metallic Co and mechanical alloying on the microstructural and mechanical properties of TiB2 ceramics prepared via pressureless sintering, Journal of the European Ceramic Society. 32 (2012) 1949–1956. https://doi.org/10.1016/j.jeurceramsoc.2011.10.033.

[2] M. Yao, Y. Wang, L. Chen, J. Ouyang, H. Li, H. Gu, Y. Zhou, Mechanical properties and microstructural evolution of pressureless sintered ceramics obtained from high-energy ball-milled TiB2–TiC powders, Materials Science and Engineering: A. 819 (2021) 141510. https://doi.org/10.1016/j.msea.2021.141510.

[3] D. Sciti, S. Failla, S. Turan, U. Savaci, P. Galizia, Properties and ballistic tests of strong B4C-TiB2 composites densified by gas pressure sintering, Journal of the European Ceramic Society. 43 (2023) 1334–1342. https://doi.org/10.1016/j.jeurceramsoc.2022.11.066.

[4] S. Failla, C. Melandri, L. Zoli, G. Zucca, D. Sciti, Hard and easy sinterable B4C-TiB2-based composites doped with WC, Journal of the European Ceramic Society. 38 (2018) 3089–3095. https://doi.org/10.1016/j.jeurceramsoc.2018.02.041.

[5] R. Telle, Analysis of pressureless sintering of titanium diboride ceramics with nickel, cobalt, and tungsten carbide additives, Journal of the European Ceramic Society. 39 (2019) 2266–2276. https://doi.org/10.1016/j.jeurceramsoc.2019.02.036.

[6] L. Silvestroni, S. Failla, N. Gilli, C. Melandri, U. Savacı, S. Turan, D. Sciti, Disclosing small scale length properties in core-shell structured B4C-TiB2 composites, Materials & Design. 197 (2021) 109204. https://doi.org/10.1016/j.matdes.2020.109204.

[7] J. Zou, S.-K. Sun, G.-J. Zhang, Y.-M. Kan, P.-L. Wang, T. Ohji, Chemical Reactions, Anisotropic Grain Growth and Sintering Mechanisms of Self-Reinforced ZrB2–SiC Doped with WC, Journal of the American Ceramic Society. 94 (2011) 1575–1583. https://doi.org/10.1111/j.1551-2916.2010.04278.x.

[8] W.G. Fahrenholtz, E.J. Wuchina, W.E. Lee, Y. Zhou, Ultra-High Temperature Ceramics: Materials for Extreme Environment Applications, John Wiley & Sons, 2014.

[9] A. Márquez-Herrera, G. Bermúdez-Rodríguez, E.N. Hernández-Rodríguez, M. Melendez-Lira, M. Zapata-Torres, Boride coating on the surface of WC–Co-based cemented carbide, International Journal of Materials Research. 107 (2016) 676–679. https://doi.org/10.3139/146.111387.

[10] J.-H. Park, Y.-H. Koh, H.-E. Kim, C.S. Hwang, E.S. Kang, Densification and Mechanical Properties of Titanium Diboride with Silicon Nitride as a Sintering Aid, Journal of the American Ceramic Society. 82 (1999) 3037–3042. https://doi.org/10.1111/j.1151-2916.1999.tb02199.x.

[11] D. Sciti, L. Silvestroni, G. Celotti, C. Melandri, S. Guicciardi, Sintering and Mechanical Properties of ZrB2–TaSi2 and HfB2–TaSi2 Ceramic Composites, Journal of the American Ceramic Society. 91 (2008) 3285–3291. https://doi.org/10.1111/j.1551-2916.2008.02593.x.

[12] L. Silvestroni, H.-J. Kleebe, S. Lauterbach, M. Müller, D. Sciti, Transmission electron microscopy on Zr- and Hf-borides with MoSi2 addition: Densification mechanisms, Journal of Materials Research. 25 (2010) 828–834. https://doi.org/10.1557/JMR.2010.0126.

[13] S. Katrych, A. Grytsiv, A. Bondar, P. Rogl, T. Velikanova, M. Bohn, Structural materials: metal–silicon–boron: On the melting behavior of Mo–Si–B alloys, Journal of Alloys and Compounds. 347 (2002) 94–100. https://doi.org/10.1016/S0925-8388(02)00676-X.

[14] R.G. Munro, Material properties of titanium diboride, J. Res. Natl. Inst. Stand. Technol. 105 (2000) 709. https://doi.org/10.6028/jres.105.057.

[15] D. Demirskyi, D. Agrawal, A. Ragulya, Tough ceramics by microwave sintering of nanocrystalline titanium diboride ceramics, Ceramics International. 40 (2014) 1303–1310. https://doi.org/10.1016/j.ceramint.2013.07.010.

[16] D. Demirskyi, Y. Sakka, High-temperature reaction consolidation of TaC–TiB2 ceramic composites by spark-plasma sintering, Journal of the European Ceramic Society. 35 (2015) 405–410. https://doi.org/10.1016/j.jeurceramsoc.2014.08.007.

[17] T.C. Murthy, B. Basu, R. Balasubramaniam, A.K. Suri, C. Subramanian, R.K. Fotedar, Processing and properties of TiB2 with MoSi2 sinter-additive: a first report, Journal of the American Ceramic Society. 89 (2006) 131–138.

5. Pressure-less sintering studies on TiB_2

This chapter examines the effect of sintering aids, preparation methods, and their combination in pressure-less sintering, a more easily scalable and more common technique at an industrial level. The best sintering conditions were identified through sintering sets at various temperatures and dwell times, because shrinkage cannot be measured during pressure-less sintering. The amount of sintering aid in the best compositions has been optimized, and scale-up tests were conducted at various temperatures for the best compositions. Residual porosity, microstructure, composition, and mechanical properties of the sintered materials were measured and compared to those obtained through hot pressing.

5.1 Introduction

Starting from the results obtained through hot pressing sintering, analyzed in the previous chapter, the same compositions were sintered for pressure-less sintering: a higher challenge that has rarely been overcome in the past but necessary for the industrialization of the process as it is much easier to scale-up compared to hot pressing or spark plasma sintering. Several sets of sintering tests were carried out. Again, B_4C, Si_3N_4 and $MoSi_2$ were used as sintering aids and the preparation of the powders involved just a ball-milling step or a further high-energy-planetary-ball-milling step.

Table 5.1 summarizes all the tests carried out with the pressure-less sintering technique. Smaller discs (Fig. 5.1 a) were sintered in a first phase of preliminary tests to evaluate the effect of sintering additives (B_4C and Si_3N_4) and high-energy-planetary-ball-milling in PLS. The scale up was subsequently evaluated by comparing small and large disks (Fig. 5.1 b) sintered under the same sintering conditions.

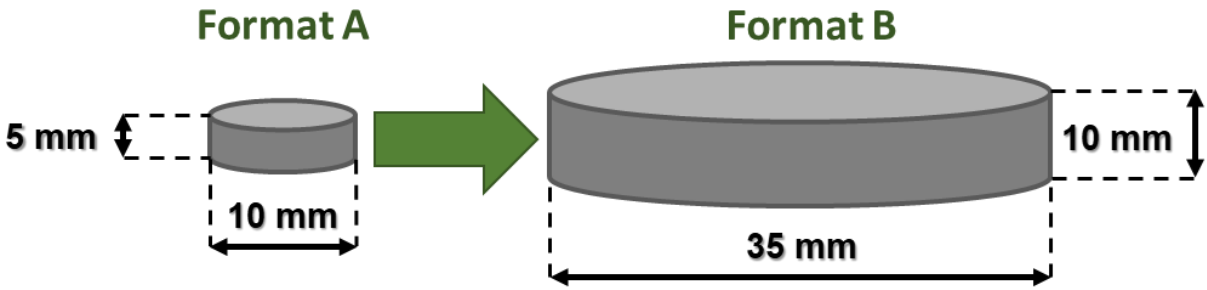

Fig. 5.1 Sintered shape and dimensions of the two formats to test scale-up in pressure-less sintering.

Label	Sintering aid (vol%)	Process	Format	Temp. (°C)	Dwell Time (min)	Apparent density (g/cm^3)	Relative density (%)
T 2000°C x 60’	-	-	A	2000	60	3.50	≈ 77
T 2000°C x 120’	-	-	A	2000	120	3.87	≈ 86
T 2100°C x 60’	-	-	A	2100	60	3.84	≈ 85
T 2100°C x 120’	-	-	A	2100	120	3.74	≈ 83
T-h 2000°C x 60’	-	HEPBM	A	2000	60	4.40	99.9
T-h 2000°C x 120’	-	HEPBM	A	2000	120	4.47	98.8
T-h 2100°C x 60’	-	HEPBM	A	2100	60	4.38	≈ 93
T-h 2100°C x 120’	-	HEPBM	A	2100	120	4.44	≈ 94
TC5 2000°C x 60’	B_4C, 5	SH	A	2000	60	3.91	≈ 88
TC5 2000°C x 120’	B_4C, 5	SH	A	2000	120	3.96	≈ 90
TC5 2100°C x 60’	B_4C, 5	SH	A	2100	60	4.18	≈ 95
TC5 2100°C x 120’	B_4C, 5	SH	A	2100	120	4.15	≈ 94
TS5 2000°C x 60’	Si_3N_4, 5	SH	A	2000	60	4.07	≈ 91
TS5 2000°C x 120’	Si_3N_4, 5	SH	A	2000	120	4.31	≈ 97
TS5 2100°C x 60’	Si_3N_4, 5	SH	A	2100	60	4.03	≈ 91
TS5 2100°C x 120’	Si_3N_4, 5	SH	A	2100	120	3.93	≈ 88
T-h 2-2000°C	-	HEPBM	A	2000	60	4.54	98.0 ± 0.2
T-h 2-2030°C	-	HEPBM	A	2030	60	4.61	98.0 ± 0.3
T-h 2-B-2030°C	-	HEPBM	B	2030	60	4.42	98.6 ± 0.3
T-h 2-2050°C	-	HEPBM	A	2050	60	4.69	97.7 ± 0.5
T-h 2-2100°C	-	HEPBM	A	2100	60	4.54	99.2 ± 0.2
T-h 2-B-2100°C	-	HEPBM	B	2100	60	4.64	99.0 ± 0.1
TM5 1900°C x 60’	$MoSi_2$, 5	SH	A	1900	60	4.21	85.4 ± 0.5

TM5 2000°C x 60’	$MoSi_2$, 5	SH	A	2000	60	4.39	93.4 ± 0.8
TM5 2100°C x 60’	$MoSi_2$, 5	SH	B	2100	60	4.08	96.6 ± 0.2
TM1 2000°C x 60’	$MoSi_2$, 1	SH	A	2000	60	-	≈ 65
TM3 2000°C x 60’	$MoSi_2$, 3	SH	A	2000	60	3.88	88 ± 2
TC5-h 1900°C x 60’	B_4C, 5	HEPBM	A	1900	60	4.34	95.8 ± 0.1
TC5-h 2000°C x 60’	B_4C, 5	HEPBM	A	2000	60	4.55	95.0 ± 0.4
TS5-h 1900°C x 60’	Si_3N_4, 5	HEPBM	A	1900	60	4.34	92.5 ± 0.1
TS5-h 2000°C x 60’	Si_3N_4, 5	HEPBM	A	2000	60	4.59	98.7 ± 0.3
TM5-h 1900°C x 60’	$MoSi_2$, 5	HEPBM	A	1900	60	4.77	96.9 ± 0.2
TM5-h 2000°C x 60’	$MoSi_2$, 5	HEPBM	A	2000	60	4.80	98.1 ± 0.1
TM1-h 2050°C x 60’	$MoSi_2$, 1	HEPBM	A	2050	60	4.70	98.6 ± 0.1

Table 5.1 Summary of sintering parameters, composition, preparation method and sintered densities of all pressure-less sintered samples.

Notes: SH—24h wet-ball-milling, HEPBM — 24h wet-ball-milling and 30 min high-energy-planetary-ball-milling, Format A—5 mm height and 10 mm diameter when sintered, Format B—10 mm height and 35 mm diameter when sintered.

5.2 First set of tests: identification of optimal sintering conditions

Since in the PLS it is not possible to evaluate the progress of sample shrinkage as done in the HP, preliminary sintering cycles on the T, T-h, TC and TS compositions were carried out to identify the optimal conditions, starting from two sintering temperatures (2000 and 2100°C) and two dwell times at the sintering temperature (60 and 120 minutes). These conditions were chosen considering the results in the literature which use temperatures approximately 200°C higher than HP and dwell times of a few hours [1–3].

From the first pressure-less sintering tests on high-energy-milled TiB_2 (T-h), one of the best compositions in the HP tests, an exaggerated grain growth was observed for the samples at 2100°C (Fig. 5.2) possibly due to the excessive sintering temperature, the samples were even more porous than samples sintered at 2000°C in PLS, possibly due to de-sintering, common in samples sintered at high temperatures with closed porosities, which contain gases at high pressure.

The samples sintered at 2000°C, on the other hand, presented an almost complete bulk densification and a finer microstructure (Fig. 5.2).

Label	Sintering aid (vol%)	Process	Format	Temp. (°C)	Dwell Time (min)	Apparent density (g/cm^3)	Relative density (%)
T 2000°C x 60’	-	-	A	2000	60	3.50	≈ 77
T 2000°C x 120’	-	-	A	2000	120	3.87	≈ 86
T 2100°C x 60’	-	-	A	2100	60	3.84	≈ 85
T 2100°C x 120’	-	-	A	2100	120	3.74	≈ 83
T-h 2000°C x 60’	-	HEPBM	A	2000	60	4.40	99.9
T-h 2000°C x 120’	-	HEPBM	A	2000	120	4.47	98.8
T-h 2100°C x 60’	-	HEPBM	A	2100	60	4.38	≈ 93
T-h 2100°C x 120’	-	HEPBM	A	2100	120	4.44	≈ 94
TC5 2000°C x 60’	B_4C, 5	SH	A	2000	60	3.91	≈ 88
TC5 2000°C x 120’	B_4C, 5	SH	A	2000	120	3.96	≈ 90
TC5 2100°C x 60’	B_4C, 5	SH	A	2100	60	4.18	≈ 95
TC5 2100°C x 120’	B_4C, 5	SH	A	2100	120	4.15	≈ 94
TS5 2000°C x 60’	Si_3N_4, 5	SH	A	2000	60	4.07	≈ 91
TS5 2000°C x 120’	Si_3N_4, 5	SH	A	2000	120	4.31	≈ 97
TS5 2100°C x 60’	Si_3N_4, 5	SH	A	2100	60	4.03	≈ 91
TS5 2100°C x 120’	Si_3N_4, 5	SH	A	2100	120	3.93	≈ 88

Table 5.2 Sintering parameters, composition, preparation method and sintered densities of the first set of pressure-less sintered samples.

Notes: SH—24h wet-ball-milling, HEPBM — 24h wet-ball-milling and 30 min high-energy-planetary-ball-milling, Format A—5 mm height and 10 mm diameter when sintered.

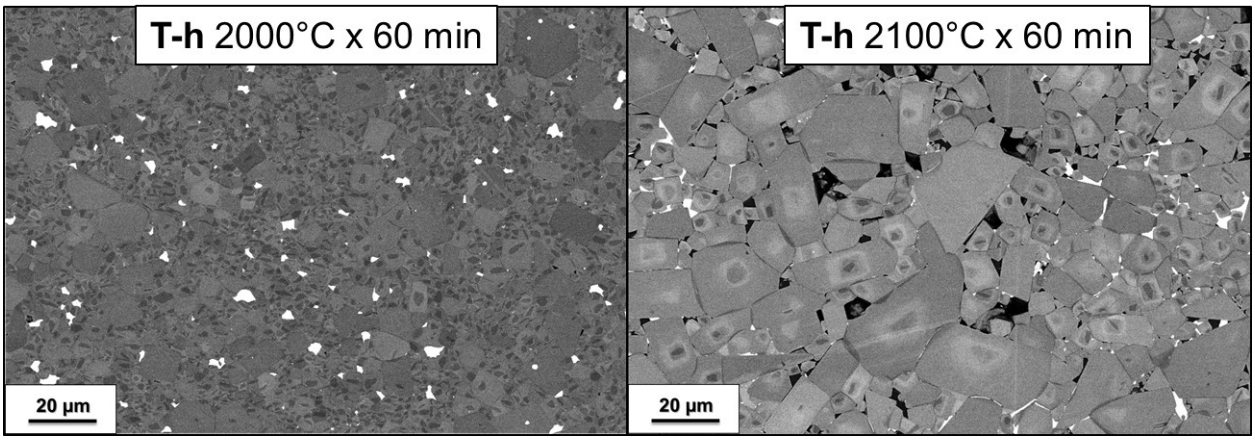

Fig. 5.2 SEM micrographs of the polished cross sections of HEPBM TiB_2 samples pressure-less sintered at 2000 and 2100°C for 60 minutes.

Another anomaly of these samples sintered for PLS concerned the edges of the sintered discs, in fact these presented a very high inhomogeneity (in particular on the upper edge), which was not found in any hot-pressed sample. In the T-h sample sintered at 2000°C for 60 minutes (Fig. 5.3) it is possible to observe a compact upper layer composed of an atomically heavy phase, which appears white in the backscattered electron mode and which therefore contains high amounts of W.

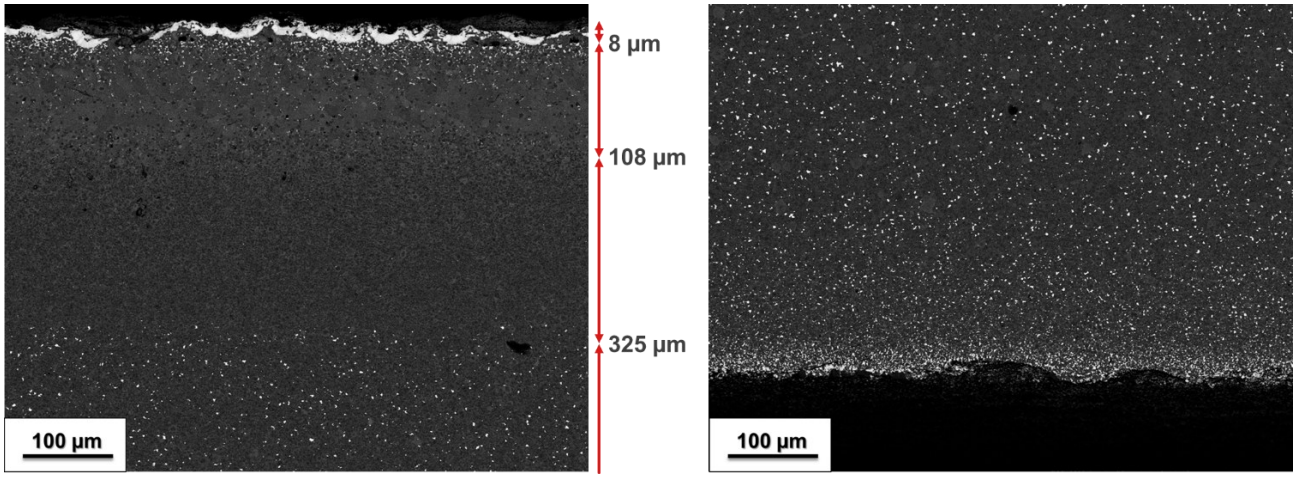

Fig. 5.3 SEM micrographs of the polished upper (left) and lower (right) edges cross sections of HEPBM TiB_2 sample sintered at 2000°C for 60 minutes.

The edges of the high-energy-planetary-ball-milled TiB_2 sample sintered at 2000°C for two hours (Fig. 5.4) were even more inhomogeneous than after just one hour. In particular, the two zones concerns 1.00 mm on the upper side and 1.35 mm on the lower side, almost half the height of the disc which measures approximately 5 mm in total.

In this case, however, the superficial 80 µm of the upper side do not contain any W but just oxide phase that appears dark in the SEM backscattered mode, and under it a 1 mm thick layer with the same microstructure as that of the bulk but without WB but more porosity.

On the lower side, on the other hand, there is a significant accumulation of W-rich phase involving a homogeneous layer of approximately 15 µm as seen on the right side of Fig. 5.4 and a heterogeneous layer together with TiB_2 for another 35 µm.

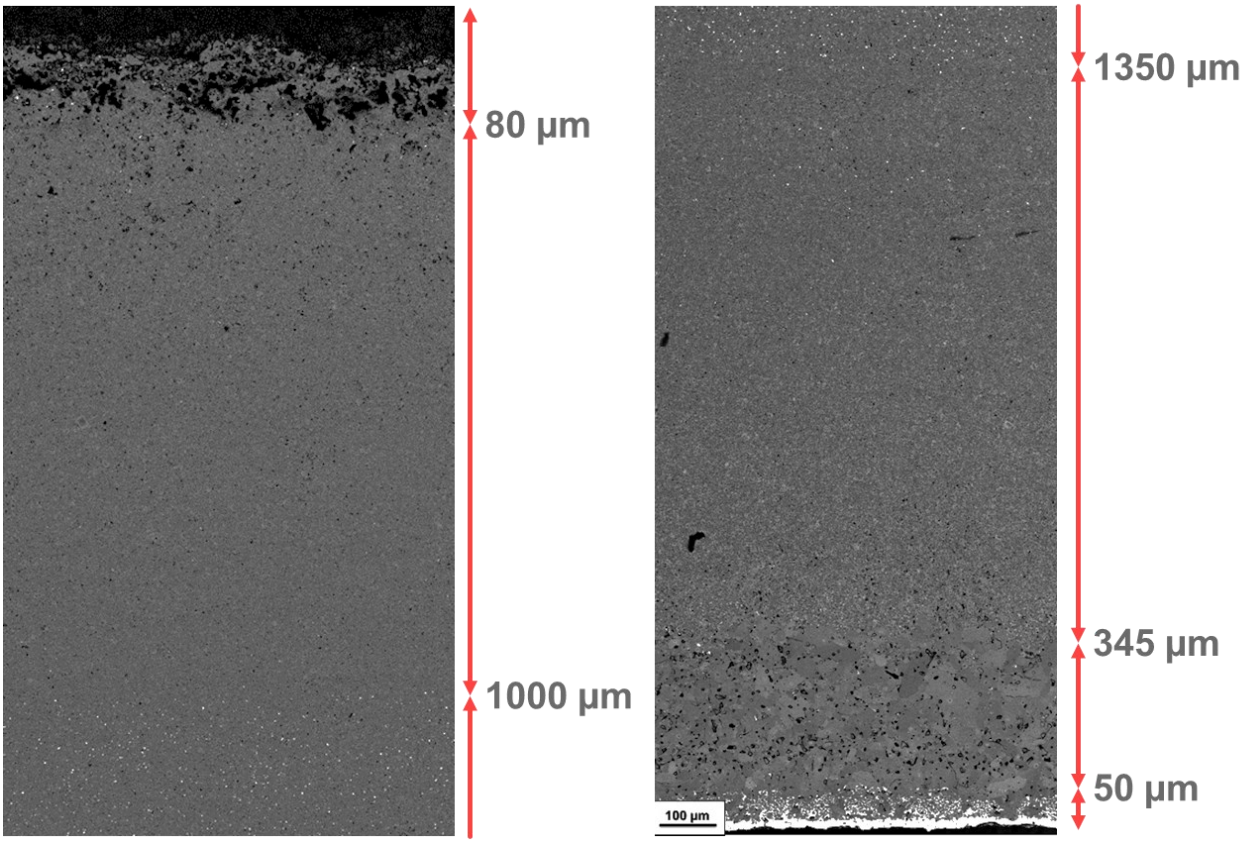

Fig. 5.4 SEM micrographs of the polished upper (left) and lower (right) edges cross sections of HEPBM TiB_2 sample sintered at 2000°C for 60 minutes.

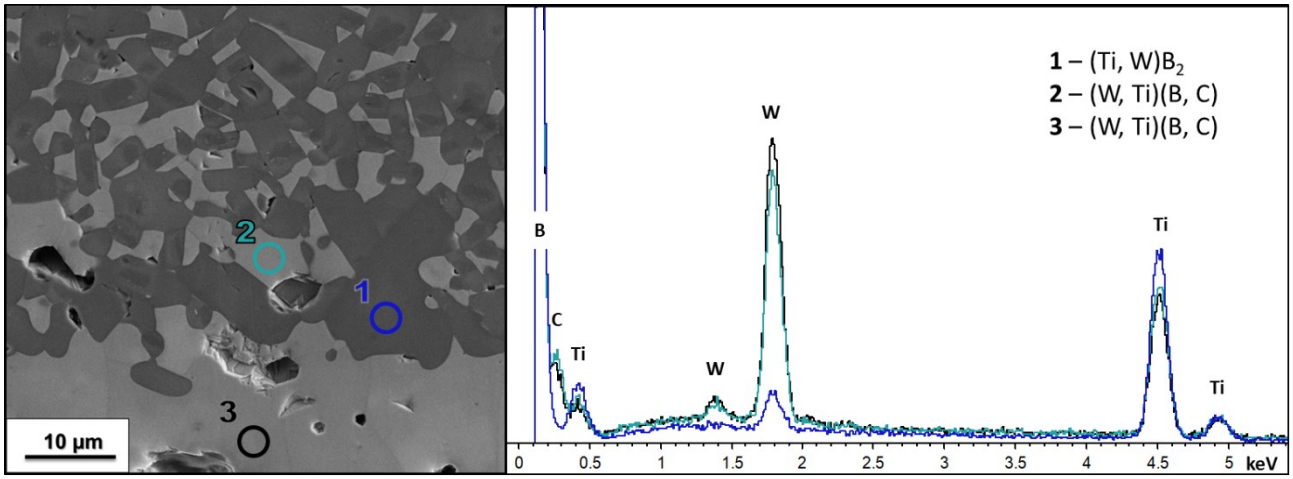

Fig. 5.5 SEM micrographs and EDS spectrum of the polished cross sections of the lower edges of HEPBM TiB_2 (T-h) sample sintered at 2000°C for 120 minutes via pressure-less sintering.

From the EDS analyses on the lower edge of the T-h sample sintered pressure-less at 2000°C for 120 minutes, it can be seen that there are no more pure TiB_2 cores present and the grey grains are made up of mixed boride (Ti, W)B_2. Furthermore, the W-rich phases of the surface layer contain both T and C, and probably there is also B but the peak is covered by that of the noise, and the phase is therefore a solid solution of tungsten titanium carboboride (W, Ti)(B, C), similar to that obtained with the addition of TaC, (Ti, Ta)(C, B) observed by Demirskyi et al. [4].

Again, under the W-rich layer there is a zone with many large pores composed of large (Ti,W)B_2 grains and without the presence of pure TiB_2 cores or WB phases with a width of about 300 μm, and finally there is a 1 mm thick zone with a microstructure similar to the bulk of the material but with very few WB phases.

While the commercial TiB_2 samples without additives (T) did not sinter under any of the four sintering conditions described above (Table 5.2), the results of the samples with 5 vol% B_4C (TC5) and Si_3N_4 (TS5) just soft homogenized with wet-ball-milling showed significant anomalies as for the HEPBM TiB_2 samples (T-h). In particular, grain growth was even higher, reaching tens of microns for the sample with B_4C (Fig. 5.6, TC) and hundreds of microns for the sample with Si_3N_4 (Fig. 5.6, TS) respectively at 2000°C for 1 hour.

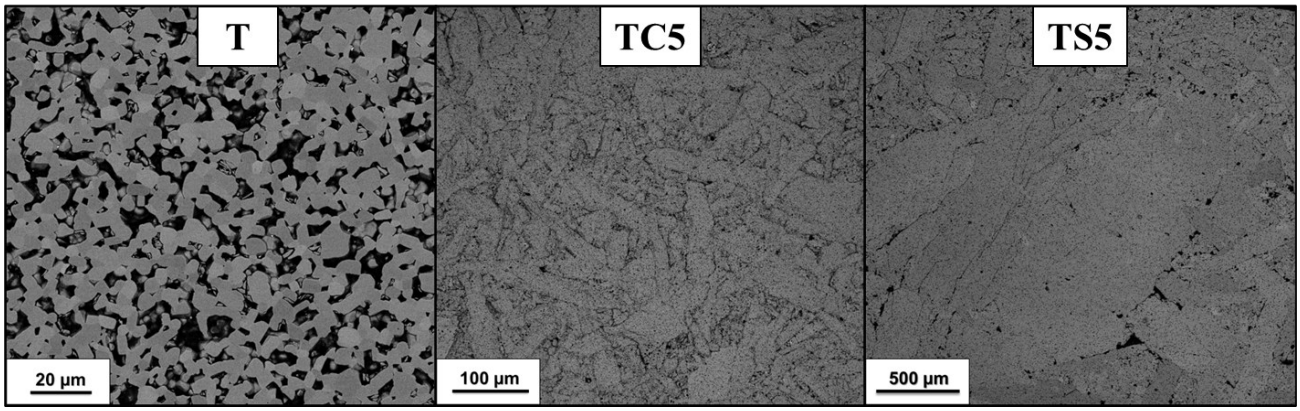

Fig. 5.6 SEM micrographs of the polished cross sections of (T) commercial TiB_2 without additives, (TC5) TiB_2 + 5 vol% B_4C and (TS5) TiB_2 + 5 vol% Si_3N_4 samples sintered at 2000°C for 60 minutes.

The additives therefore improved sintering but at the same time caused uncontrolled grain growth and non-homogeneous microstructures with non-measurable mechanical properties.
Due to the anomalies found, since the kiln used is a prototype and requires regular maintenance, it was decided to carry out an overhaul to ensure that the sintering was carried out correctly and subsequently tests were carried out to evaluate any change. The results of the new sintering cycles are described in the next section.

5.3 Second set of sintering tests and scale-up

To evaluate whether there had been a change in the sintering cycle after the kiln control, high-energy-planetary-ball-milled TiB_2 was sintered again at 2000°C for 60 minutes and compared with the previous sample sintered under the same conditions.

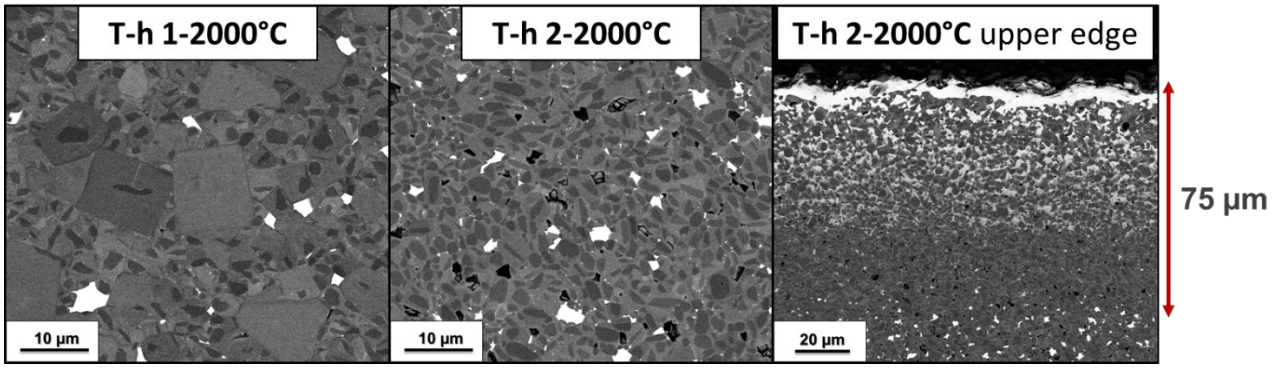

Fig. 5.7 SEM micrographs of the polished cross sections of (1-2000°C) old and (2-2000°C) II sintering cycle with HEPBM TiB_2 at 2000°C for 60 minutes. On the right, the polished cross section of the upper edge in the new sintering cycle.

From the comparison between the images of the cross sections of the samples (Fig. 5.7) it can be seen how the sample from the II cycle (2-2000°C) has a finer microstructure and a greater porosity, indicative of a less extreme condition. To confirm this, the upper edge showed a lack of homogeneity in an area with a width of approximately 75 µm (compared to 325 µm in the old cycle).

Moreover, in this case a surface layer composed of W-rich phase was identified. Finally, there is a porous core-shell layer with microstructure and composition similar to the bulk but without WB phases. The lower edge did not present microstructural inhomogeneity.

Label	Temp. (°C)	Dwell time (min)	Apparent density (g/cm^3)	Relative density (%)	MGS (µm)	HV1 (GPa)
T-h 2000°C x 60’	2000	60	4.68	99.9 ± 0.1	3.3 ± 2.3	23.3 ± 0.8
T-h 2-2000°C	2000	60	4.54	98.0 ± 0.2	1.5 ± 0.8	24 ± 4
T-h 2-2030°C	2030	60	4.61	98.0 ± 0.3	1.6 ± 0.8	22.2 ± 1.4
T-h 2-2050°C	2050	60	4.69	97.7 ± 0.5	1.6 ± 0.8	19.8 ± 1.7
T-h 2-2100°C	2100	60	4.54	99.2 ± 0.2	1.7 ± 0.9	22.5 ± 0.8

Table 5.3 Sintering parameters and microstructural features of pressure-less sintered HEPBM TiB_2.

To evaluate the impact of temperature and aim for a higher bulk density, experiments were conducted at different ascending temperatures (as shown in Table 5.3). Additionally, two of the smaller disks (at 2030 and 2100°C) were tested together with a larger disk (format B) to investigate the effects of scaling up on the microstructure.

From the cross sections of Fig. 5.8 it was observed that by increasing the sintering temperature the microstructure did not change significantly, increasing from an average grain size of 1.5 ± 0.8 μm at 2000°C to 1.7 ± 0.9 μm at 2100°C, at same time porosities increase in size and decrease in number with the temperature.

Despite an increase of 100°C for the last sample, the final microstructure still has grain sizes slightly larger than those of the sample sintered at 2000°C and almost half of the sample from the old sintering cycle (1.7 ± 0.9 versus 3.3 ± 2.3 μm), indicating that in the old cycle the temperature was underestimated and what was observed in the preliminary tests corresponded to a higher temperature, at least more than 100°C.

Despite the high densities and fine microstructures, the samples sintered with the new cycle displayed a lower Vickers hardness than that measured for the bulk of the sample sintered at 2000°C for 1 hour in the old cycle (Table 5.3). Furthermore, due to the residual stresses within the material following sintering, it was not easy to obtain good indentations, and this is reflected in the very high standard deviations. The discussion on mechanical properties is explored in depth in chapter 7.

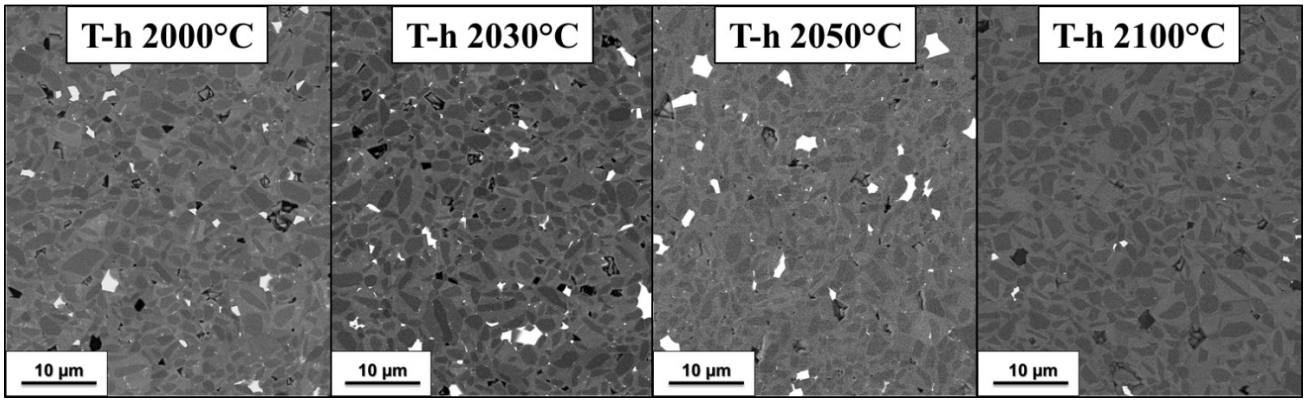

Fig. 5.8 SEM micrographs of the polished cross sections of HEPBM TiB_2 (T-h) sintered with the new cycle at different temperatures for 60 minutes.

5.3.1 III set of sintering tests: Scale up tests

To evaluate the effects of a scale-up on the microstructure and properties of TiB_2, two samples with the two sintering disks formats (A and B, Fig. 5.1) were pressure-less sintered together in two different sintering conditions (2030 and 2100°C for 60 minutes) and compared (Table 5.4).

Label	Format	Temp. (°C)	Dwell time (min)	Apparent density (g/cm^3)	Relative Density (%)	MGS (µm)	HV1 (GPa)
T-h 2-2030°C	A	2030	60	4.61	98.0 ± 0.3	1.6 ± 0.8	22.2 ± 1.4
T-h 2-B-2030°C	B	2030	60	4.42	98.6 ± 0.3	1.5 ± 0.8	22.6 ± 1.3
T-h 2-2100°C	A	2100	60	4.54	99.2 ± 0.2	1.7 ± 0.9	22.6 ± 1.0
T-h 2-B-2100°C	B	2100	60	4.64	99.0 ± 0.1	1.7 ± 0.9	23.0 ± 0.9

Table 5.4 Sintering parameters and microstructural features of pressureless sintered HEPBM TiB_2 with A and B format and different temperatures.
Notes: Format A—5 mm height and 10 mm diameter when sintered, Format B—10 mm height and 35 mm diameter when sintered.

From the comparison of the microstructure (Fig. 5.9) and relative density between the samples with format A and B, no significant differences emerged at either of the two testing temperatures (2030 and 2100°C) despite the variation in dimensions resulting in an increase in volume equal to 2350%. Vickers hardness also does not change for larger sample sizes.

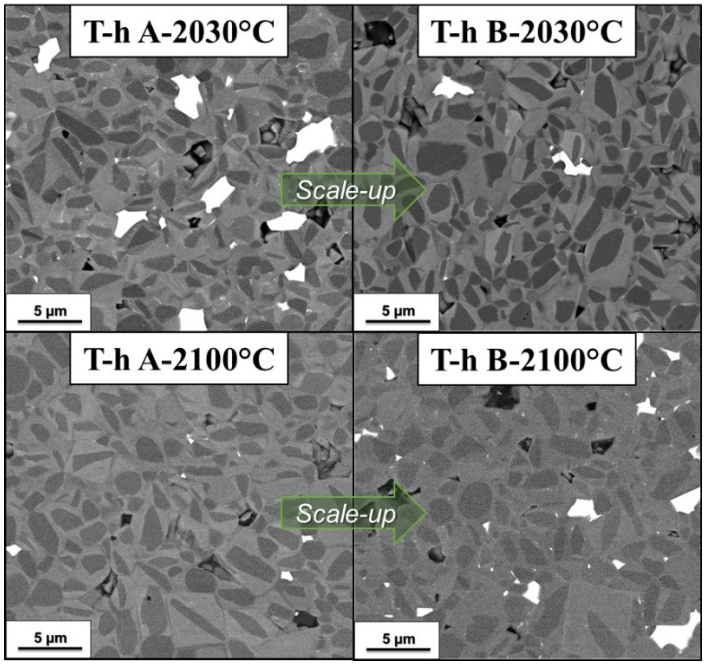

Fig. 5.9 SEM micrographs of the polished cross sections of HEPBM TiB_2 (T-h) sintered with the two pressure-less sintering disks formats (A and B) at 2030 and 2100°C.

Starting from these results it has been possible to consider the results obtained for the discs sintered with format A also valid for format B and once the best sintering conditions and the best compositions had been identified, prepare and sinter sufficient material to obtain specimens with the right dimensions for the mechanical tests.

5.4 IV set of tests: sintering behaviour of TiB_2 with $MoSi_2$ in PLS

Molybdenum disilicide was found to be the best sintering additive among those tested in hot-pressing sintering (B_4C, Si_3N_4, $MoSi_2$), it was therefore also tested in PLS (Table 5.5). Samples of TiB_2 with 5 vol% of $MoSi_2$ soft homogenized were sintered for 1 hour at 2100, 2000 and also at 1900°C since it showed a sintering curve that started at a lower temperature in the HP (≈1700°C).

Label	Method, Format	Temp. (°C)	Dwell Time (min)	Apparent density (g/cm^3)	Relative density (%)	MGS (µm)	HV1 (GPa)
TM5 HP-1900°C	HP, B	1900	10	4.43	95.1 ± 0.6	2.0 ± 1.0	24.4 ± 1.3
TM5 1900°C x 60’	PLS, A	1900	60	4.21	85.4 ± 0.5	1.7 ± 0.9	13.5 ± 2.3
TM5 2000°C x 60’	PLS, A	2000	60	4.39	93.4 ± 0.8	1.9 ± 0.9	21.4 ± 0.8
TM5 2100°C x 60’	PLS, B	2100	60	4.08	96.6 ± 0.2	3.0 ± 1.5	20.6 ± 1.4

Table 5.5 Sintering parameters and microstructural features of HP and pressure-less sintered TiB_2 with 5 vol% $MoSi_2$ at 1900 and 2000°C.

Notes: HP—hot-pressing, PLS—pressure-less sintering, Format A—5 mm height and 10 mm diameter when sintered, Format B—10 mm height and 35 mm diameter when sintered.

Although already at 1900°C the TiB_2 pressure-less sintered sample with 5 vol% $MoSi_2$ showed densification in the last stage (Fig. 5.10) where closed porosities were found, it had a relative density of 93.4 %, lower than the HP sintered sample at the same temperature which reached the 95.1 %. The sample sintered at 2000°C (TM5 PLS-2000°C) had a slightly lower relative density (93.4 %) while the one sintered at 2100°C (TM5 PLS-2100°C) had a higher relative density, reaching 96.6 %, with only 3.4 ± 0.2 % of porosity measured by image analysis (Fig. 5.10).

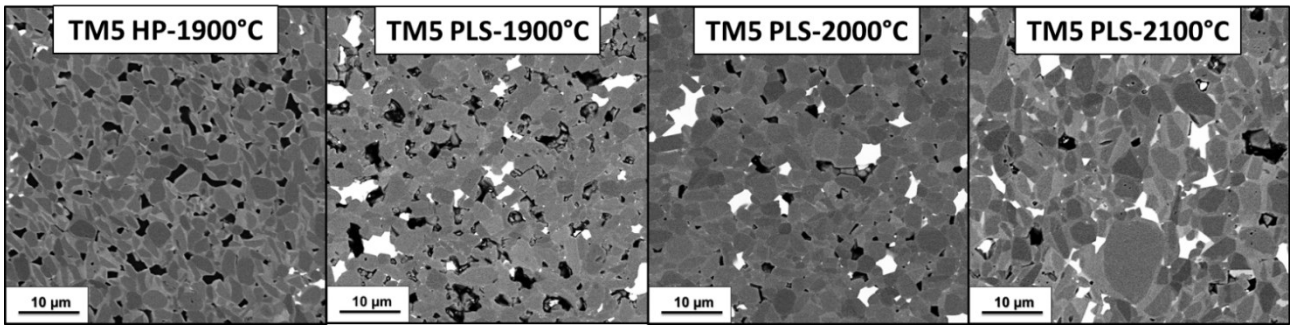

Fig. 5.10 SEM micrographs of the polished cross sections of TiB_2 + 5 vol.% $MoSi_2$ (TM5) sintered via hot pressing at 1900°C for 10 minutes and via pressure-less sintering at 1900, 2000 and 2100°C for 60 minutes.

After pressure-less sintering, all the sintered samples had a core-shell structure as in the case of the sample sintered by hot pressing, therefore they displayed pure TiB_2 cores (dark grey) surrounded by a rim of mixed boride (Ti, Mo)B_2 (light grey). While in the hot-pressed sample the white phases were made of $MoSi_2$, in the PLS samples $MoSi_2$ completely reacted with TiB_2 and B_2O_3 forming MoB (Fig. 5.11).

All PLS-TM5 samples had also empty porosities unlike HP-TM5 where only trapped silica pockets could be found, moreover the amount of residual silica present in the PLS samples pores samples seemed to decrease as the process temperature increased. It is assumed that the SiO_2 in the PLS left the bulk of the sample due to the longer times at high temperature and the absence of an applied pressure.

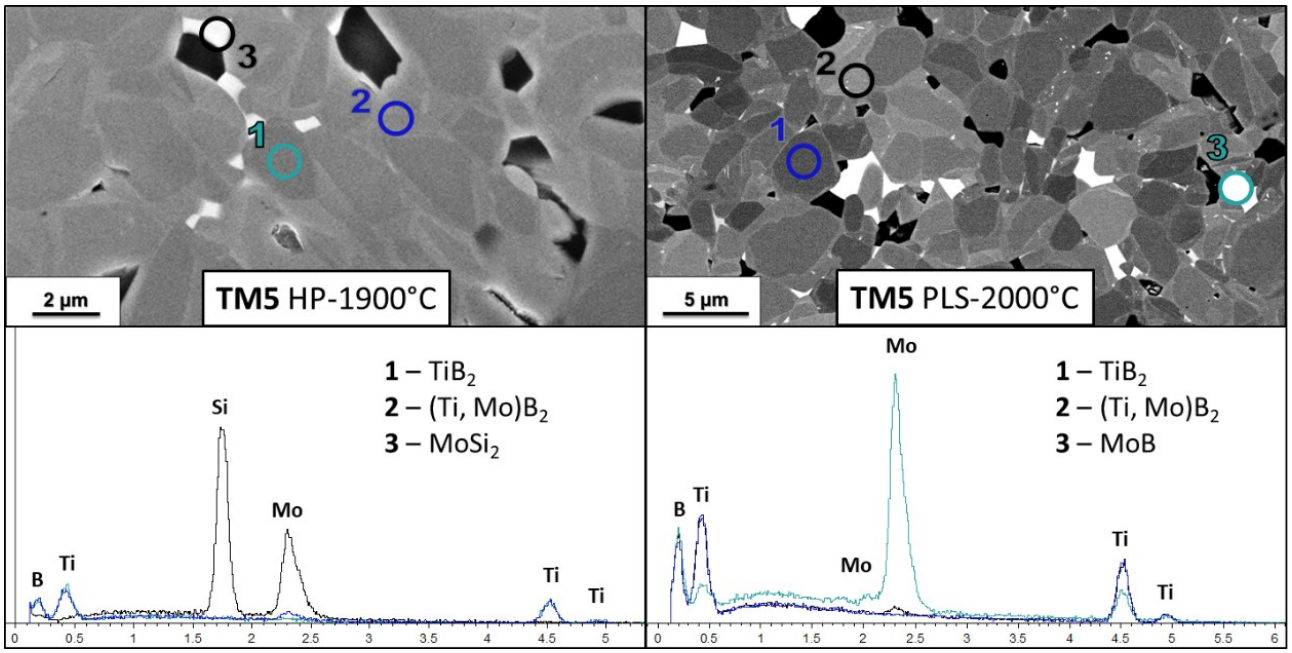

Fig. 5.11 SEM micrographs of the polished cross sections of TiB_2 + 5 vol.% $MoSi_2$ (TM5) sintered via hot pressing (left column) and via pressure-less sintering (right column) and EDS spectrum of polished sections.

Although TM5 PLS-2100°C sample had the lower residual porosity measured by image analysis, the apparent density measured with the Archimedes' method was the lowest of the four samples examined (Table 5.5). Nonetheless, the edges of the sample did not present inhomogeneities.

Worthy of note is the fact that the Vickers hardness of all pressure-less sintered samples was lower than the hot-pressed sample (24.4 ± 1.3 GPa) due higher porosity and larger mean grain size.

In their work, Raju et al. [5] identified 2.5 wt% as the optimal amount of $MoSi_2$ in TiB_2 (1700°C, HP), achieving a relative density of 99% and a flexural strength of 391 MPa. In this regard, two other TiB_2-based compositions (TM1 and TM3) were prepared and tested, the results are presented and discussed in the next section.

5.4.1 V set of sintering tests: Optimization of the amount of $MoSi_2$ as sintering aid

To evaluate the best $MoSi_2$ content to obtain high density and mechanical properties, three mixtures were evaluated: respectively with 1, 3 and 5 vol.% of $MoSi_2$, soft homogenized (TM1, TM3 and TM5). Lower contents were evaluated compared to the one initially prepared to try to have the promotion of sintering by the $MoSi_2$ with a lower production of SiO_2 during the sintering which would otherwise remain trapped between the grains. Furthermore, a smaller quantity of additive corresponds to a lower cost and a lower final density, therefore a more interesting material on a commercial level.

The three mixtures were tested in PLS at 2000°C for 60 minutes (Table 5.6).

Label	$MoSi_2$ content (vol.%)	Temp. (°C)	Dwell time (min)	Theoretical density (g/cm^3)	Apparent density (g/cm^3)	Relative density (%)	HV1 (GPa)
TM1 2000°C x 60'	1	2000	60	4.54	-	≈ 65	-
TM3 2000°C x 60'	3	2000	60	4.57	3.88	88 ± 2	-
TM5 2000°C x 60'	5	2000	60	4.61	4.39	93.4 ± 0.8	21.4 ± 0.8

Table 5.6 Sintering parameters and microstructural features of pressure-less sintered TiB_2 with 1, 3 and 5 vol% $MoSi_2$ at 2000°C for 60 minutes.

From the polished cross section of TM1 (Fig. 5.12) it can be seen that the densification after one hour is still in the initial stage, where the necks between the particles have formed but the relative density is less than 70%. A better result was obtained for TM3 which reached 88% relative density, however lower than the sample with 5% $MoSi_2$, which is therefore the minimum quantity to have good densification (>90%) at 2000°C. It was not possible to calculate the hardness of samples TM1 and TM3 due to their high porosity.

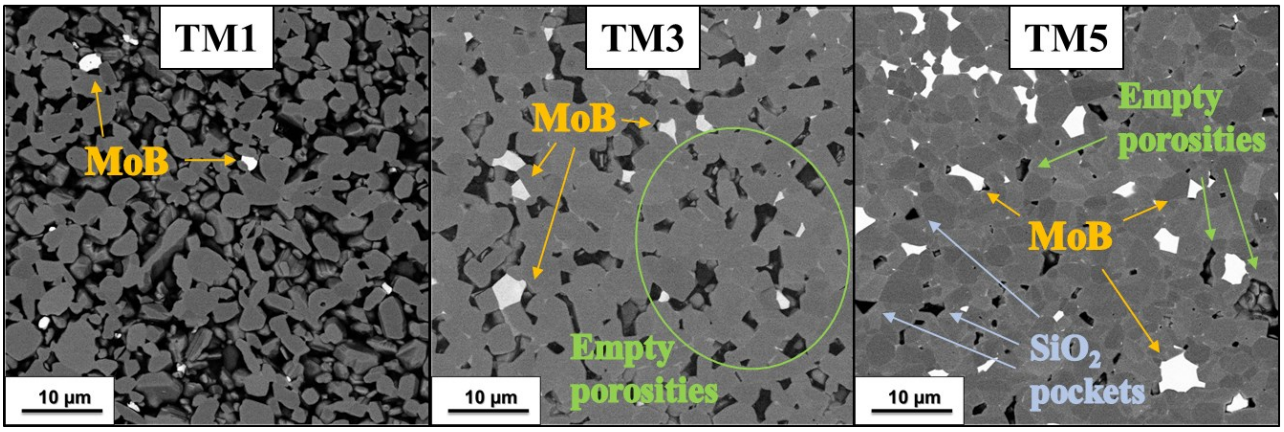

Fig. 5.12 SEM micrographs of the polished cross sections of TiB_2 + 1, 3 and 5 vol.% $MoSi_2$ (respectively TM1, TM3 and TM5) sintered via pressure-less sintering at 2000°C for 60 minutes.

5.5 VI set of sintering tests: Additives and HEPBM combination in PLS

As in the HP tests, the synergy between sintering aids and high-energy-planetary-ball-milling was also evaluated via pressure-less sintering. The additives tested were again B_4C, Si_3N_4 and $MoSi_2$ at 5 vol.% (Table 5.7). The sintering conditions chosen were 1900 and 2000°C for 60 minutes: it was decided to test lower temperatures again because the densification of also these mixtures began at a lower temperature in HP compared to the others.

Label	Process	Temp. (°C)	Dwell Time (min)	Apparent density (g/cm^3)	Relative density (%)	MGS (μm)	HV1 (GPa)
T-h 2-2000°C x 60'	HEPBM	2000	60	4.54	98.0 ± 0.2	1.5 ± 0.8	24 ± 4
TC5-h 1900°C x 60'	HEPBM	1900	60	4.34	95.8 ± 0.1	1.2 ± 0.6	14.8 ± 1.8
TC5-h 2000°C x 60'	HEPBM	2000	60	4.55	95.0 ± 0.4	1.2 ± 0.6	19.0 ± 1.3
TS5-h 1900°C x 60'	HEPBM	1900	60	4.34	92.5 ± 0.1	1.1 ± 0.5	15.4 ± 0.9
TS5-h 2000°C x 60'	HEPBM	2000	60	4.59	98.7 ± 0.3	1.2 ± 0.6	20.7 ± 0.9
TM5-h 1900°C x 60'	HEPBM	1900	60	4.77	96.9 ± 0.2	1.2 ± 0.6	24.8 ± 1.7
TM5-h 2000°C x 60'	HEPBM	2000	60	4.80	98.1 ± 0.1	1.2 ± 0.6	26.8 ± 2.7

Table 5.7 Sintering parameters, microstructural features, and Vickers hardness of HEPBM TiB_2 with 5 vol% B_4C, Si_3N_4 or $MoSi_2$ pressure-less sintered at 1900 and 2000°C for 60 minutes.
Notes: HEPBM — 24h wet-ball-milling and 30 min high-energy-planetary-ball-milling.

For all the samples sintered at 2000°C, the apparent density and relative density were higher, with the exception of the sample with B_4C as sintering aid (TC-h), in which the relative density was higher at 1900°C.

While the grain size and microstructure of all samples was similar (Fig. 5.13), also the Vickers hardness appeared to be greater for the samples sintered at 2000°C. In particular, in the samples doped with $MoSi_2$, the hardness changed less significantly from 1900 to 2000°C and was higher than that of all the other samples examined.

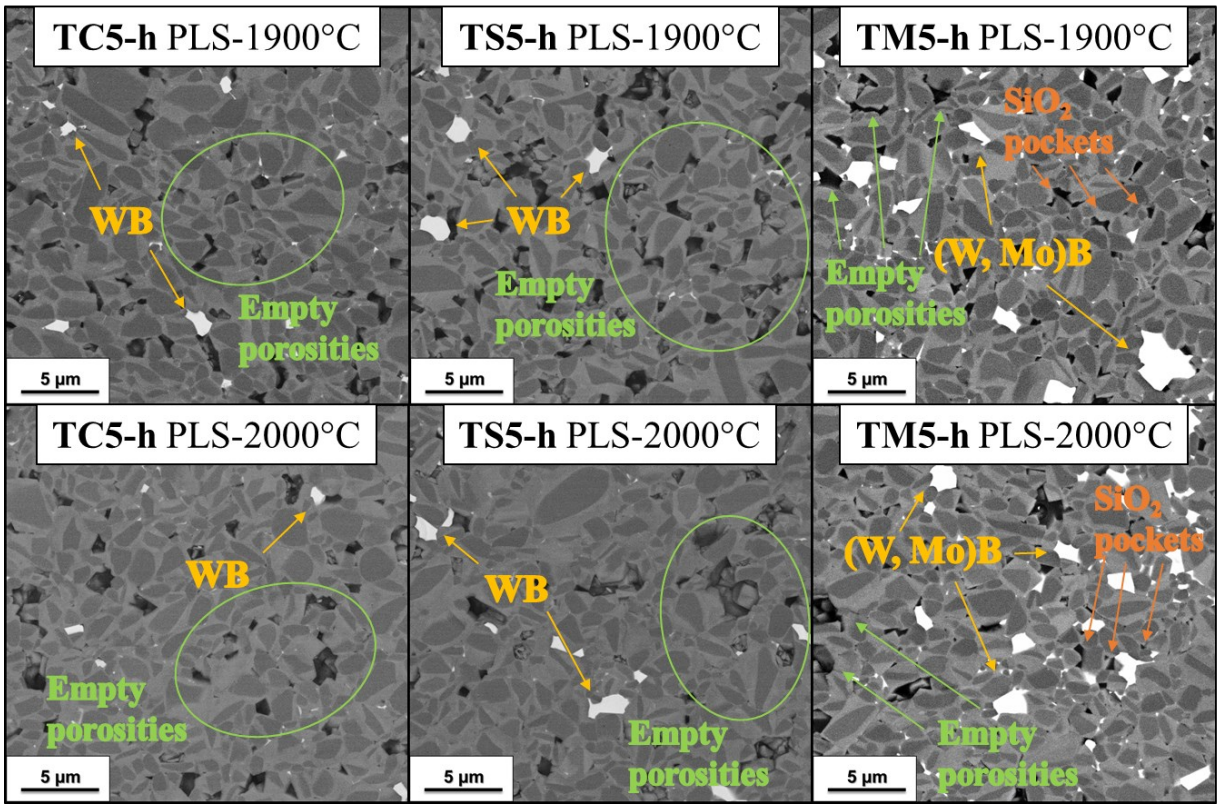

Fig. 5.13 SEM micrographs of the polished cross sections of HEPBM TiB_2 with 5 vol% B_4C, Si_3N_4 or $MoSi_2$ pressure-less sintered at 1900 and 2000°C for 60 minutes.

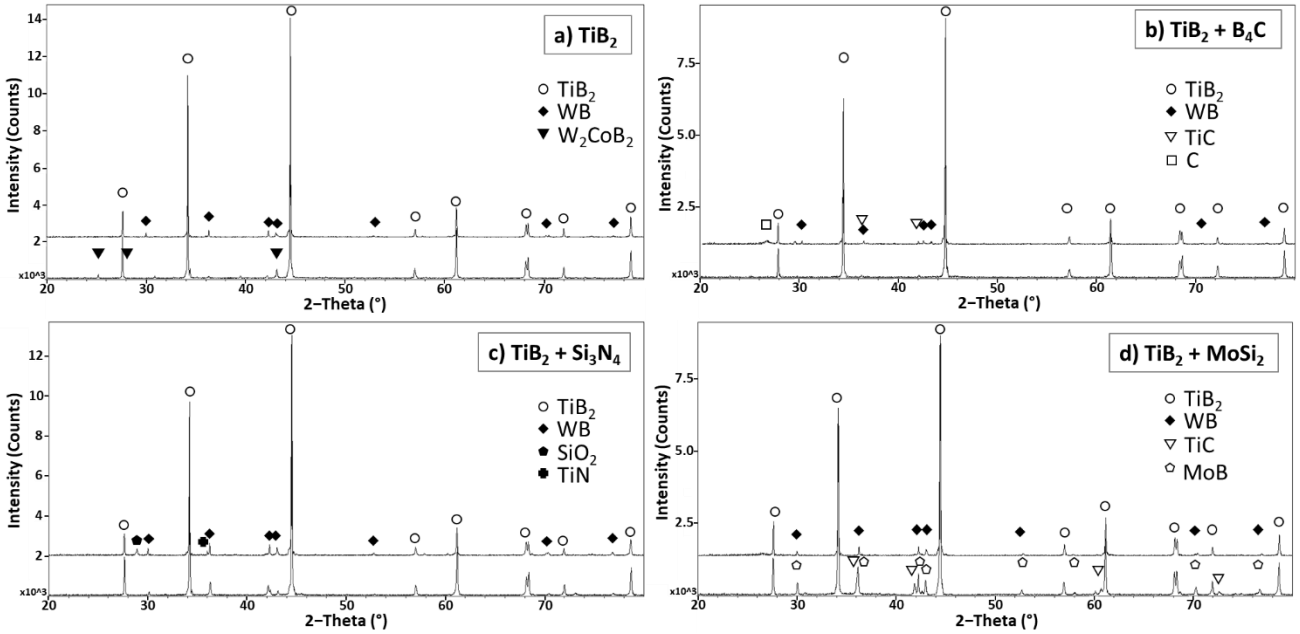

Fig. 5.14 Figure 5. X-ray diffraction patterns for the hot-pressed (line below) and pressure-less sintered (line above) sample of HEPBM TiB_2 without additives (a), with 5 vol.% of B_4C (b), 5 vol.% of Si_3N_4 (c) and 5 vol.% of $MoSi_2$ (d).

From the comparison of the XRD patterns of the HEPBM compositions sintered in HP and PLS (Fig. 5.14) it is possible to notice some differences.

T-h. In the just HEPBM TiB_2 sample the W_2CoB_2 peak disappears, this is because due to the lack of applied external pressure and long times at high temperature the Co partly came out of the sample and was found on the graphitic surface under the sample. The peaks relating to WB consequently increase in intensity.

TC5-h. After PLS sintering, unreacted B_4C phases are no longer seen in SEM images, XRD spectra indicate the presence of new phases, in particular WB, not present after HP sintering (possibly because boron carbide reacted with B_2O_3 instead of tungsten carbide). From the reaction of unreacted carbides with TiB_2 during PLS TiC is formed, confirmed by the peaks at 36.5 and 42°.

TS5-h. The XRD patterns of the PLS-sintered TS5-h also present more intense WB peaks than the HP sample. There are also peaks of crystalline SiO_2 and TiN, possibly resulting from the reaction between TiO_2 and Si_3N_4, BN or N_2.

TM5-h. In contrast to the other HEPBM samples, in the TM5-h sample sintered in PLS the disappearance of some peaks of the HP sample is observed, MoB and TiC in fact disappear while the peaks relating to the WB seem just to decrease in intensity.

Given the better densities and mechanical properties of the samples doped with $MoSi_2$, it was decided to focus the research on this composition and prepare and sinter larger disks to produce samples for mechanical tests.

5.5.1 VII set of sintering tests: Optimization of $MoSi_2$ amount in TM-h samples

As in the case of the samples with $MoSi_2$ just soft homogenized, it was decided to test a lower $MoSi_2$ content also in the high-energy-milled composition. A mixture of TiB_2 + 1 vol.% $MoSi_2$ was mixed, high-energy-milled and pressure-less sintered at 2050°C for 60 minutes (Table 5.8).

Label	$MoSi_2$, Process (vol%)	Temp. (°C)	Dwell Time (min)	Apparent density (g/cm^3)	Relative density (%)	MGS (μm)	HV1 (GPa)
T-h 2-2050°C x 60’	0, HEPBM	2050	60	4.69	97.7 ± 0.5	1.6 ± 0.8	19.8 ± 1.7
TM1-h 2050°C x 60’	1, HEPBM	2050	60	4.70	98.6 ± 0.1	1.4 ± 0.7	21 ± 2
TM5-h 2000°C x 60’	5, HEPBM	2000	60	4.80	98.1 ± 0.1	1.2 ± 0.6	26.8 ± 2.7

Table 5.8 Sintering parameters, microstructural features, and Vickers hardness of HEPBM TiB_2 with 0, 1 and 5 vol% $MoSi_2$ pressure-less sintered.

Notes: HEPBM — 24h wet-ball-milling and 30 min high-energy-planetary-ball-milling.

From the comparison of the TM1-h sample with the sample without $MoSi_2$ (T-h) sintered under the same conditions it is possible to note the presence of a synergistic effect between the high-energy-planetary-ball-milling and the presence of the additive: TM1-h reached a higher relative density (98.6 %) with the same fine and homogeneous microstructure (Fig. 5.15).

The relative density achieved was even higher than that achieved with the addition of 5 vol.% of $MoSi_2$ (TM5-h) sintered at 2000°C, however this difference was small and attributable to the difference in sintering temperature.

An increase in Vickers hardness was noted with increasing $MoSi_2$ content in the HEPBM TiB_2, with a maximum value of 26.8 GPa for TM5-h. $MoSi_2$ was therefore the best additive among those studied and shows a synergistic effect with high-energy-planetary-ball-milling the higher the silicide content.

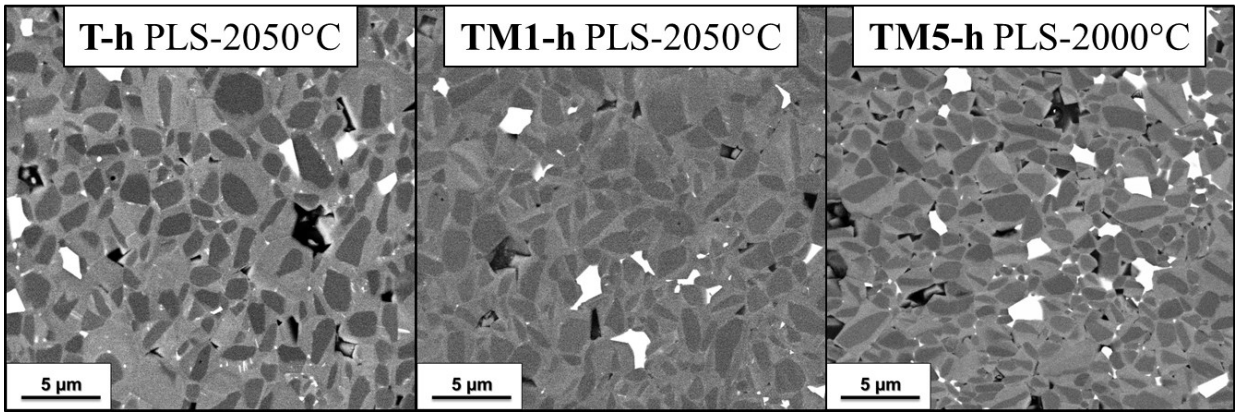

Fig. 5.15 SEM micrographs of the polished cross sections of HEPBM TiB_2 with 0 (T-h), 1 (TM1-h) and 5 vol% (TM5-h) $MoSi_2$ pressure-less sintered.

5.6 Conclusions

As for hot pressing sintering, various compositions were tested in pressure-less sintering: in particular the additives B_4C, Si_3N_4 and $MoSi_2$, the high-energy-planetary-ball-milling and their combination.

Preliminary tests on the effect of sintering aids revealed uncontrolled grain growth in all cases except that of $MoSi_2$. For this reason, different $MoSi_2$ contents were evaluated but after 60 minutes at 2000°C only the sample with 5 vol.% $MoSi_2$ (TM5) had a relative density greater than 90%.

Higher densities and finer microstructures were achieved through high-energy-planetary-ball-milling, both in the absence and presence of sintering aids. However, despite the relative densities above 90%, the Vickers hardness for the samples added with B_4C and Si_3N_4 showed lower values than the sample without additives (T-h) with a detrimental effect on the mechanical properties.

In the case of $MoSi_2$ addition, a synergistic effect is observed between the additive and the HEPBM which results in a better densification and a finer microstructure, furthermore the effect increases as the $MoSi_2$ increases. The Vickers hardness also follows the same trend, reaching the maximum value for the sample with 5 vol% of $MoSi_2$ (TM5-h).

Dwell times and temperatures of pressure-less sintering were evaluated, following an overhaul of the kiln, for the different compositions, obtaining higher density values for higher temperatures, up to 2100°C and better microstructures for dwell times of 60 minutes.

The effects of the scale-up of the sample dimensions were evaluated by sintering the just HEPBM TiB_2 at 2030 and 2100°C, and using a size compatible with the industrial standard as the final size; the density and microstructures obtained for the larger sized samples did not report significant variations, as well as Vickers hardness.

The best results in pressure-less sintering were obtained for HEPBM TiB_2 (T-h) sintered at 2100°C for 60 minutes and TiB_2 + 5vol% $MoSi_2$ high-energy-planetary-ball-milled (TM5-h) sintered at 2000°C for 60 minutes. Building on these results, other samples of these two compositions were sintered in PLS with the B format from which specimens were obtained for the mechanical, thermal, and electrical tests, which are described in detail in the chapter 7.

Before characterizing the thermomechanical properties of the PLS samples, the effects of high-energy-planetary-ball-milling were studied to optimize this process, evaluate its reproducibility, and better understand its effect on TiB_2 sintering. This study is discussed in the next chapter.

5.7 References

[1] H. Pastor, Metallic Borides: Preparation of Solid Bodies — Sintering Methods and Properties of Solid Bodies, in: V.I. Matkovich (Ed.), Boron and Refractory Borides, Springer, Berlin, Heidelberg, 1977: pp. 457–493. https://doi.org/10.1007/978-3-642-66620-9_25.

[2] H.R. Baumgartner, R.A. Steiger, Sintering and properties of titanium diboride made from powder synthesized in a plasma-arc heater, Journal of the American Ceramic Society. 67 (1984) 207–212.

[3] L. Rangaraj, C. Divakar, V. Jayaram, Processing of Refractory Metal Borides, Carbides and Nitrides, KEM. 395 (2008) 69–88. https://doi.org/10.4028/www.scientific.net/KEM.395.69.

[4] D. Demirskyi, T. Nishimura, Y. Sakka, O. Vasylkiv, High-strength TiB 2 –TaC ceramic composites prepared using reactive spark plasma consolidation, Ceramics International. 42 (2016) 1298–1306. https://doi.org/10.1016/j.ceramint.2015.09.065.

[5] G.B. Raju, A. Mukhopadhyay, K. Biswas, B. Basu, Densification and high-temperature mechanical properties of hot pressed TiB2–(0–10 wt.%) MoSi2 composites, Scripta Materialia. 61 (2009) 674–677. https://doi.org/10.1016/j.scriptamat.2009.05.031.

6. Studies on high-energy-planetary-ball-milling with WC-Co

In this chapter, the effect of high-energy-planetary-ball-milling (HEPBM) with WC-Co media on the densification of TiB_2 is explored extensively. To do this, milling cycles of different durations were tested, and the resulting powders were characterized using XRD patterns, grain size analysis, SEM microscopy, and mass measurements. The powders were then pressure-less sintered, and the effects of milling time on densification, microstructure, and mechanical properties were evaluated. The reproducibility of the HEPBM process was evaluated by repeating the same milling cycle one year later with more worn media. Finally, the role of WC was explored by preparing a mixture of TiB_2 and WC powders (without Co) and ball-milling the mixture.

6.1 Introduction

As described in section 2.4.3, one strategy to improve the sintering of TiB_2 is to high-energy-planetary-ball-mill the powders in order to reduce the size of the particles, increasing surface area.

HEPBM in this particular case presents some issues: due to the high hardness and abrasion resistance of TiB_2 it is necessary to use milling media of adequate hardness and composition, in fact, in addition to determining the milling efficiency, some debris from the grinding media remains within the powders and affect their sintering [1]. For this reason WC-Co milling media have been used, the contamination of which acts as promoters for sintering while grinding media based on ceramic oxides which can increase oxygen contamination should be avoided [2–5].

The consumption of the grinding media represents the main unknown factor on the reproducibility of the process: after each grinding cycle the mass and the dimensions of the media are reduced, potentially resulting in a progressively lower effect and less contamination.

6.2 High-energy-planetary-ball-milling cycle time

To evaluate the effect of the high-energy-planetary-ball-milling two parameters have been identified: the final dimensions of the particles and the mass of WC-Co debris obtained from the grinding media. Due to the mass losses in the various milling and sieving steps, it was not easy to have a precise estimate of the transferred WC mass, which was calculated as the average value between the mass lost by the grinding media and the jar, and that obtained from the powders. Three HEPBM cycles were carried out at 400 rpm with a total time of 10, 20 and 30 minutes respectively (see Table 6.1).

Part of the content of this chapter has been published in Nanomaterials 13 (2023) as "*S. Taraborelli, S. Failla, E. Sani, D. Sciti, Sintering, Mechanical and Optical Properties of TiB2 Composites with and without High-Energy-Milling.*"

The WC-Co content (vol %) was calculated using the following equation:

$$WC - Co\ content = \frac{100}{1+\left(\frac{m_{TiB_2} * \rho_{WC-Co}}{m_{WC-Co} * \rho_{TiB_2}}\right)}\ [vol\ \%] \qquad (6.1)$$

where m_{TiB2} is the initial mass of TiB_2, $m_{WC\text{-}Co}$ is the mass of WC-Co transferred from the grinding media and the jar to the TiB_2 powder, ρ_{TiB2} and ρ_{WC} are the theoretical densities of TiB_2 (4.52 g/cm^3) and WC-Co (14.95 g/cm^3)

Plot in Fig. 6.1 shows the values of mean particle diameter and mass of added WC-Co as a function of the milling time. After 30 minutes of HEPBM there is a significant decrease of mean grain size (from 3.80 to 2.17 µm, a decrease of approximately 43%) and increase of WC-Co contamination (~1.8 vol%). While the mass from the grinding media appears to increase linearly with time, the particle size change progressively decreases during the HEPBM process without reaching a plateau within the first 30 minutes.

Label	HEPBM time (min)	Average particle size (µm)	D_{90} (µm)	WC-Co added (g)	WC-Co content (vol %)	Theoretical density (g/cm^3)
T	0	3.80	5.8	0	0	4.52
T-h 10	10	2.84	4.7	1.49	0.4	4.56
T-h 20	20	2.52	4.1	5.12	1.3	4.65
T-h 30	30	2.17	3.6	7.45	1.8	4.71

Table 6.1 TiB_2 commercial powders and batches at different HEPBM times.

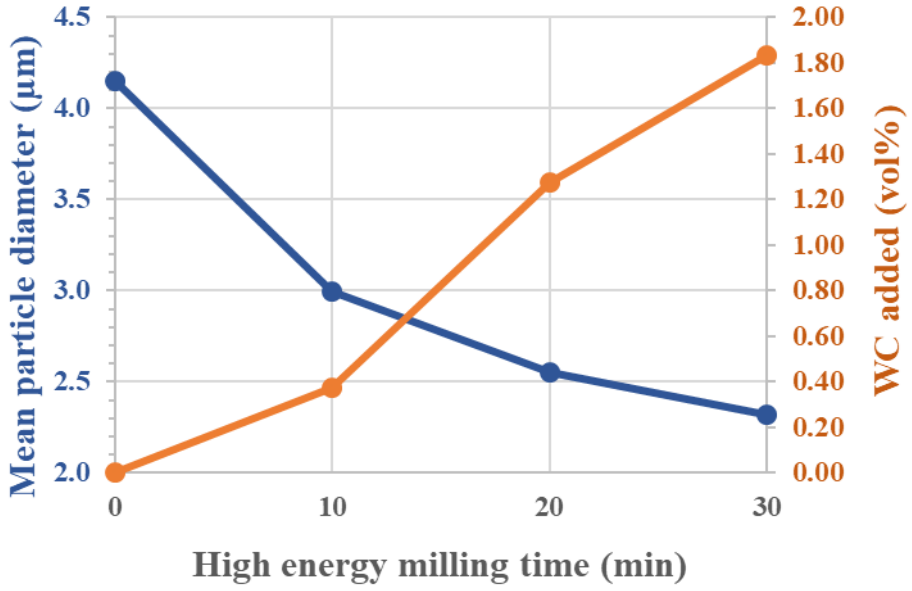

Fig. 6.1 Mean particle diameter measured through sedimentation method and WC-Co amount added after 10, 20 and 30 minutes of HEPBM.

Furthermore, as the added WC-Co increases, the powders increase in theoretical density and become progressively heavier (despite the additive content being 1.8 in the T-h 30 sample, the theoretical density increases by 4.2%).

The progressive decrease of particles dimensions and the introduction of submicrometric debris of WC-Co was confirmed by the XRD pattern (Fig. 6.2) where the peak WC increases progressively, and the SEM micrograph (Fig. 6.3). Although the debris from the grinding media are also composed of 6 wt% Co, from the XRD patterns only the WC peaks can be seen, possibly because the amount of cobalt is too low to be noticed.

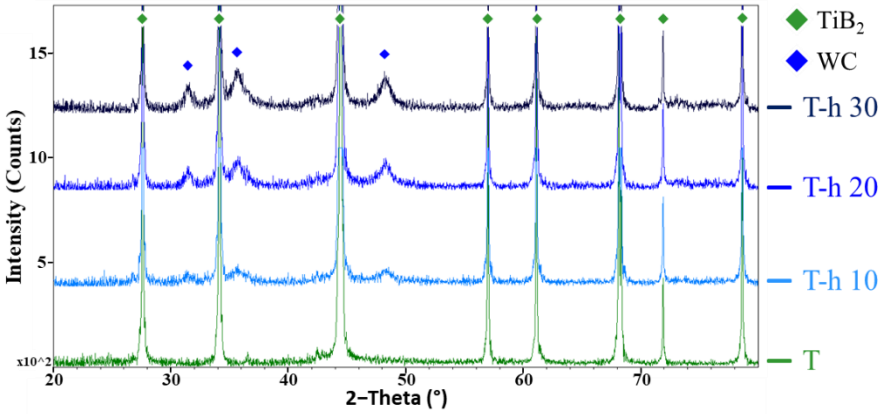

Fig. 6.2 X-ray diffraction patterns of TiB_2 powders before and after 10, 20 and 30 minutes HEPBM.

In the SEM micrographs of the powders (Fig. 6.3), TiB_2 has a gray color while the carbide, given the greater atomic mass of the tungsten, appears white. As the grinding time increases, the TiB_2 grains decrease in size while the amount of submicrometric WC-Co particles increase, and they also appear to decrease in size with time.

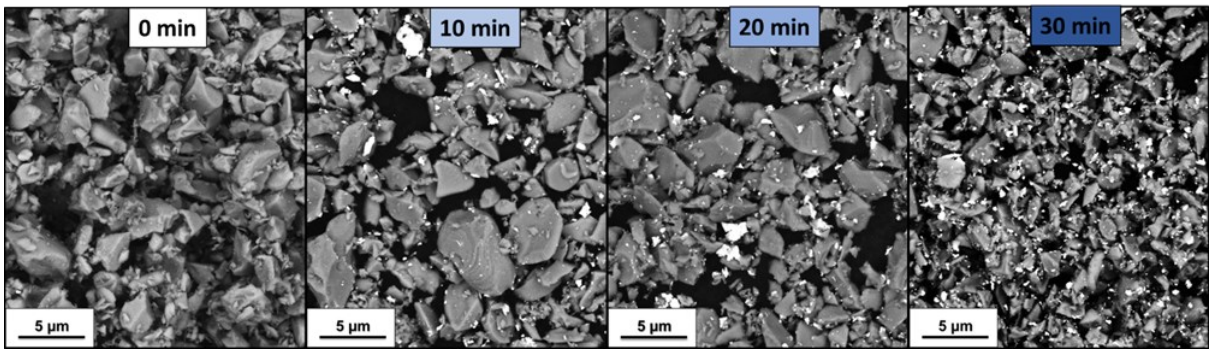

Fig. 6.3 Backscatter electron micrographs of TiB_2 powders before and after 10, 20 and 30 minutes HEPBM.

The sedimentation method (Fig. 6.4) was used to evaluate the particle size distribution for the commercial powders and batches at different HEPBM times. It can be seen from the graph that there is a first significant variation within the first 10 minutes, after which each HEPBM cycle reduces the average size but acting mainly on particles with dimensions above 1.5 µm, as below this value, the curves overlap.

The peaks observed in the distribution below 0.5 µm in Figure 6.4 and which increases progressively with time has been attributed to the lower limit of the instrument's resolution which prevented the distinction of particles with a diameter of 0.25 microns or less. This increase is due to the introduction of the submicrometric debris of WC-Co milling media.

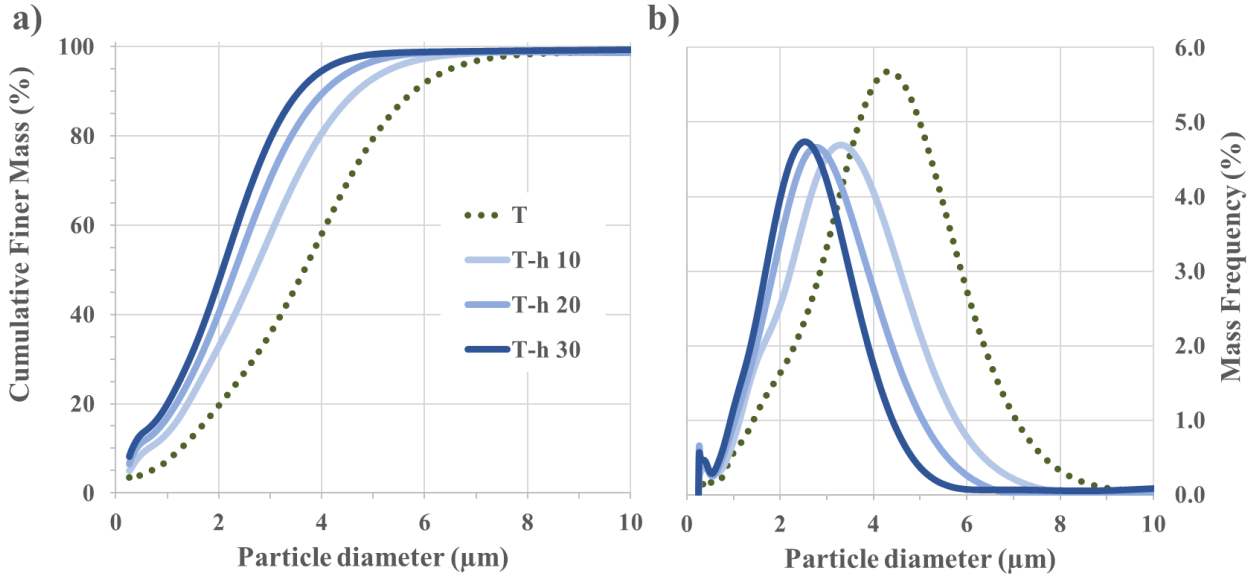

Fig. 6.4 Cumulative Finer Mass Percent vs. Diameter (a) and Mass Frequency vs. Diameter (b) for TiB_2 particles before and after 10, 20 and 30 minutes HEPBM.

The coarse fraction of the mixture was reduced, as evidenced by the change in the D90 value of the starting TiB_2 from the nominal 5.8 µm (the coarsest) to 3.6 µm in the 30-minute planetary milled mixture. It was found that TiB_2 have a significant amount of oxygen impurities. According to previous analyses (Fig. 6.5) on B_4C-TiB_2 composites, SEM/TEM images of the powder mixtures after milling revealed that TiB_2 particles were surrounded with continuous amorphous layer of about 5.5 ± 1 nm, containing Ti, W and O elements [5]. SEM analyses confirmed that high-energy-planetary-ball-milling resulted in smaller particle sizes and contamination with WC/Co-Cr due to wear of WC-Co balls. This contamination could be attributed to a mechanical alloying phenomenon [6].

Additionally, alloy nanoparticles with different chemical compositions, such as W-rich (W-Ti-Cr-Co) and Co-rich (Co-Cr-Ti-W), were observed to be attached to TiB_2 due to the mechanical alloying process during high-energy-planetary-ball-milling. These nanoparticles were formed as a result of contamination from other metallic species, such as W, Co, and Cr [5].

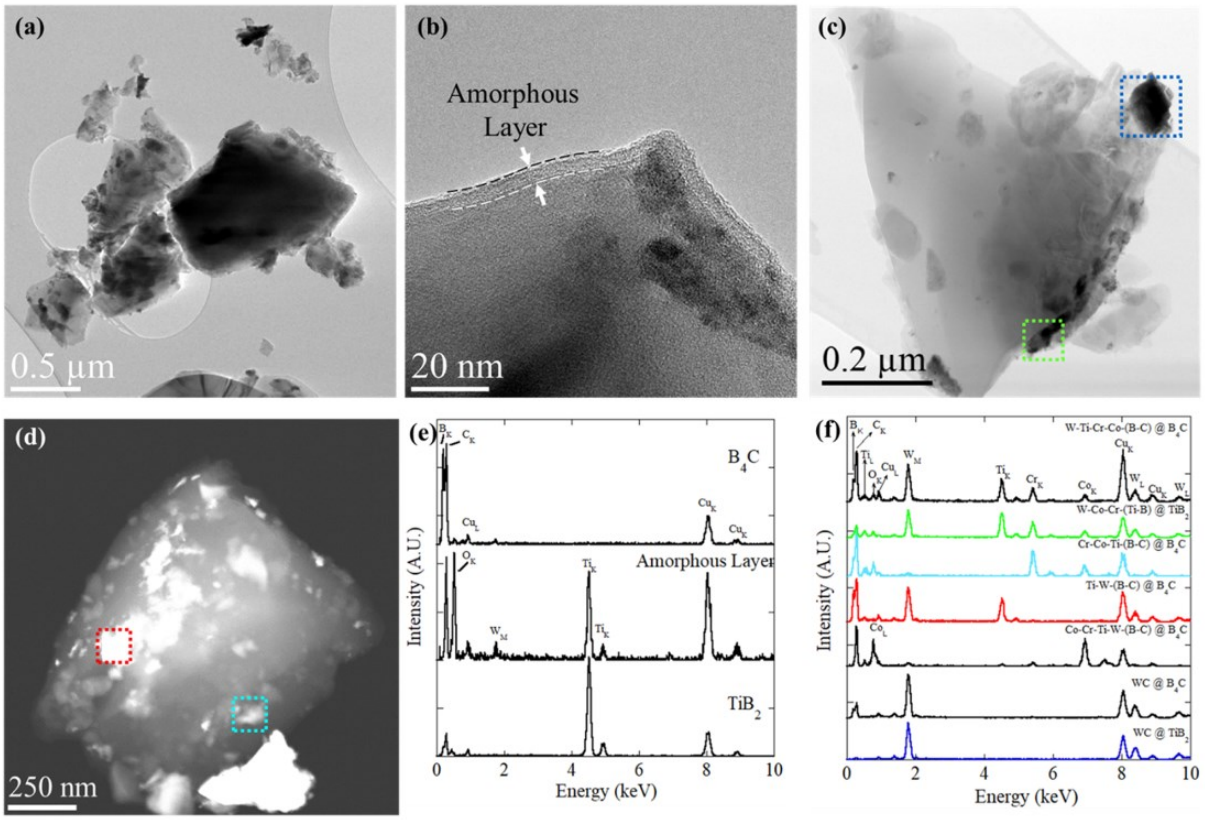

Fig. 6.5 TEM images of high-energy-planetary-ball-milled powder mixture (a) showing general overview, (b) showing continuous amorphous layer around TiB_2, (c) STEM-BF image of a TiB_2 particle attached with alloy particles, (d) STEM-HAADF image of a B_4C particle attached with alloy particles, (e) and (f) EDS results obtained from TiB_2, B_4C, amorphous layer and alloy particles (please note that EDS results given in (f) are color coded with (c) and (d)) [5].

6.3 Effect HEPBM time on sintering

The effect of different high-energy-planetary-ball-milling times on the densification of TiB_2 was tested by sintering the powders prepared at different HEPBM times (already described in the previous section) in PLS at 2100°C for 60 minutes (Table 6.2).

Although the 10-minute HEPBM sample (T-h 10) already presented a good relative density (96.7 ± 0.6 %) and a fine microstructure (Fig. 6.6), as the milling time increased there was an increase in the relative density (which reaches a maximum of 99.2 ± 0.2 % for the T-h 30 sample) and a progressive decrease in mean grain size up to 1.7 µm.

Moreover, while the T-h 10 sample exhibited good densification, it proved challenging to determine the Vickers hardness (9.8 N load) due to residual stresses present within the material. These residual stresses hindered the creation of distinct, measurable indentations, resulting in the formation of cracks or chipped edges.

Label		T-h 10	T-h 20	T-h 30
HEPBM time	(min)	10	20	30
WC-Co added	(vol%)	**0.4**	**1.3**	**1.8**
Temperature	(°C)	2100	2100	2100
Theoretical density	(g/cm^3)	**4.56**	**4.65**	**4.71**
Apparent density	(g/cm^3)	4.39	4.26	4.54
Relative density	(%)	96.7 ± 0.6	98.1 ± 0.7	99.2 ± 0.2
Mean grain size	(µm)	3.1 ± 1.9	1.9 ± 1.1	1.7 ± 0.9
Vickers hardness	(GPa)	-	22.2 ± 1.2	22.9 ± 1.0

Table 6.2 TiB_2 high-energy-planetary-ball-milled at different times pressure-less sintered at 2100°C for 60 minutes.

The samples high-energy-planetary-ball-milled for 20 and 30 minutes instead gave values comparable with those previously obtained for the T-h and not significantly different from each other, showing how 20 minutes can be enough to have an improvement in the sintering with a lower theoretical density, therefore a lighter material and a lower consumption of milling media.

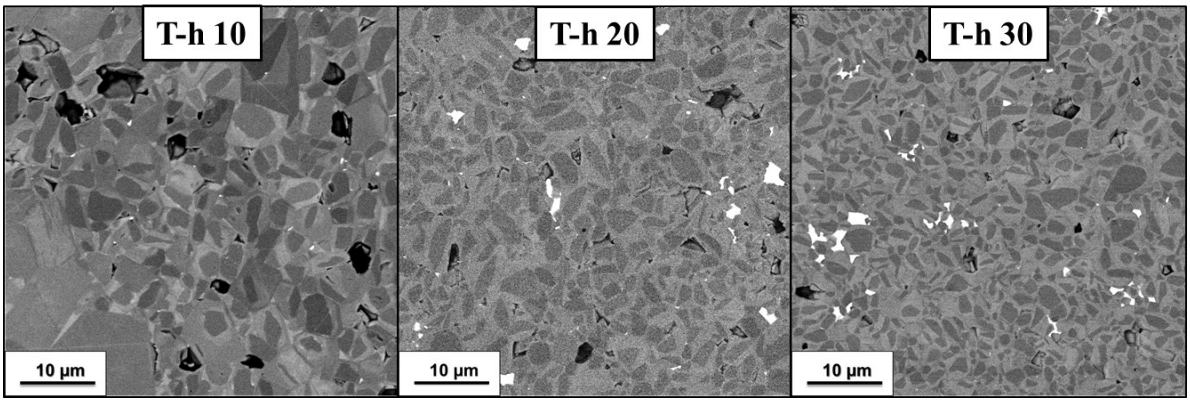

Fig. 6.6 SEM micrographs of the polished cross sections of high-energy-planetary-ball-milled TiB_2 for 10 (T-h 10), 20 (T-h 20) and 30 minutes (T-h 30) sintered at 2100°C for 60 minutes.

6.4 Reproducibility of HEPBM

To evaluate the reproducibility between the high-energy-planetary-ball-milling processes, two HEPBM experiments (Table 6.3, T-h and T-h 30) were carried out under the same conditions one year apart with same grinding media, just more consumed (therefore with lower mass and smaller dimensions).

Label	HEPBM time (min)	Milling media mass (g)	Average particle size (µm)	WC-Co added (g)	WC-Co content (vol %)	Theoretical density (g/cm^3)
T	0		3.80	0	0	4.52
T-h	30	445.70	2.03	7.78	1.9	4.72
T-h 30	30	413.76 *(-7.2%)*	2.17 *(+6.9%)*	7.45 *(-4.2%)*	1.8	4.71

Table 6.3 comparison between TiB_2 commercial powders and batches with same HEPBM times but different grinding media conditions.

In the second experiment (T-h 30), the lower mass (7.2% less) and smaller dimensions of grinding media resulted in less contamination (4.2% less) and a larger final particle size (6.9% bigger). However, the distributions of the two final powders were very similar (Fig. 6.7), with the D90 value rising from 3.3 µm in T-h to 3.6 µm in T-h 30. Their appearance from the SEM micrographs also do not present major differences (Fig. 6.8). Again, greatest difference was found for particles larger than 1.5 µm while below this value the curves overlap.

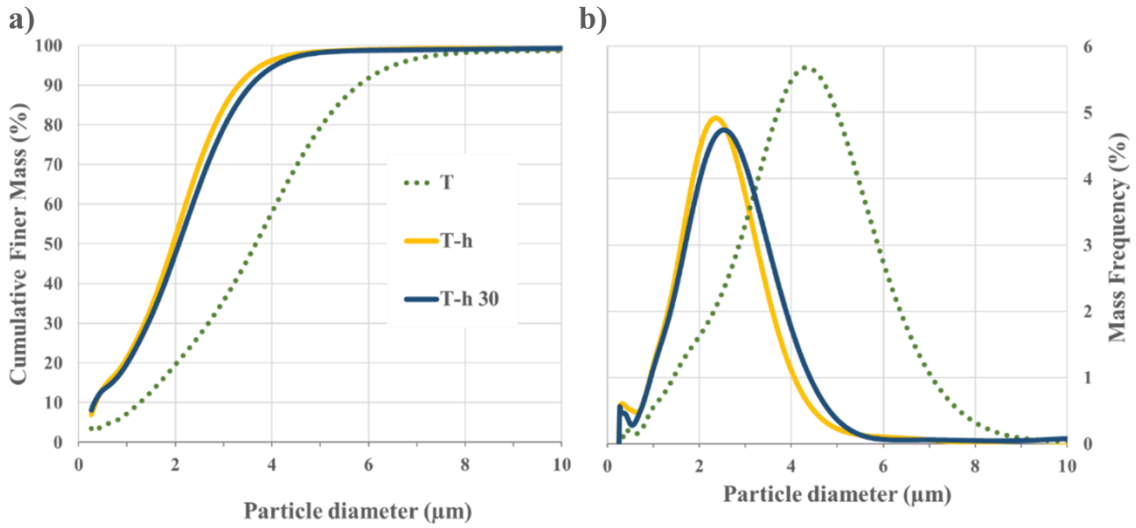

Fig. 6.7 Cumulative Finer Mass Percent vs. Diameter (a) and Mass Frequency vs. Diameter (b) for TiB_2 commercial powders and batches with same HEPBM times but different grinding media conditions.

The reproducibility of the high-energy-planetary-ball-milling is, therefore, directly influenced by the mass of the milling media used, although this issue can be fixed by using the same mass of grinding media, the influence of the media size which decreases after each cycle remains unknown.

Despite the dependence on the quantity and size of the grinding media, the process shows good reproducibility, with results proportional to the decrease in the mass of the milling media. It is therefore possible to consider non-significant variations in the starting powders between batches prepared at different times.

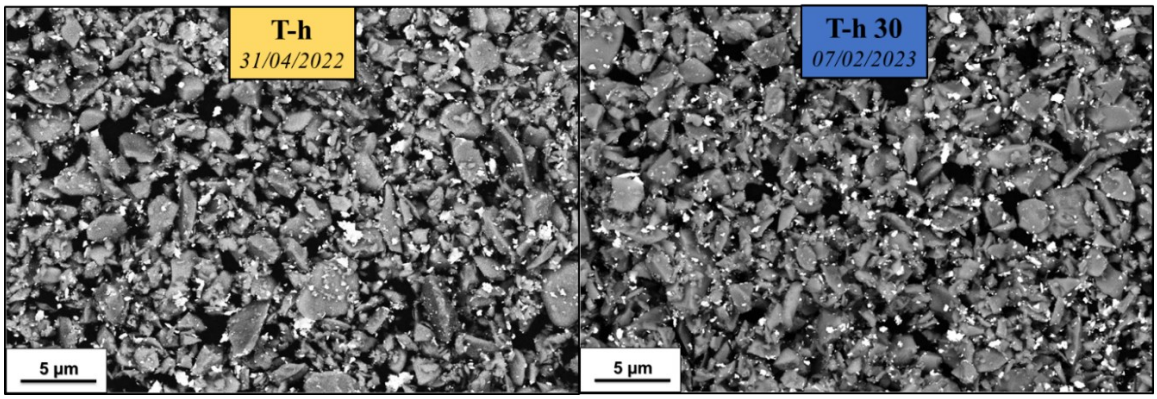

Fig. 6.8 Backscatter electron micrographs of TiB_2 powders with same HEPBM times but different grinding media conditions.

6.5 Effect of just WC content on sintering

In order to examine the impact of high-energy-planetary-ball-milling and the specific contribution of tungsten carbide in the sintering process of TiB_2, were prepared two mixtures containing 2 and 5 vol% of submicrometric WC (with no Co inclusion) just wet-ball-milled (as shown in Table 6.4).

Sample	Average particle size (µm)	WC added (vol%)	Temp. (°C)	Theoretical density (g/cm³)	Apparent density (g/cm³)	Relative density (%)
T-h 10	2.84	0.4	2100	4.56	4.39	96.7 ± 0.6
T-h 20	2.52	1.3	2100	4.65	4.26	98.1 ± 0.7
T-h 30	2.17	1.8	2100	4.71	4.54	99.2 ± 0.2
TW2	2.91	2.0	2100	4.74	3.86	≈ 75
TW5	2.41	5.0	2100	5.08	4.22	≈ 75

Table 6.4 comparison between TiB_2 with different HEPBM times and soft homogenized WC content.

The first mixture, with 2 vol% of WC (TW2) was prepared to have a direct comparison with T-h 30 which has a content equal to 1.8 vol%, while the mixture with 5 vol% of WC (TW5) was tested to compare this additive with the previous soft homogenized ones.

From the plots in Fig. 6.9 it can be seen how the TW2 sample after 24 hours of wet ball milling presents a grain size distribution very similar to that of the TiB_2 sample high-energy-planetary-ball-milled for 10 minutes (T-h 10), with a mean grain size equal to 2.91 µm versus 2.84 µm of the sample T-h 10.

Sample TW5, on the other hand, has a grain size distribution that has an intermediate trend between T-h 10 and T-h20 with an average particle diameter even lower than both and equal to 2.45 µm. Moreover, samples TW2 and TW5 have D90 of 4.6 and 4.1 µm respectively, similar to those of T-h10 and T-h20 which are 4.7 and 4.1 µm respectively.

This may be due to the fact that the instrument reports the particle size without distinguishing between TiB_2 and WC, and as the concentration of submicrometric WC particles increases, the average powder size decreases.

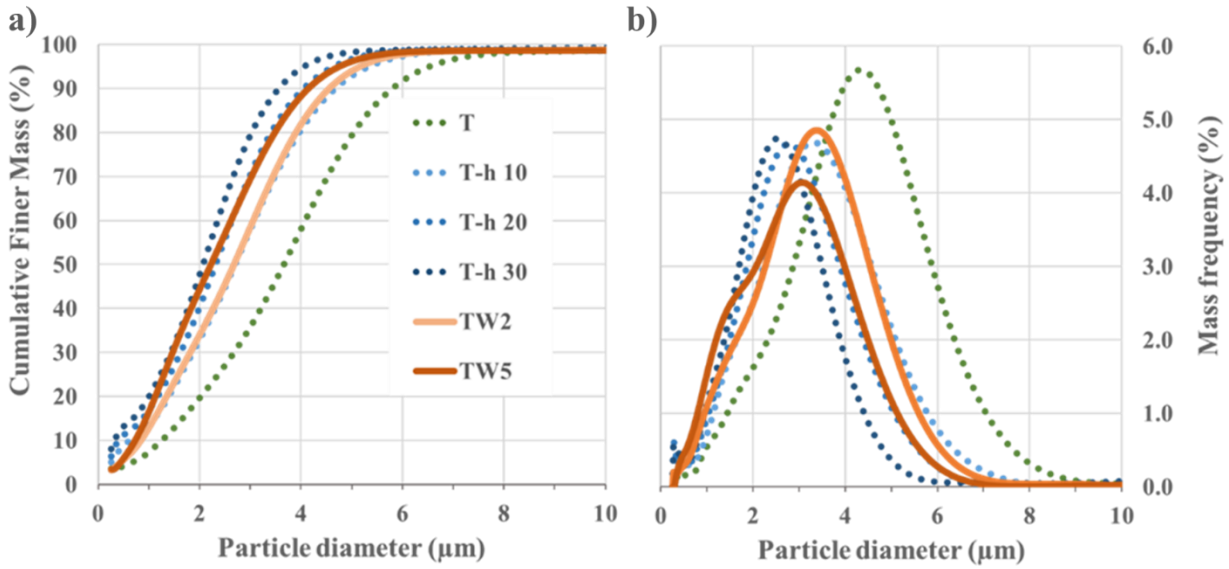

Fig. 6.9 Cumulative Finer Mass Percent vs. Diameter (a) and Mass Frequency vs. Diameter (b) for TiB_2 commercial powders and batches with different HEPBM times and soft homogenized WC content.

TW2 and TW5 were sintered in PLS at 2100°C, however after 60 min both samples showed poor densification (Fig. 6.10), still in the first stage (≈ 75% relative density). Despite the higher WC content compared to all high-energy-planetary-ball-milled samples there was no improvement in sintering indicating that WC alone is not sufficient to promote a complete TiB_2 densification.

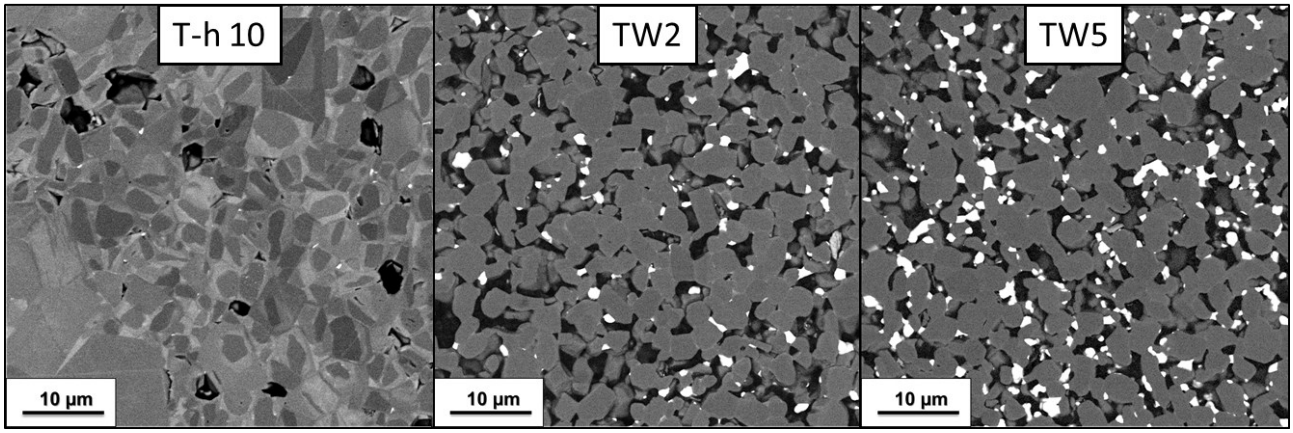

Fig. 6.10 SEM micrographs of the polished cross sections of TiB_2 high-energy-planetary-ball-milled 10 minutes (T-h 10) and soft homogenized with 2 (TW2) and 5 vol% (TW5) sintered at 2100°C for 60 minutes.

From a close-up of the TW2 and TW5 microstructure (Fig 6.11) it can be seen that the usual core-shell structure was partly formed, although to a much lower extent than in the HEPBM samples sintered in PLS. Furthermore, the necks that formed between the particles are mainly composed of solid solution (Ti, W)B_2, this solid solution in fact seems to be characterized by a higher self-diffusion rate than TiB_2.

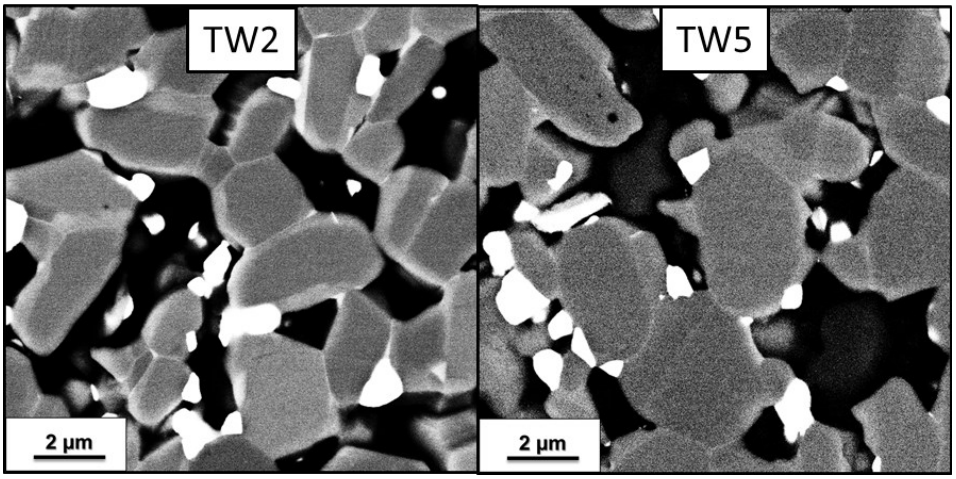

Fig. 6.11 Close-up of SEM micrographs of the polished cross sections of TiB_2 soft homogenized with 2 (TW2) and 5 vol% (TW5) sintered at 2100°C for 60 minutes.

It is possible to state that in addition to adding WC and increasing the available surface area by decreasing the average particle size, high-energy-planetary-ball-milling has other fundamental effects for promoting the densification of TiB_2 such as the addition of cobalt and chromium which contribute to the formation of a liquid phase at high temperature, which through dissolution and reprecipitation processes (Fig. 6.12) of TiB_2 and the other phases present (e.g. WC) leads to a more effective densification and the formation of the solid solution of mixed boride [7].

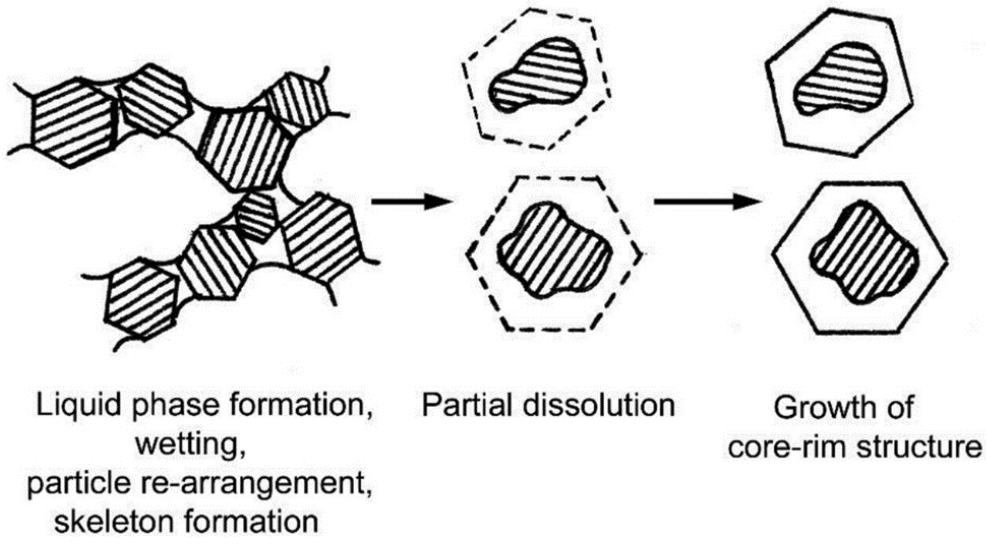

Fig. 6.12 Formation scheme of the core-shell microstructure [8].

6.6 Conclusions

The effects of different high-energy-planetary-ball-milling cycles on TiB_2 powders and their densification were investigated, while the introduction of WC-Co increased linearly with time, the average particle size decreased significantly within the first 10 minutes after which the rate of size reduction slowed down progressively.

After 30 minutes of HEPBM, TiB_2 showed an average particle diameter that was 43% smaller and a D90 of 3.6 compared to 5.8 μm of the starting powder. HEPBM mainly affected particles larger than 1.5 μm, while the added submicrometric WC-Co particles were smaller than 0.5 μm.

All HEPBM samples sintered at 2100°C for 60 minutes showed high relative densities (> 95%), however the sample high-energy-planetary-ball-milled for 10 minutes (T-h 10) showed the presence of residual stresses after sintering resulting in crack formation and edge chipping during the measurement of Vickers hardness (9.8 N load).

T-h 20 and T-h 30 showed very similar densification, microstructures and Vickers hardness, indicating that 20 minutes may be sufficient to obtain good results with lower consumption of WC-Co milling media.

The reproducibility of the HEPBM cycles was tested by repeating the same cycle one year later with the same but more consumed milling media, whose mass had decreased by 7%. Despite the smaller quantities and dimensions, the second batch of HEPBM powder displayed 7% larger dimensions and a 4% lower quantity of WC-Co, indicating a non-significant variation potentially resolvable with a replenishment of the lost mass.

Finally, the effect of HEPBM was investigated through the preparation of TiB_2 compositions with soft homogenized WC as sintering aid. Samples with 2 and 5 vol% WC (TW2 and TW5) showed a similar particle size distribution to samples T-h 10 and T-20, however after 60 minutes of PLS at 2100°C they did not fully densify (reaching about 75% of relative density).

The absence of densification and the lower quantity of solid solution following sintering indicated the presence of other effects due to HEPBM in addition to the introduction of submicrometric WC particles and the reduction of grain size, in particular it was hypothesized that densification could be also attributed to the presence of Co and Cr that lead to the production of a liquid phase which improves densification through dissolution/reprecipitation mechanisms which also give origin to the solid solution of mixed boride $(Ti, W)B_2$.

6.7 References

[1] H. Ghayour, M. Abdellahi, M. Bahmanpour, Optimization of the high energy ball-milling: Modeling and parametric study, Powder Technology. 291 (2016) 7–13. https://doi.org/10.1016/j.powtec.2015.12.004.

[2] D. Ağaoğulları, H. Gökçe, İ. Duman, M.L. Öveçoğlu, Influences of metallic Co and mechanical alloying on the microstructural and mechanical properties of TiB2 ceramics prepared via pressureless sintering, Journal of the European Ceramic Society. 32 (2012) 1949–1956. https://doi.org/10.1016/j.jeurceramsoc.2011.10.033.

[3] S. Failla, C. Melandri, L. Zoli, G. Zucca, D. Sciti, Hard and easy sinterable B4C-TiB2-based composites doped with WC, Journal of the European Ceramic Society. 38 (2018) 3089–3095. https://doi.org/10.1016/j.jeurceramsoc.2018.02.041.

[4] M. Yao, Y. Wang, L. Chen, J. Ouyang, H. Li, H. Gu, Y. Zhou, Mechanical properties and microstructural evolution of pressureless sintered ceramics obtained from high-energy ball-milled TiB2–TiC powders, Materials Science and Engineering: A. 819 (2021) 141510. https://doi.org/10.1016/j.msea.2021.141510.

[5] D. Sciti, S. Failla, S. Turan, U. Savaci, P. Galizia, Properties and ballistic tests of strong B4C-TiB2 composites densified by gas pressure sintering, Journal of the European Ceramic Society. 43 (2023) 1334–1342. https://doi.org/10.1016/j.jeurceramsoc.2022.11.066.

[6] C. Suryanarayana, T. Klassen, E. Ivanov, Synthesis of nanocomposites and amorphous alloys by mechanical alloying, J Mater Sci. 46 (2011) 6301–6315. https://doi.org/10.1007/s10853-011-5287-0.

[7] L. Silvestroni, S. Failla, N. Gilli, C. Melandri, U. Savacı, S. Turan, D. Sciti, Disclosing small scale length properties in core-shell structured B4C-TiB2 composites, Materials & Design. 197 (2021) 109204.

[8] R. Telle, Analysis of pressureless sintering of titanium diboride ceramics with nickel, cobalt, and tungsten carbide additives, Journal of the European Ceramic Society. 39 (2019) 2266–2276. https://doi.org/10.1016/j.jeurceramsoc.2019.02.036.

[9] A. Márquez-Herrera, G. Bermúdez-Rodríguez, E.N. Hernández-Rodríguez, M. Melendez-Lira, M. Zapata-Torres, Boride coating on the surface of WC–Co-based cemented carbide, International Journal of Materials Research. 107 (2016) 676–679. https://doi.org/10.3139/146.111387.

[10] Effect of MgO Solute on the Kinetics of Grain Growth in A12O3 - Bennison - 1983 - Journal of the American Ceramic Society - Wiley Online Library, (n.d.). https://ceramics.onlinelibrary.wiley.com/doi/abs/10.1111/j.1151-

2916.1983.tb10065.x?casa_token=7uRs_1kbs_IAAAAA:KgjtmHhxImCpHij59UihRIUEfYUTjoeLDV4cQojWvmnuP3WlxHhyJjjBA-ktQsXy2JNOuvnf-hHQRyc (accessed October 6, 2023).

[11] F. Monteverde, ZrB2-MoSi2 ceramics: A comprehensive overview of microstructure and properties relationships. Part I: Processing and microstructure, Journal of the European Ceramic Society. (2019). https://www.academia.edu/95366217/ZrB2_MoSi2_ceramics_A_comprehensive_overview_of_microstructure_and_properties_relationships_Part_I_Processing_and_microstructure (accessed October 7, 2023).

[12] F. Monteverde, R.J. Grohsmeyer, A.D. Stanfield, G.E. Hilmas, W.G. Fahrenholtz, Densification behavior of ZrB2-MoSi2 ceramics: The formation and evolution of core-shell solid solution structures, Journal of Alloys and Compounds. 779 (2019) 950–961. https://doi.org/10.1016/j.jallcom.2018.11.238.

7. Thermomechanical and electrical properties of pressure-less sintered TiB_2

In the previous chapters the effect of additives, high-energy-planetary-ball-milling and their combination on the densification of TiB_2 was evaluated (chapter 4); pressure-less sintering and its scale-up were studied, identifying $MoSi_2$ as the best additive in PLS and the promoter effect of high-energy-planetary-ball-milling in all tested samples, with and without additives, and finding best dwell time and temperature conditions (chapter 5); finally, after having explored the effect of HEPBM and the role of WC in the densification of TiB_2 (chapter 6), the thermomechanical and electrical properties were measured for the most promising compositions, the results of these tests are shown in this chapter.

Pressure-less sintered TiB_2 properties were explored on specimens made from PLS samples prepared during my time at the Missouri University of Science and Technology. Flexural strength and fracture toughness measurements were carried out at room and high temperature (1000-1600°C) to analyze the mechanical properties. Thermal conductivity tests were performed between 25 and 2000°C to obtain thermal properties, while electrical resistivity was measured for different currents at room temperature.

7.1 Introduction

Due to the cost and time required to machine TiB_2, in the previous chapters a preliminary study on the mechanical properties of the sintered samples was accomplished by conducting Vickers hardness measurements (using a 9.8 N load) on polished cross sections. The specific sintering cycles and composition details and the resulting mechanical properties are presented in Table 7.1.

Label	Sintering aid, Process (vol%)	Technique, max temp./time (°C, min)	Apparent density (g/cm^3)	Relative density (%)	HV1 (GPa)
T	-	HP 1950, 20	3.45	≈ 76	-
TC	5 B_4C, SH	HP 1900, 15	3.71	≈ 78	-
TS	5 Si_3N_4, SH	HP 1900, 15	4.28	85.6* (>98)	22.2 ± 1.6
TM	5 $MoSi_2$, SH	HP 1900, 10	4.43	95.1* (>98)	24.4 ± 1.3
T-h	HEPBM	HP 1900, 10	4.60	93.4	24.5 ± 0.6
TC-h	5 B_4C, HEPBM	HP 1900, 10	4.22	87.9	19.6 ± 0.8

TS-h	5 Si_3N_4, HEPBM	HP 1830, 10	4.54	92.4* (>98)	23.2 ± 0.6
TM-h	5 $MoSi_2$, HEPBM	HP 1700, 10	4.67	94.7* (>98)	24.4 ± 0.7
T-h 2-2000°C	HEPBM	PLS 2000, 60	4.54	98.0 ± 0.2	24 ± 4
T-h 2-2030°C	HEPBM	PLS 2030, 60	4.61	98.0 ± 0.3	22.2 ± 1.4
T-h 2-B-2030°C	HEPBM	PLS 2030, 60	4.42	98.6 ± 0.3	22.6 ± 1.3
T-h 2-2050°C	HEPBM	PLS 2050, 60	4.69	97.7 ± 0.5	19.8 ± 1.7
T-h 2-2100°C	HEPBM	PLS 2100, 60	4.54	99.2 ± 0.2	22.9 ± 1.0
T-h 2-B-2100°C	HEPBM	PLS 2100, 60	4.64	99.0 ± 0.1	23.0 ± 0.9
TM5 1900°C x 60’	5 $MoSi_2$, SH	PLS 1900, 60	4.21	85.4 ± 0.5	13.5 ± 0.8
TM5 2000°C x 60’	5 $MoSi_2$, SH	PLS 2000, 60	4.39	93.4 ± 0.8	21.4 ± 0.8
TM5 2100°C x 60’	5 $MoSi_2$, SH	PLS 2100, 60	4.08	96.6 ± 0.2	20.6 ± 1.4
TC5-h 1900°C x 60’	5 B_4C, HEPBM	PLS 1900, 60	4.34	95.8 ± 0.1	14.8 ± 1.8
TC5-h 2000°C x 60’	5 B_4C, HEPBM	PLS 2000, 60	4.55	95.0 ± 0.4	19.0 ± 1.3
TS5-h 1900°C x 60’	5 Si_3N_4, HEPBM	PLS 1900, 60	4.34	92.5 ± 0.1	15.4 ± 0.9
TS5-h 2000°C x 60’	5 Si_3N_4, HEPBM	PLS 2000, 60	4.59	98.7 ± 0.3	20.7 ± 0.7
TM5-h 1900°C x 60’	5 $MoSi_2$, HEPBM	PLS 1900, 60	4.77	96.9 ± 0.2	24.8 ± 1.7
TM5-h 2000°C x 60’	5 $MoSi_2$, HEPBM	PLS 2000, 60	4.80	98.1 ± 0.1	26.8 ± 2.7
TM5-h B-2100°C x 60’	5 $MoSi_2$, HEPBM	PLS 2100, 60	4.42	95.1 ± 0.9	20.9 ± 1.3

Table 7.1 Sintering parameters, microstructural features and Vickers hardness of hot-pressed and some of the pressure-less sintered samples.

Notes: HP—hot-pressing, PLS—pressure-less sintering, SH—24h wet-ball-milling, HEPBM —24h wet-ball-milling and 30 min high-energy-planetary-ball-milling.

Vickers hardness measurements conducted on the hot-pressed samples (see Fig. 7.1) revealed that T-h (high-energy-planetary-ball-milled TiB_2), TM (softly homogenized TiB_2 with 5 vol% $Mosi_2$), and TM-h (high-energy-milled TiB_2 with 5 vol% $MoSi_2$) compositions exhibited the highest levels of hardness, with values approximately at 24 .5 GPa. Conversely, samples with the addition of 5 vol% of B_4C (TC and TC-h) demonstrated significantly lower hardness values, whereas samples containing 5 vol% of Si_3N_4 (TS and TS-h) exhibited Vickers hardness ranging from 22 to 24 GPa.

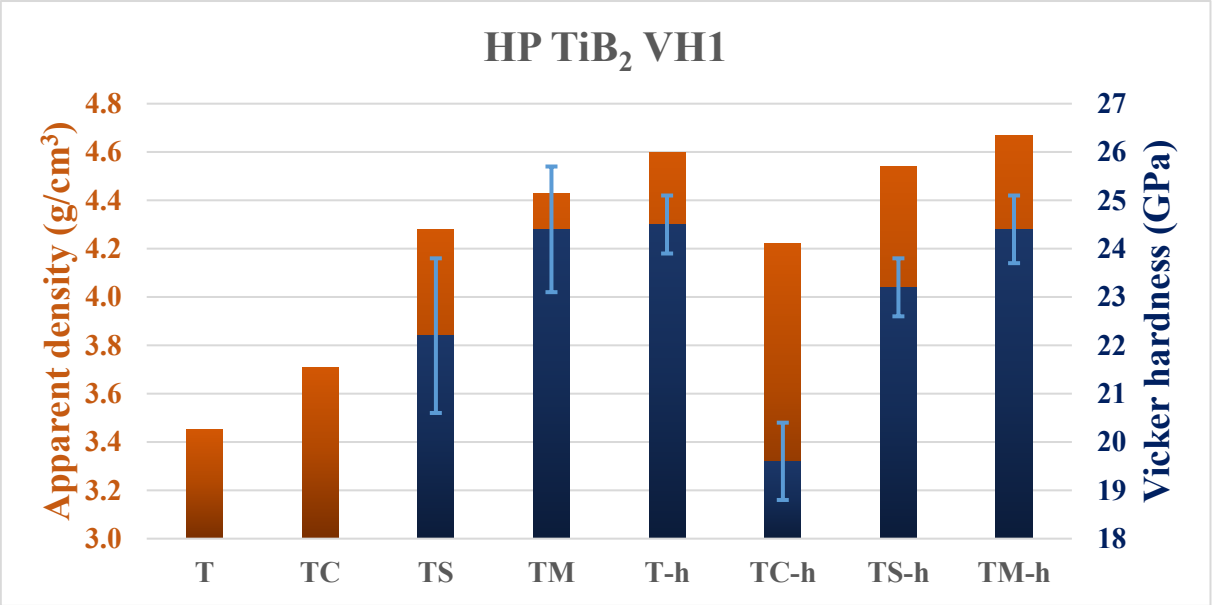

Figure 7.1 Apparent density and Vickers hardness (9.8 N load) for hot-pressed TiB_2 samples.

By comparing the T-h sample hot-pressed with those sintered using pressure-less sintering (see Figure 7.2), it can be observed that the pressure-less sintered samples exhibit lower hardness levels across all temperatures, even when the apparent density is higher. On the other hand, there are no substantial differences between samples of different sizes, thereby confirming the efficacy of the scale-up process.

Since the best hardness value with the lowest standard deviation obtained by pressure-less sintering was the one obtained at 2100°C, the T-h sample of larger dimensions (format B) was machined to obtain the specimens for the mechanical tests (section 7.2)

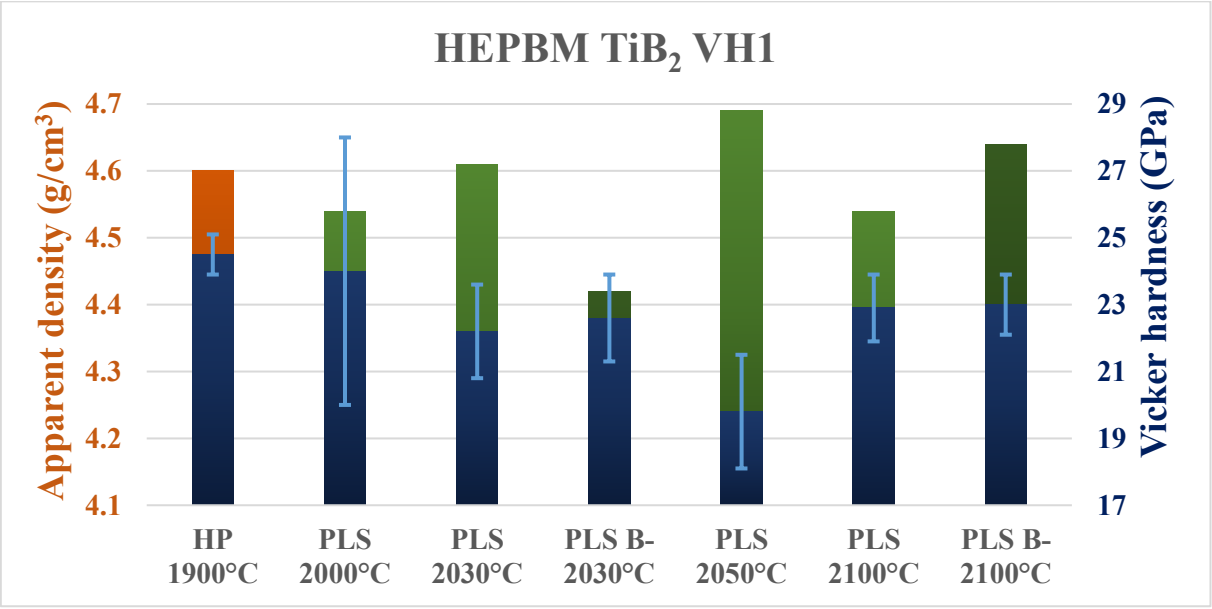

Figure 7.2 Apparent density and Vickers hardness (9.8 N load) for hot-pressed (orange) and pressure-less sintered (green) HEPBM TiB_2 samples.

Samples containing 5 vol% $MoSi_2$ (TM5) only ball-milled were also pressure-less sintered and compared to the hot-pressed sample (Figure 7.3). PLS sample sintered at the same temperature (1900°C) exhibited significantly low hardness (< 15 GPa). Samples sintered at 2000°C and 2100°C displayed Vickers hardness values of 21.4 and 20.6 GPa, respectively, both of which were lower than the hardness of the HP sample.

The samples mixed with B_4C or Si_3N_4 high-energy-planetary-ball-milled exhibited hardness values below 21 GPa at both 1900 and 2000°C. Consequently, it was determined not to proceed with any further testing on these blends.

Through the combination of incorporating 5 vol% of $MoSi_2$ and employing high-energy-planetary-ball-milling (TM5-h) in TiB_2 pressure-less sintering, it was possible to achieve not only good relative densities and Vickers hardness values but even surpass those obtained from the sample sintered via hot pressing (Figure 7.3). In fact, despite a rise in the standard deviation of hardness, the material exhibited exceptional mechanical properties, reaching 26.8 GPa after sintering at a temperature of 2000°C.

Due to these promising results, a larger sample was produced by PLS at 2100°C (TM5-h PLS B-2100°C) in order to obtain specimens for evaluating the mechanical properties of this composition as well. Unfortunately, due to the too high temperature (2100°C) or the difficulty in the sintering scale-up of this composition, a lower apparent density (4.42 versus 4.80 g/cm^3) and a lower hardness (20.9 versus 26.8 GPa, Table 7.1) were obtained compared to the small sample sintered at 2000°C (TM5-h PLS 2000°C).

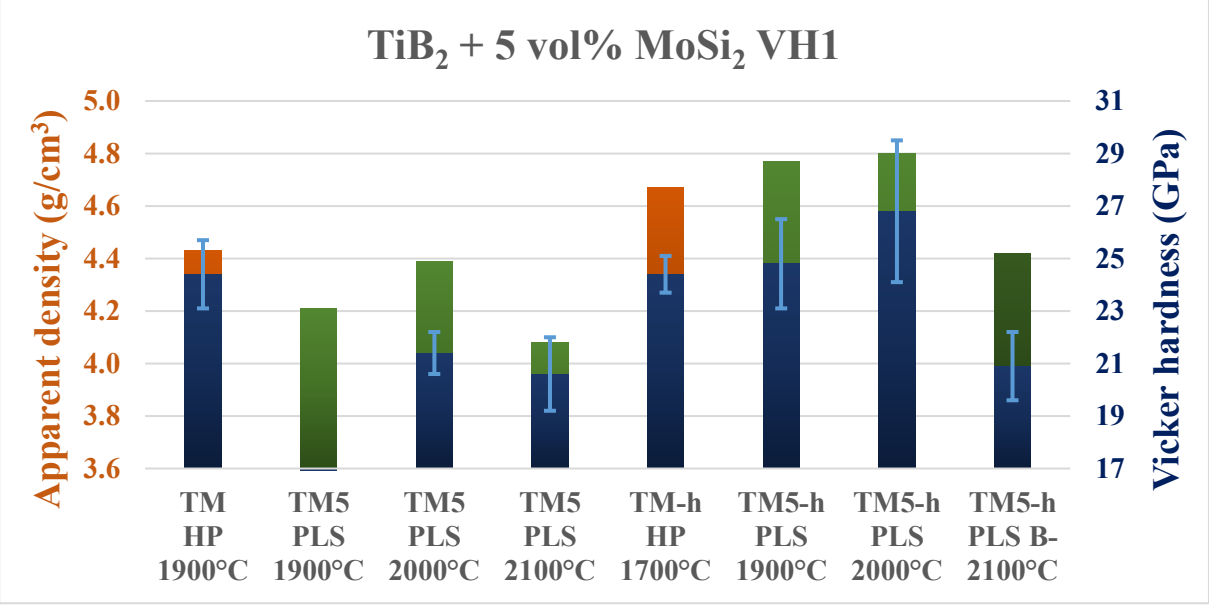

Figure 7.3 Apparent density and Vickers hardness (9.8 N load) for hot-pressed (orange) and pressure-less sintered (green) SH and HEPBM TiB_2 samples with 5 vol% $MoSi_2$.

7.2 Room temperature flexural strength

As previously stated, starting from the two most promising compositions (T-h and TM5-h), two samples were prepared with Format B (section 5.1, height 10 mm and diameter 35 mm after sintering) and pressure-less-sintered at 2100°C for 60 minutes in Ar atmosphere. Subsequently, these samples were characterized by conducting measurements of Vickers hardness (9.8 load) and flexural strength at room temperature (see Table 7.2).

3 bars measuring 2.0 x 2.5 x 25 mm were cut and chamfered on the edges just using electrical discharge machining, then were directly tested without grinding and lapping surfaces oxidized by the EDM process, in fact these processes are those that require more time and cost.

Label	Sintering aid, Process (vol%)	Max temp./time (°C, min)	Apparent density (g/cm^3)	Relative density (%)	HV1 (GPa)	Flexural strength (MPa)
T-h B-2100°C	HEPBM	2100, 60	4.64	99.0 ± 0.1	23.0 ± 0.9	460 ± 108
TM5-h B-2100°C	5 $MoSi_2$, HEPBM	2100, 60	4.42	95.1 ± 0.9	20.9 ± 1.3	259 ± 148
T-h B-2200°C	HEPBM	2200, 60	4.06/4.25	98.4 ± 0.1	22.8 ± 1.5	394 ± 27

Table 7.2 Sintering parameters, density, and Vickers hardness of pressure-less sintered HEPBM TiB_2 samples with B format.

Notes: HEPBM —24h wet-ball-milling and 30 min high-energy-planetary-ball-milling.

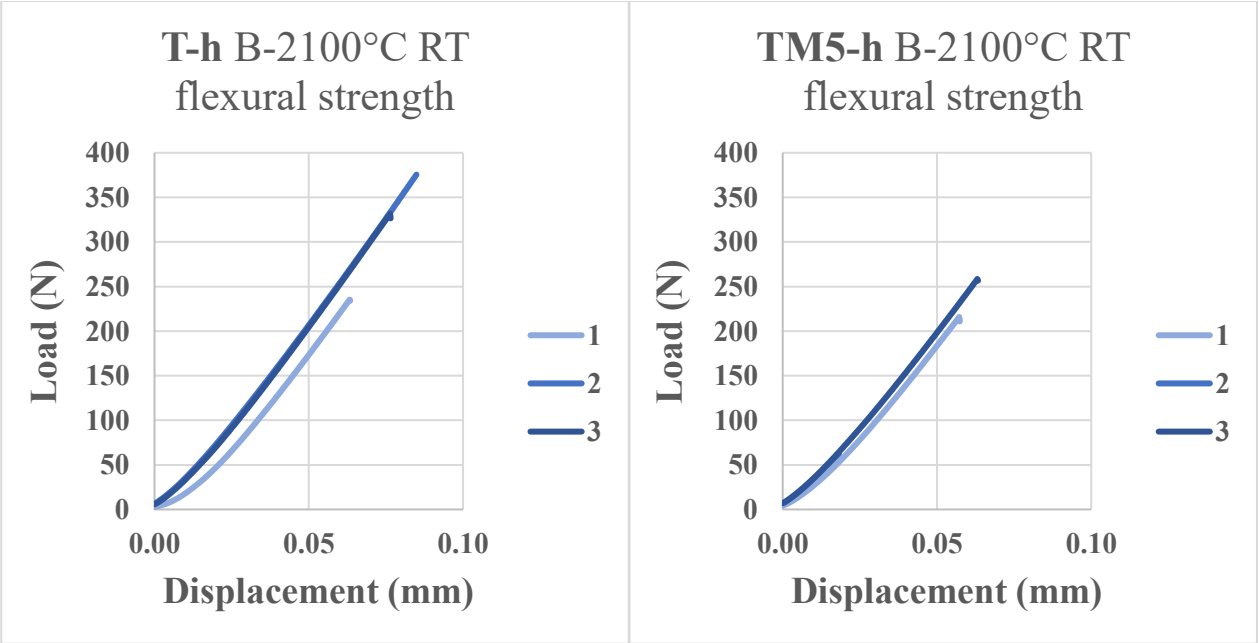

Figure 7.4 Load displacement curves for the 4-point room temperature (RT) flexural strength of HEPBM TiB_2 sample with (TM5-h B-2100°C) and without MoSi2 as sintering aid (T-h B-2100°C).

The room temperature flexural strength of HEPBM TiB_2 without additives (T-h B-2100°C) was found to be high and consistent with values found in the literature, where fully dense monolithic TiB2 reaches approximately 400 MPa [1]. On the contrary, the HEPBM sample added with $MoSi_2$ (TM5-h B-2100°C) displayed a very low flexural strength value, probably mainly due to its high porosity (about 5% measured by image analysis).

Furthermore, both samples presented very high standard deviation values, indicating a very wide dispersion of the data, possibly due to the method of preparation of the bars which left the surface of the samples oxidized and introduced defects from which it was possible that the fracture originated during the measurement of flexural strength.

From the micrographs in Figure 7.5, which show a fracture surface for each of the compositions, the numerous surface defects from which the fracture possibly starts can be seen, while it is not possible to distinguish any oxidized layer of significant dimensions.

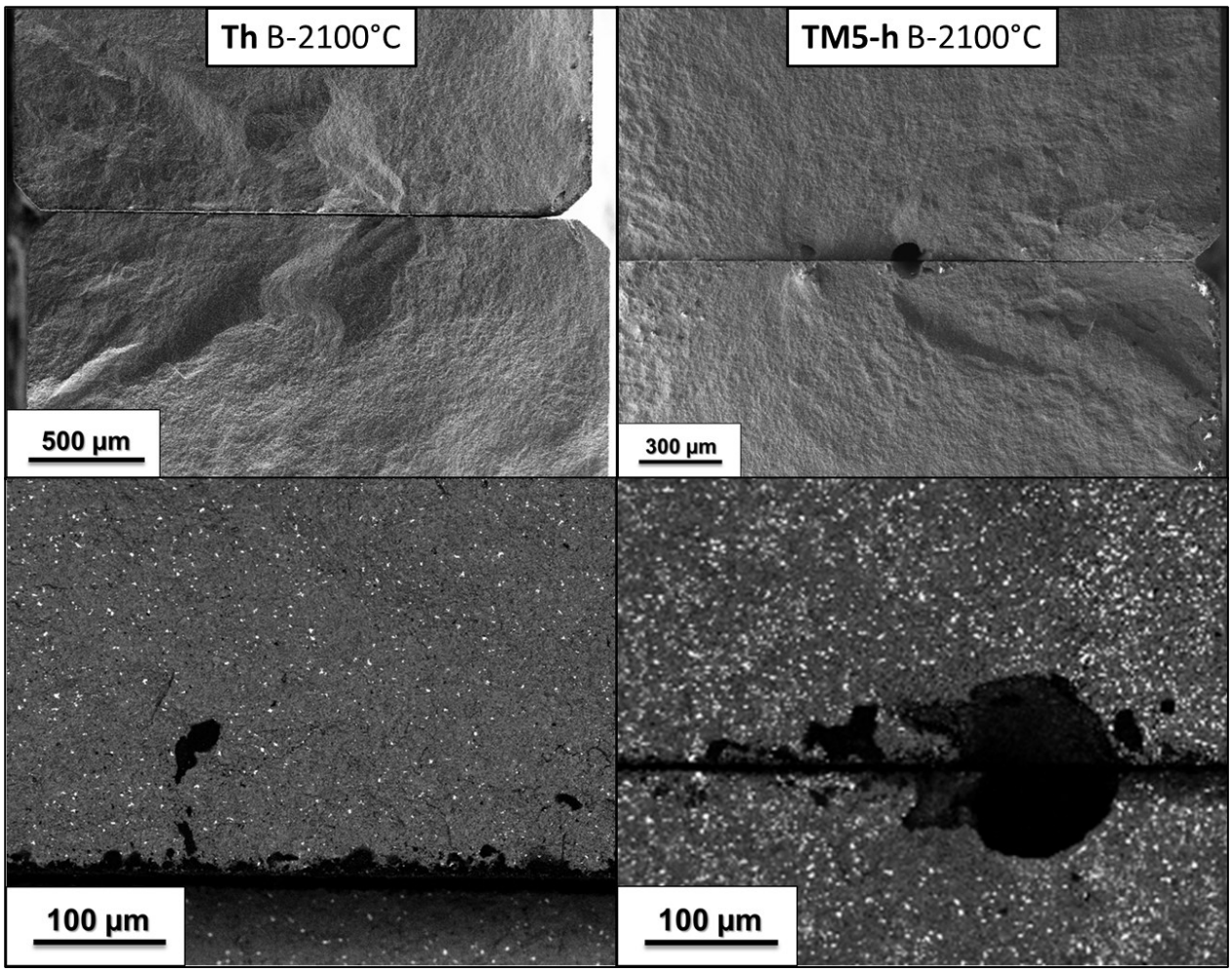

Figure 7.5 SEM micrograph in SE2 (above) and backscattered (below) mode of the fracture surface after flexural strength test for just high-energy-planetary-ball-milled TiB_2 sample (T-h B-2100°C, left column) and HEPBM TiB2 with $MoSi_2$ (TM5-h B-2100°C, right column). The two fracture surfaces were brought together on the respective tension side.

Two other samples of HEPBM TiB_2 without additives and with B format were sintered in PLS at 2200°C for 60 min (T-h B-2200°C) to evaluate hardness and flexural strength at these sintering conditions (see Table 7.2). Moreover, these samples were exploited to test the high temperature flexural strength (section 7.3), the room temperature and high temperature fracture toughness (section 7.4) and finally thermal and electrical properties (section 7.5) of HEPBM TiB_2 during my stay in Professor Fahrenholtz's research group at the Missouri University of Science and Technology.

Although the apparent density measured by the Archimedes method for the pressure-less sintered T-h samples at 2200°C is much lower than the sample sintered at 2100°C (4.06 and 4.25 versus 4.64 g/cm^3), the residual porosities measured by image analysis (1.6 versus 1.0%) and the hardness (22.8 versus 23.0 GPa) are very similar.

In the case of these samples, after cutting by electrical discharge machining, the oxidized surface was removed and the final dimensions (1.5 x 2.0 x 25mm) of the specimen were reached by surface grinding, finally the edges were chamfered, and the surface subjected to traction was polished down to 0.25 μm. The difference between the two types of bars can be seen in Figure 7.6.

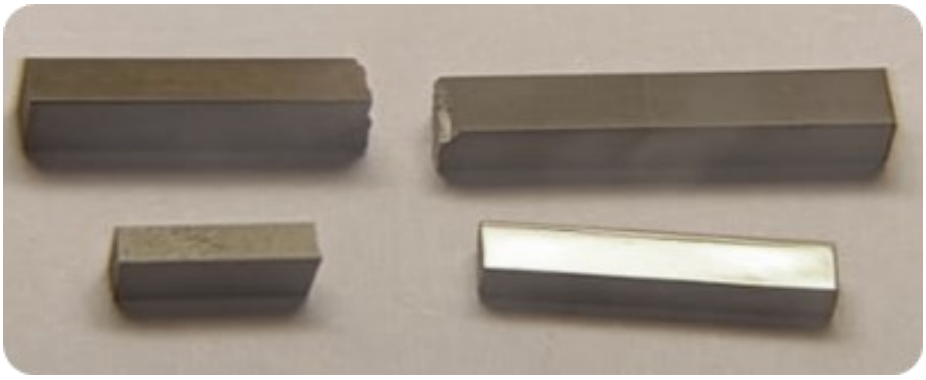

Figure 7.6 Flexural test bars just cut for EDM (above) or also ground and polished down to 0.25 μm (below).

The flexural strength of the T-h B-2200°C sample (394 ± 27 MPa), although perfectly in agreement with the results present in the literature, is lower than the sample sintered at 2100°C probably due to its lower density, however the standard deviation is significantly lower in this case (see Fig. 7.7) confirming the problems related to test samples with surfaces just cut with EDM.

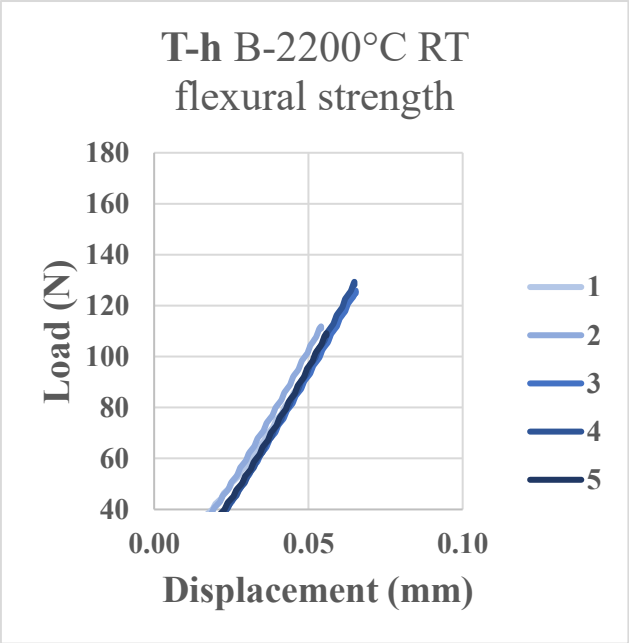

Figure 7.7 Load displacement curves for the 4-point room temperature (RT) flexural strength of HEPBM TiB_2 sample (T-h B-2200°C).

Bars processed using the same method were tested at a higher temperature, the results are described in the next section.

7.3 High temperature flexural strength

The high-temperature flexural strength tests were conducted in an Ar atmosphere starting from a temperature of 1600°C and a crossheads rate of 0.8 mm/min. However, under these conditions the sample showed non-elastic behavior, bending without breaking (see Fig. 7.8).

To achieve elastic behavior and fracture, the crossheads rate was increased to 1.6 and 2.4 mm/min (Figure 7.9), obtaining a sufficient result in the latter case. The test was repeated two more times, always obtaining an elastic fracture.

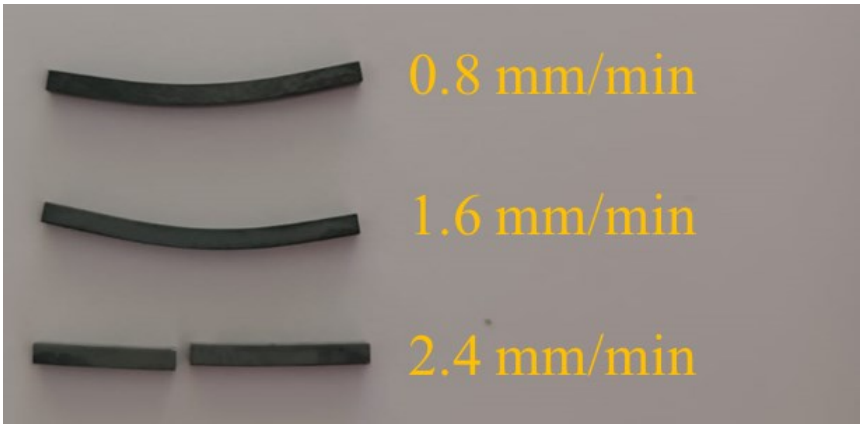

Figure 7.8 Flexural strength bars tested at 1600°C with different crossheads rate.

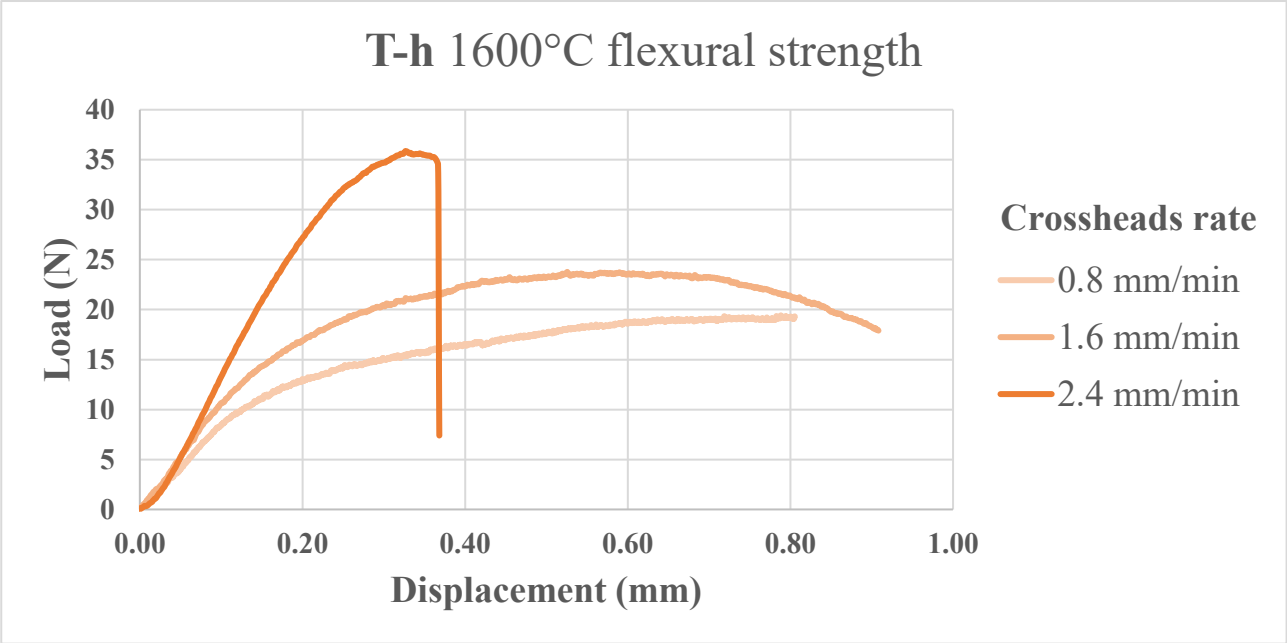

Figure 7.9 Load displacement curves for the 4-point flexural strength at 1600°C of HEPBM TiB_2 sample (T-h B-2200°C) with different crossheads rate.

Given the softening of the HEPBM TiB_2 at 1600°C, the flexural strength was also measured at 1400°C at various crossheads rates (ranging from 2.4 to 0.8 mm/min), however in this case no significant variations were recorded (Figure 7.10).

The softening of the material therefore occurs at a temperature higher than 1400°C, possibly due to softening of residual phases that derive from liquid phase formed during sintering.

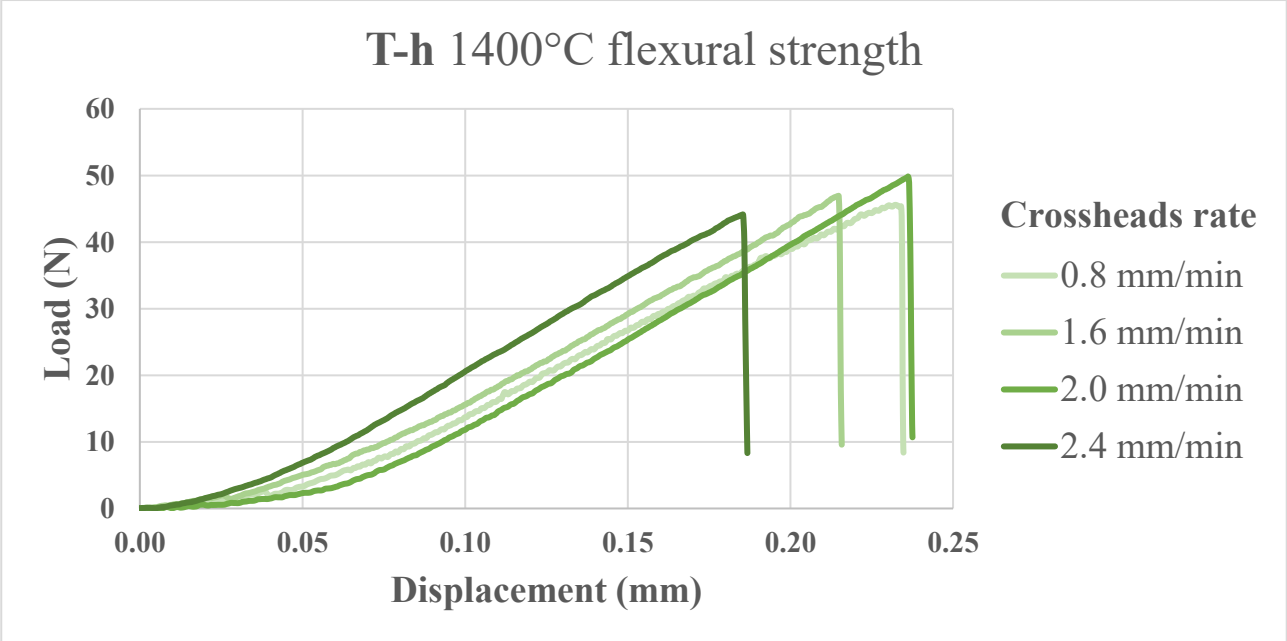

Figure 7.10 Load displacement curves for the 4-point flexural strength at 1400°C of HEPBM TiB_2 sample (T-h B-2200°C) with different crossheads rate.

In order to investigate the effect that leads the bars to bend at 1600°C, the specimen tested at 0.8 mm/min was fractured in the center, after which one of the fracture surfaces perpendicular to the long side was polished and compared with the polished cross section of the sample before the flexural strength test.

In Figure 7.11 the microstructures of T-h sample pressure-less sintered at 2200°C before and after the flexural strength test can be observed: after the test it seems that the shells have grown, a strange phenomenon given the temperature much lower than the sintering temperature. Furthermore, the grains appear to be less equiaxed after testing at 1600°C, it is possible that the bending of the bars during the test was due to softening of the mixed boride shells or to the expansion of the mixed boride shells under the bending load. The bending of the bar could also be due the formation of a liquid phase at the grain boundary and the sliding of the grains over each other, under the test load. More tests are needed to clarify this phenomenon.

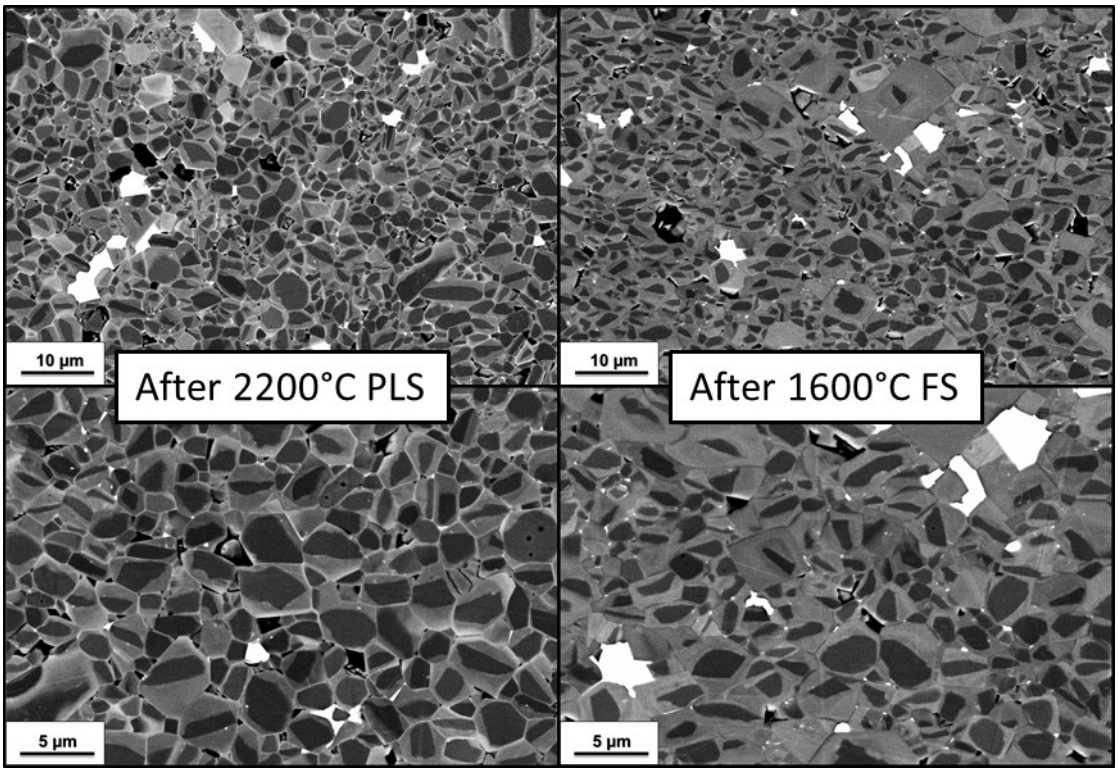

Figure 7.11 SEM micrographs of the polished cross sections T-h B-2200°C before and after flexural strength test a 1600°C

The flexural strength of the T-h B-2200°C sample was measured at two other high temperatures: 1200 and 1000°C, again at 0.8 mm/min (Table 7.3). As the temperature decreased, the flexural strength increased significantly, reaching 351 MPa at 1000°C (Figure 7.12).

Temperature (°C)	Crossheads rate (mm/min)	Flexural strength (MPa)
20	0.2	394
1000	0.8	351
1200	0.8	238
1400	0.8	157
1600	2.4	115

Table 7.3 4-point flexural strength test of T-h B-2200°C

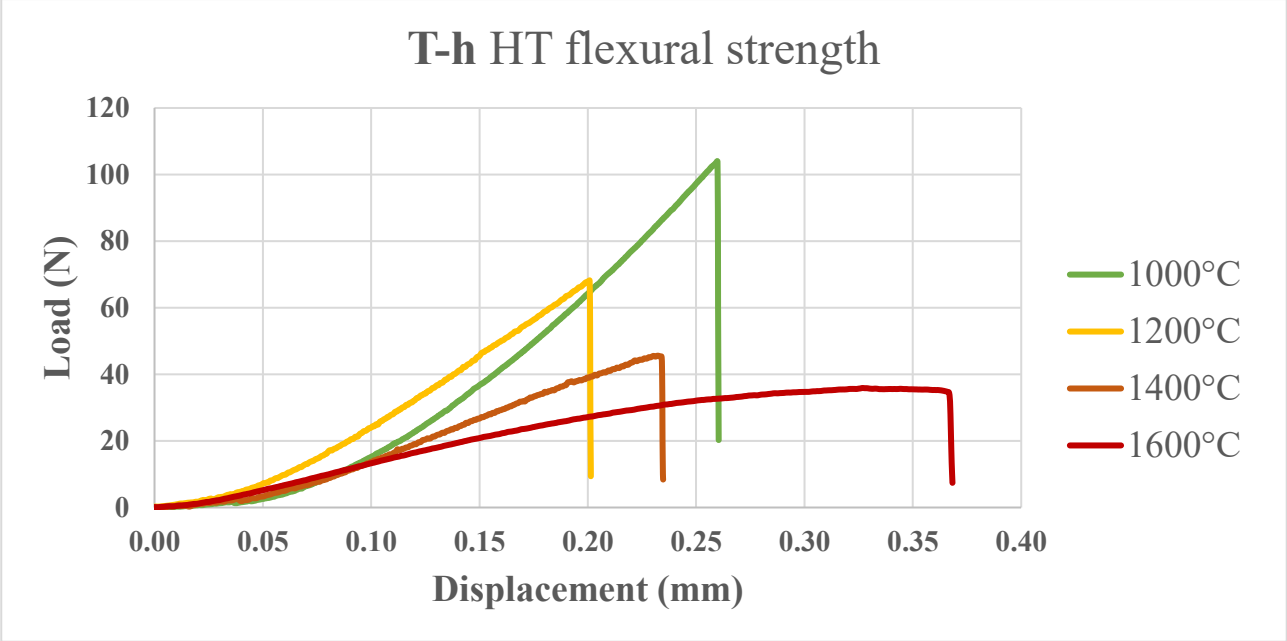

Figure 7.12 Load displacement curves for the 4-point high temperature (HT) flexural strength of HEPBM TiB_2 sample (T-h B-2200°C).

From the flexural strength versus temperature plot (Figure 7.13) it can be seen that as the temperature increases the flexural strength decreases, in particular it drops above 1000°C, decreasing of 40% by 1200°C and of 70% by 1600°C.

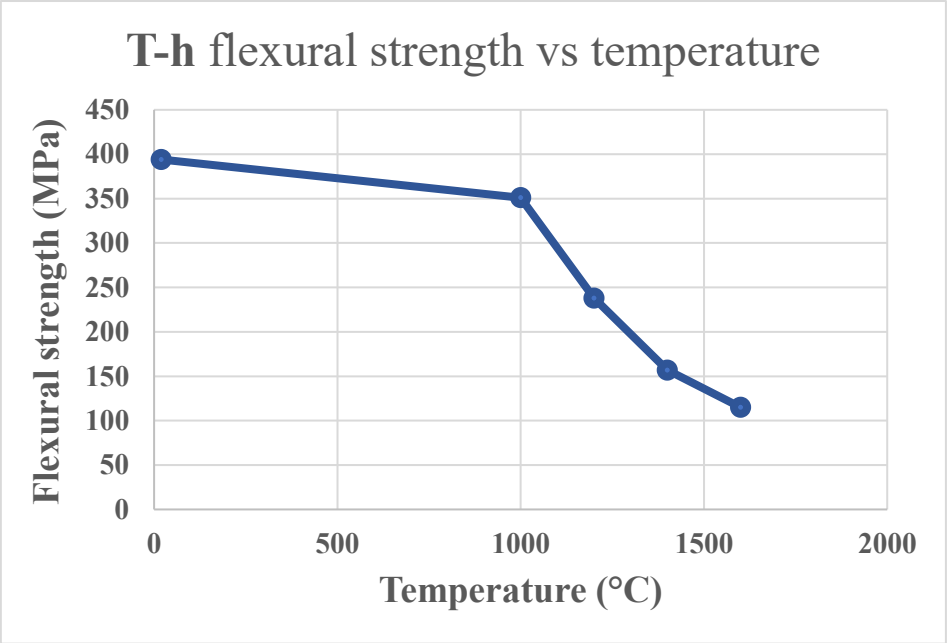

Figure 7.13 Flexural strength versus temperature plot of HEPBM TiB_2 sample (T-h B-2200°C).

Our results are in stark contrast to those presented in the literature, where an increase in flexural strength is reported as the temperature increases due to the relaxation of the material internal stresses (Fig. 7.13) [1]. This result may be due to the different microstructure of the materials, the grain boundary phases, and the presence of macro-defects and large grains formed during the long stay at high temperature in pressure-less sintering (Fig. 7.14).

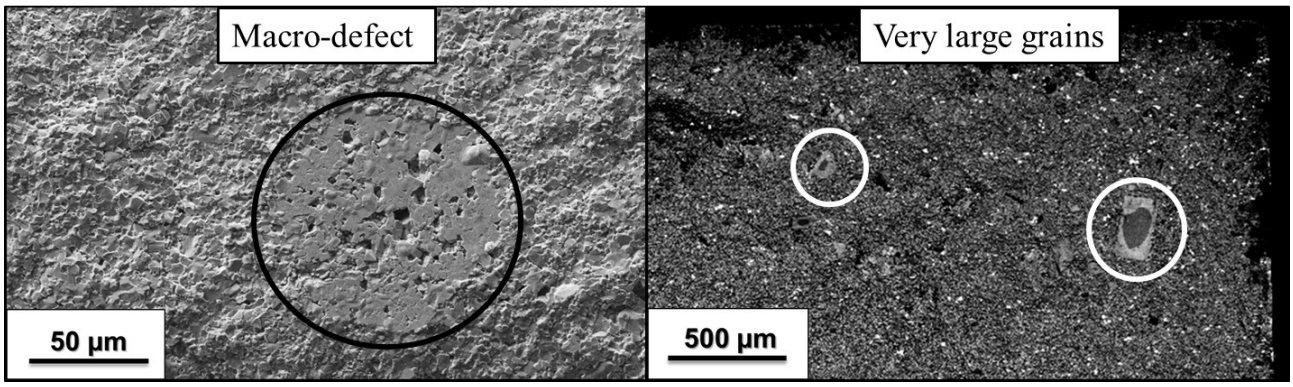

Figure 7.14 Macro-defects and very large grains in the microstructure of the bars obtained from T-h B-2200°C sample.

7.4 Fracture toughness

Bars for fracture toughness were obtained from the T-h B-2200°C sample, also in this case the sample was first cut using EDM and then the oxidized surface was removed, and the final dimensions of 2.0 x 2.5 x 25 mm were obtained by surface grinding.

After grinding, a chevron-type notch was introduced into the samples using a diamond blade, finally the fracture toughness was measured at room temperature and 1000°C under Ar atmosphere using the 4-point method (Table 7.4).

Sample	Temperature (°C)	Fracture toughness (MPa $m^{1/2}$)
T-h B-2200°C	20	4.8 ± 0.2
T-h B-2200°C	1000	5.1 ± 0.3

Table 7.4 4-point fracture toughness test of T-h B-2200°C.

The fractures obtained through measurements at room temperature, except the first (Figure 7.15 a), presented an irregular fracture which exited the notch before it ended (Figure 7.15 b and c). For the purposes of the measurement, the dimensions considered for the calculation of the fracture toughness were those of the notch as per the standard. In the case of measurements at 1000°C, the problem of the fracture coming out from the notch was not encountered (Figure 7.16).

Despite the problem found at room temperature, the fracture toughness measured for this sample displayed a low standard deviation and it was similar to that reported in the literature which varies from 4 to 6 MPa $m^{1/2}$. As the temperature increased, it was noticed an increase in fracture toughness probably due to the decrease in internal residual stresses.

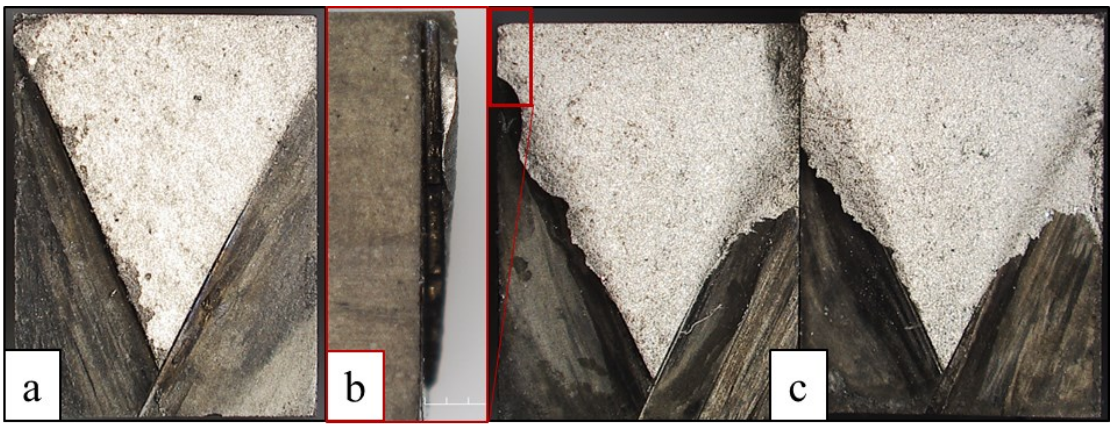

Figure 7.15 Front view of fractures in the first (a) and third (c) room temperature fracture toughness specimens. Lateral view of the fracture in the third specimen (b).

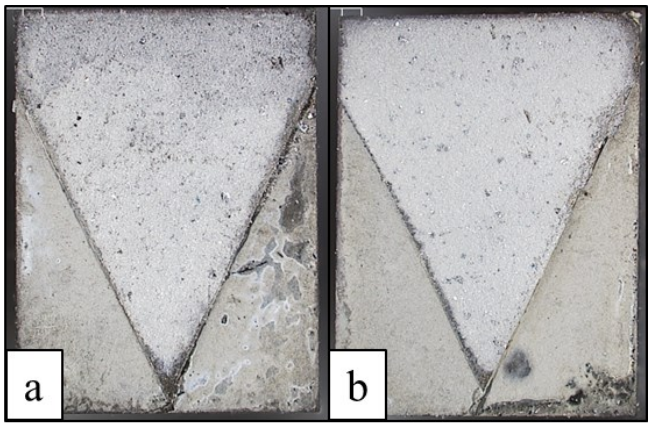

Figure 7.16 Front view of fractures in the first (a) and second (b) 1000°C fracture toughness specimens.

7.5 Thermal and electrical properties

For the measurements of the thermal and electrical properties, a cylindrical pellet with a diameter of 12.7 mm was cut with EDM from the T-h B-2200°C sample. The oxidized surface was then removed by surface grinding, obtaining a final thickness of 2.05 mm.

The density of this round specimen was measured with the Archimedes method obtaining a higher apparent density than that measured for the entire sample (4.57 versus 4.06 g/cm^3).

Thermal diffusivity, specific heat and thermal conductivity were measured by the laser flash method from room temperature to ~200°C and from 200°C to ~2000°C.

7.5.1 Low temperature (25-200°C) thermal properties

Label	Sintering method temp./time (°C, min)	Apparent density (g/cm^3)	Thermal diffusivity (cm^2/s)	Specific Heat (J/Kg K)	Thermal conductivity (W/m K).	Electrical resistivity (μΩ cm)
T-h B-2200°C	PLS, 2200, 60	4.57	0.225	491	50.5	14.6
Ref. TiB_2 [2]	HP, 1800, 60	4.35	0.24	643	68.2	13.9

Table 7.5 Room temperature thermal properties comparison between the T-h B-2200°C sample and the TiB_2 from the literature.
Notes: HP—hot-pressing, PLS—pressure-less sintering.

In Table 7.5 the room temperature thermal properties of the T-h B-2200°C sample are compared with monolithic TiB_2 sintered by Raju et al. [2] via hot-pressing at 1800°C for 60 minutes. From the comparison, lower thermal property values can be noted for the sample prepared in this work, in particular a 6 % lower thermal diffusivity (0.225 versus 0.24 cm^2/s), a 21 % lower specific heat (491 versus 643 J/Kg K) and a 26 % lower thermal conductivity (50.5 versus 68.2 W/m K). In the reference, a long dwell time (60 minutes) and an applied pressure of 30 MPa were used to achieve a high relative density (> 95%) with hot-pressing. The difference between the two samples may be due to the use of high-energy-planetary-ball-milling and the influence of (Ti, W)B_2 solid solution.

As can be seen from the graphs in Figure 7.17, thermal diffusivity decreases by approximately 25% from 25 to 200°C while the specific heat increases by approximately 35%. The thermal conductivity, however, remains stable, around an average value of 49.4 W/m K for the entire temperature range (Figure 7.18).

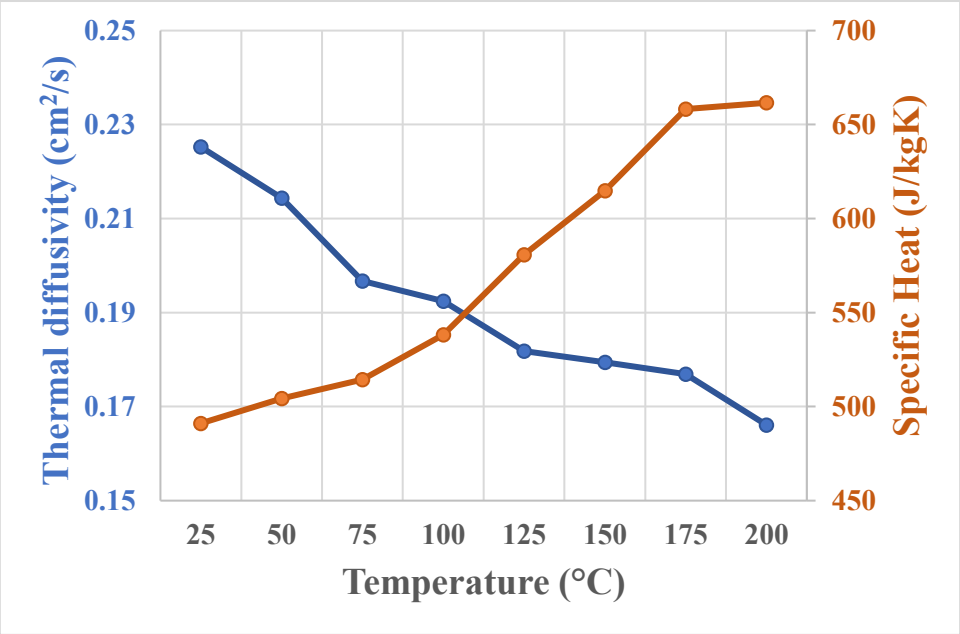

Figure 7.17 Thermal diffusivity and specific heat versus temperature (25-200°C) plot of HEPBM TiB_2 sample (T-h B-2200°C).

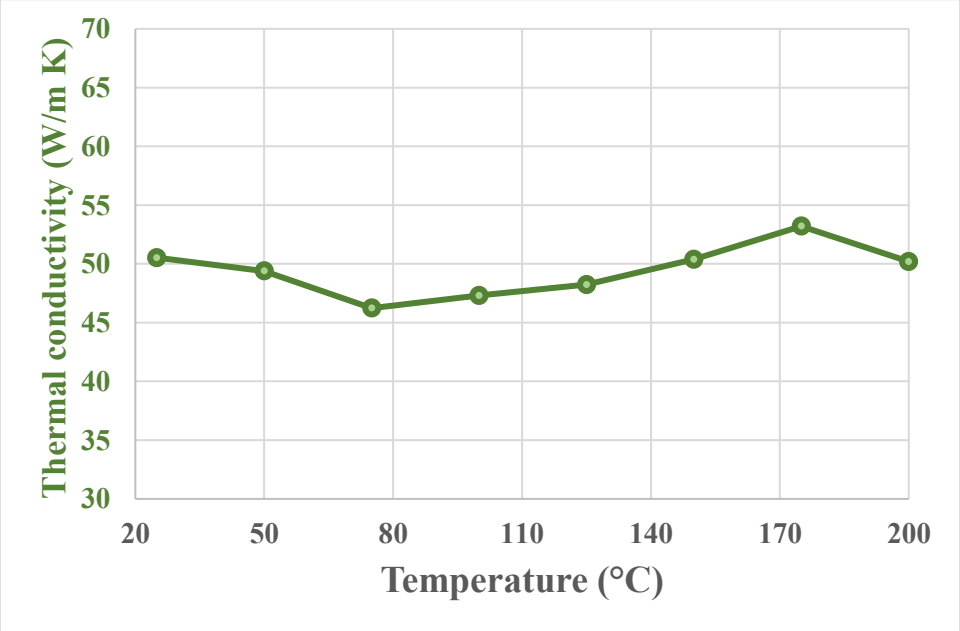

Figure 7.18 Thermal conductivity versus temperature (25-200°C) plot of HEPBM TiB_2 sample (T-h B-2200°C).

7.5.2 High temperature (200-2000°C) thermal properties

Temperature (°C)	Thermal diffusivity (cm^2/s)	Specific Heat (J/Kg K)	Thermal conductivity (W/m K).
25	0.225 ± 0.006	491	50.5
100	0.192 ± 0.010	583	47.3
200*	0.116 ± 0.002*	661*	50.2*
400	0.159 ± 0.004	899	65.3
600	0.147 ± 0.001	934	62.6
800	0.141 ± 0.004	933	60.3
1000	0.136 ± 0.003	960	59.8
1200	0.136 ± 0.003	973	60.6
1400	0.132 ± 0.003	1146	69.0
1600	0.142 ± 0.007	1748	113.4
1800	0.543 ± 0.357	1024	254.4
2000	0.122 ± 0.003	2946	164.1

Table 7.6 Thermal properties of T-h B-2200°C sample.
Notes: *— values measured in the range 25-200°C.

As shown in graph 7.19, thermal diffusivity decreases almost linearly with increasing temperature, from 0.17 cm^2/s at 200°C to 0.12 cm^2/s at 2000°C. On the other hand, heat capacity increases from 683 J/kg K at 200°C to 1145 J/kg K at 1400°C, and then increases more sharply to 2945 J/kg K at 2000 °C. The thermal conductivity (Fig. 7.20), which increases linearly with the change in thermal capacity, increases from 53 to 69 W/m K between 200 and 1400°C, then suddenly triples to 164 W/m K by 2000°C.

The values recorded above 1500°C were “unexpected” and therefore more test in future are planned to validate the trend or better identify the anomaly that occurs in that range of temperatures, possibly linked to what happens with the flexural strength.

The values measured at 1800°C have been omitted due to an anomaly in the measured thermal properties values, in fact thermal diffusivity had a standard deviation more than one hundred times higher than at other temperatures (Table 7.6).

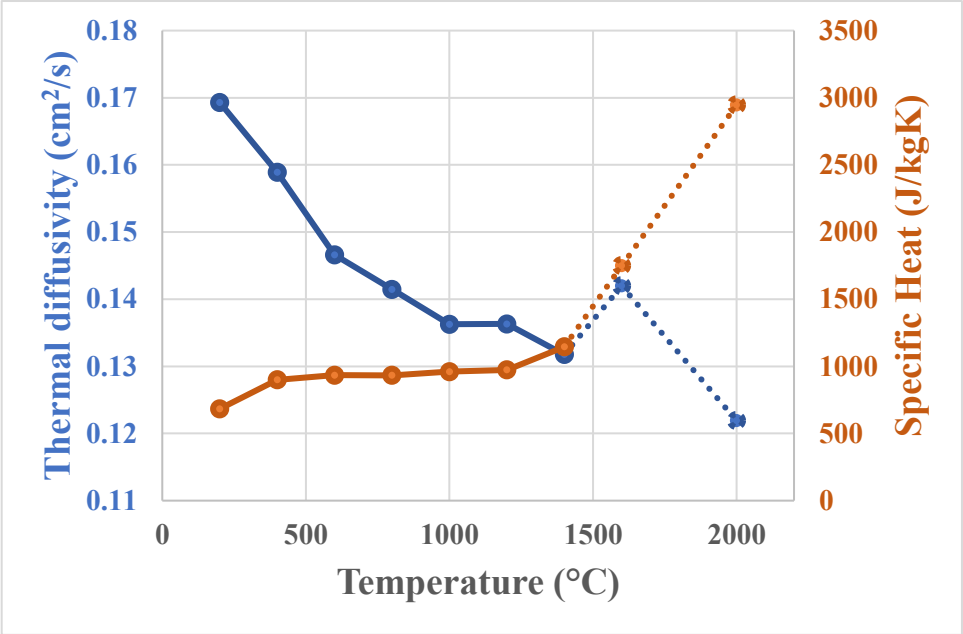

Figure 7.19 Thermal diffusivity and specific heat versus temperature (200-2000°C) plot of HEPBM TiB_2 sample (T-h B-2200°C).

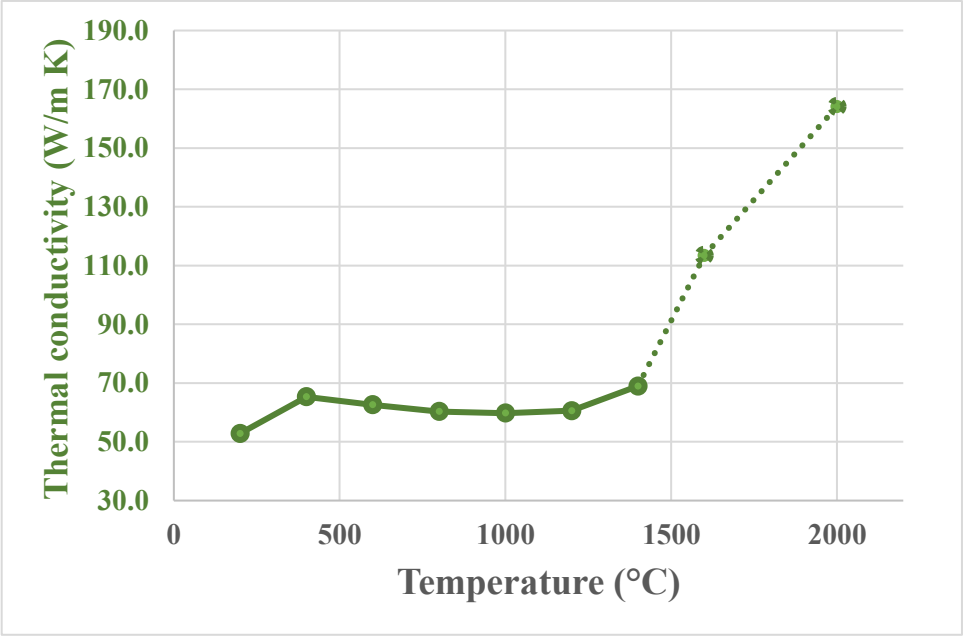

Figure 7.18 Thermal conductivity versus temperature (200-2000°C) plot of HEPBM TiB_2 sample (T-h B-2200°C).

7.5.3 Electrical resistivity

Electrical resistivity was measured by the Van der Pauw method using an in-house fixture at room temperature. The electrical resistivity value measured at room temperature was very similar to that found in the literature (14.6 versus 13.9 μΩ cm). Table 7.7 shows electrical resistivity values for some materials; TiB_2 has values similar to Zr and Hf borides and much lower than other ceramic materials, for example SiC, B_4C, Al_2O_3, being a good electrical conductor.

The electrical conductivity, similar to that of metals, in particular 47.8% compared to Ni and 11.5% to Cu, not only broadens the applications available for TiB_2 but allows good processing by electrical discharge machining.

Label	Room temperature electrical resistivity (μΩ cm)	Reference
TiB_2	14.6	Present work
ZrB_2	10	[3]
HfB_2	11	[3]
B_4C	714	[4]
SiC + 1wt% Be	$3\ 10^{19}$	[5]
SiC + 1wt% B	$2\ 10^{10}$	[5]
SiC + 1wt% Al	$8\ 10^{5}$	[5]
Al_2O_3	10^{20}	[6]
Ti	42	[7]
Ni	6.99	[7]
Cu	1.68	[7]

Table 7.7 Room temperature electrical resistivity for ceramic and metallic materials.

7.6 Conclusions

A preliminary analysis on the mechanical properties of the prepared samples was performed by measuring the Vickers hardness (load 9.8 N). Both hot-pressed and pressure-less sintered samples showed improved hardness when added with $MoSi_2$ and/or high-energy-planetary-ball-milled.

Of the most promising mixtures, two larger pressure-less sintered discs were prepared at 2100°C, from which specimens were obtained by electrical discharge machining. The specimens were tested directly without grinding or polishing, obtaining very high standard deviation values. The HEPBM TiB_2 (T-h) sample showed a high flexural strength (460 MPa), higher than those in the literature, while the HEPBM $MoSi_2$ (TM5-h) sample displayed a very low flexural strength (259 MPa) due to the residual porosity (about 5%).

Two other T-h pressure-less discs sintered at 2200°C were prepared and processed via electrical discharge machining to obtain specimens which were subsequently ground and polished. These specimens were tested to measure mechanical, thermal and electrical properties during my stay in Professor Fahrenholtz's research group at the Missouri University of Science and Technology. These samples displayed a lower standard deviation but also a lower flexural strength (394 MPa) due to their lower relative density. The flexural strength was also tested at high temperatures showing a drop above 1000°C and softening at 1600°C with non-elastic behavior and bending without breaking at low crossheads rates.

The fracture toughness was measured for the T-h sample at room temperature and 1000°C (4.8 and 5.1 MPa respectively) recording values very similar and in agreement with the literature.

The measured room temperature thermal properties had lower values than those of TiB_2 present in the literature with a 25% lower thermal conductivity (50.5 W/m K). Heat capacity and thermal conductivity moreover showed a “unexpected” sudden increase above 1400°C.

The electrical resistivity, however, was similar to that of Zr and Hf borides and much lower than other oxide and non-oxide ceramics and comparable to that of metals.

7.7 References

[1] R.G. Munro, Material properties of titanium diboride, J. Res. Natl. Inst. Stand. Technol. 105 (2000) 709. https://doi.org/10.6028/jres.105.057.

[2] G.B. Raju, B. Basu, A.K. Suri, Thermal and electrical properties of TiB2–MoSi2, International Journal of Refractory Metals and Hard Materials. 28 (2010) 174–179. https://doi.org/10.1016/j.ijrmhm.2009.08.002.

[3] W.G. Fahrenholtz, G.E. Hilmas, I.G. Talmy, J.A. Zaykoski, Refractory Diborides of Zirconium and Hafnium, J American Ceramic Society. 90 (2007) 1347–1364. https://doi.org/10.1111/j.1551-2916.2007.01583.x.

[4] J.S. says, Boron Carbide (B4C) - Properties and Information about Boron Carbide, AZoM.Com. (2001). https://www.azom.com/article.aspx?ArticleID=75 (accessed October 16, 2023).

[5] Y. Takeda, K. Nakamura, K. Maeda, Y. Matsushita, Effects of Elemental Additives on Electrical Resistivity of Silicon Carbide Ceramics, Journal of the American Ceramic Society. 70 (1987) C-266-C–267. https://doi.org/10.1111/j.1151-2916.1987.tb04895.x.

[6] Aluminum Oxide | Al2O3 Material Properties, (n.d.). https://www.accuratus.com/alumox.html (accessed October 16, 2023).

[7] A Table of Electrical Conductivity and Resistivity of Common Materials, ThoughtCo. (n.d.). https://www.thoughtco.com/table-of-electrical-resistivity-conductivity-608499 (accessed October 16, 2023).

8. Conclusions and outlook

The primary goal of this thesis was to explore the manufacturing of a high-density TiB_2-based material with favorable mechanical, thermal, and electrical properties using the pressure-less sintering (PLS) technique. Achieving fully dense TiB_2 ceramics with a fine microstructure and improved properties can be challenging due to the limited sintering capability of this covalently bonded boride.

In this thesis work, different sintering aids (B_4C, Si_3N_4 and $MoSi_2$) and powder preparation methods (ball-milling and high-energy-milling) were used to improve the densification and final properties of sintered TiB_2. In Chapter 4, samples with different additives and preparation methods were hot-pressed (HP) and their properties were compared to those reported in the literature. Based on the results of these preliminary tests, the mechanisms by which the additives promoted sintering and their effect on the final properties were hypothesized.

Chapter 5 evaluated the different compositions in pressure-less sintering with different sintering conditions. From these tests the best sintering conditions for each composition were identified. In this chapter, scale-up tests were conducted, moreover the amount of sintering aid was optimized.

Chapter 6 focused on high-energy milling with WC-Co media. The effect of this technique was investigated by milling green powders for different HEM durations and sintering them in PLS. The reproducibility of this technique was also tested by repeating experiments over time. Finally, the mechanism induced by of high energy milling with WC milling media was investigated comparing the microstructure of TiB_2 powders sintered with addition of WC powders.

Chapter 7 was dedicated to mechanical, thermal, and electrical properties of pressure-less sintered TiB_2 at room and high (1000-2000°C) temperature. The properties were compared with those of monolithic TiB_2 from the literature to evaluate the effects of additives and understand the new possibilities and limitations of the developed material.

The main results can be summarized in the following points:

- Effect of high-energy-milling

High-energy milling significantly improved the sintering of TiB_2 by reducing particle size, increasing the surface area, and introducing submicrometric WC-Co debris. This resulted in good densification and mechanical properties in both hot-pressing and pressure-less sintering.

The WC-Co added via HEM reacted with the oxide phases (mainly with B_2O_3) present on the particle surface, resulting in secondary WB phases. Addition of cobalt and chromium, present as a binder in WC media, contributed to the formation of a liquid phase at grain boundaries at high temperatures, which improved TiB_2 sintering.

Shrinkage began at 1570°C and the presence of a liquid phase caused partial dissolution of W in TiB_2, forming a core-shell microstructure in which cores of pure TiB_2 were surrounded by (Ti, W)B_2 mixed boride solid solution.

Increasing the high-energy-milling time from 10 to 30 minutes the amount of incorporated WC-Co increased linearly with time. In contrast, the average particle size decreased significantly within the first 10 minutes (passing from 3.80 to 2.84 μm). HEM mainly affected particles larger than 1.5 μm, since no significant changes in particle distribution were observed below this size, while the added submicrometric WC-Co debris were smaller than 0.5 μm. All HEM samples had high relative densities (96.7, 98.1 and 99.2 % for 10, 20, and 30 minutes HEM respectively) after PLS, increasing as the grinding time increased.

When WC powders were added to TiB_2 without high energy milling, a low densification (≈ 75 %) and limited formation of solid solution was observed. This indicates that HEM had a more extensive role than simply decreasing the grain size and introducing WC. In particular, HEPBM introduced Co and Cr in the powders, which contributed to forming the liquid phase at the grain boundary.

All in all, this method was suitable for use on a laboratory scale to produce TiB_2 with high densities and mechanical properties. However, to scale up the process, a different type of mill is needed, as planetary mills are not suitable for this purpose. One possibility is to use attrition mills.

- Effect of sintering aids

All the additives examined were shown to improve the sintering of TiB_2, with densification in hot-pressing beginning at a lower temperature than for TiB_2 alone (T, 1950°C). Specifically, shrinkage began at 1630°C with the addition of B_4C (TC5), 1770°C with Si_3N_4 (TS5), and 1710°C with $MoSi_2$ (TM5).

B_4C had a poor effect on the densification of TiB_2, while the addition of Si_3N_4 and $MoSi_2$ improved the densification up to 85.6 and 95.1 % rate respectively and resulted in the formation of secondary phases. Specifically, a liquid phase was formed at around 1600°C with both Si-based sintering aids, which improved the densification rate but left silica pockets within the sintered sample. The use of $MoSi_2$ as a sintering aid led to the formation of a core-shell structure similar to that observed with high-energy-milling where the cores were pure TiB_2 and the rims were formed by (Ti, Mo)B_2 solid solution.

Adding B_4C and Si_3N_4 to the mixture caused uncontrolled grain growth during pressure-less sintering. $MoSi_2$, on the other hand, proved to be the most promising additive, both in terms of final density and mechanical properties, in HP and PLS.

By high-energy-milling compositions with sintering aids wet-ball-milled, even more promising results were achieved. Starting shrinkages were recorded at 1530°C for the B_4C composition (TC5-h), at 1560°C for the Si_3N_4 composition (TS5-h), and at 1250°C for the $MoSi_2$ composition (TM5-h), compared to 1570°C for the just HEM TiB_2 composition (T-h). All high-energy-milled compositions presented similar core-shell microstructure, for the TM-h sample there were inclusions of (W, Mo)B and the rim were instead formed by a solid solution of (Ti, W, Mo)B_2. Moreover, TM5-h achieved almost complete densification (although limited by the presence of silica pockets) at 1700°C.

The hot-pressed samples with the highest hardness were HEM TiB_2 (24.5 GPa) and both $MoSi_2$ samples (24.4 GPa), regardless of preparation method. In the PLS tests, TM5-h had the highest hardness (26.8 GPa), followed by T-h (24 GPa). TM5 had a hardness of 21.4 GPa, and all other compositions had lower Vickers hardness.

- Pressure-less sintered TiB_2

High-energy-milled TiB_2 was pressure-less sintered at different temperatures between 2000°C and 2100°C, reaching good density (> 4.5 g/cm^3), low residual porosity (< 2 %), and a fine microstructure (mean grain size ~ 1.5 µm) for all samples. Scale-up tests for this composition revealed no significant differences in density, microstructure, or Vickers hardness for the bigger samples which indicates good scalability.

High-energy-milled samples with sintering aids were pressure-less sintered at 1900°C and 2000°C. Although shrinkage began at a very low temperature (around 1500°C) in the hot-pressing tests, all PLS samples had higher densities and hardness at 2000°C. This indicates that pressure-less sintering requires much higher temperatures than hot pressing, despite the longer dwell time used (60 minutes for PLS versus 10 minutes for HP).

The microstructure of the pressure-less sintered HEM samples was very fine for all samples (mean grain size approximately 1.2 µm) and displayed a core-shell structure. The extension of the rims was more pronounced than for the HP sintered samples because of the higher temperatures and longer holding time. The HEM samples with Si_3N_4 and $MoSi_2$ after PLS retained silica pockets at triple points but also many empty porosities because some of the silica left the bulk during sintering. Regarding $MoSi_2$ samples (TM and TM-h), mixtures with less sintering aid were also tested to try to optimize its content, however 5 vol% was the minimum amount for achieving the best mechanical properties.

In summary, the compositions that proved most promising for pressure-less sintering were those of high-energy-milled TiB_2 with and without $MoSi_2$ (T-h and TM5-h).

- Properties of PLS TiB_2

Preliminary room temperature flexural strength tests were performed on T-h and TM5-h samples sintered in PLS at 2100°C for 60 minutes and machined by EDM, without surface grinding. The values of the sample without additive (460 ± 108 MPa) were higher than those of the sample with $MoSi_2$ (259 ± 148 MPa). In both cases, the standard deviations were very high.

During the time at the Missouri University of Science and Technology, extensive testing was performed on T-h samples PLS at 2200°C for 60 minutes. The samples were surface ground after EDM cutting. The resulting flexural strength at room temperature was lower (394 ± 27 MPa) than previously reported, possibly due to the different sintering conditions, but with a much smaller standard deviation.

High-temperature flexural strength dropped above 1000°C, reaching 238 MPa at 1200°C. At 1600°C, the material softened and exhibited non-elastic behavior, bending without breaking at low crosshead rates. Increasing the crosshead speed from 0.8 to 2.4 mm/min resulted in elastic behavior, but the measured flexural strength (115 MPa) dropped to approximately 70% less than the value at room temperature. This phenomenon at 1600°C of softening was probably due to the growth of mixed boride phases or to the melting of the secondary phase at the grain boundaries present as residue of the liquid phase formed during sintering.

The fracture toughness of the T-h sample was measured at room temperature and 1000°C (4.8 and 5.1 MPa respectively), recording values similar to those reported in the literature.

The measured thermal properties had lower values than those of TiB_2 present in the literature with a 25% lower thermal conductivity (50.5 W/m K). The electrical resistivity, however, was similar to that of Zr and Hf borides and much lower than other oxide and non-oxide ceramics and comparable to that of metals.

In conclusion, this thesis developed a scalable and industrially suitable process for the preparation and pressure-less sintering of TiB_2-based material. High energy milling was found to be a very promising method for the processing of TiB_2 with enhanced mechanical properties. Thermal, mechanical and electrical properties were in agreement with state-of-art TiB_2 produced with more expensive techniques. The load/displacement curve of the high-energy-milled TiB_2 showed a linear response up to 1500°C but at 1600°C the strength dropped due to the softening.

Acknowledgement

This dissertation marks the culmination of a three-year journey that has been a source of significant growth, both academically and personally. During this time, I have had the privilege of collaborating with the exceptional researchers at the CNR of Faenza, gaining invaluable insights into the scientific method and the intricacies of ceramics. I have also had the privilege of pioneering uncharted territories in industrial research, contributing to the birth of a new department within Industrie Bitossi. It was a challenging journey, but not one I had to navigate alone. For this I want to thank all the people who accompanied and supported me in this adventure.

I would like to thank my mentors for providing the opportunity to pursue this path and guiding me through it. In particular, I am grateful to my supervisor, Dr. Diletta Sciti, for welcoming me into the Structural Ceramics Group at CNR-ISSMC and providing motivation and encouragement during challenging times. Dr. Sciti also helped me stay grounded in moments of excitement and ensured that I maintained a balanced perspective throughout my PhD journey. I would also like to express my gratitude to Dr. Riccardo Rovai of Industrie Bitossi for his unwavering support throughout my PhD journey. His mentorship and our phone calls were instrumental in providing me with a valuable industrial perspective on ceramics. I also want to thank Dr. Simone Failla who introduced me to the world of ceramic research. His patient guidance and hands-on approach enabled me to take my first tentative steps amidst the presses, kilns, the sieves and mills of the laboratory and SEM micrographs.

My heartfelt gratitude extends to the other members of the Structural Ceramics Group, particularly Dr. Matteo Mor, whose company made our shared office a truly magical space, and with Dr. Francesca Servadei, they supported me through challenging times, generously sharing their expertise and experience. They have been exceptional mentors, invaluable colleagues, and cherished friends. A special thanks also to Dr. Antonio Vinci, Dr. Pietro Galizia and Dr. Luca Zoli for their support, help and opinions in shaping my research path. I want to acknowledge the invaluable technical assistance provided by the researchers and technicians who played a pivotal role in various aspects of this PhD, from theoretical discussions to measurements and other technical support. I want also thank Claudio Capiani for his expertise in XRD analysis, Mauro Mazzocchi for his support with scanning electron microscopy, and Cesare Melandri for his contributions in the mechanical characterization of my materials.

Thanks also to Simone and Federico, great office mates even during Covid. And to all those who listened to me, supported me and joked with me, getting my bizarre speeches during lunch or on the daily journeys by bike or train to and from home. Thanks to Maria, Andrea, Sara, Lorenzo, Arianna, Giada, Alberto, Ilaria.

During these years I have often spent a few days in a row in Vinci working in Industrie Bitossi in our "Reparto dei Miracoli", but I always felt at home. For this I must thank Cosimo Cecconi, a great colleague and a dear friend with whom I faced most of the difficulties and the ruminations on the industrial challenges of an innovative process, Giacomo Rappuoli and Alice Bertolini who participated in the creation with creativity, intelligence and sympathy. And finally, Andrea Parentini and Edoardo Fossi who showed that they can shine even covered in black powder. Thanks also to Nik, who during our evening chats and Friday meetings taught me many things about ceramics and gave me a different perspective from which to look at the world. And not only them, but there were also many people who supported me along my industrial path by helping me and advising me, Marco A., Marco. P., Giulia, Enrico, Luca, Federico and Roberta.

My academic career was further enriched by my research period in the United States. I am deeply grateful to Dr. William G. Fahrenoltz, who made it possible for me to work in his group at the Missouri University of Science and Technology. I would also like to thank Dr. Jeremy Watts, Nathan, Paul, and Steve for introducing me in their group and supporting my research.

I am also deeply grateful to Prof. Enrico Dalcanale, the coordinator of this PhD program, for his prompt and insightful responses to my questions about courses, ECTS credits, and funding availability. Thanks also to Prof. Angelo Vaccari for showing me this path and giving me advice that still illuminates my journey today.

In closing, I would like to dedicate this significant milestone to my dearest friends and family. To Giorgia, my best friend, lover, and companion, who stood by me throughout these three years, in the most beautiful moments and in the most complicated ones, bringing a touch of vibrant color to my life. Thanks to her parents Cristina and Paolo who have always been there for both of us.

To my friends from Riccione and Bologna that despite the distances, have always been present, particularly Simone, Elin, Luca, and Davide. To the extraordinary people I met in Imola and with whom I nurtured our Officina Coboldi association, Sbax, Gaia, Barbara, Elisa, Monte, Giuseppe, Teo, Sara, Pierluigi, Claudia, and countless others too numerous to mention.

To my grandmothers, Antonia and Francesca and to my brother Andrea. And finally, above all to my mother and my father, who have always supported me from the beginning, took care of me and really made all this possible.

Thank you deeply.